

THEORETICAL AND NUMERICAL STUDIES OF CHAOTIC MIXING

A Dissertation

by

HO JUN KIM

Submitted to the Office of Graduate Studies of
Texas A&M University
in partial fulfillment of the requirements for the degree of

DOCTOR OF PHILOSOPHY

May 2008

Major Subject: Mechanical Engineering

THEORETICAL AND NUMERICAL STUDIES OF CHAOTIC MIXING

A Dissertation

by

HO JUN KIM

Submitted to the Office of Graduate Studies of
Texas A&M University
in partial fulfillment of the requirements for the degree of

DOCTOR OF PHILOSOPHY

Approved by:

Co-Chairs of Committee,	Ali Beskok Sai C. Lau
Committee Members,	Debjyoti Banerjee Obdulia Ley Victor M. Ugaz
Head of Department,	Dennis O'Neal

May 2008

Major Subject: Mechanical Engineering

ABSTRACT

Theoretical and Numerical Studies
of Chaotic Mixing. (May 2008)

Ho Jun Kim, B.S., Hanyang University;

M.S., Texas A&M University

Co-Chairs of Advisory Committee: Dr. Ali Beskok
Dr. Sai C. Lau

Theoretical and numerical studies of chaotic mixing are performed to circumvent the difficulties of efficient mixing, which come from the lack of turbulence in microfluidic devices. In order to carry out efficient and accurate parametric studies and to identify a fully chaotic state, a spectral element algorithm for solution of the incompressible Navier-Stokes and species transport equations is developed. Using Taylor series expansions in time marching, the new algorithm employs an algebraic factorization scheme on multi-dimensional staggered spectral element grids, and extends classical conforming Galerkin formulations to nonconforming spectral elements. Lagrangian particle tracking methods are utilized to study particle dispersion in the mixing device using spectral element and fourth order Runge-Kutta discretizations in space and time, respectively. Comparative studies of five different techniques commonly employed to identify the chaotic strength and mixing efficiency in microfluidic systems are presented to demonstrate the competitive advantages and shortcomings of each method. These are the stirring index based on the box counting method, Poincaré sections, finite time Lyapunov exponents, the probability density function of the stretching field, and mixing index inverse, based on the standard deviation of scalar species distribution. Series of numerical simulations are performed by varying the Peclet number (Pe) at fixed kinematic conditions. The mixing length (l_m) is

characterized as function of the Pe number, and $l_m \propto \ln(Pe)$ scaling is demonstrated for fully chaotic cases. Employing the aforementioned techniques, optimum kinematic conditions and the actuation frequency of the stirrer that result in the highest mixing/stirring efficiency are identified in a zeta potential patterned straight micro channel, where a continuous flow is generated by superposition of a steady pressure driven flow and time periodic electroosmotic flow induced by a stream-wise AC electric field. Finally, it is shown that the invariant manifold of hyperbolic periodic point determines the geometry of fast mixing zones in oscillatory flows in two-dimensional cavity.

DEDICATION

To my parents, Yong Sou Kim and Hyo Sook Lee

For their love and sacrifices

ACKNOWLEDGEMENTS

I will always value having Prof. Ali Beskok as my advisor. His positive influence on my professional and personal development will continue to benefit me throughout life. My biggest hurdle for first year in the dissertation research was understanding of chaotic dynamics and spectral element method. And, like many students doing their Ph.D., my research often shifted between various avenues before it settled into something meaningful enough to be publishable. I am grateful to Prof. Ali Beskok for his guidance and tremendous patience.

I sincerely thank my colleagues, Pradip Bahukudumbi, Ashwin K. Balasubramanian, Bo Hung Kim, Seungkyung Park, and Bayram Celik. During my graduate studies at TAMU, I have met and interacted with an array of interesting and gifted individuals. I feel that this section would not be complete without thanking Bong Su Koh, and Yeontack Ryu for all their help and guidance. I sincerely appreciate the rich experience that I enjoyed during my time at TAMU and I know that I will miss all that the university has to offer. Some portions of this research were supported by the National Science Foundation under Grant No. 0306622.

上善若水 - 老子

The highest goodness is such as the flowing water. - Laozi

NOMENCLATURE

Alphabet

A	velocity ratio, = U_0 / U_{HS}
C	dimensionless concentration
D	mass diffusivity
h	net stretching, = l / l_0
H	half channel height
H_n	probability density function of stretching
L	overall stretching
l_0	initial stretching or initial length of fluid filament
l_m	mixing length
$l_{m,90}$	required mixing length for 90% mixing
L	length of mixing block
n	number of mixing blocks
n_{90}	number of mixing blocks for 90% mixing
Pe	Peclet number, = $U_{HS} H / D$
Re	Reynolds number, = $U_{HS} H / \nu$
Sc	Schmidt number, = ν / D
St	Strouhal number, = $\omega H / U_{HS}$
t	dimensionless time
T	time period of the AC electric field
U_{HS}	Helmholtz-Smoluchowski velocity
U_0	Poiseuille flow channel centerline velocity
x	dimensionless horizontal coordinate

y dimensionless vertical coordinate

Greek

α *modular*($t, 2\pi$)

σ standard deviation of concentration values

ν kinematic viscosity

ω frequency of AC electric field

TABLE OF CONTENTS

	Page
ABSTRACT	iii
DEDICATION	v
ACKNOWLEDGEMENTS	vi
NOMENCLATURE	vii
TABLE OF CONTENTS	ix
LIST OF FIGURES	xii
CHAPTER	
I INTRODUCTION AND LITERATURE REVIEW	1
1.1. Development of spectral element algorithm	2
1.2. Quantification of chaotic strength and mixing in a microfluidic system	4
1.3. An electroosmotically stirred continuous flow micro-mixer	6
1.4. Numerical analysis of dynamic skeleton of chaotically stirred flows	11
II DEVELOPMENT OF SPECTRAL ELEMENT ALGORITHM	13
2.1. Governing equations and formulation	13
2.1.1. Governing equations	14
2.1.2. Weak forms and spatial discretizations using spectral element approximation	15
2.1.3. Algebraic factorization scheme	21
2.1.4. Taylor-Galerkin based algorithm	24
2.1.5. Particle tracking	27
2.2. Nonconforming spectral element method.....	31
2.2.1. Conformity matrix using pointwise matching method (PMM)	34
2.2.2. Conformity matrix using integral projection method	

CHAPTER	Page
	(IPM) 36
	2.2.3. Modified global assembly process and modified mass matrix 38
	2.3. Convergence test 40
	2.3.1. Scalar convection-diffusion problems in multi dimensions 40
	2.3.2. Stokes cell flow 44
	2.3.3. Kovasznay flow 46
III	CODE VERIFICATION BY THE ALGEBRAIC FACTORIZATION SCHEME 53
	3.1. Moving Gaussian hill 53
	3.2. Creeping flow in a wedge 56
	3.3. Singular lid driven cavity flow 58
	3.4. Transient flow over a backward facing step 62
	3.5. Transient flow past a circular cylinder 65
	3.6. Thermally driven flows 74
IV	QUANTIFICATION OF CHAOTIC STRENGTH AND MIXING IN A MICROFLUIDIC SYSTEM 81
	4.1. Introduction 81
	4.2. Flow model 82
	4.3. Particle tracking and numerical methodology 86
	4.4. Particle dispersion and box counting method 88
	4.5. Poincaré sections 94
	4.6. Lyapunov exponents 97
	4.7. Probability density of stretching 101
	4.8. Species transport equation solutions 105
V	AN ELECTROOSMOTICALLY STIRRED CONTINUOUS FLOW MICRO-MIXER 111
	5.1. Introduction 111
	5.2. Theoretical framework 112

CHAPTER	Page
5.3. Particle dispersion	117
5.4. Poincaré section	120
5.5. Stretching of fluid filaments	124
5.6. Numerical simulation of scalar transport	131
 VI NUMERICAL SIMULATIONS OF CHAOTIC STIRRERS	 138
6.1. Chaotic stirring in a three dimensional cavity	138
6.1.1. Computational issues	139
6.1.2. Particle dispersion	141
6.2. Chaotic mixing of cavity flows at finite Reynolds numbers	146
6.2.1. Problem description	147
6.2.2. Optimum kinematic conditions	150
6.2.3. Detection of periodic points	157
6.2.4. Invariant manifold and fast mixing	160
 VII SUMMARY AND DISCUSSION	 167
7.1. Quantification of chaotic strength and mixing in a microfluidic system	 168
7.2. An electroosmotically stirred continuous flow micro-mixer	171
7.3. Numerical analysis of the relation between invariant manifold and chaotic mixing in oscillatory driven cavity flow	 173
 REFERENCES	 174
 VITA	 182

LIST OF FIGURES

FIGURE	Page
1.1 Two dimensional model of mixing in a straight channel. At the entry of the mixer ($x = 0$) the marker has concentration values of $C = 0.5$ (red) and $C = -0.5$ (blue) in the upper and lower halves of the domain. Therefore, a perfect mix would reach $C_\infty = 0$ (green).	8
1.2 A series of results from analytical solutions [55] by varying the Peclet number: Concentration contours at $Pe = 400$ (a), 1000(b), 4000(c), and 6000(d).	8
2.1 Grid points in the parametric spaces: two-dimensional 6 th -order <i>GLL</i> (a) and 4 th -order <i>GL</i> (b) mesh and three-dimensional 6 th -order <i>GLL</i> (c) and 4 th -order <i>GL</i> (d) mesh.	20
2.2 Two-dimensional isoparametric mapping between the physical and the parametric spaces.	30
2.3 Interpretation of the 4 th order Runge–Kutta integration.	30
2.4 Different types of elemental interfaces: (a) Conforming mesh, (b) Conforming geometry, Nonconforming polynomially, (c) Nonconforming geometry, Conforming polynomially, (d) Nonconforming both polynomially and geometrically.	33
2.5 (a) Original element with $n_{cp} = 16$, (b) Modified element constrained by maximum rule with $n_{cp} = 17$. Nonconforming interface is indicated with a red line between two elements.	35
2.6 Convergence test of two dimensional case at $Pe = 100$: (a) Spatial convergence, $dt = 0.00001$, (b) Temporal convergence, $N_x = N_y = 10$	42
2.7 Convergence test of three-dimensional case at $Pe = 500$: (a) Spatial convergence of $dt = 0.0001$, (b) Temporal convergence of $N_x = N_y = N_z = 10$	43
2.8 Stokes cell flow (a) streamlines, (b) <i>GLL</i> mesh for velocities, (c) Spectral convergence of L_∞ error is achieved in both u_x and u_y velocity values.	45
2.9 Kovasznay flow at $Re = 40$ on two-dimensional conforming grids with curved element boundaries: Curved boundaries are indicated with thick red line in (a) and (b); (a) <i>GLL</i> mesh for velocities, (b) <i>GL</i> mesh for pressure, (c) Spectral convergence of L_∞ error is achieved in both u_x and u_y velocity values.	49

FIGURE	Page	
2.10	Kovaszny flow at $Re = 40$ on three-dimensional conforming grids: (a) <i>GLL</i> mesh for velocities, (b) Spectral convergence of L_∞ error is achieved in u_x velocity values.	50
2.11	Kovaszny flow at $Re = 40$ on two-dimensional p -type non-conforming grids: (a) u_x velocity contour plotted on the <i>GLL</i> mesh. Contour plots are produced by <i>TecplotTM</i> , which can not perform polynomial expansions, creating coarser looking results than the actual high-order ones. (b) temporal record of L_∞ error during time integration of projection scheme. The initial conditions are chosen to be zero velocity and pressure, which satisfy incompressibility constraint.	51
2.12	Kovaszny flow at $Re = 40$ on three-dimensional p -type non-conforming grids: (a) non-conforming mesh for velocities, (b) Spectral convergence of L_∞ error is achieved in u_x velocity values by utilizing both PMM and IPM. ...	52
3.1	Numerical results for the convection of Gaussian hill ($Pe = 10^6$): (a) Problem configuration and initial condition on conforming grids ($N = 8$), Contour plots of (b), (c), and (d) are captured at $t = 1.2$ and time integration is performed with time increment of $dt = 10^{-4}$. h -type refinement is done from (b) to (c). p -type refinement is done from (c) to (d) only on the pink-colored elements. The elemental discretization is shown by the thick lines and the quadrature points are shown by the thin lines.	55
3.2	Stokes flow in a wedge – (a) <i>GLL</i> computational mesh: The elemental discretization is shown by the thick lines and the quadrature points are shown by the thin lines. (b) streamlines.	57
3.3	The center-line transverse u_x velocity as a function of perpendicular height from the top of the wedge shown in figure 3.2.	57
3.4	Problem configuration for the flow in a square cavity at $Re = 1000$: (a) boundary conditions, (b) mesh A – conforming, (c) mesh B – conforming, (d) mesh C - non-conforming.	60
3.5.	(a) u_x velocity distribution along the $x = 0.5$ line, (b) u_y velocity distribution along the $y = 0.5$ line; The results are compared with the spectral solutions in [80] at $Re = 1000$	61
3.6	Problem configuration for the flow past a backward-facing step: (a) boundary conditions, (b) <i>GLL</i> computational mesh: The elemental discretization is shown by the thick lines and the quadrature points are shown by the thin lines.	63
3.7	Numerical results for the flow past a backward facing step: (a) streamlines are plotted on the vorticity contour at $Re = 500$, (b) Re and the reattachment	

FIGURE	Page
length (L_r) of the primary eddy.	64
3.8 Problem configuration for the flow past a circular cylinder at $Re = 125$ in a straight channel: (a) boundary conditions, (b) <i>GLL</i> computational mesh: The elemental discretization is shown by the thick lines and the quadrature points are shown by the thin lines. The history of the horizontal velocity, u_x , at a node situated at the point indicated with a red circle is recorded.	67
3.9 Time history of nodal u_x velocity at $Re = 125$	68
3.10 Instantaneous: (a) pressure and (b) vorticity contours at $t = 210$, for the flow past a circular cylinder at $Re = 125$ in a straight channel.	69
3.11 Problem configuration for the plug flow past a circular cylinder at $Re = 100$: (a) boundary conditions, (b) <i>GLL</i> computational mesh: The elemental discretization is shown by the thick lines and the quadrature points are shown by the thin lines. The history of the horizontal velocity, u_x , at a node situated at the point indicated with a red circle is recorded.	71
3.12 Time history of nodal u_x velocity at $Re = 100$	72
3.13 Instantaneous: (a) pressure and (b) vorticity contours at $t = 800$, for the plug flow past a circular cylinder at $Re = 100$	73
3.14 Problem configuration for the buoyancy-driven flow inside a square enclosure: (a) boundary conditions and, computational mesh (b) type A (left) and (c) B (right): The elemental discretization is shown by the thick lines and the quadrature points are shown by the thin lines.	77
3.15 Numerical results for 2D thermal cavity: temperature contours on mesh type A at $Ra =$ (a) 10^3 , (b) 10^4 , (c) 10^5 , and (d) 10^6 . Thin black lines denote isotherms at intervals of 0.05.	78
3.16 Numerical results for 2D thermal cavity: streamlines of velocity fields computed on mesh A at Ra equals to (a) 10^3 , (b) 10^4 , (c) 10^5 , and (d) 10^6	79
3.17 (a) u_x velocity and (b) temperature along the vertical midlines of the enclosure ($x = 0.5$) at $Ra = 10^6$	80
4.1 Electroosmotically induced flow patterns: A, B, C, D. Arrows show the electroosmotic flow direction induced by the zeta potential patterned surfaces. The side surfaces of the mixing domain are periodic.	83
4.2 Snapshots of spread of passive tracer particles for cases B&C at period $T = 6$ (a); and A&D at period $T = 6$ (b). A total of 40,000 passive particles are tracked in time. Snapshots show the dispersing state at respective times.	

FIGURE	Page
Figure (a) shows flow domain filled with passive tracer particles, and these particles are distributed uniformly at $t = 102$. Figure (b) shows presence of two small void regions that remain near the vertical centerline of the domain at $t = 102$. The insets show the geometric structure of the void region.	92
4.3 Time (t) variation of the stirring index, ε , for cases A&B, A&C, A&D, B&C, B&D, C&D at period $T = 6$ obtained by Rule#1 (a) and Rule#2 (b). Only ε for case B&C reaches the asymptotic limit of unity. Time variation of ε for case B&C at various excitation periods (T) obtained by Rule#1 (c), and Rule#2 (d).	93
4.4 Poincaré sections for case B&C at period $T = 0.5, 1, 1.5, 2, 3, 4, 6$ and 8 . Initial locations of the passive particles are shown with colored dots on the top left figure, and correspond to $(x, y) = (0.1, 0.5), (0.2, 0.5), (0.3, 0.5), (0.4, 0.5), (-0.1, -0.5), (-0.2, -0.5), (-0.3, -0.5), (-0.4, -0.5)$	96
4.5 The $FTLE$ contours for case B&C at period $T = 2$ (a); 4 (b); 6 (c); 8 (d). Blue regions corresponding to zero or negative $FTLE$ values, show morphological similarities with the Poincaré sections in figure 4.4.	100
4.6 Probability density functions (PDF) of stretching fields for case B&C at period $T = 2, 4,$ and 6 , obtained at $t = 120$ (a). The PDF for case B&C at period $T = 6$ obtained using horizontal and vertical l_0 at $t = 140$ (b). Evolution of red and blue particles for case B&C at period $T = 2$ (c). KAM boundaries obtained using initial particle positions of $(-0.3, -0.5), (-0.4, -0.5)$ are drawn in black. The blue particles are initially located inside the regular islands, while the red particles are placed in the sea of chaos.	104
4.7 Temporal evolution of species concentration contours at $Pe = 1,000$ conditions ($Re = 0.01$) for case B&C, at period $T = 6$	107
4.8 Variation of M^1 as a function of time for four different stirring conditions (a). Required number of time periods, n , to achieve 95% mixing using cases B&C and C&D at period $T = 6$ for various Pe values (b). For comparison purposes, steady flow for case C to achieve 80% mixing ($M^1 = 5$) is also shown ($T \approx 6$). All simulations are obtained at $Re = 0.01$	108
5.1 The mixer consists of spatially repetitive mixing blocks with ζ potential patterned surfaces as shown in (a) for pattern A and (b) for pattern B. An axial electric field induces electroosmotic flow and its streamlines are represented by solid lines in (c) for pattern A and in (d) for pattern B, while a unidirectional pressure-driven flow enables continuous flow in the system. Arrows on top and bottom of mixing block in (c) and (d) indicate the directions of Helmholtz-Smoluchowski velocity, U_{HS} (see equation (2)). Combining the pressure driven flow with electroosmotic flow under time periodic external electric field (in the form of a Cosine wave with frequency,	

FIGURE	Page
ω) results in two-dimensional time-periodic flow suitable to induce <i>chaotic stirring</i> in the mixer.	114
5.2 Snapshots of the spreads of passive tracer particles: (a) case A at $St = 1 / 2\pi$, (b) case A at $St = 1 / \pi$, (c) case A at $St = 3 / 2\pi$, (d) case B at $St = 1 / 4\pi$, (e) case B at $St = 1 / 2\pi$ and (f) case B at $St = 3 / 2\pi$. For the depiction of the instant positions of particles, we record their spatial coordinates at $t = 20\pi$	119
5.3 Poincaré sections of (a) case A at $St = 1 / 2\pi, 1 / \pi, 3 / 2\pi$, and (b) case B at $St = 1 / 4\pi, 1 / 2\pi, 3 / 2\pi$, on the $\alpha - y$ plane; Horizontal coordinates stand for α values and vertical coordinates indicate values of y directional positions. Passive tracer particles are initially placed at (0.02, 0.0), which is near the entrance of a channel and simultaneously, on the interface between two fluids.	123
5.4 Contours of stretching, h for case A at $St = 1 / 2\pi$ (a), $1 / \pi$ (b), $3 / 2\pi$ (c). h values are measured at $t = 100$. Red and blue parts are regions of high and low stretching values, respectively.	126
5.5 Contours of stretching, h for case B at $St = 1 / 4\pi$ (a), $1 / 2\pi$ (b), $3 / 2\pi$ (c). h values are measured at $t = 100$. Red and blue parts are regions of high and low stretching values, respectively.	127
5.6 Probability density functions (PDF) of stretching values, h of case A at $St = 1 / 2\pi$ (a), $1 / \pi$ (b), $3 / 2\pi$ (c) and case B at $St = 1 / 4\pi$ (d), $1 / 2\pi$ (e), $3 / 2\pi$ (f).	130
5.7 Species concentration contours at $Re = 0.01$ and $Pe = 1000$ conditions for case A at $St = 1 / 2\pi$ (a), $1 / \pi$ (b), $3 / 2\pi$ (c) and case B at $St = 1 / 4\pi$ (d), $1 / 2\pi$ (e), $3 / 2\pi$ (f). Mixing domain is within a range of $0 \leq x \leq 24$ (6 blocks), $-1 \leq y \leq 1$ and above snapshots are obtained at $t = 20\pi$	133
5.8 M^1 variation of case A at $St = 1 / \pi$ and case B at $St = 1 / 2\pi$ as a function of number of mixing blocks at $Pe = 1000$. Re is constantly set as 0.01 to keep the constant kinematic condition.	135
5.9 Temporal evolutions of M^1 of case B at $St = 1 / 2\pi$ with 8 mixing blocks. (a) a series of snapshots obtained during 1 period ($16T \leq t < 17T$) in the time interval of $0.25T$ (b) M^1 history exhibits that its fluctuation is limited within acceptable range. Above plots show that current mixer concept provides a stable mixing quality in high level (90% mixing).	136
5.10 Required number of mixing blocks of case B at $St = 1 / 2\pi$ for 90% mixing with $Pe = 500, 1000, 1500$ and 2000 . Re is fixed as 0.01.	137
6.1 Problem configuration for the 3D cavity stirrer: (a) Boundary conditions, and	

FIGURE	Page
(b) Time history of u_z velocities of top oscillatory lids.	140
6.2 Numerical results for the three dimensional cavity stirrer: snapshots of spread of passive tracer particles for case at $T = 4$. A total of 90,000 passive particles are tracked in time. Snapshots show the dispersion state at respective times of (a) 0, (b) 10, (c) 20, (d) 30, (e) 40, and (f) 50.	143
6.3 Numerical results for the three dimensional cavity stirrer: snapshots of spread of passive tracer particles for case at $T = 8$. A total of 90,000 passive particles are tracked in time. Snapshots show the dispersion state at respective times of (a) 0, (b) 10, (c) 20, (d) 30, (e) 40, and (f) 50.	144
6.4 Numerical results for the three dimensional cavity stirrer: snapshots of spread of passive tracer particles for case at $T = 20$. A total of 90,000 passive particles are tracked in time. Snapshots show the dispersion state at respective times of (a) 0, (b) 10, (c) 20, (d) 30, (e) 40, and (f) 50.	145
6.5 Problem configuration: (a) Boundary conditions and geometry of the cavity with time-periodic oscillatory lid velocity ($L = H$), (b) The spectral element mesh consists of 10×10 spectral elements each of 8 th order yielding totally 6,561 non-uniformly distributed nodal points, (c) Time variation of the top and bottom lid velocity.	149
6.6 Time variation of the stirring index, ε , for cases at $1 / 2\pi \leq St \leq 5 / \pi$ obtained by Rule #1 [11]. Only ε for case at $St = 1 / 2\pi$ reaches the asymptotic limit of unity.	152
6.7 Snapshots of dispersion of passive tracer particles for case at $St = 1 / 2\pi$ obtained at (a) initial state, (b) 2 periods, (c) 3 periods, (d) 4 periods, (e) 5 periods, and (f) 6 periods.	153
6.8 Numerical results for the oscillatory driven cavity flow: species concentration contours at $Re = 10$, $Pe = 6000$, and $St = 1 / 2\pi$. Species concentration contours at $t = 0$ (a), 10 (b), 15(c), and 20(d).	154
6.9 Numerical results for the oscillatory driven cavity flow: species concentration contours at $Re = 10$, $Pe = 6000$, and $St = 2 / \pi$. Species concentration contours at $t = 0$ (a), 10 (b), 15(c), and 20(d).	155
6.10 (a) Variation of M^{-1} as a function of time for case at $St = 1 / 2\pi$, (b) Required time t_m to achieve 90% mixing using cases at $St = 1 / 2\pi$ for various Pe values.	156
6.11 (a) Contour plot of logarithmic values of $d(\mathbf{X})$ of $St = 0.5$ case, (b) Contour plot of $\ln(h)$ for $St = 0.5$ case; Periodic point B is located inside the high	

FIGURE		Page
	stretching zone, while periodic points A and C are located inside the low stretching zones.	159
6.12	(a) Schematics of a droplet converging to an unstable manifold at times t_1 , t_2 , and t_3 , (b) Homoclinic tangle between the stable and unstable manifolds.	161
6.13	(a) Initial circle of points to be tracked for the calculation of unstable manifold: The circle surrounds the hyperbolic periodic point B . Segments of unstable manifold of $St = 0.5$ case is numerically computed at (b) $t / T = 8$, (c) $t / T = 12$, and (d) $t / T = 16$. As time increases, the chaotic flow produces a dynamic template, which is essentially identical to the structure recorded a period earlier, except that a larger number of thinner striations is found in each region.	164
6.14	(a) Initial positions of colored particles at $t / T = 0$. Tracking results of $St = 0.5$ case are obtained at (b) $t / T = 8$, (c) $t / T = 12$, and (d) $t / T = 16$	166

CHAPTER I

INTRODUCTION AND LITERATURE REVIEW

Flow and species transport in micro-scales experience mostly laminar and even Stokes flow conditions (i.e. Reynolds number, $Re < 1$). In absence of turbulence, species mixing in micro-scales become inherently diffusion dominated, and requires very long mixing length- and time-scales. This creates significant challenges in the design of micro-total-analysis-systems (μ -TAS), where mixing of macromolecules and biological species with very low mass diffusivities (D) are often desired. Although the majority of earlier research concentrated on enhancement of diffusive-mixing by increasing the interspecies contact area [1], most recent work focuses on inducing chaotic advection, which is a conceivable method for species mixing enhancement in the Stokes flow regime [2-8]. In general for two-dimensional unsteady and three-dimensional flows, fluid-particle trajectories obtained by the Lagrangian description cannot be integrated analytically, and the particle trajectories exhibit chaotic trends. Even potential flows, as well as Stokes flows are reported to induce chaotic advection [3, 7], which result in deformation and stretching of fluid elements with exponential evolution of their structural inherece that produce efficient stirring. Based on these, in order to understand and to develop an efficient mixing strategy using chaotic advection, we numerically simulated a series of new types of mixing models using numerical solution of incompressible Navier-Stokes equations with a passively advected scalar field via a spectral element algorithm.

This dissertation follows the style of *Journal of Micromechanics and Microengineering*.

1.1. Development of spectral element algorithm

Mixing simulations for high Pe is more difficult than for lower Pe cases. The reason for this is the sharper concentration variations at the interface of two fluids, making numerical solution increasingly difficult to resolve [9]. Similarly, numerical solution of chaotically stirred/mixed flow is more challenging than regular mixing due to the exponentially attenuated striation thickness by deformation and stretching of fluid elements with exponential evolution of their structural inheritance [10, 11]. Thus, in laminar chaotic mixing, by usually choosing Re much smaller than Pe , solution of the scalar transport equation requires better grid resolution than the flow solver, and utilization of abundant grid points for mixing simulation is often needed. In order to resolve these difficulties, we developed efficient numerical solvers for incompressible flows with passively advected scalar, by implementation of algebraic factorization scheme on the spectral element grids.

The spectral element method (SEM) is essentially a discretization method for approximate solution of the partial-differential equations expressed in a weak form. It is based on high-order Lagrangian interpolants used in conjunction with particular quadrature rules defined using the same quadrature/collocation points [12]. SEM combines geometrical flexibility of the finite element method (FEM) with spectral convergence and low phase/dissipation error of the spectral method. For SEM it is assumed that the solution can be expressed as a series of polynomial basis functions, which can approximate the solution well in some norm as the polynomial degree tends to infinity [12-19]. These smooth basis-functions usually form an L_2 -complete basis [12]. For the sake of computational efficiency this basis is typically chosen to be orthogonal in a weighted inner-product. Convergence to the exact solution is achieved by increasing the order of the elements or the number of elements. If the boundary condition and

solution are sufficiently smooth, numerical results converge exponentially fast with increasing of polynomial orders of interpolants [12, 13, 15]. In addition, SEM ensures that increased accuracy can be achieved at relatively low marginal cost, meaning that the computational cost is determined primarily by the physical problem, and not by numerical convergence properties [20].

In order to save computational effort, non-conforming formulations are considered. In high-order method, conforming polynomial and geometric constraints can increase the computational load by propagation of the high-order polynomial discretization to the entire domain [18, 21, 22]. By resolving the polynomial and geometric constraint, computational load could be reduced, retaining the advantages of the conforming spectral element method. Nonconforming spectral element methods have recently been developed to improve the computational efficiency as well as reduce the required computer resources. These unstructured meshes enable the arbitrary match up among multi elements in polynomial order or geometry. Thus, the non-propagating local p -refinement can be realized. In Chapter II, we discuss the artificial C^0 enforcing technique for non-conforming grid and simultaneously provide a way on how to build a stable splitting scheme on the unstructured mesh. Therefore, a critical contribution will be the use of polynomially and geometrically nonconforming spectral elements that allow localized refinement in regions of interest, coupled with a stabilized high order operator splitting formulation of the incompressible Navier-Stokes equations with a passively advected scalar field.

1.2. Quantification of chaotic strength and mixing in a microfluidic system

Due to its ability to create well-stirred systems, chaotic advection is becoming a focal point in micro-scale mixing. Aref demonstrated efficient chaotic stirring promoted by simple flow fields [3]. A prototype design for a chaotic mixer was proposed by Evans *et al.* using a thermally actuated unsteady source-sink model [23]. Niu *et al.* reported cross-channel micro-mixers consisting of several channel intersections, which are activated by an external oscillatory-flow [24]. Stroock *et al.* utilized steady Stokes flow in a rectangular micro-channel with staggered herringbone-shaped grooved bottom-surface [4]. This geometry imposed alternating secondary flow patterns, resulting in spatially evolving three-dimensional steady Stokes flow. Liu *et al.* utilized a three-dimensional serpentine structure to induce rotational flow [25]. Rodrigo *et al.* developed a cylindrical mixer, which consists of two confocal elliptic cylinders whose inner and outer boundaries glide circumferentially [26]. Jiang *et al.* investigated chaotic mixing in curved micro channels [27]. Simonnet *et al.* developed a channel mixer, which has periodically repeating segments with a custom designed profile that generates a steady three-dimensional Stokes flow [28].

Optimization of the stirring model requires enhanced understanding of the deformation mechanism of fluid elements, and a qualitative or quantitative assessment of the stirring model. A literature review shows utilization of a wide range of diagnostic techniques for estimating the stirring efficiency. For example, Jones investigated homogenized dispersion of passive tracer particles in a circular domain [5], while Liu *et al.* used the box counting method to measure particle spread in an aperiodic cavity flow [29]. Anderson *et al.* plotted Poincaré sections and displacement-stretching fields for time-periodic lid driven cavity flow [30]. Lee *et al.* calculated the Finite Time Lyapunov Exponent (*FTLE*) in a single-screw extruder [31]. Hwu

et al. reported Poincaré section of circular cavity stirrer along with temporal evolution of the *FTLE* [32]. Niu and Lee defined a modified Poincaré section for continuous flow systems, and presented the *FTLE* contours for a cross-channel mixer [24], while Niu *et al.* utilized the same assessment techniques to find the optimum stirring conditions in their high-frequency micromixer [33]. For practical purposes, stretching field has been investigated [8] and the probability density function (*PDF*) of the stretching field was constructed for chaotic flows [6]. The aforementioned techniques are based on the Lagrangian particle tracking method applied to passive tracer-particles, and they are used to assess the stirring efficiency. However, assessment of the mixing efficiency also requires consideration of the interspecies diffusion. To this end, experimental studies on mixing utilized fluorescent dyes and performed fluorescence intensity measurements in various sections of the mixer. Mixing efficiency was quantified using standard deviation of the fluorescence intensity from a perfect mix [34-37]. Most experiments utilized a single type of dye (i.e., fixed the Schmidt number Sc), and the mixing length (l_m) variation as a function of the Peclet number ($Pe \equiv Sc \times Re$) was reported under *different kinematic conditions*, obtained by systematically varying the Reynolds number [38, 39].

Given the vast number of approaches used to assess the stirring-efficiency and the use of standard deviation of fluorescence intensity in most experimental studies, there is a need to understand and correlate the predictions and performances of various stirring/mixing efficiency characterization methodologies. In Chapter IV, we present a comparative study of five diagnostic tools commonly utilized in the assessment of stirring/mixing efficiency applied to the same mixing test-bed. Our *objectives* are to demonstrate the advantages and shortcomings of each method using the “chaotic electroosmotic stirrer” concept of Qian and Bau [2] as a test-bed, and at the same time, to identify the optimum operation conditions for the “electroosmotic stirrer”.

1.3. An electroosmotically stirred continuous flow micro-mixer

Microfluidic mixing has unique challenges induced by low mass diffusivities of the mixed species that result in convection dominated transport, requiring extremely long mixing time- and length-scales (l_m). Specifically, low mass diffusivities of chemicals, macromolecules and biological species result in large Schmidt number, which leads to large Peclet number ($Pe \equiv Sc \times Re$) despite the laminar or even Stokes flows conditions experienced in microflows. These challenges adversely affect the design of micro-total-analysis systems (μ -TAS), and have attracted considerable attention of researchers in recent years. Prominent review articles on microfluidic mixing can be found in [40, 41]. Overall, Microfluidic mixers can be categorized as passive and active. Passive mixers utilize co-flowing laminates of constituents in complex geometries designed to induce either secondary flows [4, 42, 43] or repetitive combination and relamination of the mixing species [39, 44-47]. Both types of passive mixers have complex geometries, which require difficult fabrication processes, and they often have large foot-print areas. Active mixers utilize an external field (other than shear) to induce stirring [24, 48-54]. Although they may need complex fabrication processes and wiring, active mixers may ultimately enable additional control over the mixing process.

Mixing and stirring are the processes of *homogenization* of species distribution as a result of *convection* and *diffusion*. Mixing targets production of a uniform concentration for continuous species, while stirring aims to produce uniform particle distribution for colloidal dispersions. In either case, convection brings the constituents into close proximity, and diffusion homogenizes through blending. Based on this understanding, mixing studies must consider the effects of Reynolds and Peclet numbers separately. Depending on the mixer geometry, variation in Re alters the flow kinematics, which may lead to favorable kinematic conditions that enhance

stirring. However, one also needs to address the mixing efficiency for different species (Sc) under given flow conditions (fixed Re). This is a fundamentally important and at the same time practical question. A good micro-mixer should be designed to mix various kinds of species within the shortest possible mixing length (or time).

From a theoretical perspective, the species mixing should be characterized as a function of the Peclet number at *fixed kinematic conditions* (i.e., fixed Re). Mixing length for two co-flowing fluids in a straight micro-channel varies as $l_m \propto Pe$ [55], as shown in figure 1.1 and 1.2. This result is analogous to pure diffusion, since the unidirectional flow does not stretch the interface between two fluids. Mixing can be enhanced if the interface between the two fluids is increased by successive stretching and folding so that the species diffusion can easily homogenize the mixture over a relatively small striation thickness [10]. For certain laminar convective/diffusive transport, mixing length varies as $l_m \propto Pe^{0.5}$ [56]. Exponential elongation of the species interface is known as *chaotic stirring*, which drastically reduces the mixing-length. Fully chaotic stirring results in $l_m \propto \ln(Pe)$ [10], while partially chaotic systems result in $l_m \propto Pe^\alpha$, where $0 < \alpha < 1$ [56, 57]. Actual value of α depends on the extent of chaos within the system. For example $\alpha \leq 0.25$ was observed in certain partially chaotic flows [42, 43].

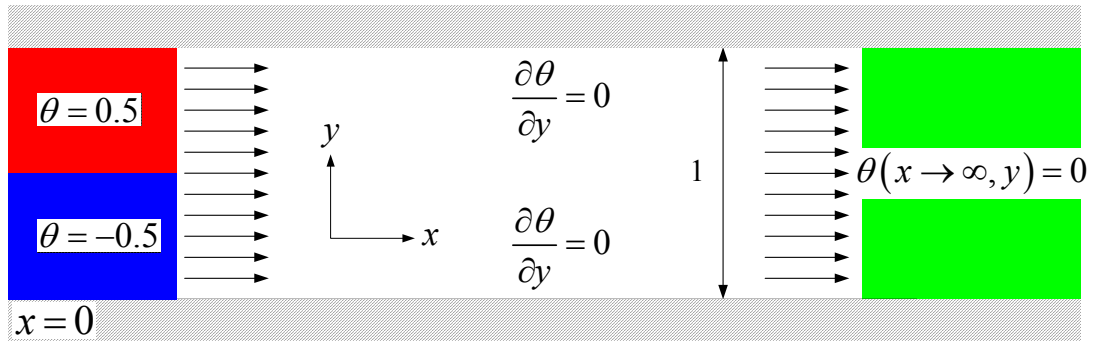


Figure 1.1. Two dimensional model of mixing in a straight channel. At the entry of the mixer ($x = 0$) the marker has concentration values of $C = 0.5$ (red) and $C = -0.5$ (blue) in the upper and lower halves of the domain. Therefore, a perfect mix would reach $C_\infty = 0$ (green).

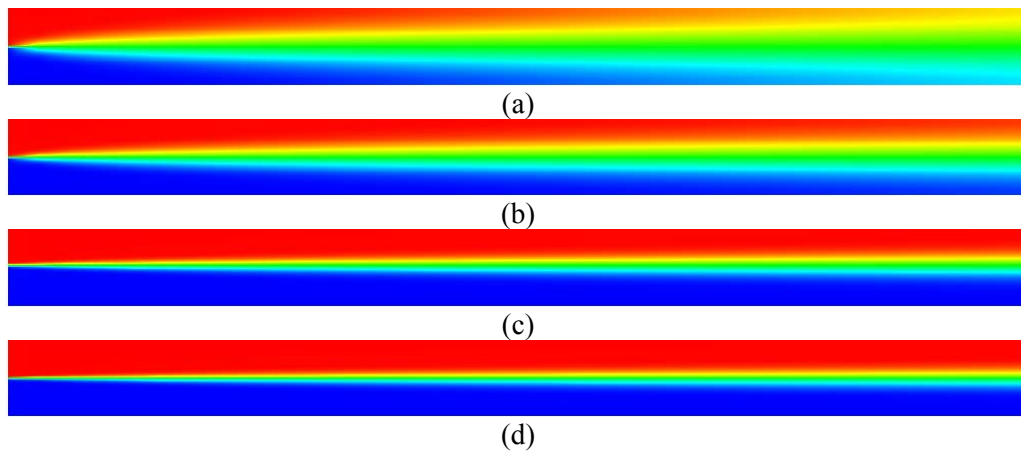


Figure 1.2. A series of results from analytical solutions [55] by varying the Peclet number: Concentration contours at $Pe = 400$ (a), 1000 (b), 4000 (c), and 6000 (d).

Application of these scaling trends in recent literature is somewhat misleading. Most experimental studies utilized a single type of molecular dye. Therefore, the species diffusivity was fixed, while the mixing characteristics were studied as a function of Re . Since variation in Re changes the flow kinematics, most of these studies with original intentions of investigation of the Pe dependence of l_m , actually reported mixing results for different flows and flow regimes. These assertions must exclude the experiments performed in the Stokes flow regime, where the flow kinematics does not vary substantially with the Reynolds number.

Mixers with non-moving boundaries often have nearly stagnant areas that experience regular (non-chaotic) flow. Often the side boundaries or geometric complexities such as grooves result in regular zones and the mixing scales as Pe^α . This limitation is common for passive mixers, but it is also observed in active mixers. For example in a peristaltic mixer, we observed mixing times scale as Pe^α with $\alpha \approx 0.3$ despite the initially small α values [58]. Reason for this performance reduction was a stagnant flow region within the closed mixer near a solid boundary, where the trapped species mixed with pure diffusion. Active mixers can be designed to eliminate the regular flow zones. Electroosmotic actuation induced by an externally applied electric field is the most appropriate for development of fully chaotic mixers, since the electroosmotic flow develops within nanometers of the zeta potential patterned surfaces [59]. An electroosmotic stirrer was conceptually developed by Qian and Bau using a DC electric field with time-modulated zeta potential surface patterns [11]. Under certain actuation conditions their design chaotic stirring is observed [11]. In [11], we adopted Qian and Bau's design reported comparative studies of five different techniques utilized in quantification of chaotic strength in a microfluidic system [11].

A literature review shows utilization of a wide range of diagnostic techniques for estimating the stirring efficiency. For example, to obtain intuitive interpretations from stirring

simulations, global dispersions of passive tracer particles were studied by Jones in a circular cavity [5] and by Liu *et al.* in a rectangular cavity [29]. As an alternative description of stirring efficiency, entropic characterization of colored tracer particles was proposed [42, 43]. Poincaré section was often plotted and this stroboscopic image was provided to detect the size or the position of bad mixing zone not only in a closed flow system [2, 3, 7, 11, 30, 32] but also in an open flow system [24, 31, 33, 42]. However, Poincaré section is limited as only a qualitative way, so that finite time Lyapunov exponents (*FTLE*) were calculated to study the characteristics of dynamic aspect of stirring mechanism in a quantitative way [24, 33, 60]. For the experiment-friendly measures, distributions of the stretching values have been investigated in various chaotic mixing studies [6, 8, 11, 29, 31, 61, 62]. Previously, as a statistical analysis of stretching field, probability density function was computed to describe the fluctuations of stretching values for chaotic bearing flows by Muzzio *et al.* [6]. Given the vast number of approaches used to assess the stirring-efficiency and the use of standard deviation of concentration intensity in most numerical and experimental mixing studies, there is still a need to understand and correlate the predictions and performances of various stirring/mixing efficiency characterization methodologies. Thus, we provide overall consolidation of multiple diagnostic studies following Kim and Beskok's previous work [11], and simultaneously, propose the new type of design for a fast stirrer employed in the micro scale channel in Chapter V.

1.4. Numerical analysis of dynamic skeleton of chaotically stirred flows

Once the Reynolds number is larger than 0, flows begin to be affected by the inertial effects, which induces nonlinearity and directionality. In addition, in such flows closed form of analytical solution is not available, thus numerical investigations are required. Breaking the symmetry of flow field, directionality of flows in the finite Reynolds numbers makes the motion of passive tracers irreversible. Several numerical studies have shown that global fluid mixing or heat/mass transfer in a cavity flow at the finite Reynolds number is greatly promoted when an unsteady component of the velocity is superimposed on the steady flow [30, 63, 64]. These studies show that an oscillatory fluid motion can lead to chaotic advection, but an analysis of the characteristics of chaos properties in the flow and its corresponding mixing properties has not yet been presented. Based on these premises, in Chapter VI, we examine the chaotic mixing in square cavity by numerically solving the Navier-Stokes equations, where stationary and unstationary inertial forces cannot be neglected and, consequently, symmetry is broken. As a flow solver, we utilize algebraic factorization scheme, which will be discussed in Chapter II and validated in Chapter III. The objective of the study described in Chapter VI is to analyze the details of the characteristics of this chaos by applying computational methods. To this end, by utilizing the periodic point analysis, it will be discussed how dynamic skeleton exposed by Lagrangian study is in accordance with a fast mixing process.

This dissertation is organized as follows: In Chapter II, we describe the implementation of algebraic factorization scheme on conforming and non-conforming spectral element grids in multi-dimensions. In Chapter III, we verify our algorithms, solving several test problems. In Chapter IV, we examine the several diagnostic tools for the estimation of chaotic strength and mixing in a microfluidic system. In Chapter V, we present theoretical and numerical

studies of particle dispersion and species mixing in a zeta potential patterned straight micro channel. In Chapter VI, by numerical solution of oscillatory driven cavity flow at finite Reynolds numbers, we study the role of dynamic skeleton in chaotic mixing. Finally, summary and conclusions are presented in Chapter VII.

CHAPTER II

DEVELOPMENT OF SPECTRAL ELEMENT ALGORITHM

In this chapter, we describe the development and implementation of numerical formulations for simulating transient incompressible flow, using spectral element discretizations in two- and three- dimensional spaces. In the spectral element discretization the elements serve as the basic building blocks for mesh generation and physics, as well as the basic units of locally structured mesh. We will first consider governing equations, starting from its strong form and work step-by-step all the way to the final algebraic matrix form. Then the semi-discrete formulation will be presented by high-order Taylor-Galerkin based algorithm. In order to avoid propagation of high-order polynomial discretizations to the entire domain, nonconforming formulation will be introduced. Finally, several test cases are provided in the aim of code verification.

2.1. Governing equations and formulation

We start by considering the spatial and temporal discretization of the incompressible Navier-Stokes equations with a passively advected scalar field. These unsteady partial differential equations form a set of coupled equations for velocity, pressure and scalar field. Due to the incompressibility pressure is an implicit variable which instantaneously adjusts itself in such a way that the velocity field remains divergence free. Incompressibility constraint often makes it impossible to solve both pressure and velocity field at once and brings many challenges to the numerical simulations. Based on these, we discuss the architectural aspects of numerical solution process, which involves the strong formulation, variational form, and final algebraic equations.

2.1.1. Governing equations

Let $\bar{\Omega}$ be the closure of an open bounded region Ω in \mathfrak{R}^d , where $d = 2$ or 3 represents the number of space dimensions, and $\mathbf{x} = (x_1, \dots, x_d) = (x, y, z)$ be a point in $\Omega = \Omega \cup \partial\Omega$, where $\partial\Omega = \Gamma$ is the boundary of Ω . We consider the solution of the transient incompressible Navier-Stokes equations with a passively advected scalar field:

$$\frac{\partial \mathbf{u}}{\partial t} + \mathbf{u} \cdot \nabla \mathbf{u} = -\nabla p + \frac{1}{Re} \nabla^2 \mathbf{u}, \quad \text{in } \Omega \times (0, \tau], \quad (2.1.a)$$

$$\nabla \cdot \mathbf{u} = 0, \quad \text{in } \Omega \times (0, \tau], \quad (2.1.b)$$

$$\frac{\partial \theta}{\partial t} + \mathbf{u} \cdot \nabla \theta = \frac{1}{Pe} \nabla^2 \theta, \quad \text{in } \Omega \times (0, \tau], \quad (2.1.c)$$

where τ denotes a positive real number, $\mathbf{u} = (u_1, \dots, u_d)$ is the velocity vector, p is the pressure, and θ is the scalar value as of temperature or normalized concentration density. All variables (\mathbf{u} , p , θ) are nondimensionalized by reference values. Re is the Reynolds number based on the characteristic velocity (U), length scale (L), and kinematic viscosity (ν), thus $Re = UL / \nu$. Pe is the Peclet number, which is the Reynolds number multiplied by either the Prandtl number (Pr : ratio of the momentum and thermal diffusivities) or the Schmidt number (Sc : ratio of the momentum and mass diffusivities), for heat transfer or species transport application, respectively.

For heat transfer problems, the nondimensional temperature is given as

$$\theta = \frac{T - T_0}{\Delta T}, \quad (2.2)$$

where T_0 is a reference temperature, and ΔT is a predefined or desired temperature difference. For the species transport applications, θ can be identified as the concentration density normalized by a reference value. First term on the left hand side of equation (2.1) drops for steady flow

problems. Second term of this equation contributes to the inertial behaviors of fluids and they are negligible for low speed flows, standing for Stokes flows [65]. We have associated initial and boundary conditions below:

$$\text{for velocity, } \mathbf{u}(\mathbf{x}, 0) = \mathbf{u}_0(\mathbf{x}) \text{ in } \Omega, \quad \mathbf{u} = \mathbf{u}_g \text{ on } \Gamma_g, \quad \nabla u_i \cdot \hat{\mathbf{n}} = 0 \text{ on } \Gamma_q, \quad (2.3.a)$$

$$\text{for scalar, } \theta(\mathbf{x}, 0) = \theta_0(\mathbf{x}) \text{ in } \Omega, \quad \theta = \theta_g \text{ on } \Gamma_g, \quad \nabla \theta \cdot \hat{\mathbf{n}} = 0 \text{ on } \Gamma_q, \quad (2.3.b)$$

where \mathbf{u}_0 is the initial values to satisfy incompressibility constraint at any place, $\hat{\mathbf{n}}$ is the outward pointing normal on the boundary, subscripts g denotes imposed Dirichlet boundary conditions and q refers to zero flux boundary condition.

2.1.2. Weak forms and spatial discretizations using spectral element approximation

As a starting point for spectral element discretization, we use the variational equivalences of equation (2.1) and they are given below:

$$\left(\frac{\partial \mathbf{u}}{\partial t}, w \right) + (\mathbf{u} \cdot \nabla \mathbf{u}, w) + \frac{1}{Re} (\nabla \mathbf{u}, \nabla w) - (p, \nabla \cdot w) = (\mathbf{f}, w), \quad \forall \mathbf{u} \in X_g, \quad \forall w \in X_0, \quad (2.4.a)$$

$$-(q, \nabla \cdot \mathbf{u}) = 0, \quad \forall q \in Y, \quad (2.4.b)$$

$$\left(\frac{\partial \theta}{\partial t}, w \right) + (\mathbf{u} \cdot \nabla \theta, w) + \frac{1}{Pe} (\nabla \theta, \nabla w) = 0, \quad \forall \theta \in X_g, \quad \forall w \in X_0, \quad (2.4.c)$$

$$\forall \phi, \psi \in L^2(\Omega), \quad (\phi, \psi) \equiv \int_{\Omega} \phi(\mathbf{x}) \psi(\mathbf{x}) d\Omega, \quad \forall \mathbf{x} \in \Omega, \quad (2.4.d)$$

where Δt is the time step, w is the test function associated with the momentum equation, \mathbf{u} and θ are the approximate solutions in X_g , q is the test function associated with the continuity equation, and $L^2(\Omega)$ denotes the Hilbert space of square integrable scalar functions [12]. As the coupled set of equations for velocity and pressure forms a saddle-point problem, the approximation spaces

for the velocity should be different from that for the pressure in order to obtain a unique pressure solution. With the aid of the space of trial solutions, the proper subspaces X_g for \mathbf{u} and θ are given as below [14]:

$$X_g := \left\{ \mathbf{u} \mid \mathbf{u} \in H^1(\Omega), \mathbf{u} = \mathbf{u}_g \text{ on } \partial\Omega \right\}, \quad (2.5.a)$$

$$X_g := \left\{ \theta \mid \theta \in H^1(\Omega), \theta = \theta_g \text{ on } \partial\Omega \right\}, \quad (2.5.b)$$

and the proper subspaces X_0 for w and Y for q are defined as follows [14]:

$$X_0 := \left\{ w \mid w \in H_0^1(\Omega), w = 0 \text{ on } \partial\Omega \right\}, \quad (2.6.a)$$

$$Y := \left\{ q \mid q \in L^2(\Omega), \int_{\Omega} q(x) dx = 0 \right\}, \quad (2.6.b)$$

where $H^1(\Omega)$ is the space of all functions belonging to $L^2(\Omega)$ whose first derivatives are also in $L^2(\Omega)$, $H_0^1(\Omega)$ is the typical Sobolev space and its values vanish at boundaries [12].

We have to define the discrete polynomial subspaces $X_{g,h} \subset X_g$ and $Y_h \subset Y$, in which the velocities (or scalar) and pressure will be approximated, respectively. Maday and Patera [66], and Bernardi and Maday [67] proposed the use of the subspaces given as below:

$$X_{g,h} = X_g \cap P_N(\Omega), \quad (2.7.a)$$

$$Y_h = Y \cap P_{N-2}(\Omega), \quad (2.7.b)$$

and the space $X_{0,h}$ is defined as:

$$X_{0,h} = X_0 \cap P_N(\Omega). \quad (2.8)$$

where $P_N(\Omega)$ is the space of a polynomial of degree less than or equal to N . The choice for the subspaces $(X_{g,h}, Y_h)$ implies the introduction of staggered grids, where interelement continuity of pressure is not enforced. Spatial discretization is based upon decomposition of the computational domain Ω into K spectral elements Ω^e which are locally mapped to $[-1, 1]^d$ in \mathfrak{R}^d .

$$\Omega = \bigcup_{e=1}^K \Omega^e . \quad (2.9)$$

Our algorithm utilizes N^{th} -order nodal expansion. As defined in equation (2.7.a), the velocity is represented by N^{th} -order Lagrange polynomials on the Gauss-Lobatto-Legendre (*GLL*) quadrature points, with C^0 continuity enforced at element interfaces. The pressure is represented by polynomials of degree $(N-2)^{\text{th}}$ based upon the Gauss-Legendre (*GL*) quadrature points. The N^{th} order Lagrange interpolation polynomials $h_m^N(\xi)$ are given by below [15]:

$$h_m^N(\xi) = -\frac{(1-\xi^2)L'_N(\xi)}{N(N+1)L_N(\xi_m)(\xi-\xi_m)}, \quad L'_N = \frac{dL_N}{d\xi}, \quad \xi \in [-1, 1], \quad m \in [0, N], \quad (2.10)$$

where L_N is the N^{th} -order Legendre polynomial; ξ_m on the parametric space are the *GLL* points, which are defined by the solutions of below equation [15]:

$$(1-\xi_m)L'_N(\xi_m) = 0 . \quad (2.11)$$

The cardinality condition must be satisfied:

$$h_m^N(\xi_n) = \delta_{mn}, \quad \forall m, n \in [0, N], \quad (2.12)$$

where δ_{mn} denotes the Kronecker delta symbol. Within each element Ω^e , the geometry, solution, and data are expanded in terms of high-order tensor-product polynomial bases in each coordinate direction:

$$\text{for } d=2, \quad \tilde{\mathbf{u}}|_{\Omega^e} = \sum_{m=0}^{N_\xi} \sum_{n=0}^{N_\eta} \tilde{\mathbf{u}}_{mn} S_{mn}(\xi, \eta), \quad \tilde{\boldsymbol{\theta}}|_{\Omega^e} = \sum_{m=0}^{N_\xi} \sum_{n=0}^{N_\eta} \tilde{\boldsymbol{\theta}}_{mn} S_{mn}(\xi, \eta), \quad (2.13.a)$$

$$S_{mn}(\xi, \eta) = h_m^{N_\xi}(\xi) h_n^{N_\eta}(\eta), \quad (2.13.b)$$

$$m \in [0, N_\xi], \quad n \in [0, N_\eta], \quad (2.13.c)$$

$$\tilde{\mathbf{u}}|_{\Omega^e} = \sum_{m=0}^{N_\xi} \sum_{n=0}^{N_\eta} \sum_{o=0}^{N_\zeta} \tilde{\mathbf{u}}_{mno} S_{mno}(\xi, \eta, \zeta),$$

for $d = 3$,

$$(2.13.d)$$

$$\tilde{\theta}|_{\Omega^e} = \sum_{m=0}^{N_\xi} \sum_{n=0}^{N_\eta} \sum_{o=0}^{N_\zeta} \tilde{\theta}_{mno} S_{mno}(\xi, \eta, \zeta),$$

$$S_{mno}(\xi, \eta, \zeta) = h_m^{N_\xi}(\xi) h_n^{N_\eta}(\eta) h_o^{N_\zeta}(\zeta),$$

$$(2.13.e)$$

$$m \in [0, N_\xi], \quad n \in [0, N_\eta], \quad o \in [0, N_\zeta],$$

$$(2.13.f)$$

where S is the shape function, (ξ, η, ζ) are the local coordinates corresponding to global coordinates (x, y, z) ; $\tilde{\mathbf{u}}$ is the nodal basis coefficient; h is the one dimensional Lagrangian interpolant basis; N_ξ, N_η and N_ζ denote expansion order in direction of ξ, η and ζ , respectively.

The example of staggered grids is shown in figure 2.1. For the spatial discretization, application of the spectral element discretization will yield a set of below equation of an equivalent variational form:

$$\mathbf{M} \frac{\partial \tilde{\mathbf{u}}}{\partial t} + \mathbf{N} \tilde{\mathbf{u}} + \frac{1}{Re} \mathbf{L} \tilde{\mathbf{u}} - \mathbf{G}^T \tilde{p} = \tilde{\mathbf{f}},$$

$$(2.14.a)$$

$$-\mathbf{G} \tilde{\mathbf{u}} = \tilde{f}_p,$$

$$(2.14.b)$$

$$\mathbf{M} \frac{\partial \tilde{\theta}}{\partial t} + \mathbf{N} \tilde{\theta} + \frac{1}{Pe} \mathbf{L} \tilde{\theta} = 0,$$

$$(2.14.c)$$

where \mathbf{M} is the mass matrix, \mathbf{N} is the convection matrix, \mathbf{L} is the diffusion or Laplacian matrix, \mathbf{G} is the divergence matrix, and \tilde{f}_p is the non-zero term derived from the inhomogeneous Dirichlet boundary condition of the velocity field in the incompressibility constraint. Coefficient matrices shown in equation (2.14) are defined by:

$$\mathbf{M}(w, \psi) \equiv \int_{\Omega} w \psi d\Omega,$$

$$(2.15.a)$$

$$\mathbf{N}(w, \tilde{\mathbf{u}}, \psi) \equiv \int_{\Omega} w(\tilde{\mathbf{u}} \cdot \nabla \psi) d\Omega, \quad (2.15.b)$$

$$\mathbf{L}(w, \psi) \equiv \int_{\Omega} \nabla w \cdot \nabla \psi d\Omega, \quad (2.15.c)$$

$$\mathbf{G}(q, \psi) \equiv \int_{\Omega} q(\nabla \cdot \psi) d\Omega, \quad (2.15.d)$$

where ψ denotes *GLL* interpolant represented as given in equation (2.13). We note that no integration by parts is performed on the nonlinear term \mathbf{N} . For \mathbf{G} , the derivatives of the velocity must be interpolated onto the *GL* points, and thus we calculate the derivatives of the velocity shape functions, passing through *GLL* points, at *GL* points [17].

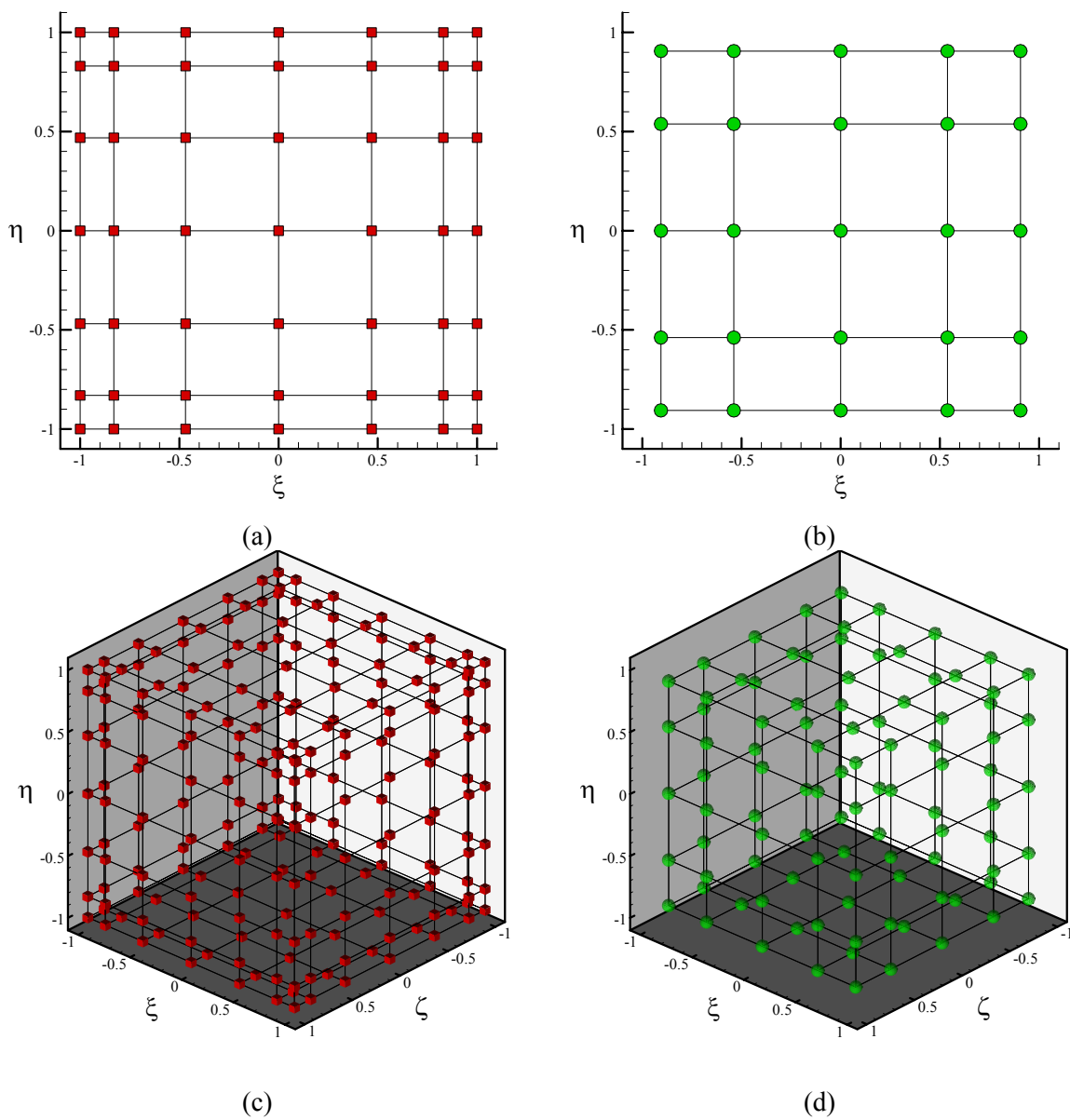


Figure 2.1. Grid points in the parametric spaces: two-dimensional 6th-order *GLL* (a) and 4th-order *GL* (b) mesh and three-dimensional 6th-order *GLL* (c) and 4th-order *GL* (d) mesh.

2.1.3. Algebraic factorization scheme

Since the nonlinear term \mathbf{N} in equation (2.14.a) does not affect the convergence rate of the consistency error in solving equation (2.14) [68], we will be concerned with the time-dependent Stokes equations from here on. Dropping \mathbf{N} , the algebraic form of equation (2.14) is set as following:

$$\begin{bmatrix} \mathbf{H} & -\mathbf{G}^T \\ -\mathbf{G} & 0 \end{bmatrix} \begin{pmatrix} \tilde{\mathbf{u}}^{n+1} \\ \tilde{p}^{n+1} \end{pmatrix} = \begin{pmatrix} \frac{\beta_1}{\Delta t} \mathbf{M} \tilde{\mathbf{u}}^n + \tilde{\mathbf{f}}^{n+1} \\ \tilde{f}_p^{n+1} \end{pmatrix}, \quad (2.16)$$

where \mathbf{H} is the discrete Helmholtz matrix, thus $\mathbf{H} = (1 / Re) \mathbf{L} + (\beta_0 / \Delta t) \mathbf{M}$, when the implicit Euler time stepping is used. A common approach is to decouple the velocity and pressure by formally carrying out the so-called *algebraic factorization schemes* on the system (2.16) [12, 68]. The main idea behind the algebraic factorization scheme is to replace the matrix in equation (2.16) by its *incomplete block LU factorization*. One of the simplest possibilities is [68] (\sim is dropped for the sake of simplicity)

$$\begin{bmatrix} \mathbf{H} & -\mathbf{G}^T \\ -\mathbf{G} & 0 \end{bmatrix} \approx \begin{bmatrix} \mathbf{H} & 0 \\ -\mathbf{G} & -\Delta t \mathbf{G} \mathbf{M}^{-1} \mathbf{G}^T \end{bmatrix} \begin{bmatrix} \mathbf{I} & -\Delta t \mathbf{M}^{-1} \mathbf{G}^T \\ 0 & \mathbf{I} \end{bmatrix}. \quad (2.17)$$

Then, equation (2.16) can be approximately solved as follows:

$$\mathbf{H} \mathbf{u}^* = \frac{\beta_1}{\Delta t} \mathbf{M} \mathbf{u}^n + \mathbf{f}^{n+1}, \quad (2.18.a)$$

$$\left(\sum_{l=1}^d \mathbf{G}_l \mathbf{M}^{-1} \mathbf{G}_l^T \right) \Phi^{n+1} = -\frac{1}{\Delta t} \mathbf{G} (\mathbf{u}^* - f_p), \quad (2.18.b)$$

$$\mathbf{u}^{n+1} = \mathbf{u}^* + \Delta t \mathbf{M}^{-1} \mathbf{G}^T \Phi^{n+1} \quad (2.18.c)$$

$$p^{n+1} = \Phi^{n+1}. \quad (2.18.d)$$

However, above form leads to consistency errors and lose temporal accuracy, thus incremental pressure-correction scheme proposed by Couzy [14] and van Kan [69] is utilized. Following Couzy [14], we rewrite the Stokes system (2.16) by introducing an auxiliary system \mathbf{Q} (\sim is dropped for the sake of simplicity):

$$\begin{bmatrix} \mathbf{H} & -\mathbf{H}\mathbf{Q}\mathbf{G}^T \\ -\mathbf{G} & 0 \end{bmatrix} \begin{pmatrix} \mathbf{u}^{n+1} \\ p^{n+1} - p^n \end{pmatrix} = \begin{pmatrix} \frac{\beta_1}{\Delta t} \mathbf{M}\mathbf{u}^n + \mathbf{f}^{n+1} + \mathbf{G}^T p^n \\ f_p^{n+1} \end{pmatrix} + \begin{pmatrix} \mathbf{r} \\ 0 \end{pmatrix}, \quad (2.19)$$

where \mathbf{r} is the residual term and it is given as below:

$$\mathbf{r} = (\mathbf{I} - \mathbf{H}\mathbf{Q})\mathbf{G}^T (p^{n+1} - p^n). \quad (2.20)$$

Couzy examines several choices for \mathbf{Q} . The choice $\mathbf{Q} = \mathbf{H}^{-1}$ yields no splitting error (i.e. $\mathbf{r} = 0$) [14], while the more computationally convenient choice $\mathbf{Q} = (\Delta t / \beta_0) \mathbf{M}^{-1}$ leads to

$$\mathbf{r} = \frac{\Delta t}{\beta_0 Re} \mathbf{L}\mathbf{M}^{-1}\mathbf{G}^T (p^n - p^{n+1}) = O(\Delta t^2). \quad (2.21)$$

Since there is a factor of Δt^{-1} in front of the velocity in equation (2.16), the local truncation error incurred by neglecting \mathbf{r} is $O(\Delta t^3)$, and the method is formally second-order accurate in time [14, 17, 70]. This is shown by numerical results in Fisher [70].

Dropping the residual in equation (2.19), formally carrying out a single round of block Gaussian elimination leads to the reformulated Stokes problem to be solved at each time step:

$$\begin{bmatrix} \mathbf{H} & -\mathbf{H}\mathbf{M}^{-1}\mathbf{G}^T \\ 0 & \frac{\Delta t}{\beta_0} \mathbf{G}\mathbf{M}^{-1}\mathbf{G}^T \end{bmatrix} \begin{pmatrix} \mathbf{u}^{n+1} \\ p^{n+1} - p^n \end{pmatrix} = \begin{pmatrix} \frac{\beta_1}{\Delta t} \mathbf{M}\mathbf{u}^n + \mathbf{f}^{n+1} + \mathbf{G}^T p^n \\ g \end{pmatrix}, \quad (2.22)$$

where g is the modified inhomogeneity arising from Gaussian elimination. Using again the incomplete block factorization given in equation (2.22), we obtain the incremental form the algebraic factorization:

$$\mathbf{H}\mathbf{u}^* = \frac{\beta_1}{\Delta t} \mathbf{M}\mathbf{u}^n + \mathbf{f}^{n+1} + \mathbf{G}^T p^n, \quad (2.23.a)$$

$$\mathbf{E}(p^{n+1} - p^n) = -\frac{1}{\Delta t} \mathbf{G}(\mathbf{u}^* - f_p), \quad (2.23.b)$$

$$\mathbf{E} = \frac{\Delta t}{\beta_0} \sum_{l=1}^d \mathbf{G}_l \mathbf{M}^{-1} \mathbf{G}_l^T \quad (2.23.c)$$

$$\mathbf{u}^{n+1} = \mathbf{u}^* + \Delta t \mathbf{M}^{-1} \mathbf{G}^T (p^{n+1} - p^n), \quad (2.23.d)$$

where n denotes time step index, \mathbf{E} is the pseudo-Laplacian matrix for the pressure Poisson equation. Especially, \mathbf{E} is the Stokes Schur complement governing the pressure in absence of the viscous term [17]. Above scheme includes solving for the pressure difference over a time step as a primary variable in Poisson equation, requiring the provision of a consistent initial condition for pressure and the introduction of an intermediate free variable \mathbf{u}^* to be associated with a *non-divergence-free* velocity vector. A seemingly magical fact is that no artificial pressure boundary condition is involved in equation (2.23). Hence, this type of method is not plagued by the artificial-pressure-boundary-condition curse that afflicts the PDE-based projection methods. At this point it is important to note that the inversed \mathbf{M} is involved in building pseudo Laplacian \mathbf{E} . In SEM, \mathbf{M} is diagonal in conforming grids. This is because of the fact that the collocation points used for numerical integration, and the points at which the shape functions are evaluated, are the same. This is an important property of spectral element methods, which is not found in classical finite element formulations [12]. However, this *generic* diagonality is broken in nonconforming grids and the details are considered in section (2.2.3).

2.1.4. Taylor-Galerkin based algorithm

In order to obtain stable numerical solutions of semi-discrete formulation given by equation (2.23), involving \mathbf{N} , it is important to wisely choose the time integration scheme. In this study, we choose the Taylor–Galerkin method to approximate the time derivative of unknowns in terms of unknowns at various time steps. This method, introduced for finite elements by Donea [71], add in a natural way a stabilizing diffusion term to the numerical scheme, using Taylor series expansions in time including second and third-order terms. For each different differential operator, one might need to apply appropriate time integration schemes. Diffusive phenomena typically occur at a much faster rate, and should therefore be integrated implicitly. Given that the pressure establishes itself immediately through the pressure-Poisson equation in equation (2.23), an implicit integration of pressure also seems appropriate. Time marching of the convection term is normally performed in an explicit way due to its nonlinear characteristics and consequent computational cost.

For implicit time integration of diffusive operator, both Adams-Moulton and backward-differencing methods can be used to discretize the space-discretized Laplacian operator. The Adams-Moulton schemes are unconditionally stable only for the 1st and 2nd order ones because 1st order one is identically same with Euler implicit scheme and 2nd order one is Crank-Nicolson scheme. Due to the stiff stability and high order accuracy, we choose the Crank-Nicolson scheme. By adopting Crank-Nicolson representation for the diffusion terms and applying 2nd order Adams-Bashforth to the explicit convection treatment, the following fully discretized Galerkin equations are derived as below (\sim is dropped for the sake of simplicity):

$$\left(\frac{1}{\Delta t} \mathbf{M} + \frac{1}{2Re} \mathbf{L} \right) (\mathbf{u}^* - \mathbf{u}^n) = \mathbf{G}^T p^n - \frac{1}{Re} \mathbf{L} \mathbf{u}^n - \mathbf{N}(\mathbf{u}^{n+1/2}) \mathbf{u}^{n+1/2} + \frac{1}{2} (\mathbf{f}^{n+1} + \mathbf{f}^n), \quad (2.24.a)$$

$$\text{where, } \mathbf{N}(\mathbf{u}^{n+1/2})\mathbf{u}^{n+1/2} = 1.5\mathbf{N}(\mathbf{u}^n)\mathbf{u}^n - 0.5\mathbf{N}(\mathbf{u}^{n-1})\mathbf{u}^{n-1}, \quad (2.24.b)$$

$$\beta\mathbf{E}(p^{n+1} - p^n) = -\frac{1}{\Delta t}\mathbf{G}\mathbf{u}^*, \quad (2.24.c)$$

$$\text{where, } \mathbf{E} = \sum_{l=1}^d \mathbf{G}_l \mathbf{M}^{-1} \mathbf{G}_l^T, \quad (2.24.d)$$

$$\mathbf{M}(\mathbf{u}^{n+1} - \mathbf{u}^*) = \beta\Delta t \mathbf{G}^T (p^{n+1} - p^n), \quad (2.24.e)$$

$$\left(\frac{1}{\Delta t} \mathbf{M} + \frac{\beta}{Pe} \mathbf{L} \right) (\theta^{n+1} - \theta^n) = -\frac{1}{Pe} \mathbf{L} \theta^n - \{ 1.5 \cdot \mathbf{N}(\mathbf{u}^{n-1}) \theta^{n-1} - 0.5 \cdot \mathbf{N}(\mathbf{u}^{n-2}) \theta^{n-2} \}, \quad (2.24.f)$$

where n denotes the time step index, \mathbf{M} is the mass matrix, \mathbf{L} is the diffusion matrix, \mathbf{N} is the convection matrix, \mathbf{f} is forcing vector due to non-zero essential boundary condition and \mathbf{G} is the matrix that arises from incompressibility. To assure second order accuracy in time the Crank-Nicolson choice of $\beta = 0.5$ is adopted [69]. To ensure the temporal second-order accuracy, the convection term is explicitly treated with the Adams-Bashforth scheme. The key idea is to predict first a velocity field from the current flow variables without taking the divergence constraint into account. In a second step, the divergence constraint is enforced by solving a pressure-Poisson equation. We note that for time-independent boundary conditions,

$$\mathbf{f}^n = \mathbf{f}^{n+1}. \quad (2.25)$$

In equation (2.24.c), \mathbf{E} has a symmetrical dense structure. This is solved per time step by a direct Bunch-Kaufman method [72]. It is of note that Helmholtz matrix is symmetric positive definite (SPD) and again possesses a strongly banded structure. In case of high Re or Pe , the iteration matrix is then dominated by the presence of the mass matrix, being diagonally dominant.

For an explicit update of convection term, multi-level schemes such as Adams-Bashforth have been normally utilized. The problem with schemes of this kind is that they use the values at the current and previous time step, which makes them awkward in the context of

adaptive refinement, moving meshes, and local or global re-meshing, degrading flexibility and adaptability [73]. Therefore, multistage schemes are often preferable and we choose 2nd order Runge-Kutta as an alternative choice for an explicit update of convection term. By adopting Crank-Nicolson representation for the diffusion terms as before, and applying 2nd order Runge-Kutta to the explicit approach of convection, the following fully discretized Galerkin equations are given as below:

$$\left(\frac{2}{\Delta t} \mathbf{M} + \frac{\beta}{Re} \mathbf{L} \right) (\mathbf{u}^* - \mathbf{u}^n) = \mathbf{G}^T p^n - \frac{1}{Re} \mathbf{L} \mathbf{u}^n - \mathbf{N}(\mathbf{u}^n) \mathbf{u}^n + \beta (\mathbf{f}^{n+1/2} + \mathbf{f}^n), \quad (2.26.a)$$

$$\beta \mathbf{E} (p^{n+1/2} - p^n) = -\frac{1}{\Delta t} \mathbf{G} (\mathbf{u}^* - f_p^{n+1/2}), \quad (2.26.b)$$

$$\mathbf{M} (\mathbf{u}^{n+1/2} - \mathbf{u}^*) = \beta \Delta t \mathbf{G}^T (p^{n+1/2} - p^n), \quad (2.26.c)$$

$$\left(\frac{1}{\Delta t} \mathbf{M} + \frac{\beta}{Re} \mathbf{L} \right) (\mathbf{u}^{**} - \mathbf{u}^n) = \mathbf{G}^T p^n - \frac{1}{Re} \mathbf{L} \mathbf{u}^n - \mathbf{N}(\mathbf{u}^{n+1/2}) \mathbf{u}^{n+1/2} + \beta (\mathbf{f}^{n+1} + \mathbf{f}^n), \quad (2.26.d)$$

$$\beta \mathbf{E} (p^{n+1} - p^n) = -\frac{1}{\Delta t} \mathbf{G} (\mathbf{u}^{**} - f_p^{n+1}), \quad (2.26.e)$$

$$\mathbf{M} (\mathbf{u}^{n+1} - \mathbf{u}^*) = \beta \Delta t \mathbf{G}^T (p^{n+1} - p^n), \quad (2.26.f)$$

$$\text{where } \mathbf{E} = \sum_{l=1}^d \mathbf{G}_l \mathbf{M}^{-1} \mathbf{G}_l^T, \quad (2.26.g)$$

$$\left(\frac{2}{\Delta t} \mathbf{M} + \frac{\beta}{Pe} \mathbf{L} \right) (\theta^{n+1/2} - \theta^n) = -\frac{1}{Pe} \mathbf{L} \theta^n - \mathbf{N}(\mathbf{u}^n) \theta^n, \quad (2.26.h)$$

$$\left(\frac{1}{\Delta t} \mathbf{M} + \frac{\beta}{Pe} \mathbf{L} \right) (\theta^{n+1} - \theta^n) = -\frac{1}{Pe} \mathbf{L} \theta^n - \mathbf{N}(\mathbf{u}^{n+1/2}) \theta^{n+1/2}, \quad (2.26.i)$$

where n denotes the time step index, \mathbf{M} is the mass matrix, \mathbf{L} is the diffusion matrix, \mathbf{N} is the convection matrix, \mathbf{f} is forcing vector due to non-zero Dirichlet boundary condition and \mathbf{G} is the

matrix that arises from incompressibility. With the aim of achieving second order accuracy in time the Crank-Nicolson choice of $\beta = 0.5$ is adopted as similar to a case of equation (2.24). In the case of Runge-Kutta scheme, the inclusion of *half-step* within the first fractional step characterizes the extension of first-order projection methods to second order Taylor-Galerkin/projection methods. This inclusion of half-step also improves the temporal accuracy of passive particle tracking, and its details are explained next.

2.1.5. Particle tracking

In many circumstances the Lagrangian behavior of a fluid particle is more important for scalar transport than the diffusive component. To understand how scalar transport occurs it is necessary to know fluid particles move under the action of the fluid velocity field. Based on this, a detailed analysis of the scalar transport process has been undertaken by calculating the trajectories of a large number of fluid particles dominated under the influence of the computed velocity field [74]. Numerical result of Lagrangian particle tracking is dominantly affected by three different errors, which come from numerical calculation of velocity field, spatial interpolation, and temporal integration. To resolve error from velocity field, highly accurate and explicit descriptions of velocity field are required, thus we utilize SEM. From the spectral element discretization, the velocity is only known in a limited number of computational grid points. Particle tracking requires the knowledge of the velocity of the fluid in any arbitrary point in the flow domain. Therefore, interpolation on the velocity field is necessary.

Particle tracking can lose its spatial accuracy in low order interpolation schemes, such as the 4th order biquadratic algorithm presented in [11]. Ultimately, it is difficult to obtain accurate solutions for long-time integration due to accumulation of temporal and spatial

discretization errors. Inconsistencies between the high-order velocity field and a linear representation might result in kinematic changes that could have a significance effect on the particle tracking in *critical regions* which are very sensitive to the spatial resolution [75]. To overcome the critical shortcomings of interpolation with low order polynomials, it was proposed to use the high-order polynomials by Coppola *et al.* [75] or C^∞ functions by Giona *et al.* [76]. In two dimensional spaces, we use quadrilateral spectral elements that are isoparametrically mapped to a master element in $-1 \leq \xi(\xi, \eta) \leq 1$. In three dimensional spaces, hexahedral spectral elements are mapped to a master element in $-1 \leq \xi(\xi, \eta, \zeta) \leq 1$. The mapping between the physical space represented by \mathbf{x} , and the parametric space identified by the local Cartesian coordinate ξ is denoted by

$$\xi = J^{-1}(\mathbf{x}), \quad \mathbf{x} = \mathbf{x}(x, y) \quad \text{for } d = 2, \quad \text{and} \quad \mathbf{x} = \mathbf{x}(x, y, z) \quad \text{for } d = 3, \quad (2.27)$$

where J^{-1} is the inversed Jacobian matrix. A visual explanation of two-dimensional mapping is depicted in figure 2.2. The velocity field on the master element is interpolated using *GLL* interpolation polynomials defined in equations (2.10 ~ 13). And the velocity of particle for any other \mathbf{x} point is obtained by spectral interpolation with mapping in equation (2.27):

$$\text{for } d = 2, \quad \tilde{\mathbf{u}}(x, y) = \sum_{m=0}^{N_\xi} \sum_{n=0}^{N_\eta} \tilde{\mathbf{u}}_{mn} h_m^{N_\xi}(\xi) h_n^{N_\eta}(\eta), \quad (2.28.a)$$

$$\text{for } d = 3, \quad \tilde{\mathbf{u}}(x, y, z) = \sum_{m=0}^{N_\xi} \sum_{n=0}^{N_\eta} \sum_{o=0}^{N_\zeta} \tilde{\mathbf{u}}_{mno} h_m^{N_\xi}(\xi) h_n^{N_\eta}(\eta) h_o^{N_\zeta}(\zeta), \quad (2.28.b)$$

where $\tilde{\mathbf{u}}_{mn}$ is the velocity field obtained from the numerical solution of equation (2.4) at the *GLL* points.

As an effort to minimize temporal integration error, we utilize high order temporal integration such as 4th order Runge-Kutta scheme, which is given below:

$$\mathbf{x}^{n+1} = \mathbf{x}^n + \frac{1}{6}(\mathbf{k}_1 + 2 \cdot \mathbf{k}_2 + 2 \cdot \mathbf{k}_3 + \mathbf{k}_4), \quad (2.29.a)$$

$$\mathbf{k}_1 = \Delta t \cdot \tilde{\mathbf{u}}(t^n, \mathbf{x}^n), \quad (2.29.b)$$

$$\mathbf{k}_2 = \Delta t \cdot \tilde{\mathbf{u}}\left(t^{n+1/2}, \mathbf{x}^n + \frac{\mathbf{k}_1}{2}\right), \quad (2.29.c)$$

$$\mathbf{k}_3 = \Delta t \cdot \tilde{\mathbf{u}}\left(t^{n+1/2}, \mathbf{x}^n + \frac{\mathbf{k}_2}{2}\right), \quad (2.29.d)$$

$$\mathbf{k}_4 = \Delta t \cdot \tilde{\mathbf{u}}(t^{n+1}, \mathbf{x}^n + \mathbf{k}_3), \quad (2.29.e)$$

where n denotes the time step index, and Δt is the time increment. The interpretation of Runge-Kutta scheme is depicted in figure 2.3. As we see equation (2.29), 4th order Runge-Kutta scheme requires the calculation of velocity fields at $t^{n+1/2}$. Anderson *et al.*, for their chaotic mixing study in an oscillatory driven cavity, utilized a linear interpolation between time levels:

$$\tilde{\mathbf{u}}^{n+1/2} = \frac{1}{2}(\tilde{\mathbf{u}}^{n+1} + \tilde{\mathbf{u}}^n) \quad [30]. \quad (2.30)$$

However, in transient flows such as chaotically stirred flows, above linear interpolation can deteriorate solution quality, and consequently fail to detect the instantaneous position of fluid particle in an accurate way. Calculation of particle trajectories is very sensitive to small changes in kinematics. Thus, we directly obtain intermediate velocity from the proposed scheme, where time marching of the convection term in the Navier-Stokes equations is explicitly performed using a 2nd order Runge-Kutta in conjunction with 4th order Runge-Kutta for particle tracking.

We often need to track huge number of particles (normally, more than $10^6 \sim 10^{12}$) simultaneously to detect dynamic structure of fluid field such as invariant manifold or stretching field, or to calculate their statistical measures as study on chaotic advection in Chapter IV, V, and VI. Fortunately, there is no communication required between these non-interacting and passive

particles, thus computation of particle tracking may be thought to be *embarrassingly parallel* and thus lend itself to efficient parallel implementation [77]. This has enabled the calculation of a very large number of trajectories, thus improving the accuracy of statistical determination of the quantitative mixing measures.

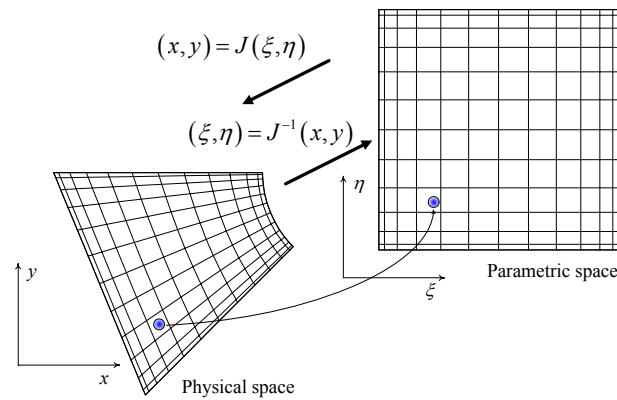


Figure 2.2. Two-dimensional isoparametric mapping between the physical and the parametric spaces.

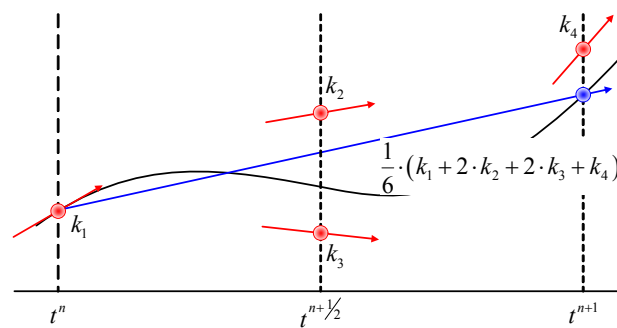


Figure 2.3. Interpretation of the 4th order Runge–Kutta integration.

2.2. Nonconforming spectral element method

If we use only conforming mesh in the problem of complex engineering geometries, there can be severe restrictions on mesh refinements. By efficient discretizations, it is expected that nonconforming SEM can resolve the problems on the computational load by avoiding the propagation of high-order polynomial discretization to the entire domain [18, 21]. Thus, in this study, we consider three different elemental interfaces, which are conforming, p -type nonconforming, and h -type nonconforming. Figure 2.4. illustrates different permutations of polynomial and geometrical nonconformity. A conforming interface is consisted with two geometrically matching elemental boundaries, with the same order of expansion used at each boundary. Figure 2.4(a) corresponds to the conforming mesh, where the neighboring elements share an entire edge and the order of approximation is the same in each expansion direction. A p -type nonconforming interface is consisted with two-geometrically matching elemental boundaries, with different order of expansion used at each boundary, as shown in Figure 2.4(b). Figure 2.4(c) illustrates an h -type nonconformity, which has geometrical mismatching between the elemental boundaries. Figure 2.4(d) depicts both p - and h - type non-conformities.

To bring flexibility on building computational mesh by polynomial and geometric nonconformity, several ways of mathematical conformity enforcing are proposed. We select two famous schemes like what Sert and Beskok have done in their previous comparative study [21]. One of the selected methods is the Pointwise matching (also known as the Constrained Approximation) Method (PMM). It regains the lost C^0 continuity at the non-conforming interfaces by enforcing pointwise projection of the unknowns. Another method is the integral projection (Mortar Element) Method (IPM). In this method, C^0 continuity is not regained, however the jump at the non-conforming interfaces are minimized by enforcing a weighted-integral matching. In this chapter, we will explain how to build the conformity matrix, by considering only p -type nonconforming interfaces using PMM and IPM. Interface, which has h -type nonconformity, requires a similar procedure to calculate the conformity matrix of p -type nonconforming interface. For the sake of brevity, we skip the details explained in Sert [18], Sert and Beskok [21].

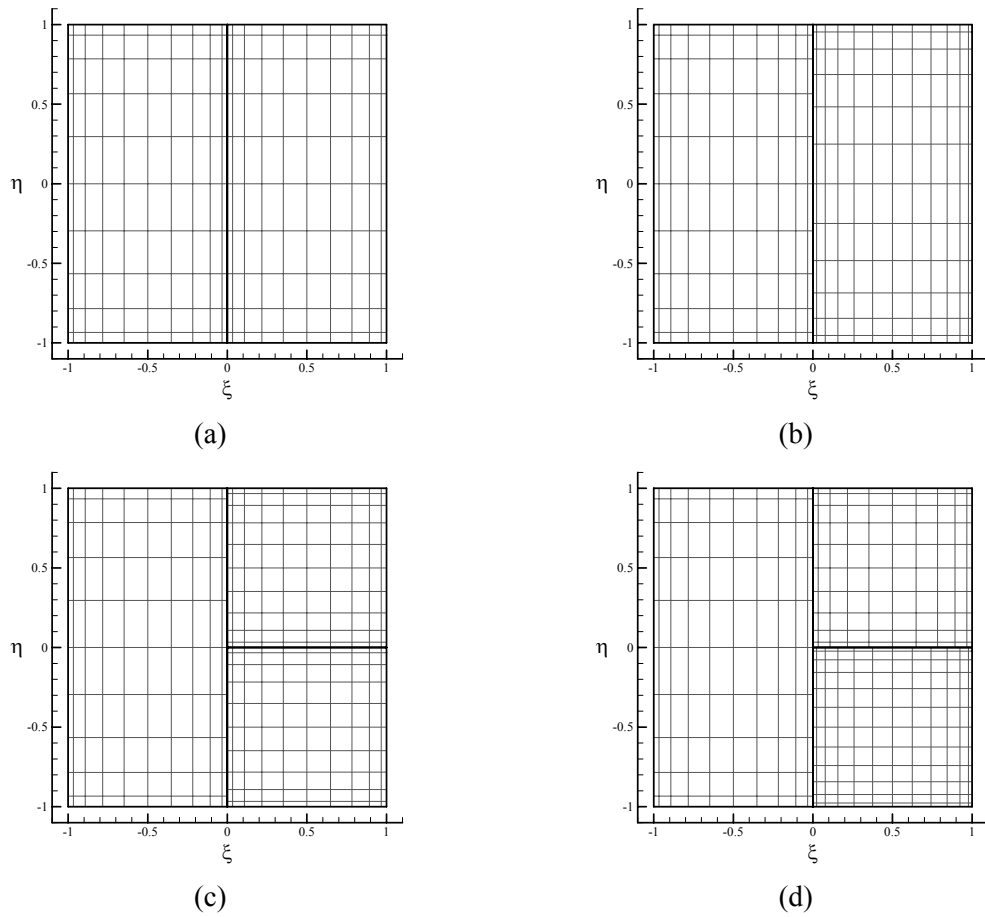


Figure 2.4. Different types of elemental interfaces: (a) Conforming mesh, (b) Conforming geometry, Nonconforming polynomially, (c) Nonconforming geometry, Conforming polynomially, (d) Nonconforming both polynomially and geometrically.

2.2.1. Conformity matrix using pointwise matching method (PMM)

In this section we consider the methodology to build the conformity matrix by PMM. As described above, at the nonconforming interfaces collocation points of two neighboring faces are not matching. Both set of points cannot be directly used in the global assembly process. For given example shown in figure 2.5, maximum rule will be used. Following [21], East side of left element is constrained because expansion order of left element is less than that of right element. Thus, figure 2.5 shows the constrained element obtained by replacing the points on the passive face of the original element by the points of the active neighboring face. Deleted points of the original element are the passive points. By definition all the points of the constrained element are active points. These are the points that will go into the global assembly process.

Before obtaining conformity matrix, we need to write the unknowns at the passive points 2 and 3 in terms of the unknowns at the active points $\hat{1}-\hat{18}$. For this purpose, Lagrangian interpolant basis in equation (2.10) can be used on the constrained element. For example, at point 2 (~ is dropped for the sake of clarity),

$$\theta_5^e = \sum_{j=1}^{\widehat{ncp}} \theta_j^e S_j(\xi_5, \eta_5), \quad (2.31)$$

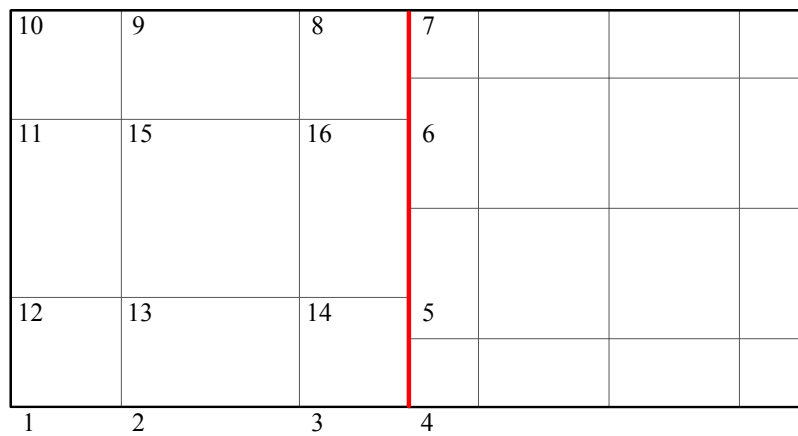
Note that point 5 is on a face, hence two-dimensional shape functions reduce to one-dimensional Lagrange interpolants. Using this fact, equation (2.31) can be simplified to

$$\theta_5^e = \theta_4^e h_4^A(\eta_5) + \theta_5^e h_5^A(\eta_5) + \theta_6^e h_6^A(\eta_5) + \theta_7^e h_7^A(\eta_5) + \theta_8^e h_8^A(\eta_5), \quad (2.32)$$

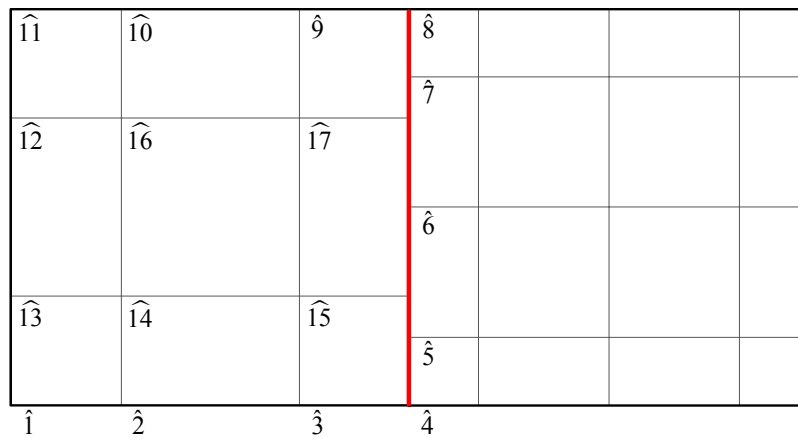
where h is the one dimensional Lagrangian interpolant. This is called the constraint approximation for the passive point 5. A similar equation can be written for point 6, and together they can be expressed in the following vector equation:

$$\begin{Bmatrix} \theta_5^e \\ \theta_6^e \end{Bmatrix} = \begin{bmatrix} h_4^4(\eta_5) + h_5^4(\eta_5) + h_6^4(\eta_5) + h_7^4(\eta_5) + h_8^4(\eta_5) \\ h_4^4(\eta_6) + h_5^4(\eta_6) + h_6^4(\eta_6) + h_7^4(\eta_6) + h_8^4(\eta_6) \end{bmatrix} \begin{Bmatrix} \theta_4^e \\ \theta_5^e \\ \theta_6^e \\ \theta_7^e \\ \theta_8^e \end{Bmatrix} = \mathbf{C}_E \begin{Bmatrix} \theta_4^e \\ \theta_5^e \\ \theta_6^e \\ \theta_7^e \\ \theta_8^e \end{Bmatrix}, \quad (2.33)$$

where \mathbf{C}_E is the conformity matrix.



(a)



(b)

Figure 2.5. (a) Original element with $n_{cp} = 16$, (b) Modified element constrained by maximum rule with $n_{cp} = 17$. Nonconforming interface is indicated with a red line between two elements.

2.2.2. Conformity matrix using integral projection method (IPM)

In this section we consider the way to build conformity matrix by utilizing IPM. Unlike PMM, IPM does not regain the lost C^0 continuity at the non-conforming interfaces via pointwise projection. Instead, it employs L^2 -projection operators to enforce weak continuity at the nonconforming interface in a weighted integral sense. As an example of p -type non-conformity, the same configuration given at figure 2.5 is examined, using the maximum rule. First, we need to write the unknowns at passive points 5 and 6 in terms of the unknowns at the active points in figure (2.5). In the following discussion, at a p -type non-conforming interface, expansion orders of the passive and active faces will be denoted by N_1 and N_2 , respectively. This time the constraint functions will not enforce a pointwise matching but rather a weaker matching. We will take a weighted line integral at the East face of the original element,

$$I_1 = \oint_{4-7} \theta \psi_i ds, \quad (2.34)$$

where ψ_i is the weight function associated with the i^{th} passive point. In order to obtain two equations for unknowns at the two passive points (5 and 6), two weight functions are necessary. They are usually selected to be modified *GLL*-based Lagrange interpolants that are two orders less than the order of the original face.

$$\psi_i = (-1)^{N_1-i} \frac{L'_{N_1}(\eta)}{\eta_i - \eta}, \quad i = 1, \dots, N_1 - 1, \quad (2.35)$$

Two orders less, because the end point conditions ($\theta_4 = \theta_4$, $\theta_7 = \theta_8$) removes two degrees of freedom from the constraint at each passive face. By utilizing the discretized form of the unknown θ , equation (2.34) becomes:

$$I_1 = \sum_{j=4}^7 \oint_{4-7} \theta_j h_j \psi_i ds. \quad (2.36)$$

Note that the summation includes only the points of the East face. There will be no contribution from other points because shape functions associated with those points have zero value at the East face. Also note that two-dimensional shape functions reduce to one-dimensional Lagrange interpolants at the faces. Now let us take a similar line integral but this time at the East face of the constrained element:

$$I_2 = \sum_{j=4}^{\hat{8}} \oint_{4-\hat{8}} \theta_j h_j \psi_i ds. \quad (2.37)$$

Constrained functions for IPM can be obtained by equating I_1 and I_2 :

$$\sum_{j=4}^7 \oint_{4-7} \theta_j h_j \psi_i ds = \sum_{j=4}^{\hat{8}} \oint_{4-\hat{8}} \theta_j h_j \psi_i ds. \quad (2.38)$$

Using *GLL* quadrature for the integrals and the two end-point conditions, this system can be reduced to

$$\mathbf{B}_E \begin{Bmatrix} \theta_5^e \\ \theta_6^e \end{Bmatrix} = \mathbf{P}_E \begin{Bmatrix} \theta_4^e \\ \theta_5^e \\ \theta_6^e \\ \theta_7^e \\ \theta_8^e \end{Bmatrix} \Rightarrow \begin{Bmatrix} \theta_5^e \\ \theta_6^e \end{Bmatrix} = (\mathbf{B}_E)^{-1} \mathbf{P}_E \begin{Bmatrix} \theta_4^e \\ \theta_5^e \\ \theta_6^e \\ \theta_7^e \\ \theta_8^e \end{Bmatrix} = \mathbf{C}_E \begin{Bmatrix} \theta_4^e \\ \theta_5^e \\ \theta_6^e \\ \theta_7^e \\ \theta_8^e \end{Bmatrix}, \quad (2.39)$$

where \mathbf{B}_E and \mathbf{P}_E are described in detail in [18].

Equation (2.39) has the same form as equation (2.33) derived from PMM. Of course, the numeric values of entries of the conformity matrix \mathbf{C}_E are different, and they depend on the order of the *GLL* quadrature used for the integrals, I_1 and I_2 . From equation (2.36), it can be seen that I_1 includes polynomials of order $(N_1 + N_1 - 2)$, which can be calculated exactly with N_1^{th} -order *GLL* quadrature (N^{th} -order *GLL* quadrature can evaluate $(2N - 1)^{th}$ -order polynomials

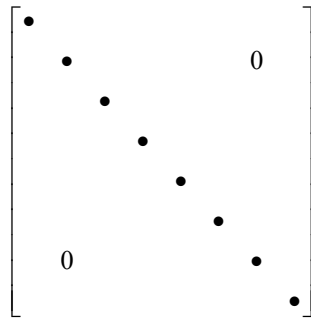
$$\mathbf{M} = \sum_{e=1}^{ne} (\mathbf{C}^e)^T \mathbf{M}^e \mathbf{C}^e, \quad (2.40.a)$$

$$\mathbf{L} = \sum_{e=1}^{ne} (\mathbf{C}^e)^T \mathbf{L}^e \mathbf{C}^e, \quad (2.40.b)$$

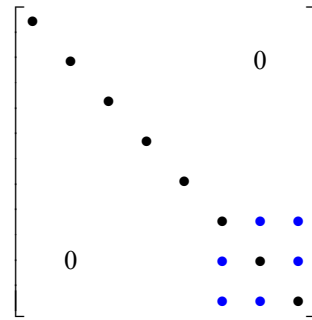
$$\mathbf{f} = \sum_{e=1}^{ne} (\mathbf{C}^e)^T \mathbf{f}^e, \quad (2.40.c)$$

where \mathbf{M}^e is the elemental mass matrix, \mathbf{L}^e is the elemental Laplacian operator, and \mathbf{f}^e is the elemental forcing vector. As shown above, elemental conformity matrices are very sparse. To perform matrix multiplications in equation (2.40), we utilized Intel sparse BLAS routines [78]. In the spectral element discretization, quadrature points coincide with computational grid points, and thus it is incurred that the mass matrix is exactly diagonal by construction, which drastically simplifies the implementation and reduces the computational cost in explicit temporal integration and its inversion. Unfortunately, this property will be lost when the Galerkin formulation is modified with nonconforming formulations [16, 17]. Topological difference between two mass matrices on conforming and nonconforming grids is depicted below:

\mathbf{M} in conforming grids: diagonal



\mathbf{M} in nonconforming grids: non-diagonal



where blue dots denote additional non-zero values incurred by the conformity enforcing process described in equation (2.40).

2.3. Convergence test

To test the convergence properties of our algorithm we consider the validation problems with their analytical solutions in two- and three-dimensions.

2.3.1. Scalar convection-diffusion problems in multi-dimensions

In $d = 2$ or 3 , we consider the following unsteady convection-diffusion problem:

$$\frac{\partial \theta}{\partial t} - \frac{1}{Pe} \nabla^2 \theta + \frac{\partial \theta}{\partial x} = 0 \quad (2.41)$$

If velocity vector \mathbf{u} in equation (2.1.a) is set as $(1, 0)^T$ in $d = 2$ space dimensions, or $(1, 0, 0)^T$ in $d = 3$ space dimensions, scalar transport equations (2.1.c) are reduced to equation (2.41). For the initial condition of

$$\text{for } d = 2, \quad \theta(x, y, t) = \sin(2 \cdot \pi \cdot x) \cdot \sin(\pi \cdot y), \quad (2.42.a)$$

$$\text{for } d = 3, \quad \theta(x, y, z, t) = \sin(2 \cdot \pi \cdot x) \cdot \sin(2 \cdot \pi \cdot y) \cdot \sin(2 \cdot \pi \cdot z), \quad (2.42.b)$$

and the analytical solutions are given by

$$\text{for } d = 2, \quad \theta(x, y, t) = \sin(2 \cdot \pi \cdot (x - t)) \cdot \sin(\pi \cdot y) \cdot e^{\left(\frac{5 \cdot \pi^2 \cdot t}{Pe}\right)}, \quad (2.43.a)$$

$$\text{for } d = 3, \quad \theta(x, y, z, t) = \sin(2 \cdot \pi \cdot (x - t)) \cdot \sin(2 \cdot \pi \cdot y) \cdot \sin(2 \cdot \pi \cdot z) \cdot e^{\left(\frac{12 \cdot \pi^2 \cdot t}{Pe}\right)}. \quad (2.43.b)$$

Solution for this problem is a modified sine wave traveling in the positive x -direction. In two dimensional problem, on the top and bottom boundaries, exact solution given in equation (2.43.a) is specified as Dirichlet boundary conditions, and left and right boundaries are periodic. In three dimensional problem, on the top and bottom ($x - z$ planes), front and back ($x - y$ planes)

boundary *surfaces*, we impose Dirichlet boundary conditions using analytical solution shown in equation (2.43.b). As similar to two-dimensional problem, left and right boundary *surfaces* in direction of $y - z$ planes are periodic. As given by equation (2.43), the analytical solution decreases exponentially by time, and so is the error. In order to circumvent this, we normalized the error by dividing it with exponential term of analytical solution.

For the space accuracy, we perform a p -type refinement study by successively increasing the elemental nodal expansion order N from $N = 4$ up to $N = 10$ in both spatial dimensions. N is equally applied into all spectral elements in all directions. Domain of interest is $\Omega \in [0, 1] \times [0, 1]$ for two-dimensional problem and $\Omega \in [0, 1] \times [0, 1] \times [0, 0.5]$ for three-dimensional problem. Problem domain Ω is decomposed into four equally sized elements in both spatial dimensions. The time steps are fixed at $\Delta t = 1.0 \times 10^{-5}$ for two-dimensional case, and $\Delta t = 1.0 \times 10^{-4}$ for three-dimensional case. In both two- and three-dimensional cases, by adopting Adams-Moulton representation for the diffusion terms, and applying 2nd order Adams-Bashforth to the explicit convection treatment, we utilized a second-order Talyor-Galerkin scheme described in section 2.2. The error evolutions by time are plotted in figure 2.6(a) and 2.7(a). Although, for $N = 4$ the spatial resolution is relatively poor in both spatial dimensions, overall exponential decreases of errors are still observed for increased nodal expansion orders, indicating spectral convergence, where doubling the degrees of freedom per direction results in more than two orders of magnitude reduction in the discretization errors [9]. Finally, we establish time accuracy of the algorithm by keeping the nodal expansion order $N = 10$, and then systematically varying the time increment Δt from $\Delta t = 1.0 \times 10^{-2}$ up to $\Delta t = 1.0 \times 10^{-5}$ and running the code until time $t = 5$ in both spatial dimensions. Error evolutions are plotted in figure 2.6(b) and 2.7(b), and second-order time accuracies are demonstrated, being consistent with the integration scheme provided in section 2.2.

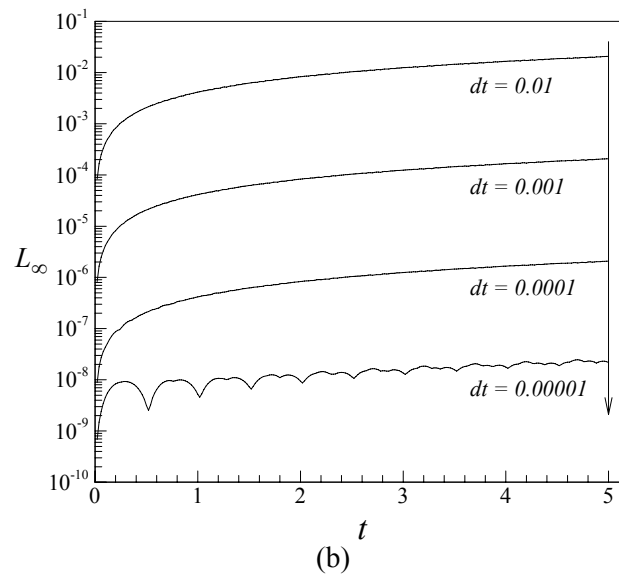
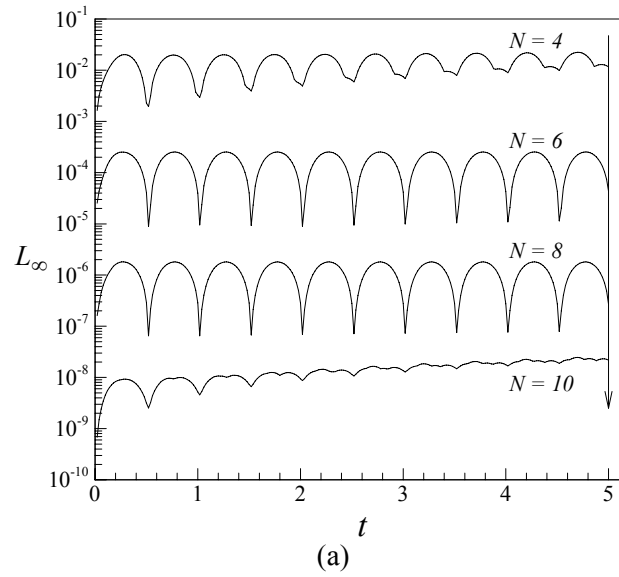


Figure 2.6. Convergence test of two dimensional case at $Pe = 100$: (a) Spatial convergence, $dt = 0.00001$, (b) Temporal convergence, $N_x = N_y = 10$.

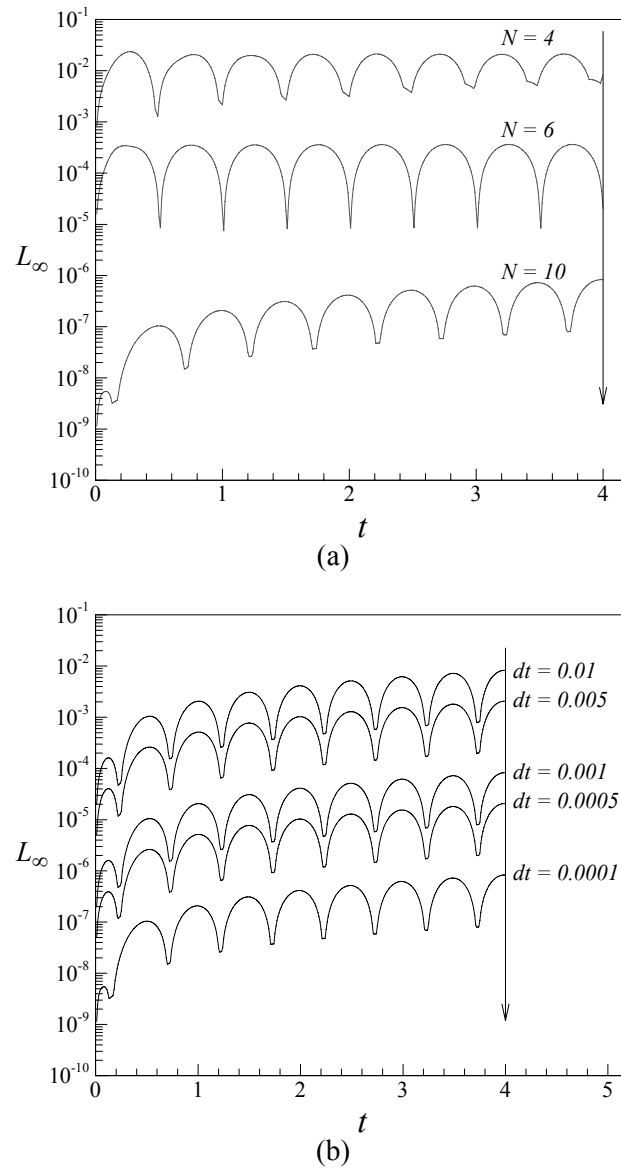


Figure 2.7. Convergence test of three-dimensional case at $Pe = 500$: (a) Spatial convergence of $dt = 0.0001$, (b) Temporal convergence of $N_x = N_y = N_z = 10$.

2.3.2. Stokes cell flow

For the space accuracy of Stokes solver, we perform validation using Stokes cell flow. Its analytical solutions are given as below:

$$u_x = \begin{pmatrix} C_2 \cdot \sinh(\pi \cdot y) + \pi \cdot (C_1 + C_2 \cdot y) \cdot \cosh(\pi \cdot y) \\ -C_1 \cdot \pi \cdot \cosh(\pi \cdot y) - C_1 \cdot \pi^2 \cdot y \cdot \sinh(\pi \cdot y) \end{pmatrix} \cdot \sin(\pi \cdot x), \quad (2.44.a)$$

$$u_y = -\left((C_1 + C_2 \cdot y) \cdot \sinh(\pi \cdot y) - C_1 \cdot \pi \cdot y \cdot \cosh(\pi \cdot y) \right) \cdot \cos(\pi \cdot x) \cdot \pi, \quad (2.44.b)$$

$$C_1 = -\frac{\sinh(\pi)}{\sinh^2(\pi) - \pi^2}, \quad C_2 = \frac{\sinh(\pi) - \pi \cosh(\pi)}{\sinh^2(\pi) - \pi^2}. \quad (2.44.c)$$

Dirichlet boundary conditions on velocities are specified on the top and bottom boundaries using the exact solution given by equation (2.44). Left and right boundaries are periodic. Streamlines obtained with the present formulation for the Stokes cell flow are shown in figure 2.8(a). We perform a p -type refinement study. For such a study, same eight element mesh on $\Omega \in [0, 2] \times [0, 1]$ shown in figure 2.8(b) is utilized and same nodal expansion order N is equally applied into all spectral elements. A time increment of 10^{-3} is used for all the cases of various expansion orders and we integrate our results until the relative residual is less than 10^{-14} , by varying the nodal expansion order $4 \leq N \leq 10$ in both x - and y -directions. Figure 2.8(c) shows L_∞ discretization error of the u_x and u_y velocities against N . In this study, we do not attempt to measure L_∞ discretization error of pressure. As explained in previous sections, pressure points are not reached to physical boundaries by using staggered grids, thus their numeric value can be obtained only in an implicit way. An exponential convergence rate is achieved by u_x and u_y velocities, appearing as a straight line on a log-lin graph.

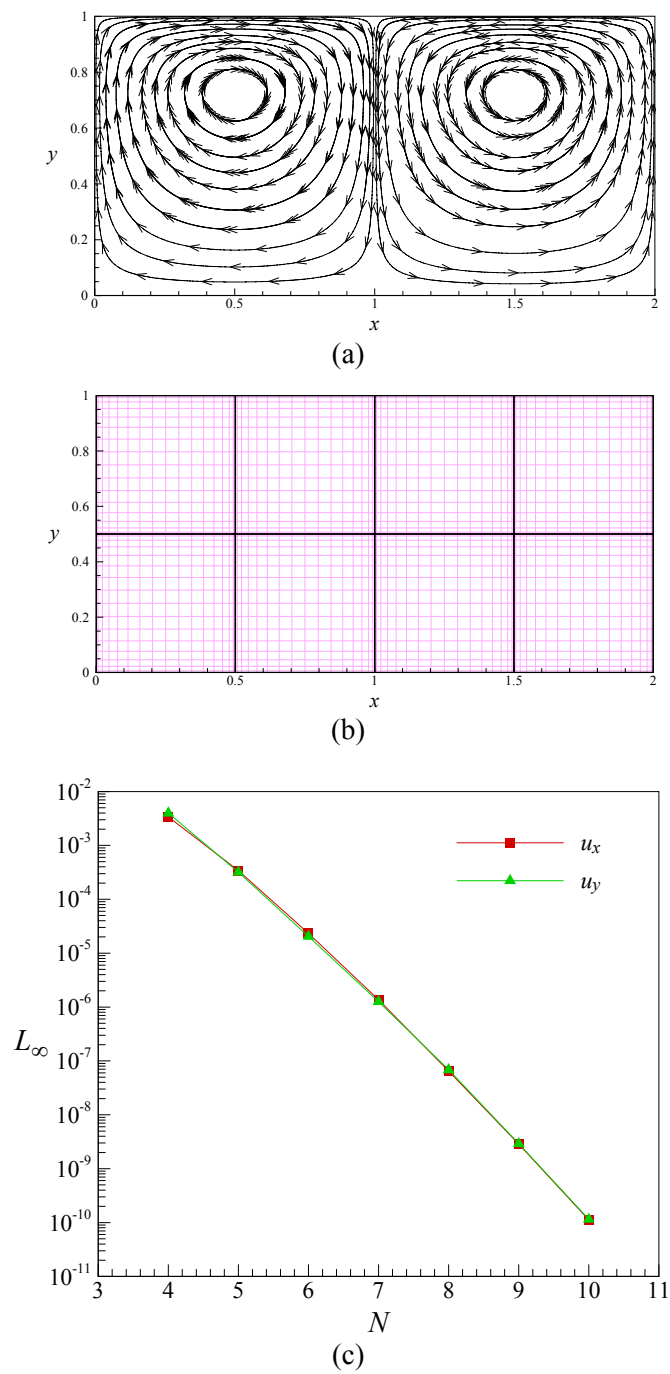


Figure 2.8. Stokes cell flow (a) streamlines, (b) GLL mesh for velocities, (c) Spectral convergence of L_∞ error is achieved in both u_x and u_y velocity values.

2.3.3. Kovaszny flow

Kovaszny flow problem is used for the purpose of validation of incompressible Navier-Stokes solution by projection scheme based spectral elements. Kovaszny flow is a popular test problem for high-order methods [12]. The analytical solutions of Kovaszny flow is sufficiently smooth, thus one can expect spectral convergence with p -type refinement. The flow topology looks similar to the low-speed flow of a viscous flow past an array of cylinders [79]. The analytical solution is given by

$$u_x = 1 - e^{\lambda x} \cdot \cos(2 \cdot \pi \cdot y), \quad u_y = \frac{\lambda}{2\pi} \cdot e^{\lambda x} \cdot \sin(2 \cdot \pi \cdot y), \quad u_z = 0, \quad (2.45.a)$$

$$\lambda = \frac{Re}{2} - \sqrt{\left(\frac{Re}{2}\right)^2 + (2 \cdot \pi)^2}, \quad (2.45.b)$$

where Re is the Reynolds number, and $Re = 40$. The flow actually is two-dimensional but the computer code pretends not to know this for three-dimensional problems. We perform validation on two- / three-dimensional conforming grids, two- / three-dimensional non-conforming grids, as follows:

- (a) Two-dimensional conforming grids: Six elements mesh shown in figure 2.9(a) and (b) on page 48 is used. In all elements, same expansion orders are used in both x - and y -directions: $N = N_x = N_y$. Domain of interest is $\Omega \in [0, 1] \times [0, 1]$.
- (b) Three-dimensional conforming grids: Same four elements mesh shown in figure 2.10(a) is used. Same order nodal expansions are used in both x - and y -directions, whereas we fix the less nodal expansion in z -direction: $N_x = N_y$, $N_z = \min(N_x, N_y, N_z)$. Domain of interest is $\Omega \in [0, 1] \times [0, 1] \times [0, 0.1]$.

- (c) Two-dimensional non-conforming grids: Same four elements mesh shown in figure 2.11(a) is used. For each element, same order nodal expansions are used in both x - and y -directions: $N = N_x = N_y$. Domain of interest is $\Omega \in [0, 1] \times [0, 1]$.
- (d) Three-dimensional non-conforming grids: Same eight elements mesh shown in figure 2.12(a) is used. For each element, same order nodal expansions are used in both x - and y -directions, whereas we fix the less nodal expansion in z -direction: $N_x = N_y$, $N_z = \min(N_x, N_y, N_z)$. Domain of interest is $\Omega \in [0, 0.5] \times [0, 0.5] \times [0, 0.2]$.

A time increment of 10^{-3} is used for all the cases and we integrate our results until the relative residual is less than 10^{-14} . Analytical solutions are specified at all boundaries as Dirichlet boundary conditions. For two-dimensional conformity case, we vary the nodal expansion orders $4 \leq N \leq 18$ in both x - and y -directions. Elements 2, 3, 4, and 5 have curved boundaries and in the mean time, elements 4 and 5 are partially skewed by the positive curvature of elements 2 and 3 in outward directions. Although the given computational mesh has these bad shaped elements, figure 2.9(c) shows the results for the nodal basis, demonstrating that exponential convergence is achieved by u_x and u_y velocities. For 3d conformity case, we vary the nodal expansion orders $4 \leq N \leq 10$ in both x - and y -directions, fixing z -directional expansion order as 4. An exponential convergence rate is achieved by u_x velocity, appearing as a straight line on a log-lin graph as shown in figure 2.10(b).

In Cuneyt and Beskok's previous work [21], it was of note that PMM with minimum rule and IPM with minimum rule provided acceptable results for several cases on p -type nonconformities. Based on these premise, we use minimum rule in both PMM and IPM. For two-dimensional non-conformity case, elements 1 and 2 have 12th order nodal expansion in both x - and y -directions, whereas elements 3 and 4 have 10th order nodal expansion as shown in figure

2.11(a). The initial conditions are chosen to be zero velocity and pressure. Figure 2.11(b) shows the decay of L_∞ discretization error by integration time. In three-dimensional non-conformity case, while the nodal expansion order of elements 1, 3, 5, and 7 are fixed as 7 in both x - and y -directions, for elements 2, 4, 6, and 8, we vary the nodal expansion orders $4 \leq N \leq 6$ in both x - and y -directions. For all elements, z -directional expansion order is constantly set as 3. We use minimum rule for both PMM and IPM. Figure 2.12(b) shows L_∞ discretization errors against N of elements 2, 4, 6, and 8. In these two different formulations, same exponential convergence rates are achieved by u_x velocity, appearing as a straight line on a log-linear graph. However, the additional consistency error associated with a polynomially nonconformity is found by the fact that the solution space X_N is not a subspace of standard Sobolev space [17]. Consequently, PMM and IPM results are practically the same. When the elemental nodal expansion orders of elements 2, 4, 6, and 8 are set to 6 in the x - and y -directions, u_z values are limited within acceptable levels of $10^{-9} \sim 10^{-8}$.

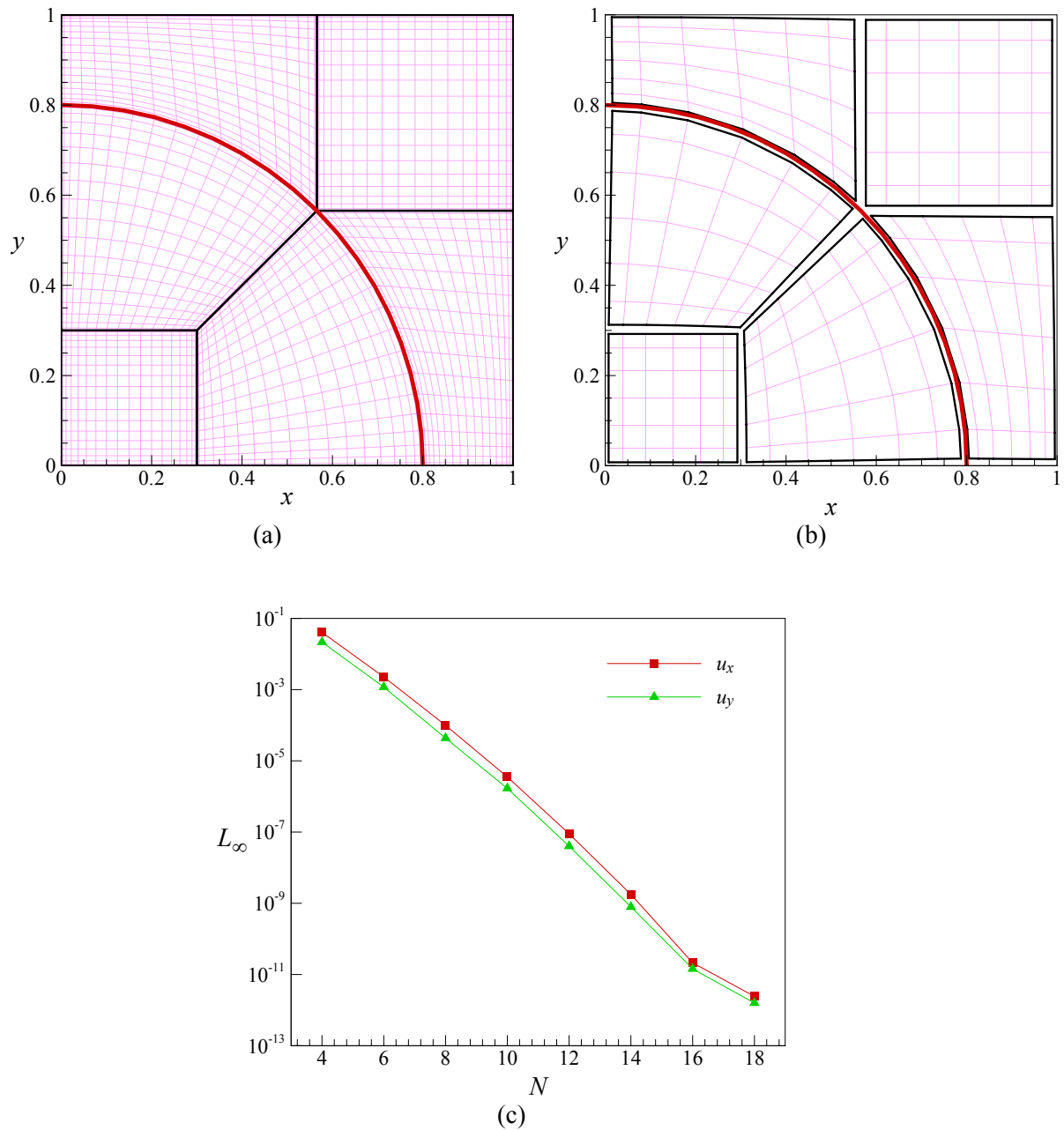


Figure 2.9. Kovaszny flow at $Re = 40$ on two-dimensional conforming grids with curved element boundaries: Curved boundaries are indicated with thick red line in (a) and (b); (a) *GLL* mesh for velocities, (b) *GL* mesh for pressure, (c) Spectral convergence of L_∞ error is achieved in both u_x and u_y velocity values.

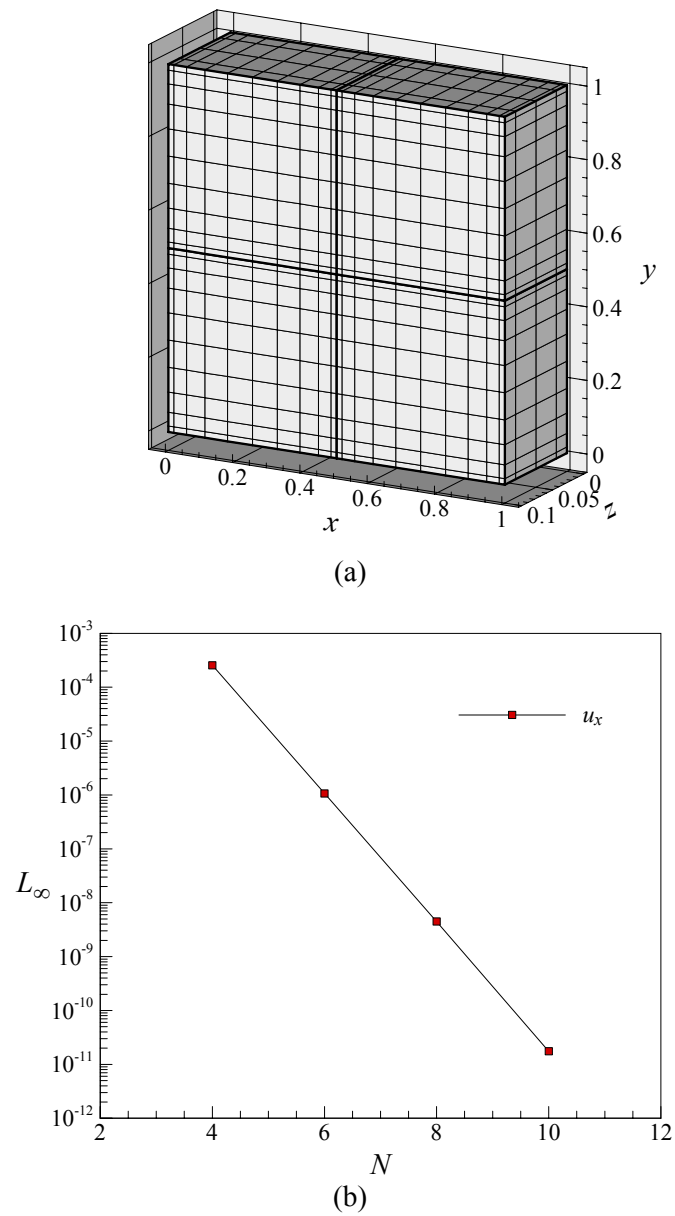


Figure 2.10. Kovaszny flow at $Re = 40$ on three-dimensional conforming grids: (a) *GLL* mesh for velocities, (b) Spectral convergence of L_∞ error is achieved in u_x velocity values.

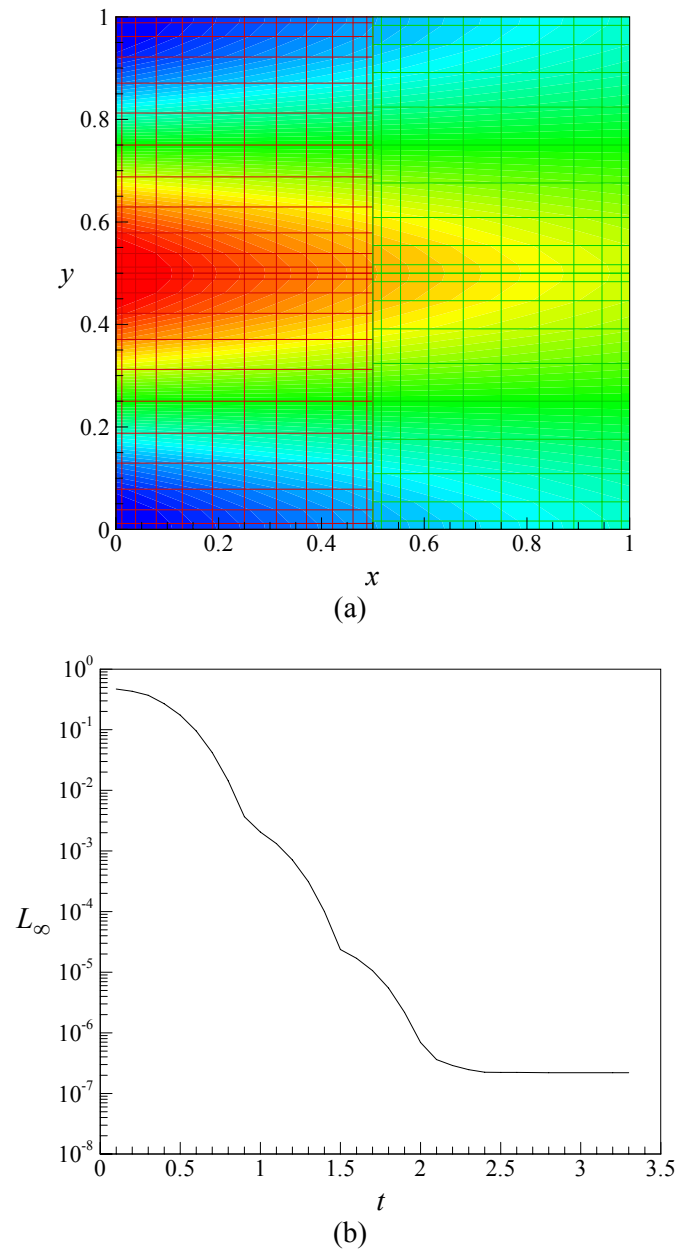


Figure 2.11. Kovaszny flow at $Re = 40$ on two-dimensional p -type non-conforming grids: (a) u_x velocity contour plotted on the *GLL* mesh. Contour plots are produced by *Tecplot*TM, which can not perform polynomial expansions, creating coarser looking results than the actual high-order ones. (b) temporal record of L_∞ error during time integration of projection scheme. The initial conditions are chosen to be zero velocity and pressure, which satisfy incompressibility constraint.

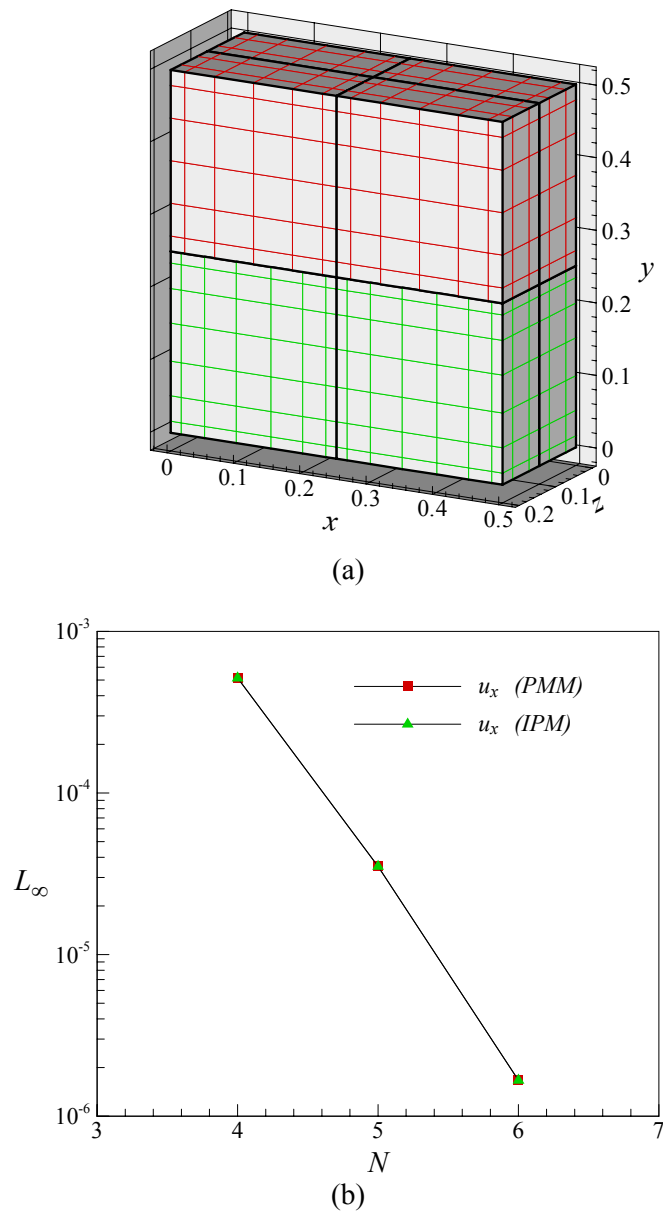


Figure 2.12. Kovaszny flow at $Re = 40$ on three-dimensional p -type non-conforming grids: (a) non-conforming mesh for velocities, (b) Spectral convergence of L_∞ error is achieved in u_x velocity values by utilizing both PMM and IPM.

CHAPTER III

CODE VERIFICATION BY THE ALGEBRAIC FACTORIZATION SCHEME

In this chapter, we examine several model problems to illustrate the advantages of applying high-order spatial discretizations and validate our transient simulations by comparing with previously reported data conducted by other researchers. Here we center our attention on two-dimensional cases that provide the foundation for more complicated simulations.

3.1. Moving Gaussian hill

First we consider a moving Gaussian hill problem governed by the unsteady convection-diffusion equation (2.41). The initial condition is given below:

$$\theta(x, y) = \alpha^{\beta((x-x_0)^2 + (y-y_0)^2)}, \quad (x_0, y_0) = (0.5, 0.5) \quad (3.1)$$

where $\alpha = 0.01$, $\beta = 100$. It represents a *sharp* Gaussian hill with height equal to 1 and with radius equal to 0.1 centered at (0.5, 0.5). Domain of interest is $\Omega \in [0, 1] \times [0, 1]$, and on the top and bottom boundaries, zero value is specified as Dirichlet boundary conditions, and left and right boundaries are periodic. Problem configuration is depicted in figure 3.1 (a). By adopting Crank-Nicolson representation for the diffusion terms, and applying 2nd order Adams-Bashforth to the explicit convection treatment, fixing time step $\Delta t = 1.0 \times 10^{-4}$, we utilized a second-order Talyor-Galerkin scheme described in section 2.2. If the Peclet number is set to very high, the problem becomes convection dominated. Numerical instabilities for pure convection equation will be observed regardless of time integration scheme as reported in [17, 22]. Nevertheless,

Ronquist has shown that physical diffusion due to the viscous terms may lead to stable solutions, although the presence of a spurious eigenmode with positive growth causes difficulty in discretization of the convection operator [22].

Using the Peclet number of 10^6 , we performed a series of h - and p -type refinements. Results are shown in figure 3.1 (b), (c), and (d) as contour plots of θ . Case (b) uses sixteen elements of order $N = 8$. In order to resolve the species distribution in the streamwise-direction, in case (c), each element is divided into two, by h -type refinements. However, there were still some ‘wiggles’ visible in this solution, thus, finally in case (d) elements at the centerline are further refined and approximation orders of the pink elements are increased to 12. This last case has both h - and p -type nonconformities. Although we are not presenting any numerical values, smoothness of the θ contours clearly shows that h - and p -type refinements provide better resolution. As reported in [21], the results for PMM and IPM are practically the same.

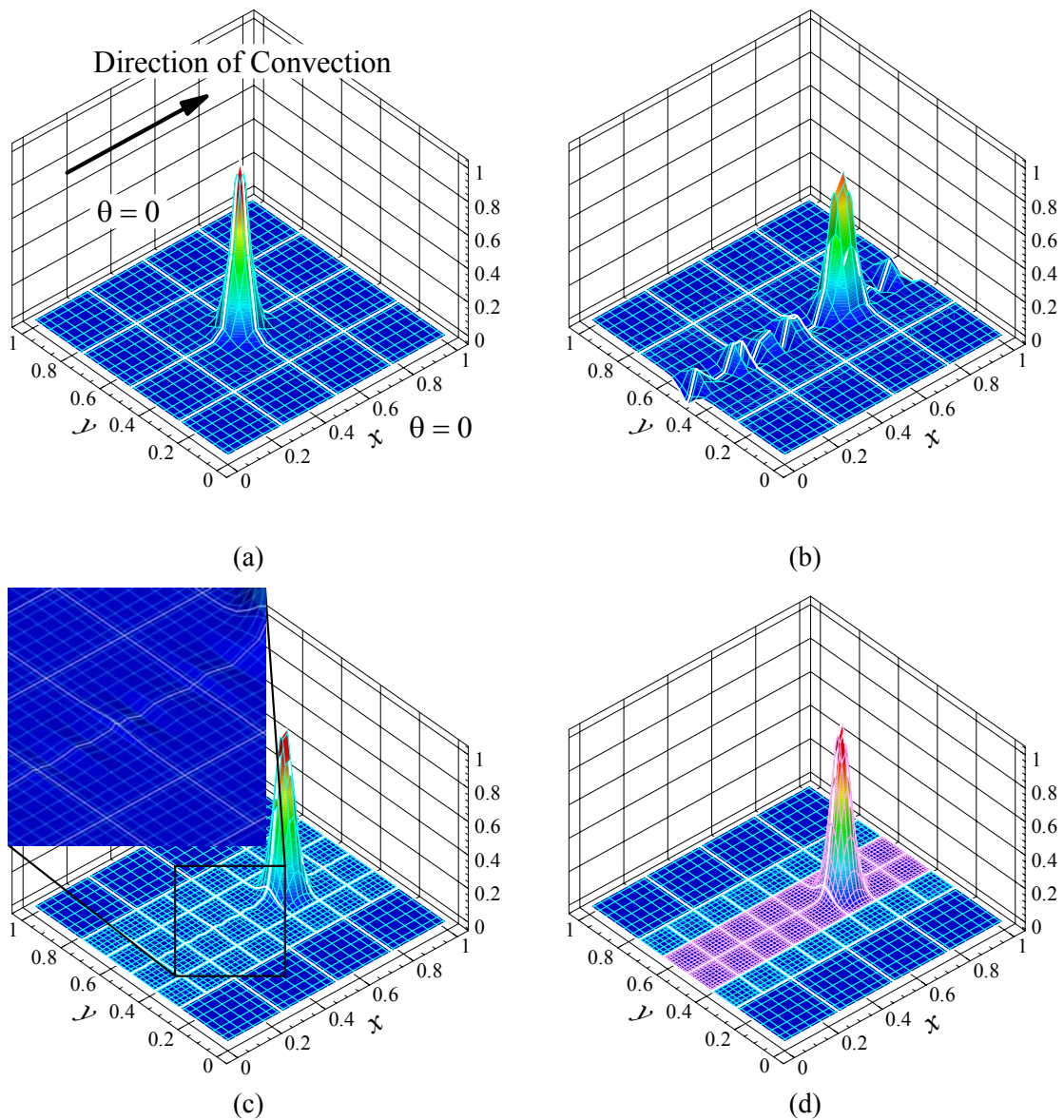


Figure 3.1. Numerical results for the convection of Gaussian hill ($Pe = 10^6$): (a) Problem configuration and initial condition on conforming grids ($N = 8$), Contour plots of (b), (c), and (d) are captured at $t = 1.2$ and time integration is performed with time increment of $dt = 10^{-4}$. h -type refinement is done from (b) to (c). p -type refinement is done from (c) to (d) only on the pink-colored elements. The elemental discretization is shown by the thick lines and the quadrature points are shown by the thin lines.

3.2. Creeping flow in a wedge

Next we consider the solution of Stokes flow in a wedge where the lid moves with a constant velocity. The solution is characterized by a series of Moffat's eddies, each one decaying exponentially in an infinite cascade towards the tip [12]. A wedge with an aspect ratio of 1 : 0.6 was discretized using twenty elements and an expansion order of $N = 10$, as shown in figure 3.2 (a). Stokes flow was then computed in this domain driven by a prescribed lid velocity:

$$u_{lid}(x) \begin{cases} \tanh(\beta(x+0.6)), & -0.6 \leq x \leq 0, \\ \tanh(\beta(x-0.6)), & 0 < x \leq 0.6, \end{cases} \quad (3.2)$$

while all other walls were stationary. Here we take $\beta = 1$, which gives a smooth transition from $u_{lid} = -0.6$ to $u_{lid} = 0.6$ near the walls of the driven surface. This boundary condition results in a well-posed boundary condition, in a sense that singularities at the corners of the driven surface are eliminated. The initial conditions were chosen to be zero velocity and pressure. This means that the fluid is initially at rest and is put into motion by the sudden translation of the top boundary. In present calculations, the converged state was reached through an unsteady integration in time using the algorithm described in section 2.2. At steady state, four eddies are observed, as indicated by a streamline plot in figure 3.2 (b). This example shows the reason why high accuracy is required in fluid dynamics simulations. We took a profile along the center-line and plot the transverse velocity of u_x as a function of perpendicular distance from the top of wedge in figure 3.3. Velocity distribution shows that absolute transverse value of u_x of fourth eddy approximately reaches the double precision limit of 10^{-16} .

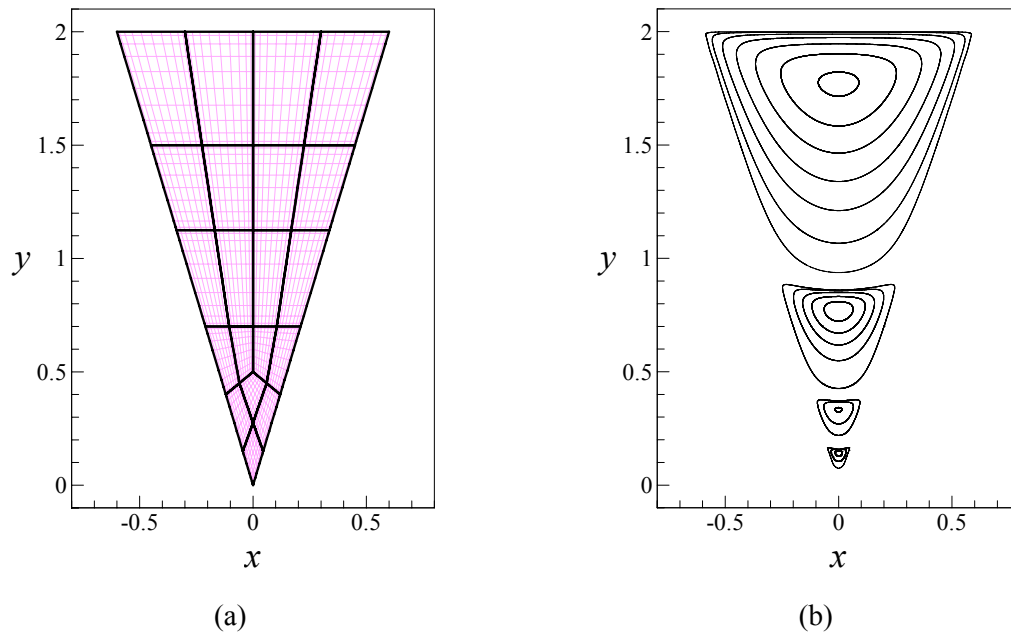


Figure 3.2. Stokes flow in a wedge – (a) *GLL* computational mesh: The elemental discretization is shown by the thick lines and the quadrature points are shown by the thin lines. (b) streamlines.

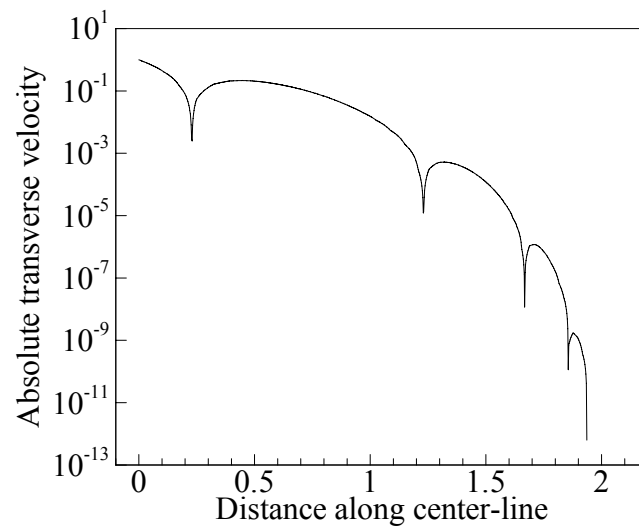


Figure 3.3. The center-line transverse u_x velocity as a function of perpendicular height from the top of the wedge shown in figure 3.2.

3.3. Singular lid driven cavity flow

Lid-driven cavity problem is a classical Navier-Stokes test case due to its simple geometry, yet challenging nature. Although this problem does not have a closed form exact solution, it has been studied extensively and many highly accurate benchmark results are available. The challenging aspect of this problem is due to the resolution of the corner singularities. Pressure and vorticity are not finite at the top corners, which makes the problem difficult for high-order formulations. Fortunately, oscillations induced by the corner singularity do not propagate into the domain but are essentially limited to the corner elements. This limited influence is a general feature of the C^0 interface condition and a good indication of why proper h -refinement is still an important ingredient of SEM [16].

The computational domain is taken to be the unit square, $\Omega = [0, 1] \times [0, 1]$. Top wall is moving with a velocity of $u_x = 1$, while all other walls are stationary. The problem configuration is depicted in figure 3.4 (a). We performed a series of simulations of flow at $Re = 1000$, utilizing the three different types of mesh, type A, B, and C shown in figure 3.4 (b), (c), and (d). Type A and B consist of 10×10 non-uniform 8th order quadrilateral elements used to discretize the domain with the corner element having dimension 0.0625×0.0625 for type A, and 0.02×0.02 for type B.

While type A and B are conforming, type C has various levels of p - and h -type nonconformities, as shown in figure. As Sert and Beskok's previous work [21], we deliberately under-resolved the corner-singularity regions of the flow, by utilizing 6×12 elements in the top-right and top-left corners. In the present calculations the converged state was reached through an unsteady integration in time using the inexact algebraic factorization scheme described in section 2.2. The initial conditions were chosen to be zero velocity and pressure. This means that the fluid is initially at rest and is put into motion by the sudden translation of the top boundary. In figure 3.5, we present u_x and u_y velocity profiles along $x = 0.5$ and $y = 0.5$, respectively. In figure, we also present comparisons of our solutions with spectral solutions of [80]. Our numerical results are in quantitative agreement with the published data. Due to the difference of mesh, it is possible to do point-wise comparison only at $(0.5, 0.5)$. Type A and B requires total 81×81 grid points, while type C of nonconformities utilizes only the half of those of conforming cases to obtain up to four significant digits, demonstrating the scientific accuracy.

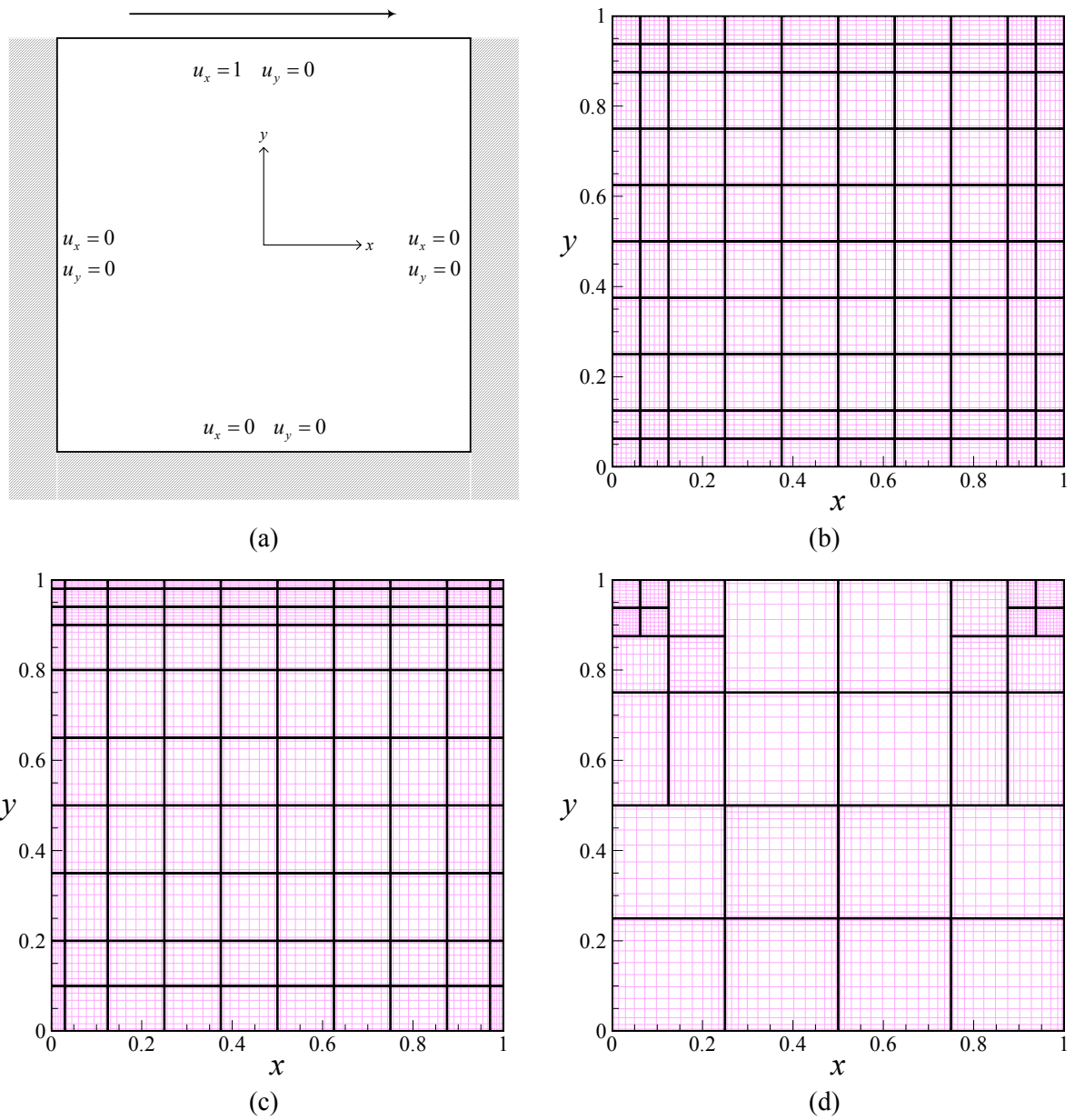


Figure 3.4. Problem configuration for the flow in a square cavity at $Re = 1000$: (a) boundary conditions, (b) mesh A – conforming, (c) mesh B – conforming, (d) mesh C - non-conforming.

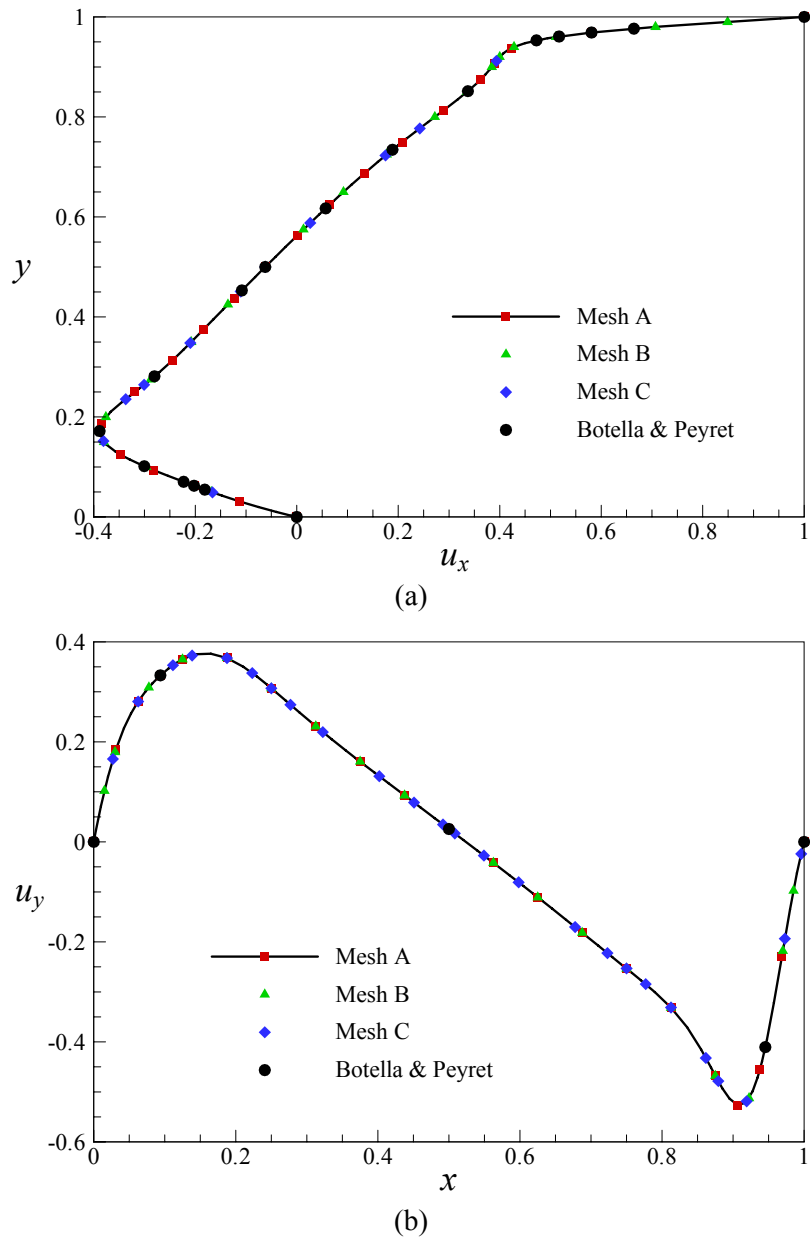


Figure 3.5. (a) u_x velocity distribution along the $x = 0.5$ line, (b) u_y velocity distribution along the $y = 0.5$ line; The results are compared with the spectral solutions in [80] at $Re = 1000$.

3.4. Transient flow over a backward facing step

We consider the two-dimensional transient flow over a backward facing step for various Re . This type of flow is a canonical example of a separated flow with reattachment, and the relative simplicity of its domain geometry has made it a popular benchmark case. For $Re < 400$, a single eddy is formed in the corner between the step and the bottom wall. As Re increases, the second eddy is generated at the top wall. The reattachment lengths caused by eddies are sensitive to numerical schemes and outflow boundary condition.

The initial conditions are chosen to be zero velocity and pressure. In the present calculations the converged state is reached through an unsteady integration in time using the algorithm described in section 2.2. The boundary condition used here is those used in Zhang [81] and Keskar and Lyn [82]:

$$\text{inlet for } 0.5 \leq y \leq 1 \quad : \quad u_x = 24 \cdot (1 - y) \cdot (y - 0.5), \quad u_y = 0, \quad (3.3.a)$$

$$\text{walls} \quad : \quad u_x = 0, \quad u_y = 0, \quad (3.3.b)$$

$$\text{outflow for } x = 20 \quad : \quad \frac{\partial u_x}{\partial x} = 0, \quad \frac{\partial u_y}{\partial x} = 0, \quad (3.3.c)$$

and the outflow boundary (3.3.c) is imposed in a weak sense at $x = 20$. The problem configuration is shown in figure 3.6 (a). The domain of interest is $\Omega = [0, 1] \times [0, 20]$. The given rectangular computational domain permits to decompose whole domain into approximately equal sub-domains as shown in figure 3.6 (b). We show the streamlines and vorticity contour of flow at $Re = 500$ in figure 3.7 (a). For the quantitative validation, we plot the reattachment length L_r as a function of the Reynolds number, in figure 3.7 (b). Results show the quantitatively good agreement with benchmark solutions in [81].

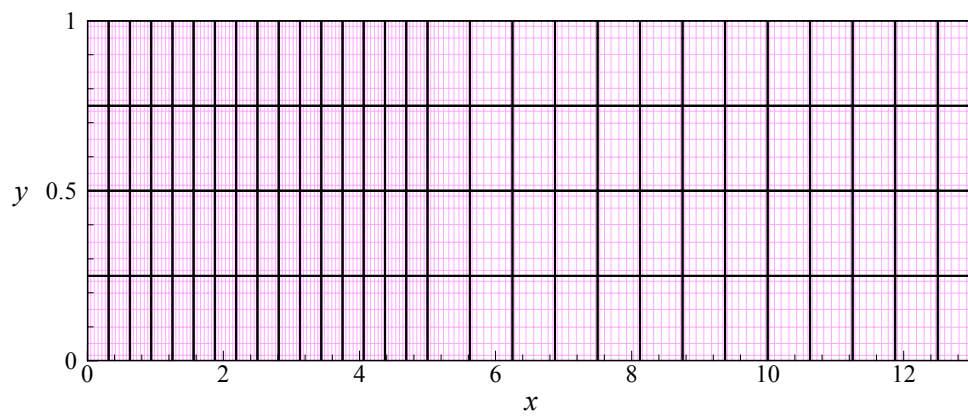
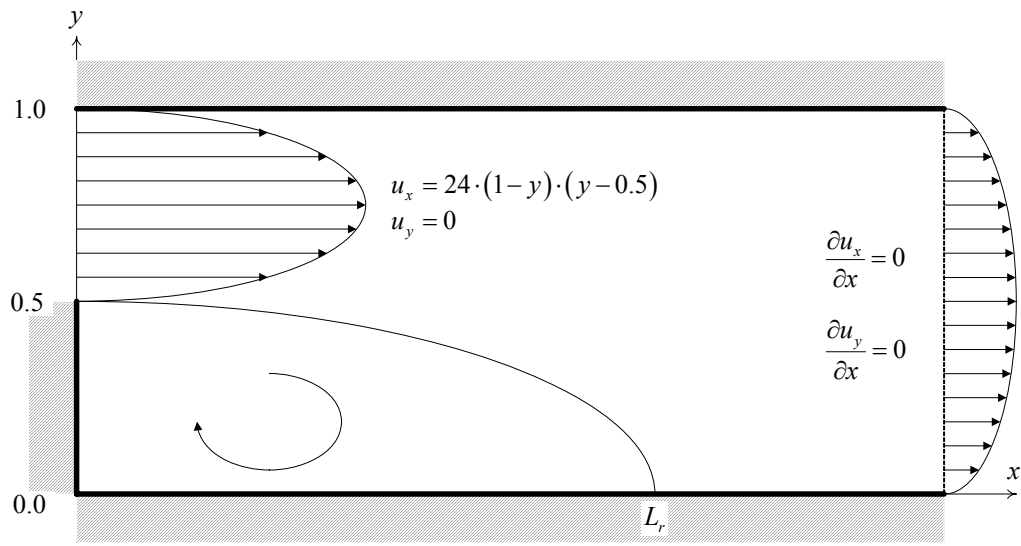


Figure 3.6. Problem configuration for the flow past a backward-facing step: (a) boundary conditions, (b) *GLL* computational mesh: The elemental discretization is shown by the thick lines and the quadrature points are shown by the thin lines.

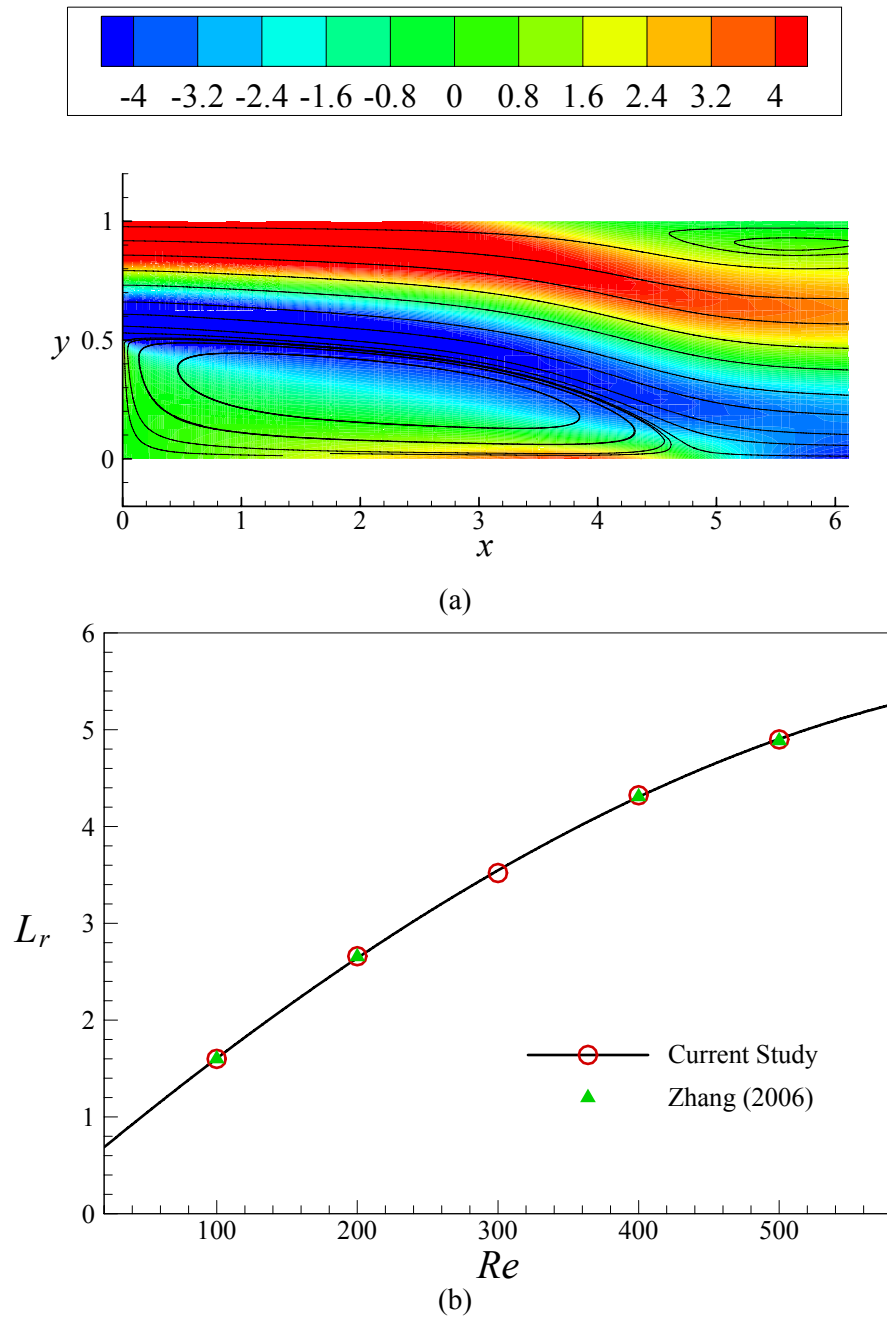


Figure 3.7. Numerical results for the flow past a backward facing step: (a) streamlines are plotted on the vorticity contour at $Re = 500$, (b) Re and the reattachment length (L_r) of the primary eddy.

3.5. Transient flow past a circular cylinder

The challenging problem of the flow past a circular cylinder is considered. This transient problem is frequently used to assess the accuracy of finite element formulations, as it is characterized by a handful of well known quantities, such as a non-dimensionalized frequency of the vortex shedding known as the Strouhal number. At low Reynolds numbers the flow is stationary, symmetric, and characterized by a pair of standing vortices appearing behind the cylinder [65]. It was reported that the Reynolds number at which separation first occurs behind the cylinder is found to be 5.75 [83]. The size of the separated flow region increases with increasing Reynolds number. However, above critical Reynolds number (normally, $Re \geq 40$) the flow around a circular cylinder becomes essentially unsteady undergoing its first bifurcation towards a periodical regime – the so called von Karman vortex shedding. We simulated in two different problem settings such as cylinder inside a channel and cylinder located on the open domain. In these examples we consider flow conditions of $Re = 100$ and 125 , where the flow in the wake is already unsteady. The Reynolds number is based on the averaged inlet velocity and the cylinder diameter.

First, we examine the channel flow at $Re = 125$. A cylinder of unit diameter and a computational domain Ω consisting of the rectangle $[-2.5, 9] \times [-1.5, 1.5]$ are considered, the center of the cylinder being situated at the point $(0, 0)$. Two fluids are introduced at the channel entrance (at $x = -2.5$) from separate inlets as shown in figure 3.8 (a). Fully developed conditions are assumed at the inlet, with parabolic velocity profiles. The boundary conditions are specified as follows:

$$\text{inlet 1 for } y \geq 0 \quad : \quad u_x = -2.67 \cdot y \cdot (y - 1.5), \quad u_y = 0, \quad (3.4.a)$$

$$\text{inlet 2 for } y \leq 0 \quad : \quad u_x = -2.67 \cdot y \cdot (y + 1.5), \quad u_y = 0, \quad (3.4.b)$$

$$\text{wall} \quad : \quad u_x = 0, \quad u_y = 0, \quad (3.4.c)$$

$$\text{cylinder} \quad : \quad u_x = 0, \quad u_y = 0, \quad (3.4.d)$$

$$\text{outflow for } x = 0 \quad : \quad \frac{\partial u_x}{\partial x} = 0, \quad \frac{\partial u_y}{\partial x} = 0 \quad (3.4.e)$$

and the outflow boundary (3.4.e) is imposed in a weak sense at $x = 9$. The problem configuration is depicted in figure 3.8 (a). In the present calculations the *periodic* state was reached through an unsteady integration in time using the algorithm described in section 2.2. It is observed that the solution starts oscillating freely at a time near $t = 110$; the final periodicity of the solution is reached by $t = 170$. Figure 3.9 shows the history of the horizontal velocity at a node situated at the point indicated with a red circle as show in figure 3.8 (b), i.e. downstream of the cylinder and slightly higher. The pressure and vorticity contours obtained at $t = 210$ are shown in figure 3.10.

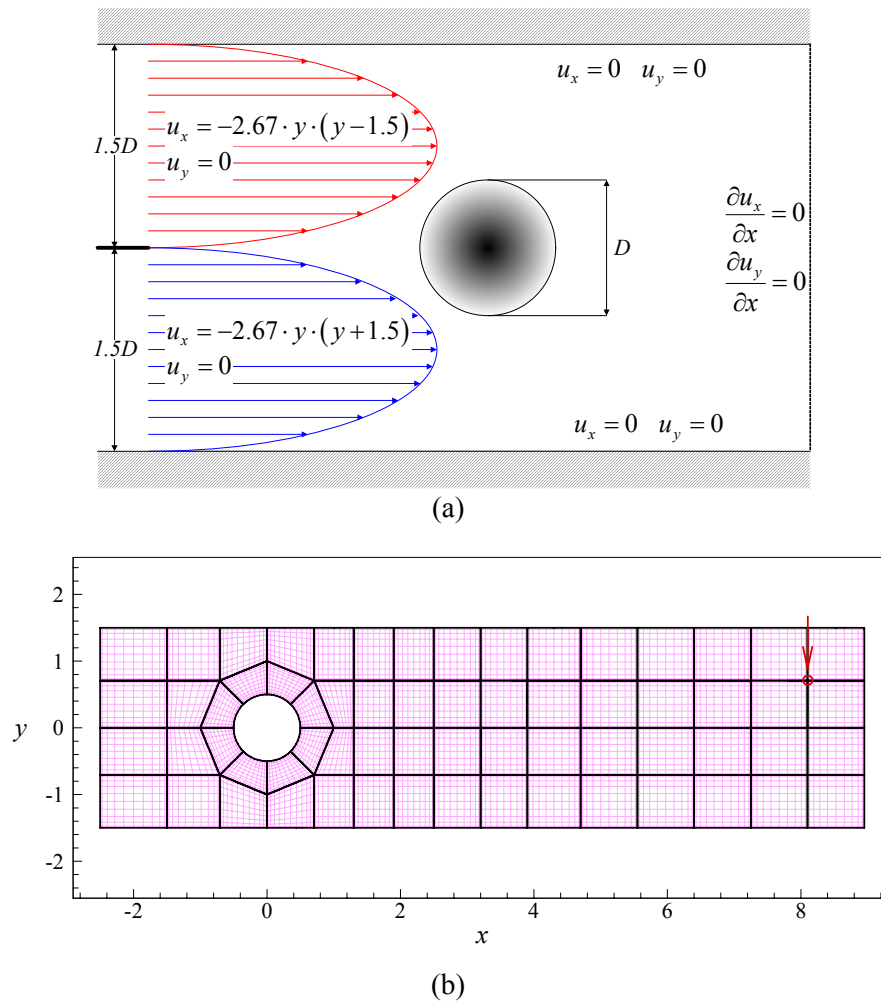


Figure 3.8. Problem configuration for the flow past a circular cylinder at $Re = 125$ in a straight channel: (a) boundary conditions, (b) *GLL* computational mesh: The elemental discretization is shown by the thick lines and the quadrature points are shown by the thin lines. The history of the horizontal velocity, u_x , at a node situated at the point indicated with a red circle is recorded.

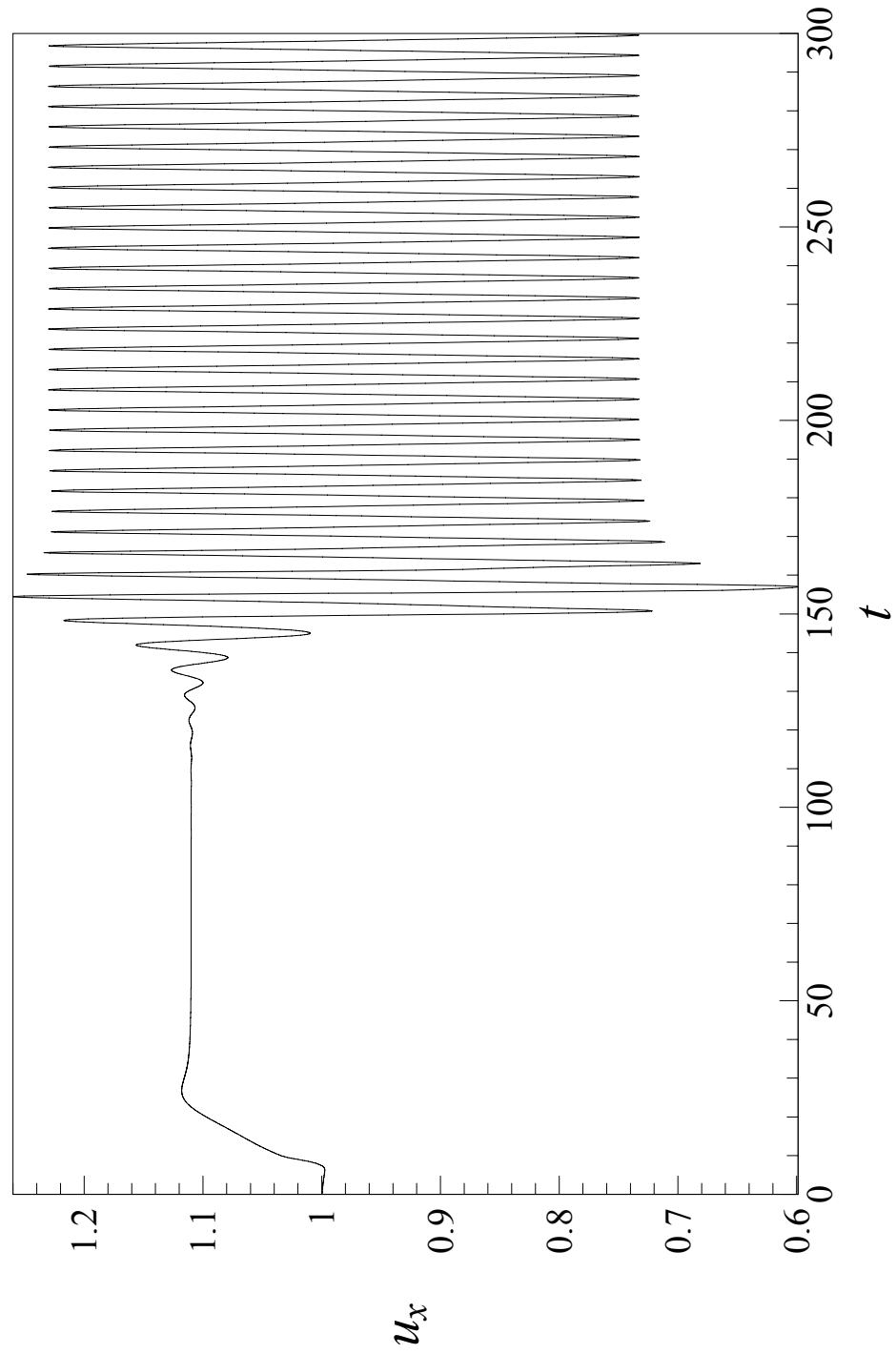
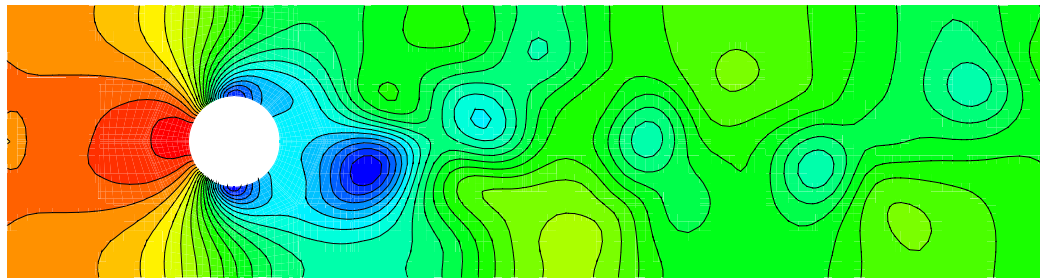
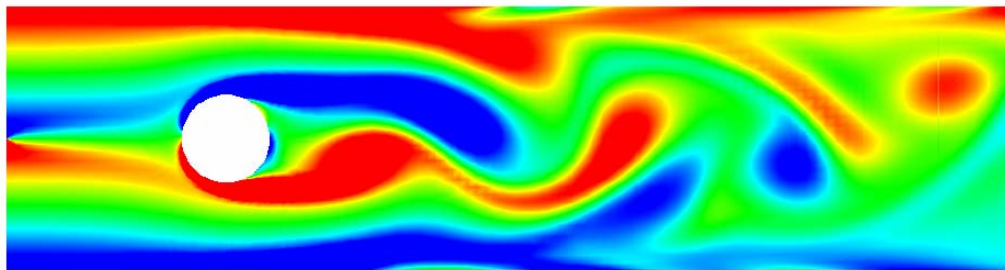
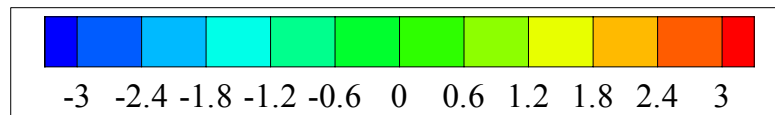


Figure 3.9. Time history of nodal u_x velocity at $Re = 125$.



(a)



(b)

Figure 3.10. Instantaneous: (a) pressure and (b) vorticity contours at $t = 210$, for the flow past a circular cylinder at $Re = 125$ in a straight channel.

In order to validate our transient algorithm, based on time history of nodal values of the velocity field shown in figure 3.10, the Strouhal number is calculated; it is defined as $St = fD / u_0$, where D is the cylinder diameter, u_0 is the averaged velocity and f is the shedding frequency of the solution. A Fourier analysis of the nodal velocity signal is performed within the time range [175, 475] to find the dominant frequency of the solution. As a result, we find $St = 0.33$, which indicates two times larger value than the Strouhal number of flow in the quasi-open domain at the same Reynolds number of $Re = 125$. These computational results are similar with Celik *et al.* [84].

Now we turn our interest to the problem for *quasi-open* domain. A cylinder of unit diameter and a computational domain Ω consisting of the rectangle $[-2.5, 9] \times [-4.0, 4.0]$ are considered, the center of the cylinder being situated at the point $(0, 0)$. On the left, top and bottom boundaries, velocity boundary conditions of $(u_x, u_y) = (1, 0)$ are imposed as Dirichlet boundary conditions. The problem configuration is depicted in figure 3.11 (a). It should be of note that the current computational domain may not be sufficient to prevent any effect of the introduction of *artificial lateral boundaries* on the computed solution [85].

As similar to the problem for channel, with figure 3.12, Fourier spectrum analysis is performed referring to the time history of nodal values of u_x velocity at the point indicated with a red circle as show in figure 3.11 (b), and a major peak in the calculated spectrum is found on the Strouhal number of $St = 0.187$, which has small discrepancy with $St = 0.17$ from the published data of Henderson [16]. This discrepancy is attributed to the location of the lateral boundaries in the current computational domain may not be far enough from the cylinder to avoid any influence on the solution [85]. As reported in [85], at least 12 cylinder diameters on each side of the cylinder are needed to avoid the influences of lateral boundaries, otherwise larger Strouhal numbers are obtained. This may be a major cause of the increase of the computed Strouhal

number. The pressure and vorticity contours obtained at $t = 800$ are shown in figure 3.13.

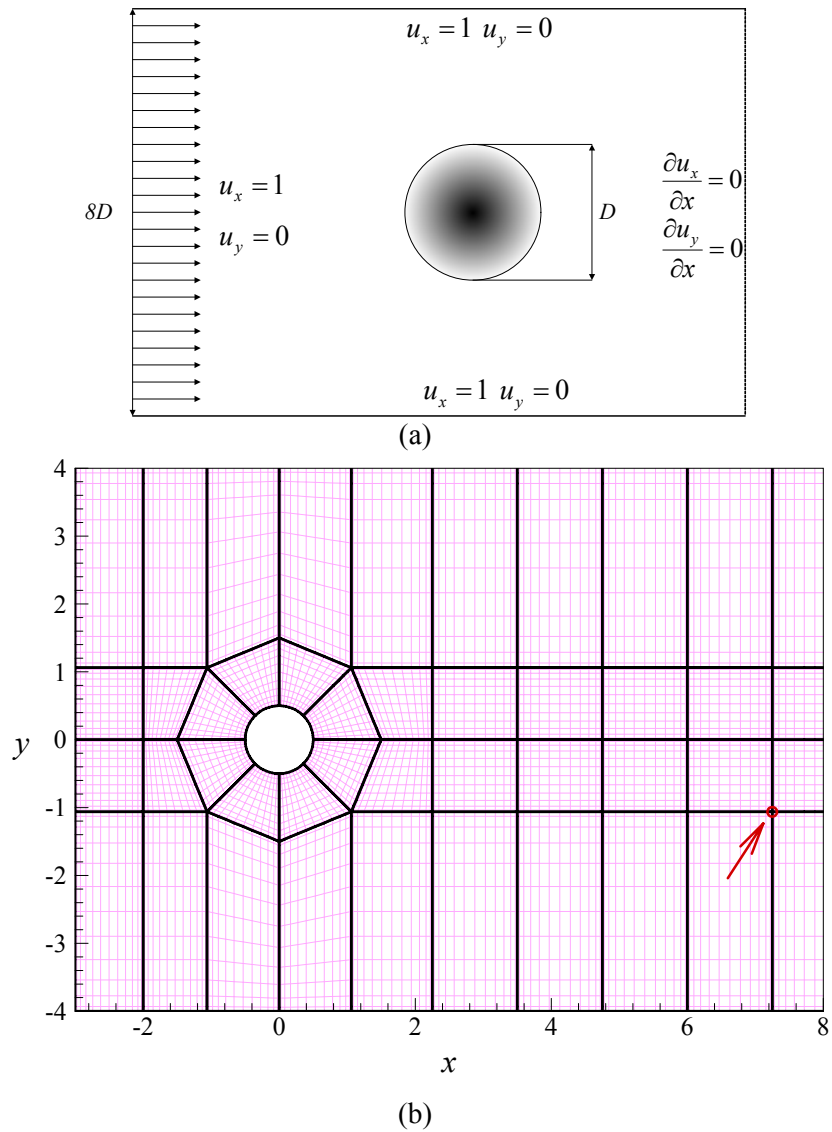


Figure 3.11. Problem configuration for the plug flow past a circular cylinder at $Re = 100$: (a) boundary conditions, (b) *GLL* computational mesh: The elemental discretization is shown by the thick lines and the quadrature points are shown by the thin lines. The history of the horizontal velocity, u_x , at a node situated at the point indicated with a red circle is recorded.

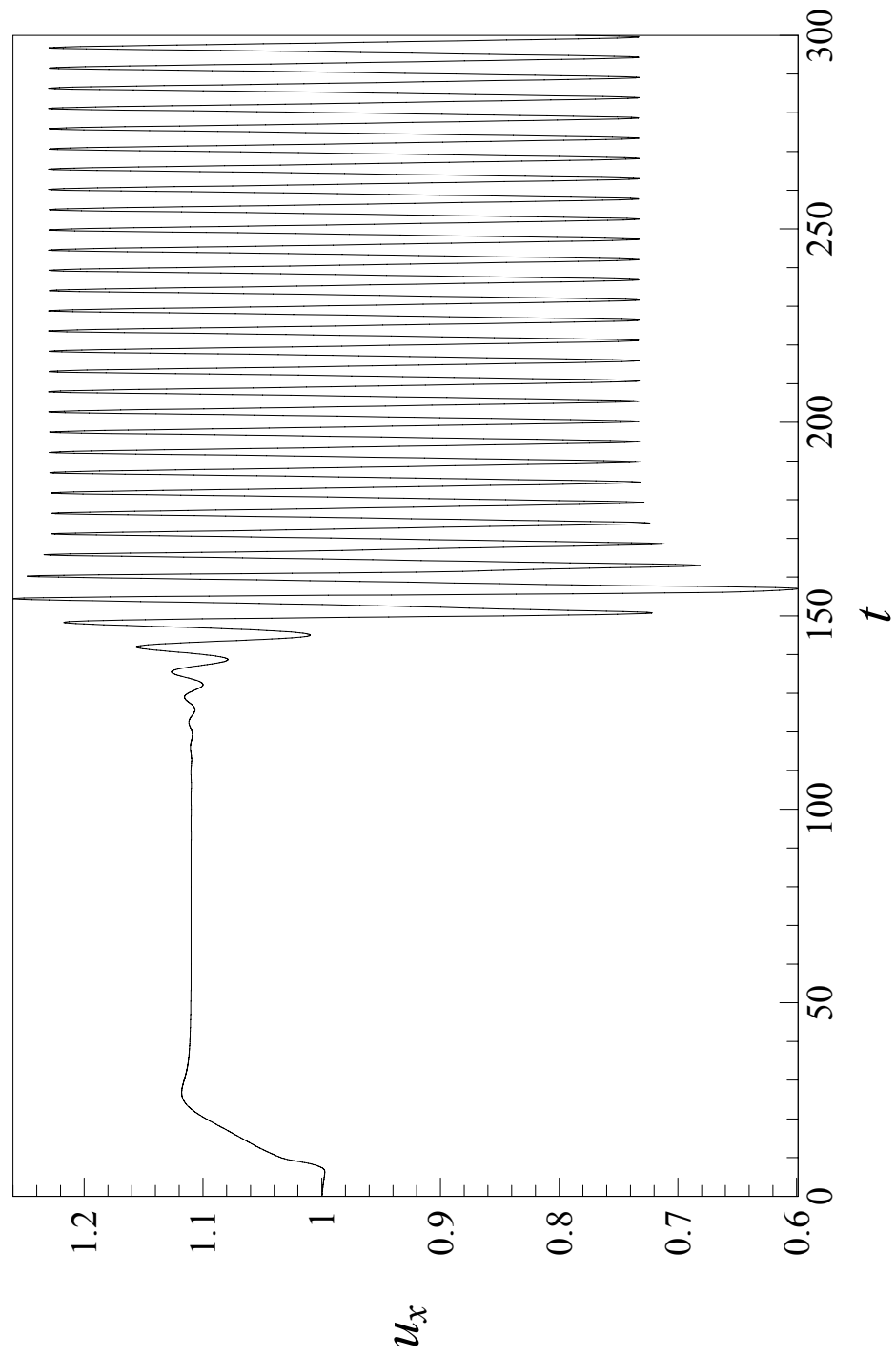
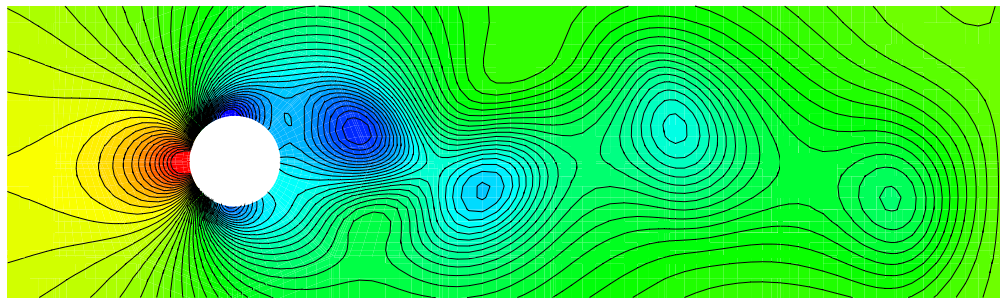
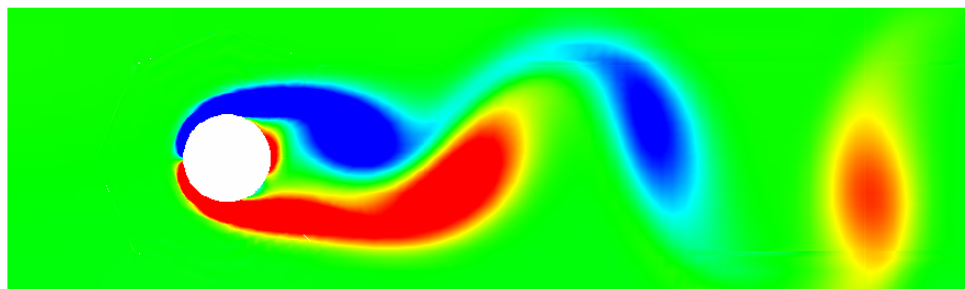
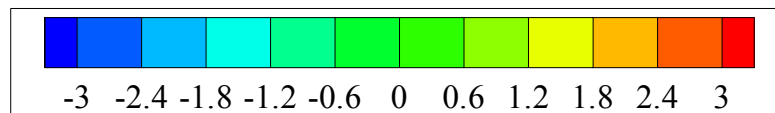


Figure 3.12. Time history of nodal u_x velocity at $Re = 100$.



(a)



(b)

Figure 3.13. Instantaneous: (a) pressure and (b) vorticity contours at $t = 800$, for the plug flow past a circular cylinder at $Re = 100$.

3.6. Thermally driven flows

Highly convection-dominated thermally-driven problems appear frequently in engineering practice. Here we consider the fluid motion induced by the temperature gradient in a square cavity of domain $\Omega \subset \mathfrak{R}^2$ bounded by the isothermal and the adiabatic walls. It is subjected to a temperature difference ΔT across the vertical isothermal walls while the top and bottom walls are adiabatic. The cavity is filled with a fluid of Prandtl number (Pr) equal to 0.71 corresponding to air. The two-dimensional unsteady Boussinesq equations in primitive variables, which govern the buoyancy-driven flow in the cavity, are made dimensionless with the following reference quantities:

$$L_r = H, \quad (3.5.a)$$

$$V_r = \frac{(\alpha / H)}{Ra^{1/2}}, \quad (3.5.b)$$

$$t_r = \frac{(H^2 / \alpha)}{Ra^{1/2}}, \quad (3.5.c)$$

$$Ra = \frac{\beta |g| \Delta T H^3}{\nu \alpha}, \quad (3.5.d)$$

where L_r is the characteristic length, H is the height of cavity, V_r is the characteristic velocity, α is the thermal diffusivity, ν is the kinematic viscosity, β is the volumetric thermal expansion coefficient, ΔT is the characteristic temperature, g is the gravitational acceleration vector acting in a vertically downward direction, and Ra is the Rayleigh number. With reference quantities, the dimensionless equations in Cartesian coordinates are given as below:

$$\frac{\partial u}{\partial x} + \frac{\partial v}{\partial y} = 0, \quad (3.6.a)$$

$$\frac{\partial u}{\partial t} + u \frac{\partial u}{\partial x} + v \frac{\partial u}{\partial y} = -\frac{\partial p}{\partial x} + \frac{Pr}{Ra^{1/2}} \left(\frac{\partial^2 u}{\partial x^2} + \frac{\partial^2 u}{\partial y^2} \right), \quad (3.6.b)$$

$$\frac{\partial v}{\partial t} + u \frac{\partial v}{\partial x} + v \frac{\partial v}{\partial y} = -\frac{\partial p}{\partial y} + \frac{Pr}{Ra^{1/2}} \left(\frac{\partial^2 v}{\partial x^2} + \frac{\partial^2 v}{\partial y^2} \right) + Pr\Theta, \quad (3.6.c)$$

$$\frac{\partial \Theta}{\partial t} + u \frac{\partial \Theta}{\partial x} + v \frac{\partial \Theta}{\partial y} = \frac{1}{Ra^{1/2}} \left(\frac{\partial^2 \Theta}{\partial x^2} + \frac{\partial^2 \Theta}{\partial y^2} \right), \quad (3.6.d)$$

where x and y are the horizontal and vertical coordinates respectively, u and v are the horizontal and vertical velocity components respectively, and p is the pressure. Θ is the dimensionless temperature defined as $(T - T_r) / \Delta T$, where T_r is the average of the cold and hot wall temperatures. This system of equations resembles a lot the Navier-Stokes equations except for the buoyancy term in the right-hand side of the momentum equations and the energy equation is added to the system. This, however, involves a coupling between the momentum and energy equations which makes the solution of the whole system more difficult than in the case of the Navier-Stokes equations.

The computational domain is taken to be the unit square, $\Omega = [0, 1] \times [0, 1]$. In order to show grid independence, we utilized two different types of spectral element mesh – type A and B. Type A consists of 4×4 equal quadrilateral elements of 18th order nodal expansion, and type B consists of 10×10 non-uniform 7th order quadrilateral elements used to discretize the domain with the corner element having dimension 0.03×0.03 . No slip velocity boundary condition was imposed on all solid walls. Zero heat flux boundary conditions were applied to top and bottom walls, while left side wall is kept at $\Theta = 1$ and right side at $\Theta = 0$. The geometry of computational domain and the boundary conditions are presented in figure 3.14. In present calculations the converged state was reached through an unsteady integration in time using the algorithm described in section 2.2. The initial conditions were chosen to be zero velocity,

pressure and temperature. Figure 3.15 and 3.16 contain plots of streamlines of the flow field and temperature distribution at 4 different values of the Rayleigh number: 10^3 , 10^4 , 10^5 , and 10^6 . Numerical results from both type A and B are in qualitative agreement with previously reported spectral solutions of Minev *et al.* [86], and Prabhakar and Reddy [87]. For the low Rayleigh number, the flow is relatively weak and thermal field is only slightly perturbed from a conduction solution. At the higher Rayleigh number, the flow field develops a considerable structure while the thermal field becomes vertically stratified in the core of the cavity with high heat flux regions along the vertical boundaries [88]. By utilizing both type A and B, figure 3.17 (a) shows the plot of u_x -velocity profiles along the vertical mid-line ($x = 0.5$) at the Rayleigh number of $Ra = 10^6$. Again, by utilizing both type A and B, figure 3.15 provides the plot of temperature profiles along the vertical mid-line at the Rayleigh number of $Ra = 10^6$. Temperature profiles in figure 3.17 (b) from both type A and B are quantitatively in good agreement with previously reported spectral solutions of Prabhakar and Reddy [87].

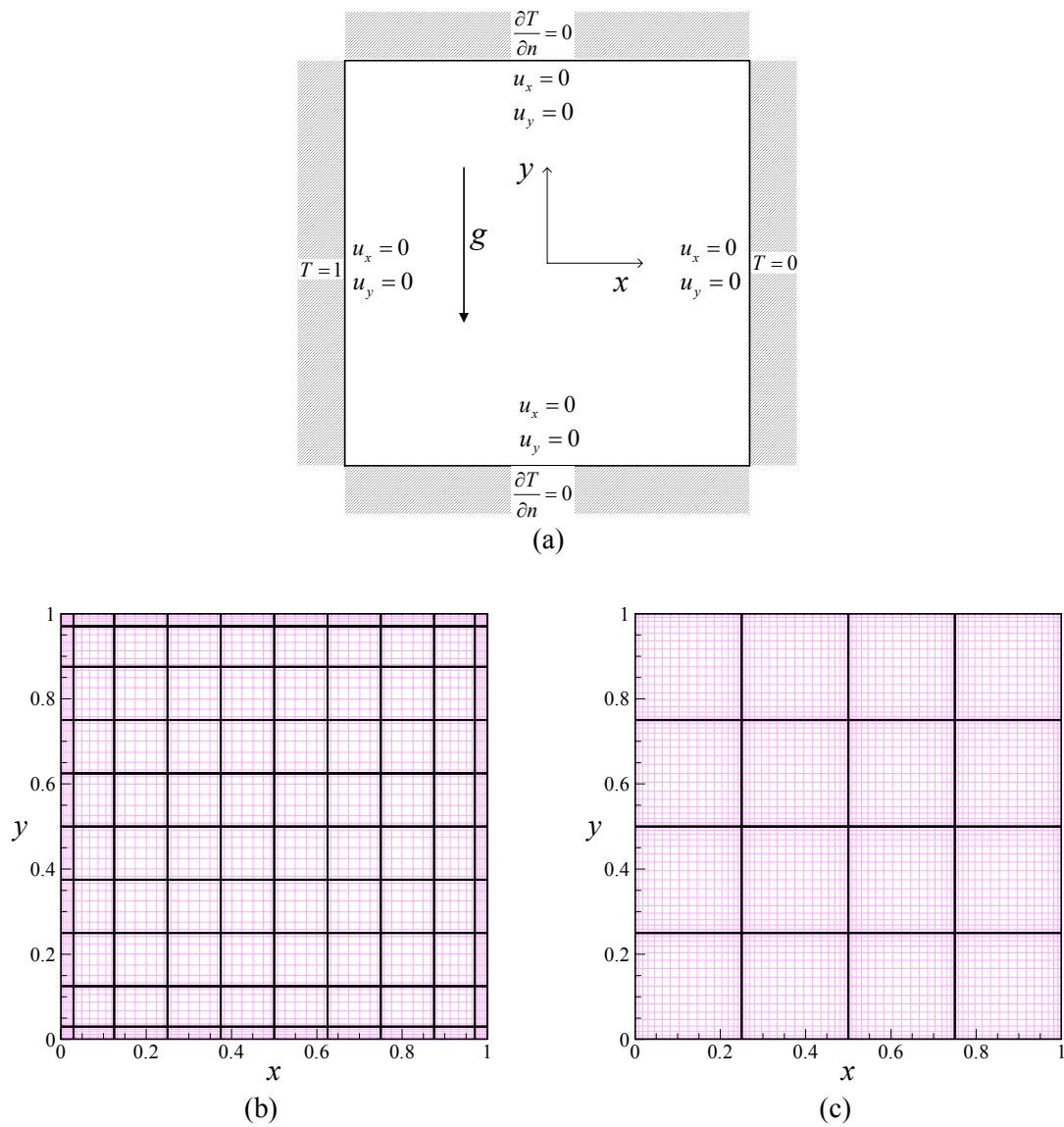


Figure 3.14. Problem configuration for the buoyancy-driven flow inside a square enclosure: (a) boundary conditions and, computational mesh (b) type A (left) and (c) B (right): The elemental discretization is shown by the thick lines and the quadrature points are shown by the thin lines.

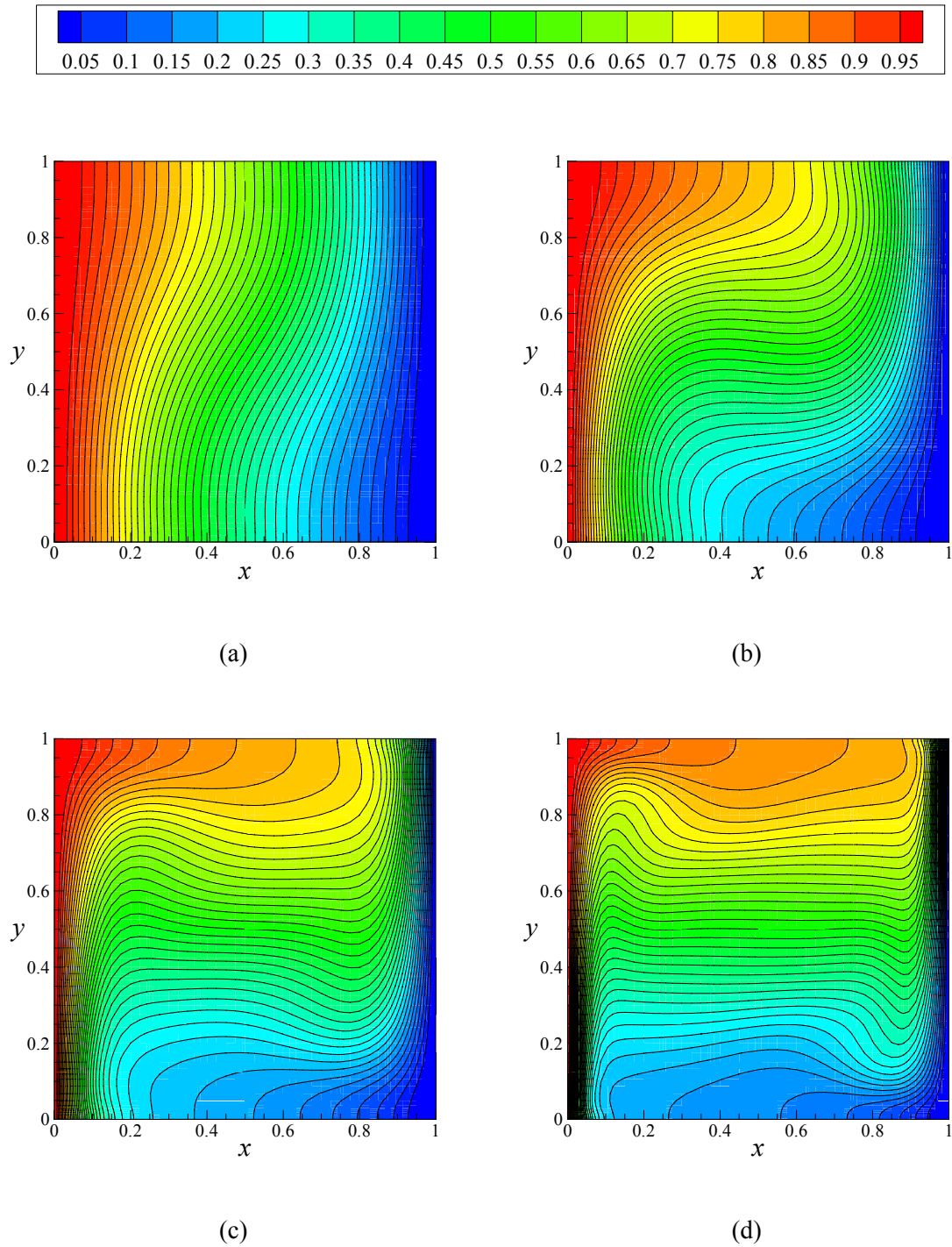


Figure 3.15. Numerical results for 2D thermal cavity: temperature contours on mesh type A at Ra = (a) 10^3 , (b) 10^4 , (c) 10^5 , and (d) 10^6 . Thin black lines denote isotherms at intervals of 0.05.

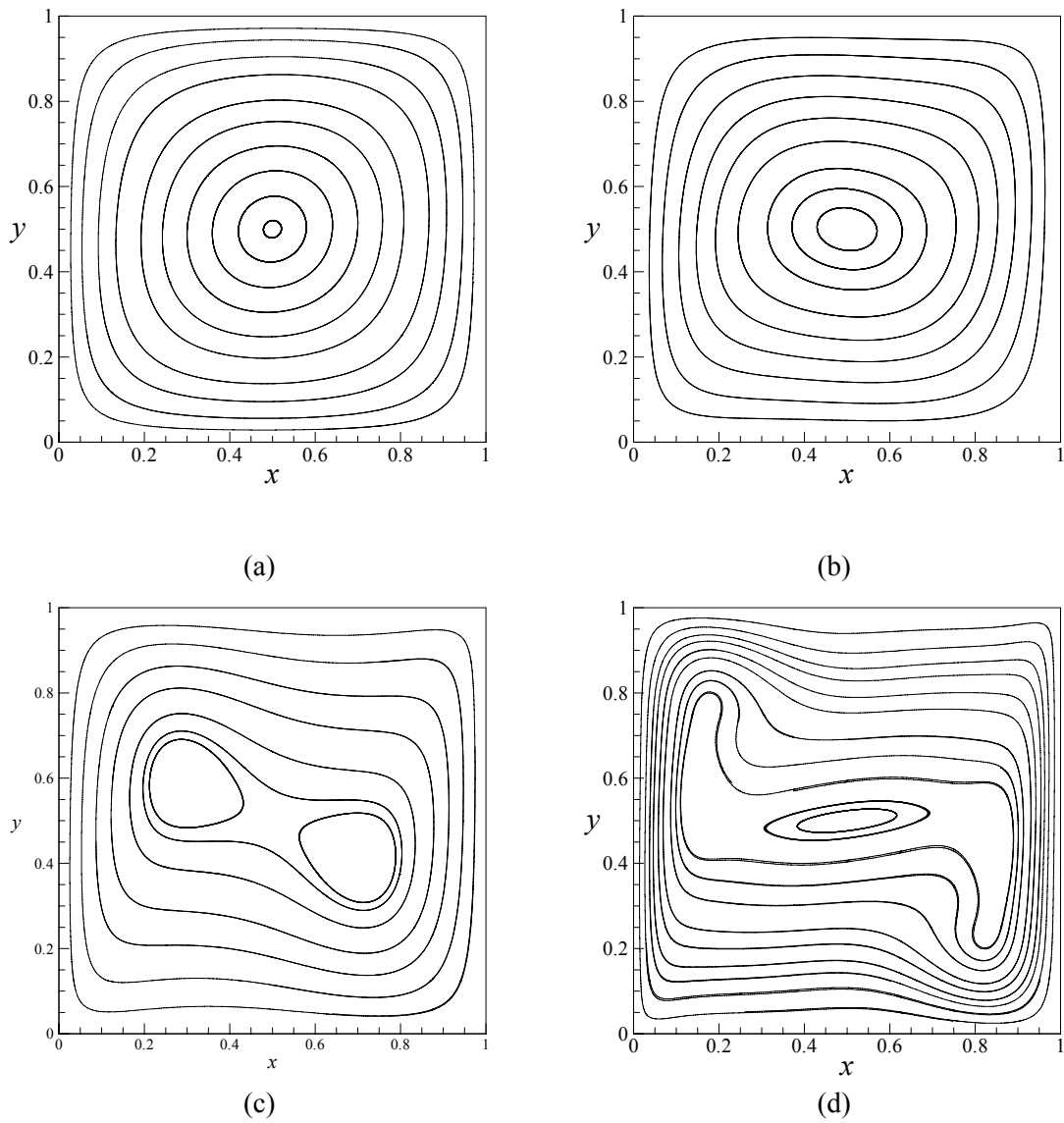


Figure 3.16. Numerical results for 2D thermal cavity: streamlines of velocity fields computed on mesh A at Ra equals to (a) 10^3 , (b) 10^4 , (c) 10^5 , and (d) 10^6 .

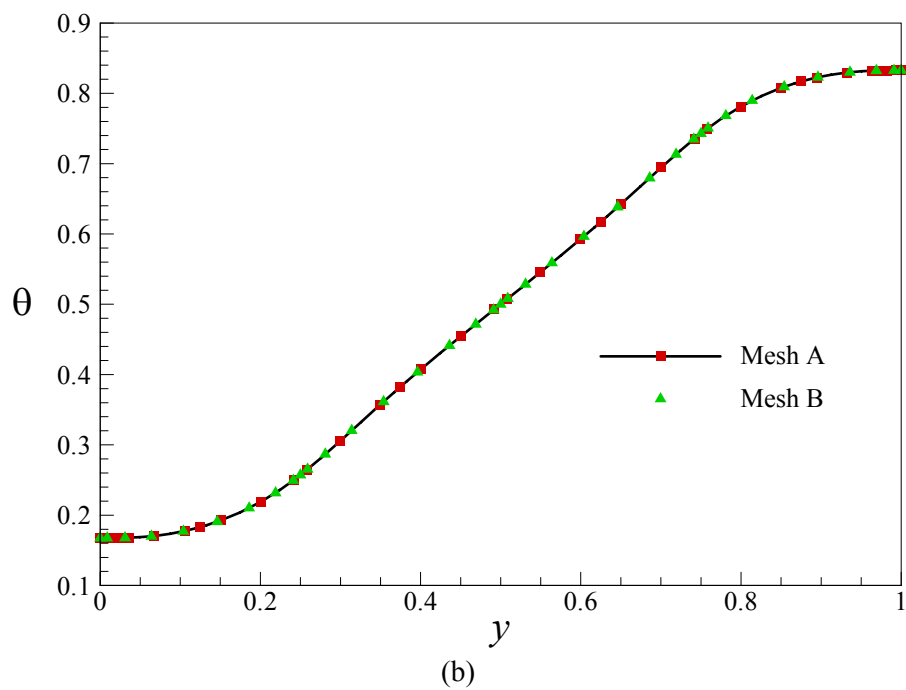
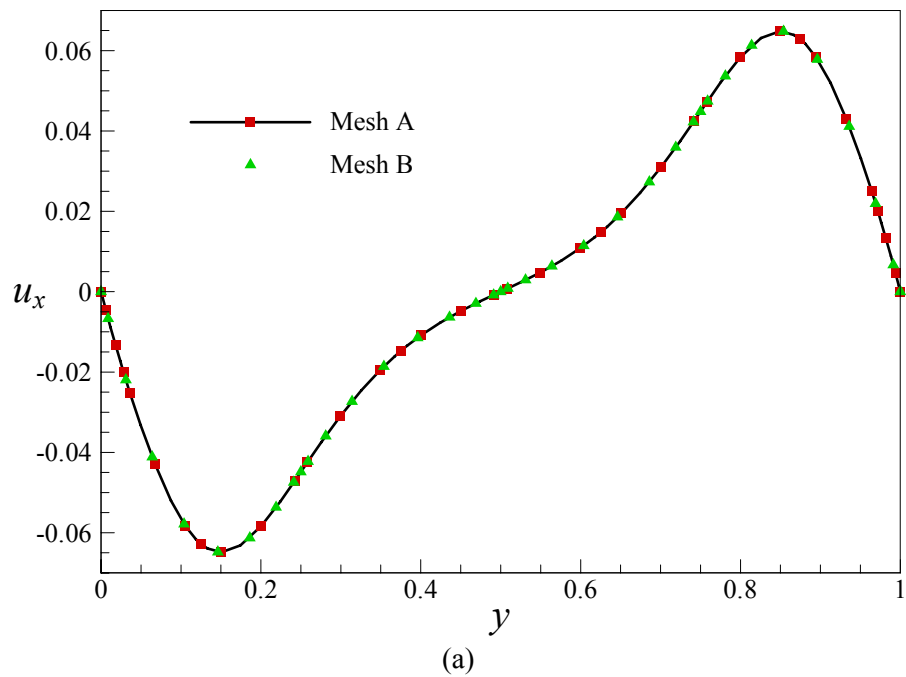


Figure 3.17. (a) u_x velocity and (b) temperature along the vertical midlines of the enclosure ($x = 0.5$) at $Ra = 10^6$.

CHAPTER IV
QUANTIFICATION OF CHAOTIC STRENGTH AND MIXING
IN A MICROFLUIDIC SYSTEM*

4.1. Introduction

In this chapter, considering the importance of objective estimation of chaotic strength and mixing in microfluidic systems, comparative studies of different diagnosis techniques commonly employed to identify chaotic states are presented to demonstrate the competitive advantages and shortcomings of each method. The “chaotic electroosmotic stirrer” of Qian and Bau [2] is utilized as the benchmark case due to its well defined flow kinematics. This chapter is organized as follows: In the next section, we summarize the proposed design and flow conditions obtained in the “chaotic electroosmotic stirrer” of Qian and Bau [2]. This is followed by the Lagrangian particle tracking results and the particle dispersion and box counting methods sections. Particle dispersion studies provide intuitive information in understanding the results of stirring operation. For example, actuation conditions that result in homogenized state of particle dispersion are preferred. In the following section, Poincaré sections are shown to identify the positions and sizes of bad mixing zones. With the destruction of Kolmogorov-Arnold-Moser (KAM) boundaries, we demonstrate the route from quasi-periodic state to chaos in the stirrer.

*Reprinted with permission from “Quantification of chaotic strength and mixing in a microfluidic system” by Kim H J and Beskok A, 2007. *J. Micromech. Microeng.* 17, 2197-2210, Copyright [2007] by Institute of Physics.

To circumvent shortcomings of the Poincaré section, we present the *FTLE* values to quantify chaotic strength under various actuation conditions. Then we report the results of stretching field and the probability density function (*PDF*) of stretching under various operation conditions. This is followed by the numerical solution of species transport equations, where species mixing in partially and globally chaotic states are demonstrated. Mixing results are presented as a function of the “Mixing Index Inverse (M^{-1})”.

4.2. Flow model

In this section, we briefly review the “chaotic electroosmotic stirrer” developed by Qian and Bau [2]. The device concept is based on two-dimensional time-periodic electroosmotic flows. Electroosmosis is the process of inducing motion of ionized liquid relative to the stationary charged surfaces using applied electric fields [59]. Therefore, it enables pumping of ionized fluids without any mechanical components. Since electroosmosis is driven by electric fields, switching between the several electric-field configurations and/or temporal variations in surface charges create time-dependent flow fields, susceptible to chaotic stirring. To this end, electroosmosis enables fast flow response, limited only by the flow development time-scales [2, 59].

The mixer consists of a rectangular chamber, where the bottom and top surfaces each have two surface electrodes that are covered with a thin insulator, while the side-surfaces are periodic. Zeta potential on the insulated surface can be altered by applying electrostatic potential on these electrodes [89]. It is possible to create various flow patterns in the mixing chamber by using different zeta potentials under a constant horizontal electric field. For simplicity, Qian and Bau utilized zeta potential combinations of $\pm \zeta_o$, and obtained analytical solutions of Stokes flow

in the rectangular chamber using thin electric-double-layer approximation based on the Helmholtz-Smoluchowski slip velocity. Figure 4.1 shows four steady Stokes flow patterns obtained under different zeta potentials, which are identified as patterns A, B, C, and D. The arrows on the top and bottom of the mixing chambers show the electroosmotic flow direction. The main idea in the electroosmotic stirrer is to alter the zeta potential, and hence the flow patterns periodically, to induce chaotic mixing in Stokes flow. Although the flow is time-periodic, the particle paths for two-dimensional unsteady flow may become non-integrable, resulting in chaotic advection in the Stokes flow regime.

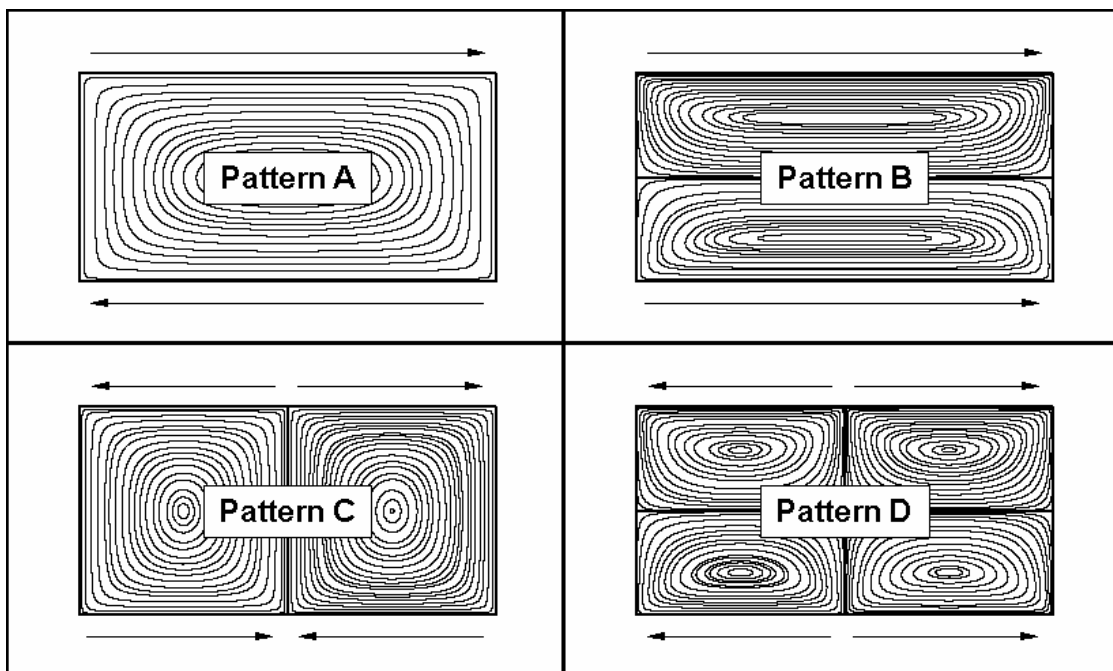


Figure 4.1. Electroosmotically induced flow patterns: A, B, C, D. Arrows show the electroosmotic flow direction induced by the zeta potential patterned surfaces. The side surfaces of the mixing domain are periodic.

Utilization of a single flow pattern would result in two-dimensional steady flow, which does not lead to significant dispersion of passive tracer particles. In absence of Brownian motion, tracer particles will follow the streamlines without any transport transverse to the streamlines [90]. One needs to alternate patterns periodically or aperiodically between two or more different flow fields to induce chaotic advection [3]. In general two-dimensional unsteady incompressible flows exhibit the dynamics of one degree of freedom time-dependent Hamiltonian, which are non-integrable [5]. This non-integrable characteristic gives rise to chaos in the passive particle trajectories. We must indicate that the actual device in [2] requires precise control over the zeta potential magnitude, and the time-scales for zeta potential alterations. Although this may have several practical limitations, the chaotic stirrer of Qian and Bau is an excellent test-bed due to its finite mixing area, and well defined flow fields generated using electroosmotic flows.

Electroosmotic flows are generated by interaction of the external electric field with the mobile charges in the EDL. Polarity of the zeta potential patterned surfaces dictates the flow direction. Velocity in the vicinity of the zeta-potential patterned surface can be approximated using the Helmholtz–Smoluchowski electroosmotic slip velocity given as

$$V_{HS} = -\frac{\zeta \varepsilon E_x}{\mu}. \quad (4.1)$$

where ζ is the zeta potential, ε is permittivity of the liquid, μ is the dynamic viscosity, and E_x is the electric field applied in the stream wise direction [59].

A time periodic flow, with period T , can be generated by switching between any two flow-patterns with half period time scales ($T/2$). Using flow patterns A, B, C and D for half a period each, one can obtain six different pattern combinations (A&B, A&C, A&D, B&C, B&D, and C&D). In this study we varied the normalized time-period from $T = 2$ to 8, where

normalization was done using the convective time-scale (H/V_{HS} , where H is the half channel height). Qian and Bau modeled the flow using the Stokes equations given as

$$\rho \frac{\partial \mathbf{u}}{\partial t} = -\nabla p + \mu \nabla^2 \mathbf{u}, \quad (4.2)$$

$$\nabla \cdot \mathbf{u} = 0, \quad (4.3)$$

where $\mathbf{u} = (u, v)$ is the velocity vector, u and v are the velocity components in the x and y directions, respectively, p is pressure, and t is time. Equation (4.2) was normalized using the fluid kinematic viscosity (ν), Helmholtz–Smoluchowski electroosmotic slip velocity (V_{HS}), and the conduit’s half-height (H). Analytical solutions of Stokes equations for patterns A, B, C and D can be found in [2]. In their analysis, Qian and Bau assumed that the gap between any adjacent electrodes is large compared to the EDL thickness, but small compared to H . Hence for mathematical simplicity, they neglected the gap between the adjacent electrodes. They also demonstrated that when the gap is relatively small compared to H , it had no significant effects on the flow pattern.

In Stokes flows, flow transients represented by the time derivative term in equation (4.2) is very fast. Therefore, Qian and Bau neglected flow transients, as they switched between various flow patterns [2]. In the current study, we alternate between two flow patterns during a period T by imposing the first flow pattern for a time interval of $0 < t < T/2$. This is followed by the second pattern for $T/2 < t < T$. The process is repeated continuously in time. Time period for ζ potential alterations is large enough compared to the EDL relaxation time so that the flow is quasi-static, and the instantaneous flow fields are given by the solutions of the steady Stokes equation. Mixing studies in the Stokes flow regime commonly utilize these approximations [3, 8].

4.3. Particle tracking and numerical methodology

Passive (tracer) particle tracking studies are based on the Lagrangian analysis of motion, and they depend on the investigation of the following dynamical system,

$$\frac{d\mathbf{x}}{dt} = \mathbf{u}(\mathbf{x}, t), \quad (4.4.a)$$

$$\mathbf{x} = \mathbf{\Phi}_t(\mathbf{X}), \quad (4.4.b)$$

where $\mathbf{x}(x, y, t) = \mathbf{X}(X, Y, 0)$ at time $t = 0$, $\mathbf{u}(\mathbf{x}, t)$ is the known velocity field, and $\mathbf{\Phi}_t$ is the mapping of the particle position from \mathbf{X} to \mathbf{x} after time t . In the particle tracking studies, highly accurate and explicit descriptions of velocity fields are required to solve the initial value problem described by equation (4.4). In [2], Qian and Bau obtained analytical solutions for Stokes flow using Fourier series expansions. They utilized the asymptotic behavior of series' coefficients to overcome the slow convergence of Fourier series solution, induced by the jumps in the Helmholtz-Smoluchowski slip velocity on domain boundaries. Even though the critical shortcomings of Fourier series solutions are overcome, calculation speed of the analytical solution is often too slow to perform practical case studies with reasonable computational efforts [8]. In order to address this issue, we utilized spectrally accurate interpolation of the velocity field using the analytical solution on a grid. Passive particle tracking can lose its spatial accuracy in low order interpolation schemes, such as the 4th order biquadratic algorithm presented in [75, 91]. Ultimately, it is difficult to obtain accurate solutions for long-time integration due to accumulation of temporal and spatial discretization errors. To overcome the critical shortcomings of low order methods, we discretized the stirrer domain using quadrilateral elements that are isoparametrically mapped to a master element in $-1 \leq x \leq 1$ and $-1 \leq y \leq 1$. The velocity field on the master element is interpolated using N^{th} order Gauss Lobatto Legendre

(*GLL*) interpolation polynomials written in the tensor product form as

$$\mathbf{u}(x, y) = \sum_{i=0}^N \sum_{j=0}^N \mathbf{u}_{ij,known}(x_i, y_j) L_i(x) L_j(y), \quad (4.5.a)$$

where x_i and y_j are the *GLL* collocation points in x and y directions, and $\mathbf{u}_{i,j,known}$ is the velocity field obtained directly from the Fourier series solution at the *GLL* points. The Lagrange interpolation polynomials $L_i(x)$ are given by

$$L_i(x) = \frac{-1}{N(N+1)} \frac{(1-x^2)P'_N(x)}{(x-x_i)P_N(x_j)}, \quad P'_N = \frac{dP_N}{dx}, \quad (4.5.b)$$

where P_N is the N^{th} -order Legendre polynomial [12]. We must emphasize that the Lagrange interpolation polynomials exactly recover the analytical solution on the *GLL* points by construction, and interpolate the solution for any other (x, y) point with spectral accuracy. Exponential convergence of the Lagrange interpolation is guaranteed for flows that yield analytical solutions [12]. For all flow patterns, 8 equally spaced 20^{th} -order spectral elements are utilized. Time integration of equation (4.4) is obtained using a 4^{th} -order Runge-Kutta algorithm with time-step $\Delta t = 10^{-3}$. For an exact velocity field (\mathbf{V}_{ex}), we expect time-integration error grow linearly with the number of time steps (m), resulting in $|\mathbf{X}_{num} - \mathbf{X}_{ex}| \propto 10^{-12} \times m$, due to the time-step used and fourth-order accuracy of the algorithm in time. Since exact locations of particles (\mathbf{X}_{ex}) are unknown, we monitored time-evolution of the maximum error in velocity $|\mathbf{V}_{num} - \mathbf{V}_{ex}|$ at numerically calculated particle locations (\mathbf{X}_{num}), where \mathbf{V}_{ex} was evaluated using 20-term Fourier series solution. The maximum error in particle velocity, $|\mathbf{V}_{num} - \mathbf{V}_{ex}|$ was sporadically changing between 10^{-13} and 10^{-9} with time, depending on the proximity of \mathbf{X}_{num} to the *GLL* points in the spectral element mesh. The *RMS* error in particle velocities per time step is $|\mathbf{V}_{num} - \mathbf{V}_{ex}|_{RMS} = 10^{-11}$, which is an order of magnitude larger than the time integration error. Assuming that *RMS* errors in velocity dominate over the time integration errors and using equation (4.4), we predict

the errors in particle location grow linearly with the number of time steps m , resulting in $|\mathbf{X}_{num} - \mathbf{X}_{ex}| \propto |\mathbf{V}_{num} - \mathbf{V}_{ex}|_{RMS} \times m$. For certain cases, we integrated particle trajectories for 10^5 time steps (till time $t \approx 10^2$). Based on the error trends in our numerical discretization, we expect maximum errors in particle location to be about 10^{-6} . We must emphasize that direct use of 20-term Fourier series solution for integration of equation (4.4) with $\Delta t = 10^{-3}$ would result in $|\mathbf{X}_{num} - \mathbf{X}_{ex}| \propto 10^{-7}$. However, this would require approximately four times increase in the computational load, which becomes increasingly challenging for tracking tens of thousands of particles for very long times.

4.4. Particle dispersion and box counting method

Uniform dispersion of particles that were initially confined in a small zone to the entire mixing domain can be considered as a well-stirred state. However, such observations need to be quantified to obtain reasonable measures of the stirring efficiency. We utilized the *box counting method* to quantify the rate at which particles are dispersed by the flow into small uniform boxes [29]. In the box counting method, the box size (s) is related to the total number of tracked particles (N). For a perfectly random distribution of N particles, 98 % of the boxes would contain at least one particle, if the box size for a unit-square domain is chosen as [29]

$$s \approx 2N^{-1/2}. \quad (4.6)$$

Once the number of particles (N) is selected, the domain is divided into boxes of size s , and the motion of each particle is calculated as a function of time. Then the dispersed particles in each box are counted, and a decision is made regarding to the mixing state of each box. For an instance, if one tracks 40,000 particles, $s = 1 / 100$, and a total of $K = 100 \times 100 = 10,000$ boxes are required in the entire mixing domain. In order to access the stirring efficiency, a *stirring index*, ε , is computed using two different rules

Rule 1: Each box is filled when at least one particle is located inside the box. To calculate ε , the number of filled boxes is counted, and this is divided by the total number of boxes.

Rule 2: Number of particles at each box is used as a weighting factor. If one tracks 40,000 particles in a domain with $K = 10,000$ boxes, four particles per box are expected at homogeneous mixing state (i.e, $n_{max} = 4$). For such conditions, the weighting factor (ω_i) for the i^{th} box can be defined as a function of the number of particles n_i in the box using

$$\omega_i = \frac{n_i}{n_{max}} \quad \text{if } n_i \leq n_{max}$$

$$\omega_i = 1 \quad \text{if } n_i \geq n_{max}.$$

There will be empty boxes in the domain for each over-populated box ($n_i > n_{max}$) [59]. Assuming over-populated boxes as “well stirred” is justifiable, since the impact of this decision will be compensated by the low ω values of under-populated boxes in the domain. For both cases, an over all *stirring index*, ε , can be defined as

$$\varepsilon = \frac{1}{K} \sum_{i=1}^K \omega_i, \quad (4.7)$$

where $\omega_i=1$ or 0 for Rule 1 and K is the total number of boxes. Rule 1 is more useful for experimental realization of the box counting method, since it is practically impossible to observe homogeneous mixing state for all the boxes in the domain.

In figure 4.2, we present dispersion of 40,000 particles for case B&C at $T = 6$, and case A&D at $T = 6$ at various times. As we observe in figure 4.2 (a), particles initially located at the center has spread to cover the entire mixing domain for case B&C actuated at $T = 6$. Such behavior is desired in an efficient stirrer. However, case A&D in figure 4.2 (b) exhibits several ‘*unmixed*’ zones that do not contain any passive tracer particles, and these domains prevent the spread of particles. Although a large portion of particles is concentrated near the center of the

stirring zone, ‘void’ areas (i.e. ‘*unmixed*’ zones) are observed even after a long time ($t \geq 100$). In figure 4.2 (b), snapshot obtained at $t = 102$ shows a zoomed view of the *unmixed* zones near the center of the mixer.

In figure 4.3 (a), (b), we present the temporal evolution of the *stirring index* ε for cases A&B, A&C, A&D, B&C, B&D, C&D at $T = 6$, obtained using Rules 1 and 2, respectively. In figures 4.3 (c), and (d), we show the temporal evolution of ε for case B&C at various time periods changing from $T = 2$ to 10, obtained using Rules 1 and 2, respectively. In these cases, $N = 2,500$ particles were tracked for $t \leq 100$ in $K = 625$ boxes. In figures 4.3 (a) and (b) we observe that the *stirring index* for case B&C with $T = 6$ reaches its asymptotic limit of unity faster than any other case excited at $T = 6$. Similarly in figures 4.3 (c) and (d) we observe the *stirring index* for case B&C excited at $T = 6$ to reach its asymptotic limit of unity much faster than any other time-period of excitation. Please note that figures are drawn in logarithmic scale and asymptotic behavior of ε for other time periods is different than the period $T = 6$ case. Since all results are given as a function of time, direct comparison between the various cases or time-period of excitation can be done, provided that the stirrer dimensions (H) and the Helmholtz-Smoluchowski velocity (V_{HS}) are fixed. Based on these results we can conclude that case B&C excited at $T = 6$ gives the best stirring state among all the selected cases. Due to the use of *log-lin* graphs, variations in the ε values between the two rules are indistinguishable. However, the ε values for case B&C at $T = 6$ reach 0.98 and 0.8 using Rules 1 and 2, respectively. Despite the differences between the absolute values of ε , both rules result in consistent predictions regarding the behavior of ε variation as a function of time. Therefore, either rule predicts the dynamics and the best stirring state equally well. Due to this reason, practically easier Rule 1 should be preferred over Rule 2.

The box counting method is very useful because the box size can be changed

depending on the total number of passive tracer particles. Even though the number of tracked particles can be small, one can obtain acceptable result using equation (4.7). For example, $K = 10,000$ is required for tracking 40,000 particles, while 625 boxes are used for tracking 2,500 particles. In [62] we have shown that the behavior of the *stirring index*, ε is mostly insensitive to the number of particles for as long as the box size is selected using equation (4.6), and there are enough boxes to properly discretize the mixing domain. This can save computational effort, and can also be useful in experimental studies. In experimental implementations, fixing the particle volume fraction should approximately fix the number particles in a closed domain, and particle tracking methods could be utilized to identify particle dispersion and apply the box counting method. Small volume fractions that would lead to approximately 4 particles per cell would be required. This is a number significantly smaller than the average number seeding particles utilized in a typical particle image velocimetry system. Further details of possible experimental implementation of the box counting method are out of scope of the current paper. An important limitation of the box counting method is that it should be applicable to mixers with bounded domains. The box counting method becomes inapplicable for continuous flow mixers, where the mixing domain is unbounded.

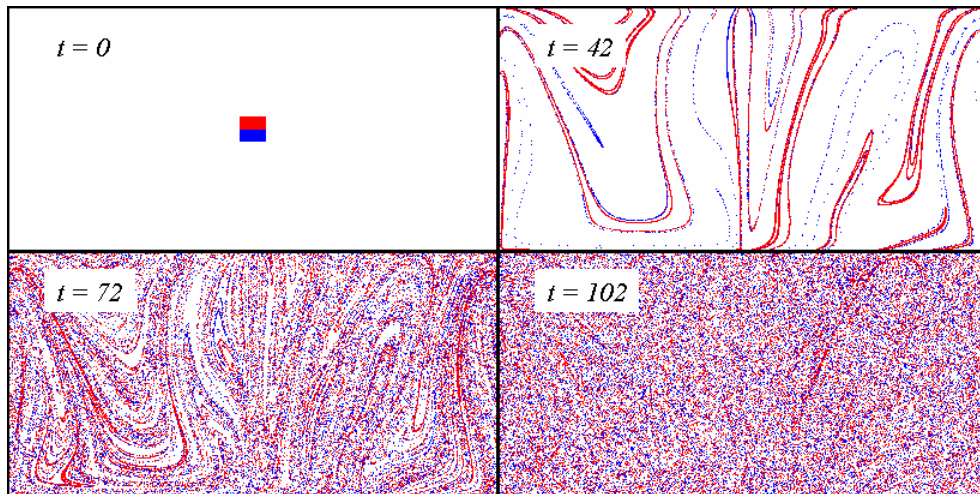
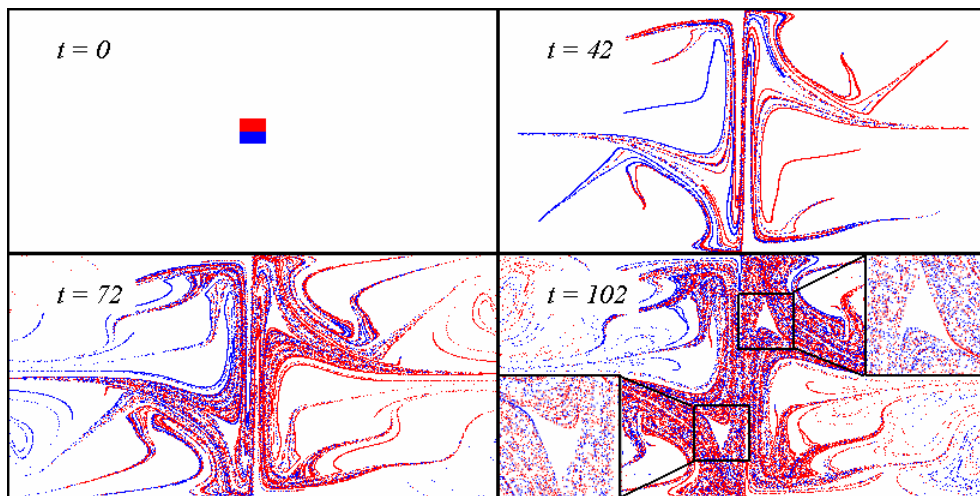
(a) case B&C at period $T = 6$ (b) case A&D at period $T = 6$

Figure 4.2. Snapshots of spread of passive tracer particles for cases B&C at period $T = 6$ (a); and A&D at period $T = 6$ (b). A total of 40,000 passive particles are tracked in time. Snapshots show the dispersing state at respective times. Figure (a) shows flow domain filled with passive tracer particles, and these particles are distributed uniformly at $t = 102$. Figure (b) shows presence of two small void regions that remain near the vertical centerline of the domain at $t = 102$. The insets show the geometric structure of the void region.

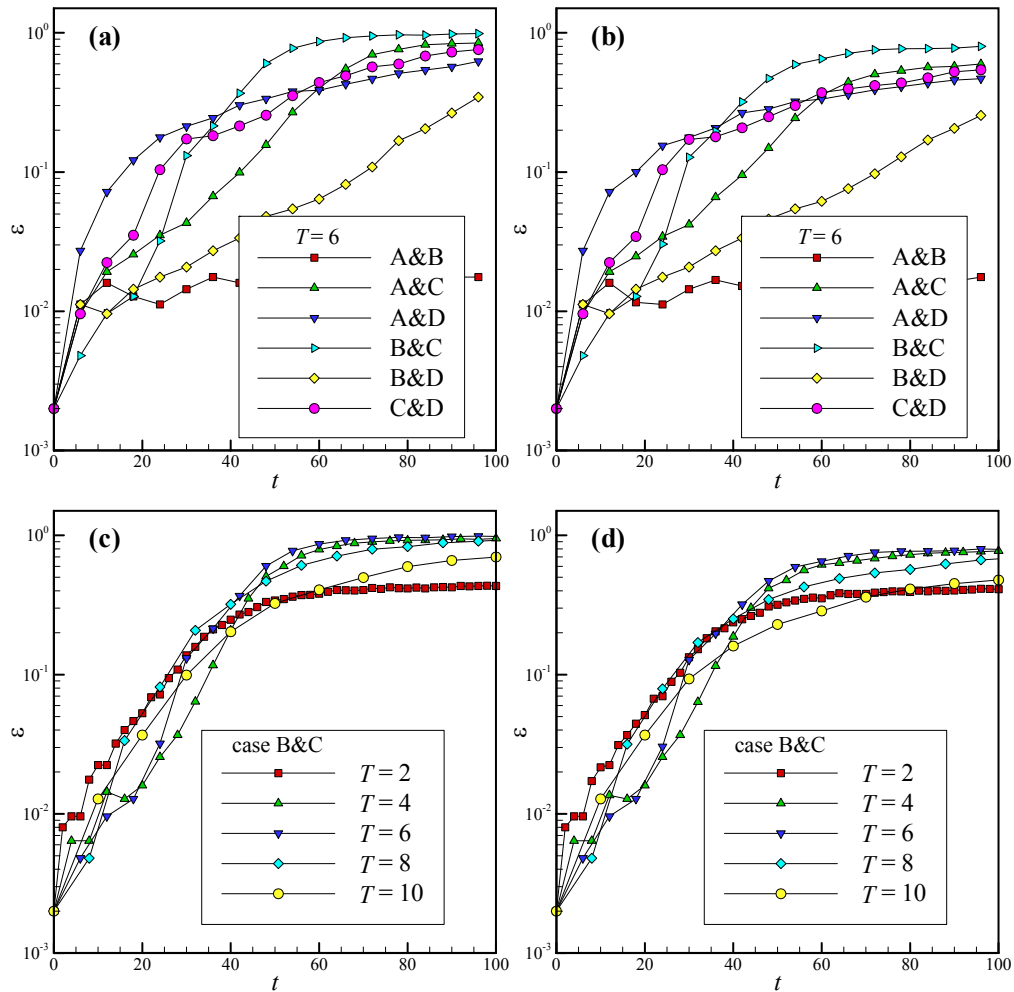


Figure 4.3. Time (t) variation of the stirring index, ε , for cases A&B, A&C, A&D, B&C, B&D, C&D at period $T=6$ obtained by Rule#1 (a) and Rule#2 (b). Only ε for case B&C reaches the asymptotic limit of unity. Time variation of ε for case B&C at various excitation periods (T) obtained by Rule#1 (c), and Rule#2 (d).

4.5. Poincaré sections

Based on the particle dispersion results, case B&C at $T = 6$ has the best stirring efficiency compared to the other cases. To study the effect of time period, T in detail, we gradually increase T from 0.5 to 8 for case B&C, and utilize the Poincaré sections to investigate the best stirring state. The Poincaré section is a stroboscopic image of passive tracer particles [92], obtained as a collection of points where the trajectory pierces *the phase plane*. In general, the time interval between successive visits of the trajectory in the Poincaré section is the period of the motion [93]. Thus, spatial trajectories of passive tracer particles are projected to Poincaré sections by mapping every period. And mapping is defined as,

$$P_{n+1} = \Phi_p(P_n), \quad (4.8)$$

where Φ_p is the Poincaré mapping, P_n is the position of particle at n^{th} period. The Poincaré map Φ_p can be derived using the instantaneous velocity field. This repetitive process of projection can significantly reduce the complexity of analysis by decreasing one degree of freedom in analysis. In current context, due to the time periodicity of flow, the Poincaré sections are drawn as a function of x and y . The curves that separate the periodic area from the chaotic sea are called Kolmogorov-Arnold-Moser (KAM) curves. If the particle trajectories exhibit exponential divergence, then the trajectory on its second visit to a particular neighborhood will have subsequently different behavior, than its behavior on the previous visit [92]. KAM boundaries are destructed through non-periodicity of chaotic motion. By the destruction of KAM curves and shrinkage of the quasi-periodic areas, the route from quasi-periodic behavior to chaos can be observed.

In figure 4.4, we present Poincaré sections for case B&C at time periods of $T = 0.5, 1, 1.5, 2, 3, 4, 6$ and 8 . These plots are obtained by tracking 8 passive tracer particles, which were

initially placed at $(0.1, 0.5)$, $(0.2, 0.5)$, $(0.3, 0.5)$, $(0.4, 0.5)$, $(-0.1, -0.5)$, $(-0.2, -0.5)$, $(-0.3, -0.5)$ and $(-0.4, -0.5)$ for 2500 time periods. In Poincaré section for $T = 0.5$, initial positions of 8 passive tracer particles are shown by dots with various colors, and grid lines are drawn to recognize the coordinates of the initial positions.

Increasing the time period T , we observe reduction in the area of the regular islands. As the time period is increased from $T = 0.5$ to $T = 1$, the outer KAM curves of the initial point $(0.1, 0.5)$ breaks up first. With increasing T from 1 to 1.5, the outer periodic area (outer island from $(-0.2, -0.5)$) shrink gradually and then separate to a chain of periodic islands. This chain acts as a barrier separating the inner and outer chaotic areas. Other curves of initial points $(0.1, 0.5)$, $(0.2, 0.5)$, $(0.3, 0.5)$, $(-0.1, -0.5)$ are ultimately destructed and form a chaotic sea at $T = 1.5$. Also, it is observed that the inner regular area (quasi-periodic zone of initial points $(-0.4, -0.5)$) disappear and then become connected with an outer chaotic area through the destruction of the inner KAM curves for time period changing from 2 to 4. However, two regular islands still exist in the top-right and bottom-left parts of the mixing zone at $T = 4$. KAM boundaries cannot be broken up until $T = 6$, as shown in figure 4.4. For $T \geq 6$, all regular islands are unrecognizable, and featureless Poincaré sections are observed. Asymmetry in the KAM curves at the lower-left and upper-right portions of the domain are induced by the B&C flow pattern, as can be deduced by examining the stream-line patterns of cases B and C in figure 4.1.

It is clear that Poincaré section gives intuitive and visually persuasive result to estimate chaotic state qualitatively. However, after Poincaré sections become featureless, it is very hard to decide which case has higher chaotic strength. For example, in figure 4.4, the chaotic state for case B&C at $T = 6$ cannot be distinguished from that of $T = 8$ using Poincaré sections. In addition, aperiodic or randomly stirred flows do not have time definite periods, and therefore, Poincaré sections can not be utilized. In the next section, we describe the Lyapunov

Exponent, which enables quantification of chaotic strength for general flows.

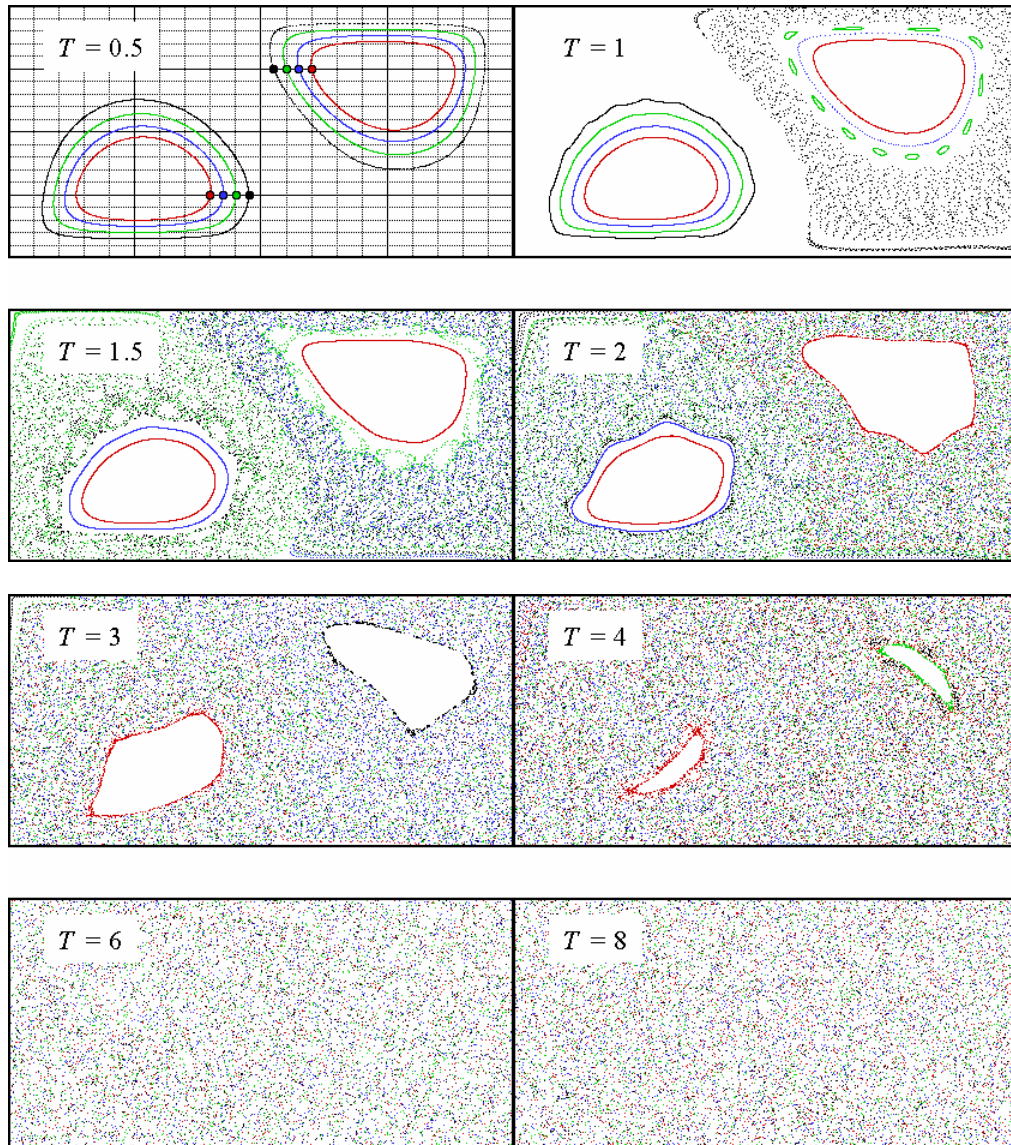


Figure 4.4. Poincaré sections for case B&C at period $T = 0.5, 1, 1.5, 2, 3, 4, 6$ and 8 . Initial locations of the passive particles are shown with colored dots on the top left figure, and correspond to $(x, y) = (0.1, 0.5), (0.2, 0.5), (0.3, 0.5), (0.4, 0.5), (-0.1, -0.5), (-0.2, -0.5), (-0.3, -0.5), (-0.4, -0.5)$.

4.6. Lyapunov exponents

Chaotic behavior is characterized by the divergence of nearby trajectories in the phase space. Exponential divergence of two initially nearby particles result in drastically different behavior of two particles, which results in a non-integrable Hamiltonian system [92]. This sensitivity to the initial conditions is the main characteristic of chaotic systems, and chaotic motion of fluid particles increases the stirring efficiency by enhancing the dispersion of passive tracer particles. Lyapunov exponent (LE , σ) is the average exponential rate of divergence or convergence of nearby orbits in the phase space. The LE describes chaos in a quantitative manner, and it is given by

$$\sigma(\mathbf{X}, \mathbf{M}) = \lim_{T \rightarrow \infty} \frac{1}{T} \int_0^T \frac{D \ln \lambda}{Dt} dt = \lim_{T \rightarrow \infty} \frac{1}{T} \ln \lambda \quad (4.9.a)$$

$$\mathbf{M} \equiv \frac{d\mathbf{X}}{|d\mathbf{X}|}, \quad (4.9.b)$$

where σ is the LE , \mathbf{X} is the position of original fluid element and \mathbf{M} is a unit directional vector of an infinitesimal material element, and λ is the stretch length defined as

$$\lambda \equiv \lim_{|d\mathbf{X}| \rightarrow 0} \frac{|d\mathbf{x}|}{|d\mathbf{X}|}, \quad (4.10)$$

where $d\mathbf{x}$ is the material element vector after deformation via $d\mathbf{x} = \mathbf{F} \cdot d\mathbf{X}$ where \mathbf{F} is the deformation gradient tensor (i.e. Jacobian matrix). The stretched length, λ , can be described by

$$\lambda = (\mathbf{C} : \mathbf{M}\mathbf{M})^{1/2}, \quad (4.11)$$

where \mathbf{C} is the Cauchy-Green strain tensor, $\mathbf{C} \equiv \mathbf{F}^T \cdot \mathbf{F}$ [10].

Calculation of the LE requires extremely long time integration because of its mathematical definition given in equation (4.9.a). In addition, one can experience difficulties in

calculation of the deformation gradient tensor, \mathbf{F} and Cauchy-Green strain tensor \mathbf{C} analytically for most practical cases. For practical reasons, λ can be obtained numerically by calculating its largest value within a certain finite time. For this reason, we are using the finite time Lyapunov exponent (*FTLE*), which has been widely used for mixing problems in numerical [24, 32, 33] and experimental [94] studies.

Calculation of the *FTLE* is often implemented using the algorithm suggested by Sprott [93]. First, arbitrary pairs of nearby points are chosen with initial distance $|d\mathbf{X}|$. Then a new distance $|d\mathbf{x}(\Delta t)|$ is evaluated after integrating particle paths for a time Δt , and $\ln(|d\mathbf{x}(\Delta t)| / |d\mathbf{X}|)$ is calculated. This process is repeated n times using the following mathematical expression,

$$\sigma = \frac{1}{n} \sum \frac{1}{\Delta t} \ln \left(\frac{d\mathbf{x}(\Delta t)}{d\mathbf{X}} \right) = \frac{1}{n\Delta t} \sum \ln \left(\frac{d\mathbf{x}((n+1)\Delta t)}{d\mathbf{x}((n)\Delta t)} \right). \quad (4.12)$$

Figure 4.5 shows the *FTLE* contour plots for case B&C at $T = 2, 4, 6$ and 8 . In the figure, x and y are the horizontal and vertical coordinates of the initial positions of passive tracer particles, respectively. The depth in the figure indicates the *FTLE* magnitudes. For each case, we utilized 10,000 particles that were uniformly distributed through the entire mixing domain. All particles for $T = 6$ exhibit positive *FTLE* values, thus this case presents a globally chaotic state.

However, the other cases have regular and quasi-periodic areas of zero or negative *FTLE* values. These regular areas are segregated from the non-periodic chaotic sea by the KAM boundaries. In addition, elliptic periodic point at center of the regular island prevents stretching of the fluid filaments due to its strong periodicity [10]. Qualitatively, large-sized segregated regions of zero or negative *FTLE* values were not observed for the period $T = 8$ case. This flow has almost featureless Poincaré section, and it doesn't exhibit large periodic zones. However, the *FTLE* contour plot reveals considerably segregated regions of efficient dispersion states with very small-sized regular zones at almost non-recognizable scales. Therefore the *FTLE* contours overcome the shortcomings of the featureless Poincaré sections for $T \geq 6$ cases. Based on these results, we identify the B&C pattern at $T = 6$ as the “optimum” stirring state.

We must indicate that calculation of the *FTLE* values are more expensive than the Poincaré sections, since every particle needs to have a pairing satellite particle, and one must additionally implement calculation of the length between the particle pairs using equation (4.12). It will be very difficult to impose the desired proximity between the two particles in an experimental set up. Therefore, the *LE* or *FTLE* can not be calculated using Lagrangian particle tracking experiments. Despite these shortcomings, the *FTLE* contours uniquely identify the chaotic and regular regions in the flow, and the *FTLE* values quantify the chaotic strength.

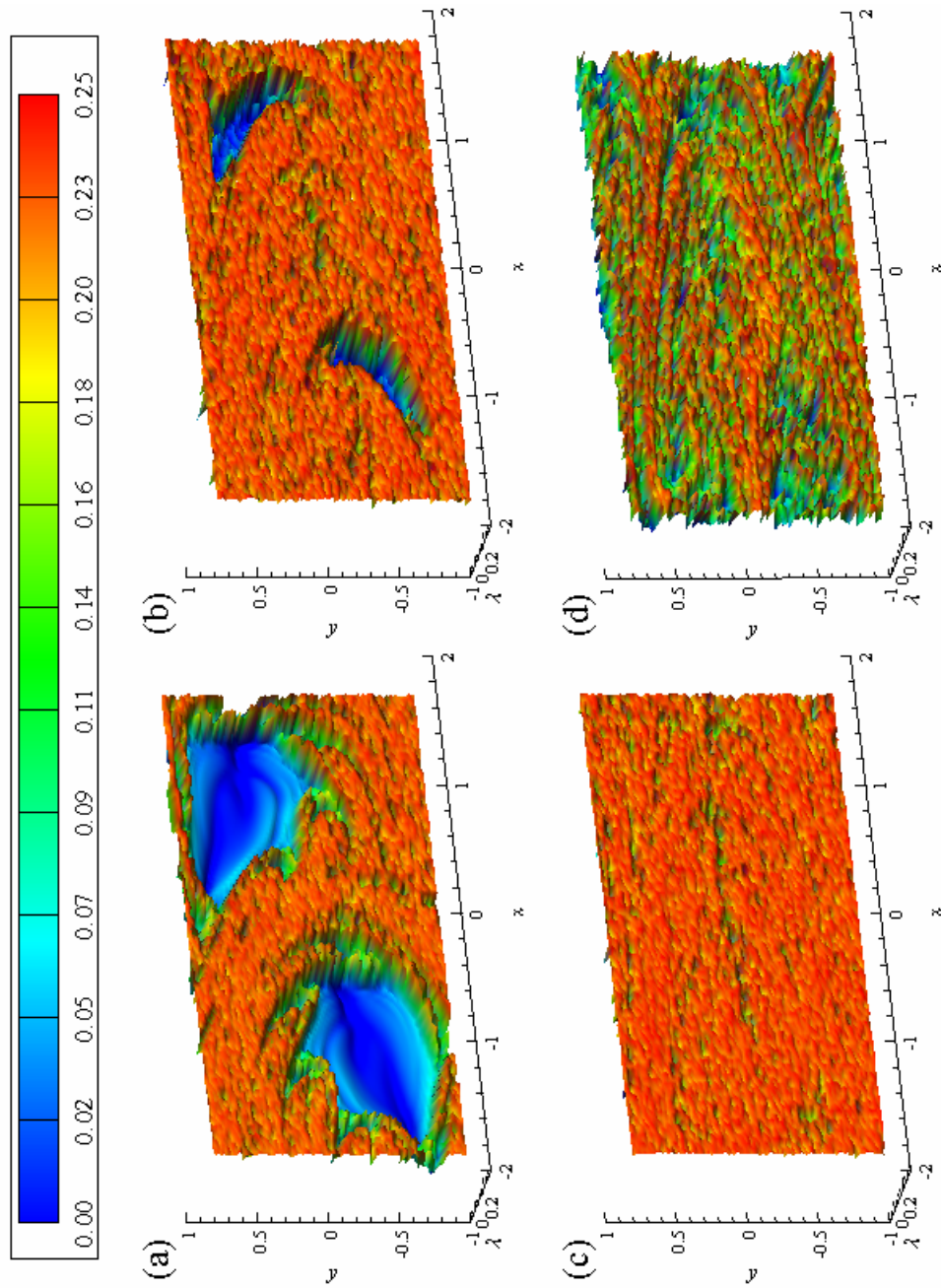


Figure 4.5. The *FTLE* contours for case B&C at period $T = 2$ (a); 4 (b); 6 (c); 8 (d). Blue regions corresponding to zero or negative *FTLE* values, show morphological similarities with the Poincaré sections in figure 4.4.

4.7. Probability density of stretching

Analysis of the stretching field provides physical interpretations in mixing study, because important aspects of the spatial structure of mixing are immediately revealed by direct examination of the stretching field [8]. The attenuated striation thickness by stretching is the key for enhancement of mixing efficiency [10]. Higher stretching results in increased contact area between diffusing two fluids. Therefore stretched fluid filaments induce shorter diffusion distances between the mixing fluids [6]. The stretching field was utilized to characterize mixing in previous studies [6, 8, 29, 31], including the experimental work of Voth *et al.*, where stretching was calculated using the experimentally measured velocity field [95].

The total amount of stretching at time t is determined by tracking the position \mathbf{x} and length $|l|$ of infinitesimal vector l whose evolution is given by [10]

$$l(t) = \int_{l(0)} (\mathbf{C} : \mathbf{M}\mathbf{M})^{1/2} |d\mathbf{X}|, \quad (4.13)$$

where $l(0)$ is the initial length of the fluid filament, and \mathbf{X} is the position of original fluid element. \mathbf{M} is a unit directional vector of an infinitesimal material element, which is defined in equation (4.9.b). \mathbf{C} is the Cauchy-Green strain tensor, $\mathbf{C} \equiv \mathbf{F}^T \cdot \mathbf{F}$, and \mathbf{F} is the deformation gradient tensor [10]. Material element $d\mathbf{x}$ is deformed from original element $d\mathbf{X}$ via $d\mathbf{x} = \mathbf{F} \cdot d\mathbf{X}$. Thus, the net stretching (h) is defined as

$$h = \frac{|l|}{|l(0)|}. \quad (4.14)$$

Integration of equation (4.13) is carried out numerically with respect to the initial configuration of line $l(0)$, because analytical calculation of the Cauchy-Green strain tensor (\mathbf{C}) is nearly impossible in chaotic flows [31]. In addition, when the initial length $l(0)$ is set coarsely (i.e. $l(0) > O(10^{-2})$), fluid filament can lose its structure and become fully dispersed, so that h doesn't have

physical meaning after a certain time period [62]. Therefore, rather than measuring the stretching of one long fluid filament, we investigate the distribution of stretching of many finite sized fluid segments.

Fluctuations of h are described by calculation of the probability density function (H_n) of $\log(h)$ (hereafter, *PDF*), [8] defined as,

$$H_n(\log h) = dN(\log h) / d(\log h), \quad (4.15)$$

where $dN(\log(h))$ is the number of particles experiencing the stretching values in the range of $[\log(h), \log(h) + d(\log(h))]$ [8]. By this definition stretching values smaller than unity correspond to contraction, while values larger than unity show stretching in the computed direction. Initial positions of particles are located in a uniform array, distributed in the whole mixing domain. These positions include both chaotic and regular zones inside the KAM boundaries. It is intuitively expected that points of low stretching values will be placed on regular zones and high values will be found in strongly chaotic regimes.

In figure 4.6 (a), PDF for case B&C at $T = 2, 4,$ and 6 are plotted by tracking 100,000 particles till $t = 120$. In the PDF, regions populated by particles experiencing the highest and lowest stretching values correspond to the regions of best and worst mixing zones, respectively. The sub peaks of low stretching are numbered as **A** ($T = 2$), **B** ($T = 4$) in figure 4.6 (a). The low stretching part of each case shows a significant amount of malformation, when compared with the globally chaotic case that exhibits Gaussian distribution. These malformations are expected because low stretching territories are prevented from extension due to KAM boundaries. In other words, the low-order elliptic periodic point tightly restricts the dispersing motion of unstable manifold of hyperbolic periodic point [10].

Stretching values can be dependent on the initial orientation of material lines (**M**) in steady flow. However, vectors in chaotic regions are reoriented in the eigendirections of

deformation gradient tensors, \mathbf{F} , at every instance, so that the initial orientation of material lines becomes unimportant. Figure 4.6 (b) shows $H_n(\log(h))$ of initially vertical and horizontal orientation for case B&C at $T = 6$, obtained at $t = 140$. PDF of the horizontal and vertical l_0 are similar to each other as expected from a fully chaotic flow.

Figure 4.6 (c) shows the deformation of blue and red particles using case B&C at $T = 2$ in the zoomed region of $-2 \leq x \leq 0$, $-1 \leq y \leq 1$. A total of 40,000 particles are initially positioned in the form of red and blue circles. The KAM boundaries obtained using two particles at initial positions of $(-0.3, -0.5)$, $(-0.4, -0.5)$ are shown in black, and superposed to the picture to identify the boundary between the chaotic and regular regions of the flow. Blue particles are initially located inside the regular islands, while the red particles are placed in the sea of chaos. The series of snapshots show the stretching and folding taking place around the islands, while a simple periodic rotation is observed inside the islands, where zero stretching values are detected. Red particles are experiencing exponential stretch and multiple times folding. However, they are not dispersing but wrapping around the islands, because the elliptic periodic point in regular islands is detaining these red tracer particles. In addition, blue particles inside the KAM boundaries cannot escape from the island, and they keep rotating periodically because the particle trajectories passing close to islands tend to stick to the periodic zones.

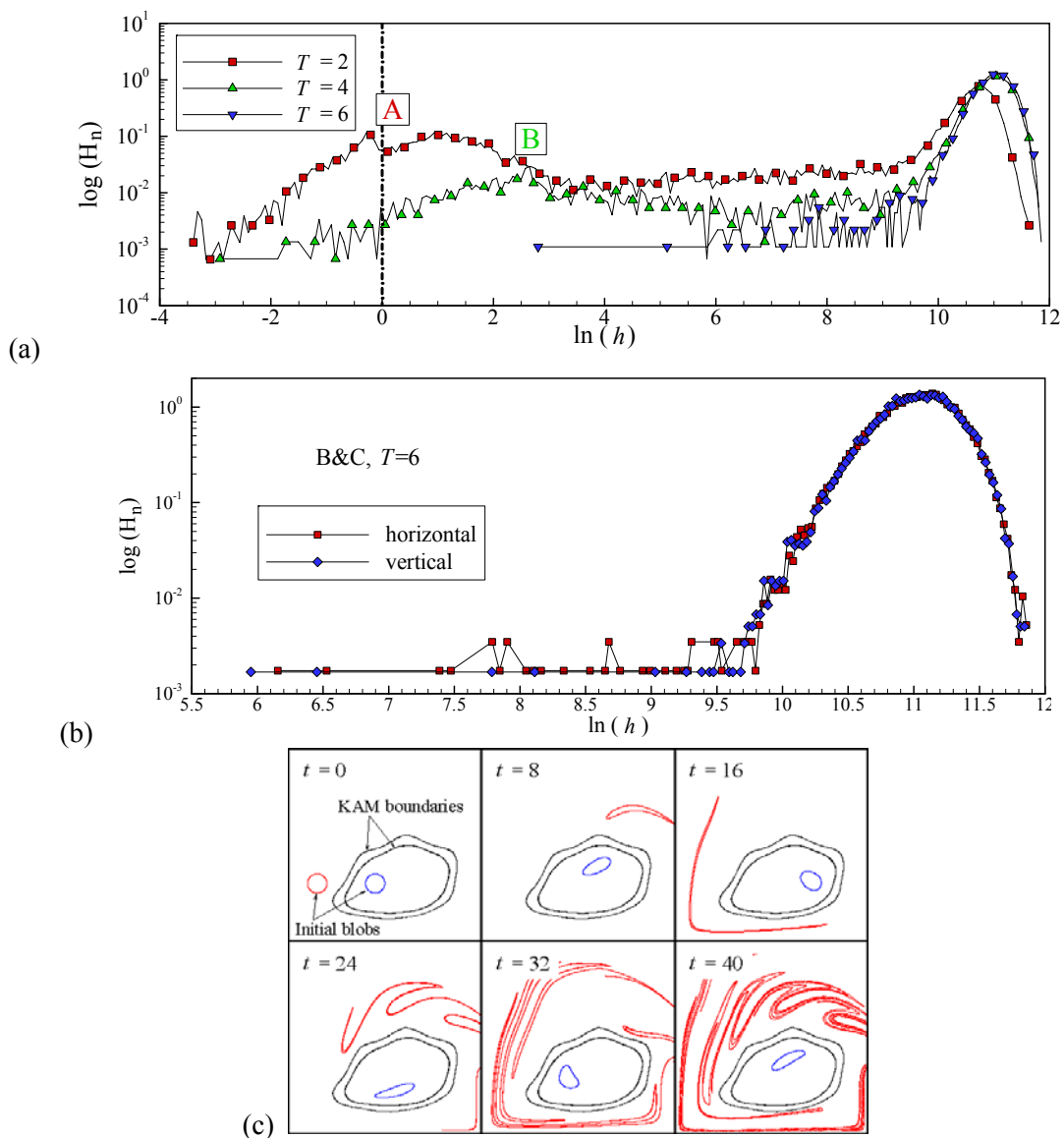


Figure 4.6. Probability density functions (*PDF*) of stretching fields for case B&C at period $T=2$, 4, and 6, obtained at $t=120$ (a). The *PDF* for case B&C at period $T=6$ obtained using horizontal and vertical l_0 at $t=140$ (b). Evolution of red and blue particles for case B&C at period $T=2$ (c). KAM boundaries obtained using initial particle positions of $(-0.3, -0.5)$, $(-0.4, -0.5)$ are drawn in black. The blue particles are initially located inside the regular islands, while the red particles are placed in the sea of chaos.

4.8. Species transport equation solutions

In the previous sections, we have shown the kinematic dependence of stirring and stretching effects using Lagrangian passive particle tracking results. In this section, we present the species mixing results as a function of time and Pe number in the Stokes flow regime. Numerical simulation of mixing requires solution of equation (2.1.a) and the species transport equation (2.1.c). All simulations were performed for mixing of a scalar marker that has concentration of $\theta = 1$ and $\theta = 0$ in the upper and lower halves of the domain, respectively. Therefore, the initial interface between the $\theta = 1$ and $\theta = 0$ conditions were at $y = 0.0$ (centerline), and a perfect mix would reach $\theta = 0.5$ everywhere in the domain. In all simulations, the velocity field developed from quiescent initial conditions and the flow patterns are changed in time smoothly within 10^{-3} convective time steps. In figure 4.7, we present evolution of the species concentration contours at various times. The results are obtained at $Pe = 1000$. Although the velocity and pressure fields are time periodic, species transport is transient. The portions of “well mixed” regions ($\theta \approx 0.5$, grey contours) are propagated to the whole mixing domain for $t > 4T$.

In order to verify the mixing efficiency we used the mixing index, which is based on the “homogenized” distribution of the concentration values in the domain. The mixing index is defined as

$$M = \frac{\sigma}{\theta_0} = \frac{1}{\theta_0} \sqrt{\langle \theta^2 \rangle - \langle \theta \rangle^2} \approx \sqrt{\frac{1}{N-1} \sum_{i=1}^N \left(\frac{\theta_i}{\theta_\infty} - 1 \right)^2}, \quad (4.16)$$

where θ_i is the average concentration inside the i^{th} section of a total of N interrogation areas, and σ is the standard deviation. Based on initial distribution of the species in our problem, a perfect mix would reach $\theta_0 = 0.5$. We decided on the total number of interrogation areas N by subdividing each spectral element into $K \times K$ sub sections.

According to the definition in equation (4.16), a perfect mix results in $M = 0$. Hence, smaller values of M show better mixing. For the closed mixer considered here, the mixing index varies as a function of time, and it can be used as a metric to assess the mixing efficiency. Better comparisons between various cases are possible using the *mixing index inverse* (M^{-1}), since, $M^{-1} \rightarrow \infty$, while $M \rightarrow 0$. Therefore in the following, we present variation of M^{-1} as a function of time. One can associate the M^{-1} values with the concentration range ($\theta_0 \pm \sigma$) using equation (4.16). For example, $M^{-1} = 20$ corresponds to $\sigma = 0.025$. This gives 95% mixing, if we define the mixing percentage as: $(1 - \sigma / \theta_0) \times 100\%$. Similarly, $M^{-1} = 10$ corresponds to 90% mixing.

As explained in the previous section, exponentially stretched fluid filaments enhance molecular diffusion due to two main reasons: First, exponential stretching increases the area available for diffusion, Second, it increases the concentration gradients normal to striations [96]. Thus, changing of striation thickness can control local diffusion time-scale. Figure 4.8 (a) shows evolutions of inverse mixing index for cases B&C at $T = 6$, C&D at $T = 4, 6$ and steady flow case of pattern C obtained at $Pe = 1,000$. In the *convective mixing*, M decays by time. However, its *decay rate* is very sensitive to the dynamical state of the stirrer. In cases B&C and C&D at $T = 6$, M^{-1} grow exponentially during the entire simulation time. However, for case C&D at $T = 4$, we observe linear growth of M^{-1} for $t > 30$, for which the flow is not dominated by a globally chaotic state. Thus, the *unbroken* KAM boundaries are responsible for slow decay of scalar field. Steady flow case shows much slower growth of M^{-1} value than the C&D at $T = 4$ case, as expected from a steady laminar flow. In addition, M^{-1} fluctuates with period of $T \approx 6$ for steady laminar flow (steady C case). This time periodicity is imposed by convective motion of the striation layers due to the steady flow, as shown in figure 4.1.

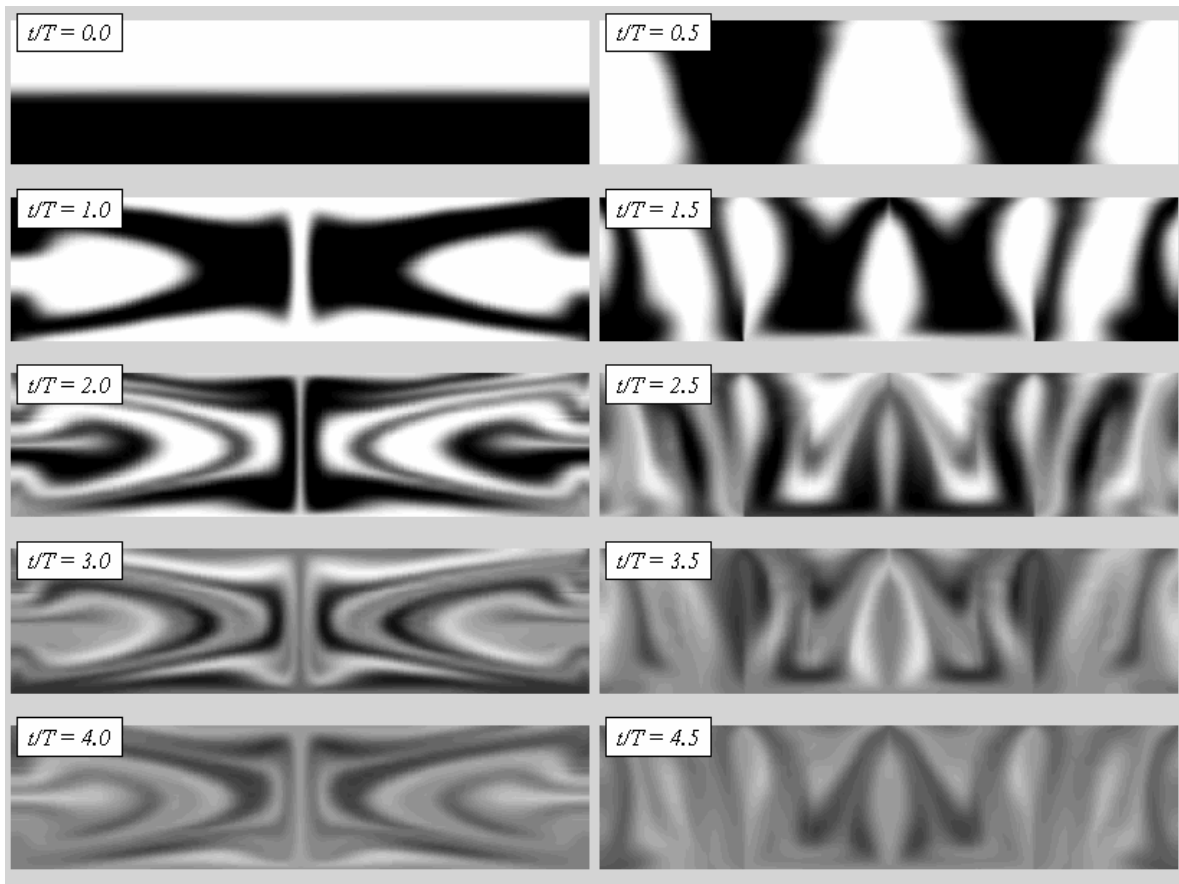


Figure 4.7. Temporal evolution of species concentration contours at $Pe = 1,000$ conditions ($Re = 0.01$) for case B&C, at period $T = 6$.

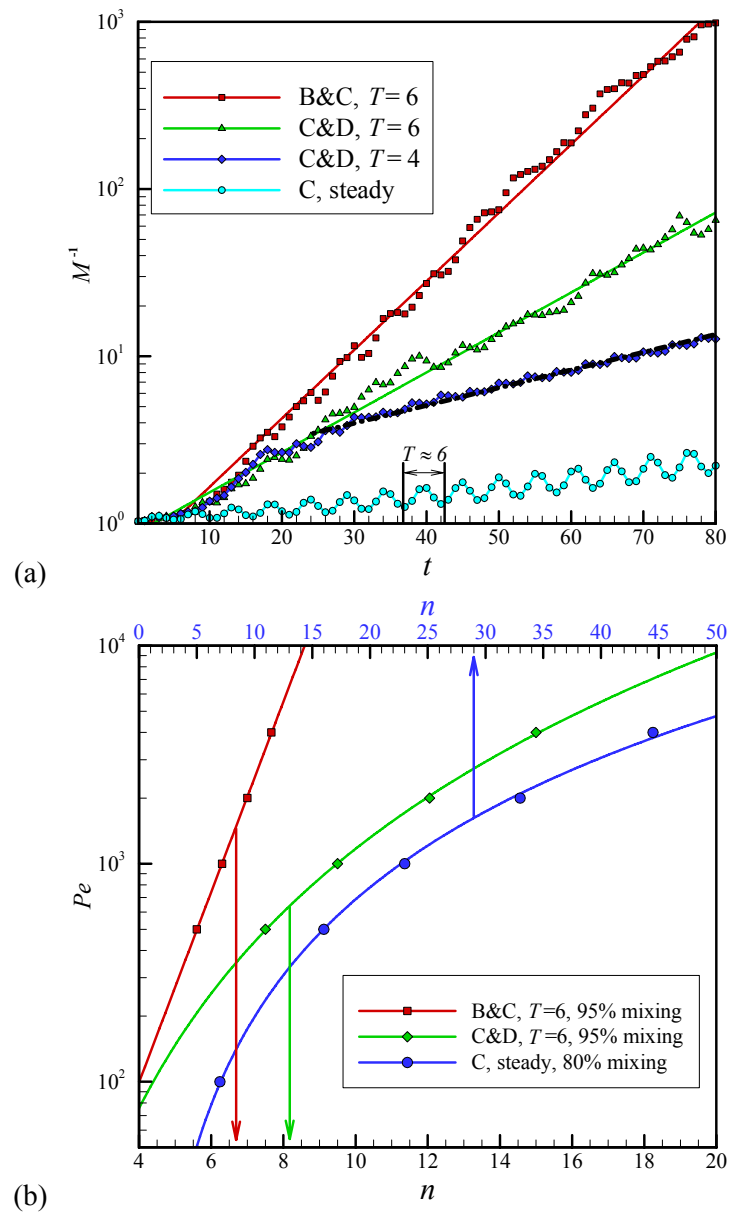


Figure 4.8. Variation of M^{-1} as a function of time for four different stirring conditions (a). Required number of time periods, n , to achieve 95% mixing using cases B&C and C&D at period $T = 6$ for various Pe values (b). For comparison purposes, steady flow for case C to achieve 80% mixing ($M^{-1} = 5$) is also shown ($T \approx 6$). All simulations are obtained at $Re = 0.01$.

Some theoretical approaches were proposed to explain the reason why the exponential decay of scalar field is connected with the chaotic advection or Batchelor turbulence [56, 57, 97]. Antonsen *et al.* derived that the long time decay of concentration variance would obey

$$\langle \theta(t)^2 \rangle \approx (\theta_0 \cdot M(t))^2 + \theta_0^2 \propto \int_0^\infty \lambda^{1/2} d\lambda P(\lambda, t) e^{(-\lambda t)}, \quad (4.17)$$

where $P(\lambda, t)$ is the probability density function of λ [97]. In the globally chaotic system, $P(\lambda, t)$ is normally distributed centering the mean value [98]. Thus, it is understood that the mixing efficiency is determined by the mean value of *FTLE* spectrum of globally chaotic system. Although equation (4.17) was criticized for failing to interpret global mixing mechanisms [56] and its limitations in calculation of the mixing rate near the boundaries [99], it is the only mathematical formulation that can predict the mixing efficiency explicitly.

As a succinct and clear evidence of fully chaotic state, the logarithmic relation between mixing time and Pe is often investigated [4, 10, 59, 100, 101]. At a fixed Re (i.e. fixed kinematic motion), Pe dependence of mixing time, t_m for fully chaotic flows is given by [4, 101]

$$t_m \propto \ln(Pe). \quad (4.18)$$

While partially chaotic or steady convection flow cases exhibit [35-37]

$$t_m \propto Pe^\alpha. \quad (4.19)$$

In figure 4.8 (b), we plot the convection time of 95% mixing for case B&C excited at $T = 6$ and for case C&D at $T = 6$ by changing Pe ($500 \leq Pe \leq 4000$). At the same Pe value, mixing time of the C&D case is longer than that of the B&C case, as expected from the Lagrangian particle tracking results. For case B&C, the 95% mixing time (t_{95}) scales as $\ln(Pe)$ (figure 4.8 (b)), while the mixing time for case C&D scales as a power law, Pe^α , with $\alpha \approx 0.33$. Giona *et al.* have shown that a wide class of unidirectional flows in periodic domains (two-dimensional steady flows) have a scaling of $t_m \propto Pe^{0.5}$ [35]. Figure 4.8 (b) shows that 80% mixing time for the steady

case of pattern C scales as $Pe^{0.5}$. In fully chaotic state, any regular or periodic zones cannot survive. This means that the fluid filaments are stretched exponentially in any place of fluid domain, then mixing becomes insensitive to Pe . Thus, $\ln(Pe)$ behavior can be observed only in certain situation such as fully chaotic state due to its global irregularity. However, if regularity is preserved even in small parts of the mixing domain, the mixing time does not scale as $\ln(Pe)$, but exhibit Pe^α behavior.

CHAPTER V

AN ELECTROOSMOTICALLY STIRRED CONTINUOUS FLOW MICRO-MIXER

5.1. Introduction

In this chapter, we present theoretical and numerical studies of particle dispersion and species mixing in a zeta potential patterned straight micro channel. Providing overall consolidation of multiple diagnostic studies presented in the previous chapter, a new type of stirrer design is presented. This chapter is organized as follows. In section 5.2, we describe the proposed micro mixer and its stirring mechanism. Particularly, a continuous flow is generated by superposition of a steady pressure driven flow and time periodic electroosmotic flow induced by a stream-wise AC electric field. Zeta potential patterns are placed critically in the channel to achieve spatially asymmetric time-dependent flow fields that lead to chaotic stirring. In following sections, parametric studies are performed as a function of the normalized AC frequency (Strouhal number), while the mixer geometry, ratio of the Poiseuille flow and electroosmotic velocities and the flow kinematics (Reynolds number) are kept constant. In section 5.3, we provide a series of results on direct simulation of particle dispersion to mimic the morphological behavior of interfacial layer by changing the Strouhal number. In section 5.4, we report qualitative dynamic analysis using Poincaré sections. In section 5.5, as a quantitative study, we show the distribution of stretching values and provide its temporal trend by statistical analysis. With scalar transport simulations, we study species mixing with chaotic advection in section 5.6.

5.2. Theoretical framework

In this section we describe the theoretical framework utilized in the design of *chaotically stirred electroosmotic micro-mixer* concept. Chaotic advection is observed for cases, in which the equation of motion for fluid particles can be represented as a *non-integrable Hamiltonian system*. Hence, the particle motion is sensitive to slight variations in particle position. Following the work of Aref [3], particle trajectories, located initially at \mathbf{x}_0 and flowing under the influence of a deterministic velocity field $\mathbf{u}(\mathbf{x}, t)$, can be obtained using

$$\frac{d\mathbf{x}}{dt} = \mathbf{u}(\mathbf{x}, t). \quad (5.1)$$

For steady two dimensional flows, this dynamical system is integrable, and the particle paths coincide with the streamlines. In the Stokes flow regime, stream function plays the role of the Hamiltonian [102]. Steady two-dimensional Stokes flow is an *integrable dynamical system*, thus it cannot be chaotic. However, for time periodic two-dimensional flows the dynamical system becomes *non-autonomous*, and particle trajectories *may* result in chaotic advection [3]. A necessary condition for chaos is the crossing of the streamline patterns at two successive times to produce either homoclinic tangles from the intersections of the stable and unstable manifolds of the same hyperbolic point, or heteroclinic tangles from the intersections of the unstable manifold of one hyperbolic point with the stable manifold of another [10, 102]. These tangles induce extreme sensitivity to the initial conditions, and a consequent inability to predict the outcome of evolution in a chaotic system. Based on this premise, we designed a mixer, which experiences time-periodic two-dimensional flow using periodically repeating mixing blocks, shown in figure 5.1. We present two different mixing block designs (patterns A and B), each utilizing zeta potential (ζ) patterned surfaces that induce two-dimensional electroosmotic (EO) flow under an

axial electric field. The streamline patterns generated under an axial steady electric field are also shown in figure 5.1. In order to obtain a *non-autonomous* system, we alternate the axial electric field in the form of a cosine wave with frequency, ω , and superpose this flow field with a unidirectional pressure-driven flow. The EO flow under AC electric field can not solely induce crossing of the streamlines, since reversing the electric field direction simply reverses the flow direction on each streamline. To resolve this problem Qian and Bau utilized zeta potential patterned surfaces in a closed mixer and proposed alteration of the zeta potential patterns on the mixer surface [2]. Although zeta potential alterations have been demonstrated in the literature, their practical implementation is quite challenging [59]. In order to circumvent this difficulty and to obtain a continuous flow system, we superposed pressure driven flow with the electroosmotic flow under AC electric field. The resulting flow system allows crossing of streamlines at different instances, and the flow is spatially and temporally periodic.

The mixing block has half channel height H , and length $L = 4H$. Theoretical studies assume two-dimensional flow. For pattern A, we assume two different surfaces with positive and negative zeta potential values ($\pm\zeta_0$) shown by red and blue surfaces in figure 5.1, while pattern B also includes an electrically neutral surface shown in white. Since zeta potential depends on the surface, buffer, ionic concentration and pH, it may be difficult to select three different surfaces that satisfy $\zeta_0 \approx 0$ and $\pm\zeta_0$ at the same time. Examining the EO flow literature we identified that in 1 mM KCl solution at pH = 7.0, PMMA has $\zeta = -34$ mV [103], Aluminum-oxide $\zeta = 37$ mV [104], while Chromium-oxide surfaces $\zeta \approx 0$ mV [105], which satisfies the necessary ζ values in the proposed mixer.

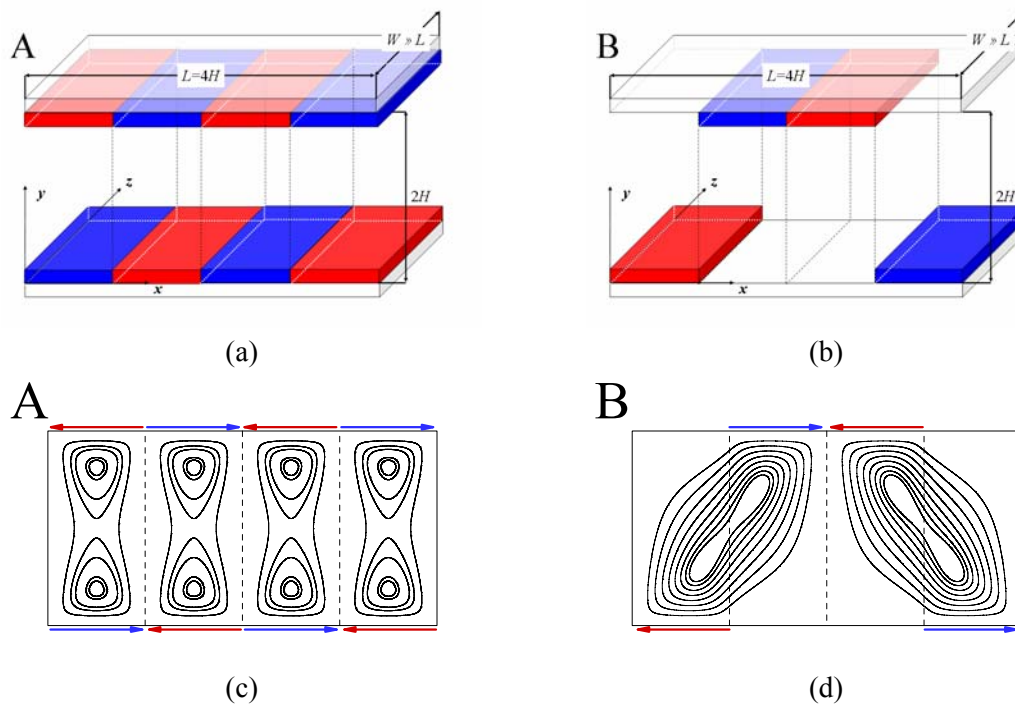


Figure 5.1. The mixer consists of spatially repetitive mixing blocks with ζ potential patterned surfaces as shown in (a) for pattern A and (b) for pattern B. An axial electric field induces electroosmotic flow and its streamlines are represented by solid lines in (c) for pattern A and in (d) for pattern B, while a unidirectional pressure-driven flow enables continuous flow in the system. Arrows on top and bottom of mixing block in (c) and (d) indicate the directions of Helmholtz-Smoluchowski velocity, U_{HS} (see equation (2)). Combining the pressure driven flow with electroosmotic flow under time periodic external electric field (in the form of a Cosine wave with frequency, ω) results in two-dimensional time-periodic flow suitable to induce *chaotic stirring* in the mixer.

Electroosmotic flow is generated as a result of interactions between the net electric-charge density within the electric double layer (EDL) and the externally applied electric field. In a series of papers [106, 107], Dutta and Beskok investigated response of electroosmotic flow under AC and DC electric fields, and have shown that fluid velocity at the edge of EDL and bulk flow region reaches the Helmholtz-Smoluchowski velocity (U_{HS}) given by

$$U_{HS} = -\frac{\varepsilon\varepsilon_0\zeta}{\mu}E, \quad (5.2)$$

where ε is the dielectric constant, ε_0 is the permittivity of vacuum and μ is the absolute viscosity. The EDL thickness for the ionic strength proposed above is on the order of 10 nm. Electroosmotic flow response time (i.e., development of U_{HS} at the EDL/bulk-flow interface) due to temporal fluctuations in the externally applied electric field is on the order of nano-seconds (the prediction is based on ion-diffusion time-scales through the EDL). Therefore, we expect almost immediate response from the electroosmotic flow by forming U_{HS} at the EDL/bulk-flow interface for low frequency excitations [107]. This enables us to use U_{HS} as an “effective slip boundary condition”, by neglecting the velocity profile within the EDL, and eliminates the numerical stiffness imposed by resolution of very thin EDL region near surfaces. In the mixer design, Poiseuille flow channel centerline velocity (U_0) becomes an additional velocity scale. Fluid flow in the mixer is described by U_{HS} , U_0 , ω , H , L , ν (kinematic viscosity). Using *dimensional analysis*, we identify the following dimensionless parameters:

$$Re = \frac{U_{HS}H}{\nu}; \quad St = \frac{\omega H}{U_{HS}}; \quad A = \frac{U_0}{U_{HS}}; \quad \frac{L}{H} = 4 \quad (5.3)$$

where Re and St are the Reynolds and Strouhal numbers, and A is the ratio of the electroosmotic and Poiseuille flow velocities, and L / H indicates the mixer geometry, respectively. For simplicity of our design, we utilized $L / H = 4$.

Due to the physical limitations of electroosmotic flow imposed by the external electric field and the zeta potential, simulations were restricted to Stokes flow. We utilized $Re = 0.01$ to satisfy this restriction. Overall, we expect the bulk flow and streamline patterns to be *insensitive* to the Reynolds number for Stokes flow conditions ($Re < 1$). Hence the Reynolds number is not a critical design parameter, for as long as $Re < 1$ is satisfied. We also chose $A = 0.8$ in order to reduce the parametric space solely to the investigation of the effects of Strouhal frequency variations in patterns A and B. For practical purposes $A \approx 1$ so that continuous flow can be maintained in the channel where EO and Poiseuille flows have similar order of magnitudes, and the streamline patterns can cross each other at different instances. In the following sections, we will utilize the Lagrangian particle tracking techniques for Stokes flow to obtain Poincaré sections [24, 33] and stretching calculations for fluid filaments [6, 8, 10, 29, 95] to identify the *locally optimized* operation conditions. Since our parametric studies are performed for a discrete set of St , we present here only the *locally optimized* conditions. More extensive studies that vary both St and A are required to determine the *globally optimized* operation conditions.

5.3. Particle dispersion

Dispersion of passive tracers in the mixing domain can provide both qualitative and quantitative information on mixing efficiency. In [11], we presented Lagrangian particle tracking techniques that utilize numerical integration of equation (5.1) using a fourth-order Runge-Kutta algorithm. An essential feature of our approach is utilization of a spectral element discretization of the velocity field that results in exponential accuracy. Typically, 8th order spectral element discretizations with a time step of $\Delta t = 10^{-3}$ maintain the maximum error in the tracked particle velocity and location below 10^{-11} for each time step. This allows us to perform long time integration of particle paths with great computational efficiency and accuracy [11]. In figure 5.2 we present a series of particle dispersion results as a function of the Strouhal number. Particularly, development of an interfacial layer is conducted by continuously feeding red and blue fluid particles into the flow near the channel entrance. The color labeling of particles indicate their species, entering the mixer from the top and bottom at the channel entrance, respectively. For poor mixing cases, the results in figure 5.2 provide qualitative information on the behavior of the interface between the two liquids. However, for better mixing cases two different colored passive tracer particles disperse uniformly to the whole mixing domain, which can be considered as a chaotically stirred state. Chaotic motion is characterized by the divergence of nearby trajectory in the phase space. Exponential divergence of initially nearby particles means that the neighboring particle will soon behave quite differently from the original particle [92]. Sensitivity to initial conditions is the main characteristic of chaotic systems. Chaotic motion enhances particle dispersion and increases the stirring efficiency. Therefore global chaotic stirring is highly desirable for design of efficient micro-mixers.

Particle dispersion results in figure 5.2 for case A at $St = 1 / 2\pi$ and $3 / 2\pi$, and case B

at $St = 1 / 4\pi$ and $3 / 2\pi$ show oscillatory vertical motions of the red/blue particle interface in the vicinity of the channel center line, which does not enhance particle stirring. However, case A at $St = 1 / \pi$ and case B at $St = 1 / 2\pi$ in figure 5.2 exhibit extensive particle dispersion. In figure 5.2 (b) and (e), the material lines undergo severe stretching, and form extremely convoluted periodic patterns of scattered clusters flowing along the straight channel. These dramatic morphological changes of material lines represent the evolution of an initially straight interfacial layer. Generation of lobe-like structures by the periodic perturbation increases the surface contact area between the two-streaming fluids. A time-periodic stretching and folding process can be clearly observed in these cases towards the downstream of the mixer. One should note the void regions surrounded by the well-dispersed particles in figure 5.2 (b). As we will show later in section 5.4, these regions are due to the Kolmogorov-Arnold-Moser (KAM) boundaries that separate the chaotic and regular regions of the flow, preventing transport of particles between the both regions. Distributive mixing requires uniform dispersion of passive tracer particles in the entire the mixing domain [11]. Therefore, efficient chaotic mixers should avoid KAM boundaries.

Particle dispersion results need to be quantified to obtain objective measures of the stirring efficiency. For closed mixers, we can precisely measure the dispersing state in the mixer using the conservation of total number of passive tracers [11]. For continuous flow mixers, the parabolic velocity profile induces particle dispersion along the channel length, and as a consequence, we can not employ conservation of total number of passive tracers within each mixing block. Therefore, parametric studies of the Strouhal number effects on mixing will be discussed using dynamic methodologies in the following sections.

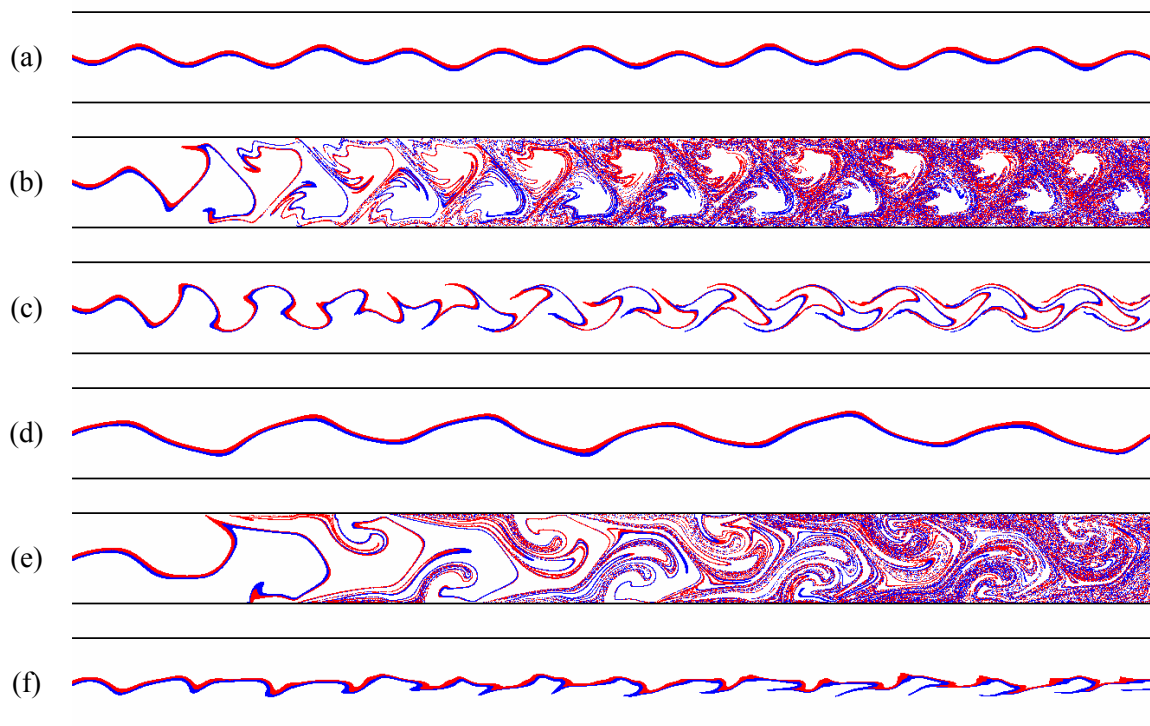


Figure 5.2. Snapshots of the spreads of passive tracer particles: (a) case A at $St = 1 / 2\pi$, (b) case A at $St = 1 / \pi$, (c) case A at $St = 3 / 2\pi$, (d) case B at $St = 1 / 4\pi$, (e) case B at $St = 1 / 2\pi$ and (f) case B at $St = 3 / 2\pi$. For the depiction of the instant positions of particles, we record their spatial coordinates at $t = 20\pi$.

5.4. Poincaré section

In order to investigate the effects of excitation frequency in detail, we gradually increase the Strouhal number (St) for cases A and B, and utilize the Poincaré sections to investigate the best stirring state. Poincaré section is a stroboscopic image of passive tracer particles, obtained as a collection of points where the trajectory pierces the phase plane. In a closed flow system, the time interval between successive visits of the trajectory in the Poincaré section is the period of the motion [93]. Thus, spatial trajectories of passive tracer particles are projected onto Poincaré sections by mapping every time period. However, for an open flow system such as a channel flow, it is impossible to obtain images to display the dynamic states in a physical channel domain ($x - y$) through time periodic projections, because motions of passive tracer particles are not bounded within a limited physical domain.

Niu and Lee proposed a useful mapping method to develop Poincaré sections for open flow systems [24]. The continuous flow mixer utilizes time-periodic flow in periodically repeating mixing blocks. Utilizing this fact, we choose Poincaré section to be $x_n = n \times L$ for the trajectory of any initial point, where L is the length of the mixing block and $n = 1, 2, \dots, N$. Particle trajectories will intersect boundaries of the mixing blocks successively at points P_1, P_2, \dots, P_N . This mapping can be defined as,

$$P_{n+1} = \Phi_p(P_n), \quad (5.4)$$

where Φ_p is the Poincaré mapping. At point P_n , the vertical positions of passive tracer particles are recorded in y axis of the Poincaré section, while time (t) increases to infinity with the repetition of mapping. In order to convert t into a periodic variable, we adopt a new variable α . Since the flow is periodic with a specified St , and 2π is a common factor in our definition of St , we defined $\alpha = \text{modular}(t, 2\pi)$. The values of α are recorded in the horizontal axis of the

Poincaré section. Thus, mathematical expression of projection points on Poincaré section is $P_n(\alpha_n, y_n)$ [24, 33]. This repetitive process of projection can significantly reduce the complexity of analysis by decreasing one degree of freedom of the dynamical system.

Figures 5.3 (a) and (b) depict Poincaré sections for cases A and B at different excitation frequencies, respectively. Single passive tracer particle that was initially placed at (0.02, 0.0) is tracked for $t = 10^5$. Initial location of the particle was near entrance of the mixer and on the interface between the two flow streams. In figure 5.3 (a), Poincaré sections of case A at $St = 1 / 2\pi$ and $3 / 2\pi$ show regular patterns in the form of sinusoidal curves. Our use of 2π in the definition of α manifests itself as a sinusoidal curve with 1 and 3 periods for $St = 1 / 2\pi$ and $3 / 2\pi$ cases, respectively. These ordered formations indicate quasi-periodic motions of passive tracer particles. In case A at $St = 1 / \pi$, the Poincaré section loses its structural coherence in most of the $\alpha - y$ plane with the exception of four void zones. Despite the temporal integration performed for 10^5 convective time scales, the particle can not penetrate to these void zones, which are regular islands surrounded by the chaotic sea.

Scattering of the passive tracer particle in the Poincaré section qualitatively implies a chaotic state, while quasi-periodic flow generates an asymptotic barrier called Kolmogorov-Arnold-Moser (KAM) boundary. If the particle trajectory exhibits exponential divergence, then the trajectory on its second visit to a particular neighborhood will have subsequently different behavior than its previous visit [92]. KAM boundary is destructed through the process for irregularity or non-periodicity. By the destruction of KAM curves and shrinkage of the quasi-periodic areas (i.e. regular islands), the route from quasi-periodic to chaos is built up, showing morphological irregularity in the phase plane. Thus, a successive record of such behavior is the signature of chaos in the entire flow domain. Based on these premises, regularly shaped void zones should not survive in the Poincaré section. In figure 5.3 (b), case B at $St = 1 / 4\pi$ and $3 / 2\pi$

still show presence of sinusoidal curves. However, the Poincaré section for case B at $St = 1 / 2\pi$ is filled with scattered dots - *chaotic sea*. Qualitatively, case B at $St = 1 / 2\pi$ is dominated under the globally chaotic state and it can be considered as a *locally optimum* case among all selected cases.

It is already known that Poincaré section provides an intuitive and visually convincing result to qualitatively estimate the stirring performance. However, once the Poincaré sections become featureless, it is hard to precisely determine which case has relatively higher chaotic strength [11]. In addition, Poincaré sections require integration of passive tracer's motion for an extremely long time. Consequently, integration time may exceed the physical diffusion time scale ($t_{diff} = L^2 / D$), and the final position of the passive tracer can overshoot the channel length. These are the drawbacks for utilization of Poincaré section as a *general mixing metric*. In the next section, we provide the distribution of stretching values of infinitesimally small fluid filaments for explicit quantification of mixing performance.

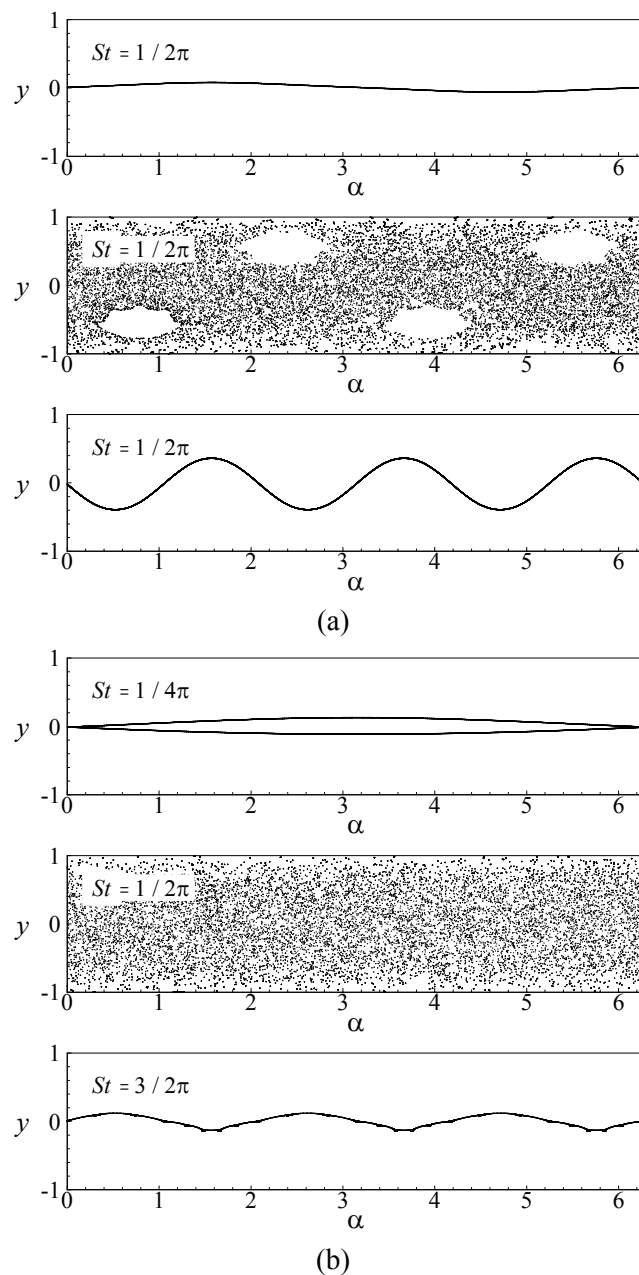


Figure 5.3. Poincaré sections of (a) case A at $St = 1/2\pi$, $1/\pi$, $3/2\pi$, and (b) case B at $St = 1/4\pi$, $1/2\pi$, $3/2\pi$, on the $\alpha - y$ plane; Horizontal coordinates stand for α values and vertical coordinates indicate values of y directional positions. Passive tracer particles are initially placed at $(0.02, 0.0)$, which is near the entrance of a channel and simultaneously, on the interface between two fluids.

5.5. Stretching of fluid filaments

Analysis of the stretching field of infinitesimally small fluid filaments provides physical insights in mixing studies. Important aspects of the spatial structure of stirring can be revealed by direct examination of the stretching field [8]. Attenuation of the striation thickness by stretching is the key for enhancement of mixing efficiency [10]. Higher stretching results in increased contact area, and thus shorter diffusion distances between the mixing fluids [6]. For practical design of micro-scale mixers, several researchers utilized stretching field to quantify the mixing performance [6, 8, 29, 31].

The total amount of stretching at the time t is determined by tracking the position \mathbf{x} and length l of an infinitesimal vector $l(0)$ whose evolution is given by [10]

$$l(t) = \int_{l(0)} (\mathbf{C} : \mathbf{M}\mathbf{M})^{1/2} |d\mathbf{X}|, \quad (5.5.a)$$

$$\mathbf{C} \equiv \mathbf{F}^T \cdot \mathbf{F} \quad (5.5.b)$$

$$\mathbf{M} \equiv \frac{d\mathbf{X}}{|d\mathbf{X}|} \quad (5.5.c)$$

where $l(0)$ is the initial length of the fluid filament, \mathbf{X} is the position of original fluid element and \mathbf{M} is the unit directional vector of an infinitesimal material element. In equation (5.5.a), \mathbf{C} is the Cauchy-Green strain tensor, $\mathbf{C} \equiv \mathbf{F}^T \cdot \mathbf{F}$ [10] and \mathbf{F} is deformation gradient tensor. Material element $d\mathbf{x}$ is deformed from original element $d\mathbf{X}$ via $d\mathbf{x} = \mathbf{F} \cdot d\mathbf{X}$. Thus, the net stretching h is defined as

$$h = \frac{|l|}{|l(0)|}. \quad (5.6)$$

Integration of equation (5.5.a) is carried out numerically with respect to the initial configuration

of line $l(0)$, because analytical calculation of the Cauchy-Green strain tensor (\mathbf{C}) is nearly impossible in chaotic flows [31]. Fluid filaments can lose their structural coherence by dispersing, when their initial length $l(0)$ is set coarsely (i.e. $l(0) > O(10^{-2})$), resulting in physically meaningless h values after a certain time [62]. In order to avoid such cases, we utilized $l(0) = 1.0 \times 10^{-6}$ and followed evolution of h as a function of time. Since a single h value cannot be used to detect global homogenization and the stirring performance within the whole domain, we calculated the stretching of thousands of fluid filaments and analyze their statistical distribution. Through extensive numerical simulations, we have shown that the statistical distribution of h is insensitive to the initial direction of the fluid filaments (i.e., \mathbf{M}) for chaotic flows [11].

In figure 5.4, we present the stretching contours for case A at $St = 1 / 2\pi, 1 / \pi, 3 / 2\pi$ and case B at $St = 1 / 4\pi, 1 / 2\pi, 3 / 2\pi$ with h values obtained at time $t = 100$. In the figure, x and y are the horizontal and vertical coordinates of the *initial positions* of fluid filaments, while the depth and the contour colors indicate $\ln(h)$. In each case, we utilized 250,000 particle pairs, which were uniformly distributed through *the entire mixing domain of the first mixing block*. Each particle pair was with separated by 1.0×10^{-6} . For case A at $St = 1 / 2\pi, 3 / 2\pi$ and case B at $St = 1 / 4\pi, 3 / 2\pi$, $\ln(h) < 1$ are detected in the vicinity of the center line of the channel, which correspond to contracting filaments. Obviously, the results in figure 5.4 (a), (c), (d) and (f) correspond to poor mixing cases, consistent with the corresponding results shown in figures 5.2 and 5.3. Particle stretching contours for case A at $St = 1 / \pi$, show low $\ln(h)$ values within the regular zones that are sharply segregated from the chaotic regions by KAM boundaries.

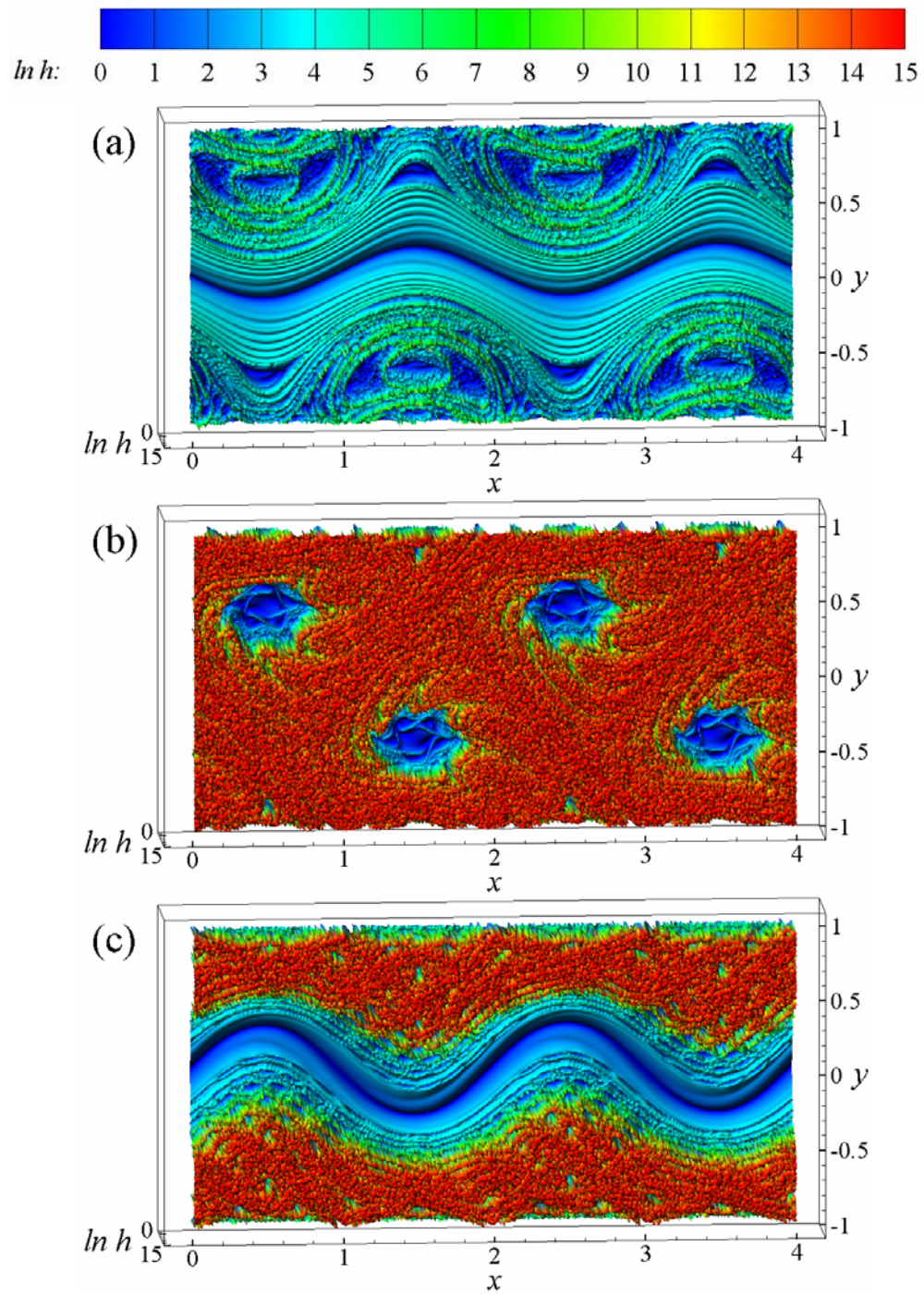


Figure 5.4. Contours of stretching, h for and case B at $St = 1 / 2\pi$ (a), $1 / \pi$ (b), $3 / 2\pi$ (c). h values are measured at $t = 100$. Red and blue parts are regions of high and low stretching values, respectively.

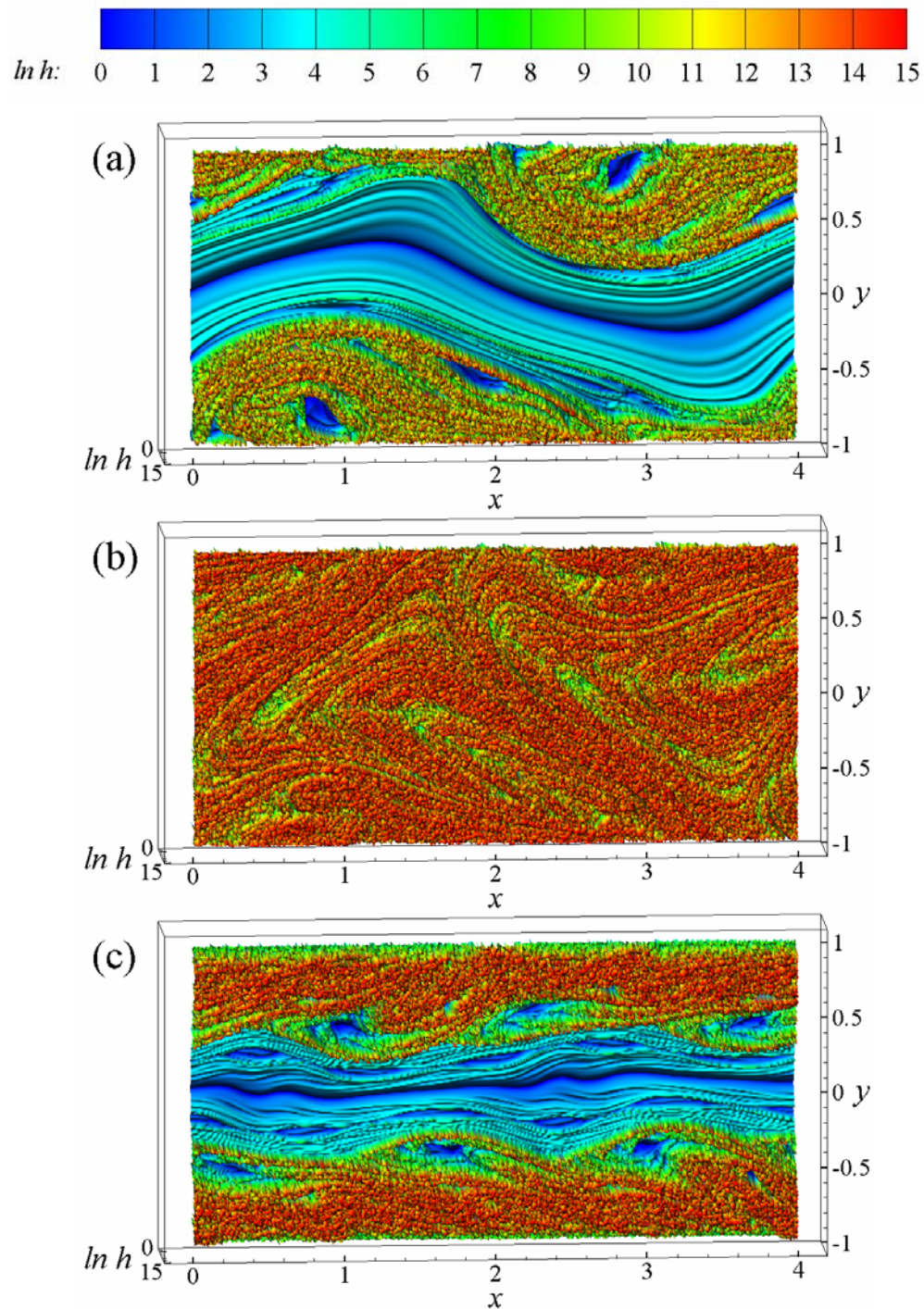


Figure 5.5. Contours of stretching, h for case B at $St = 1/4\pi$ (a), $1/2\pi$ (b), $3/2\pi$ (c). h values are measured at $t = 100$. Red and blue parts are regions of high and low stretching values, respectively.

Uniform distribution of high stretching values can be found only in case B at $St = 1 / 2\pi$. Overall, the results from the stretching contours are consistent with the particle tracking results shown in figures 5.2 and 5.3. Fluctuations of h are described by calculation of the probability density function (H_n) of $\ln(h)$ (hereafter, PDF), defined as,

$$H_n(\ln h) = dN(\ln h) / d(\ln h), \quad (5.7)$$

where $dN(\ln h)$ is the number of particles experiencing the stretching values in the range of $[\ln h, \ln h + d(\ln h)]$ [8]. By this definition, stretching values smaller than unity correspond to contraction, while values larger than unity show stretching in the computed direction. Initial positions of particles are located in a uniform array, distributed in the whole mixing domain of the first mixing block. These positions include both chaotic and non-chaotic zones inside the KAM boundaries. It is intuitively expected that points of low stretching values are placed on non-chaotic zones and while high stretching values are found in strongly chaotic regimes. H_n can be conceptually interpreted as a spectrum of intensities of the fluid mechanical mixing process. Figure 5.5 shows H_n computed for case A at $St = 1 / 2\pi$ (a), $1 / \pi$ (b), $3 / 2\pi$ (c) and case B at $St = 1 / 4\pi$ (d), $1 / 2\pi$ (e), $3 / 2\pi$ (f) using 250,000 particles. The figure shows distributions of stretching values computed until $t = 100$ with time interval of 20. As t increases, all H_n curves shift to the right. In figure 5.5 (a), after a few convection times, the central part of each curve develops a bell shape. However, the peak of curve is located only around the low stretching part.

Regions populated by particles experiencing the highest and lowest stretching values correspond to the regions of best and worst stirring, respectively. Figure 5.5 (b), (c), (d) and (f) show PDF with two peaks. While the peak to the right is bell-shaped and corresponds to the chaotic region, the peak to the left is produced by the regular islands, and it is characterized by the presence of multiple sub-peaks. As t increases, the peak associated with the chaotic region moves to the right, indicating exponential stretching of fluid filaments, while the peak corresponding to the regular region hardly moves at all. The low stretching part of each case shows a significant amount of malformation when compared with the globally chaotic case that exhibits bell shape or Gaussian distribution. These malformations are expected since fluid filaments are prevented from stretching due to KAM boundaries. In other words, elliptic periodic point at the center of the regular island prevents stretching of fluid filaments due to its strong periodicity, as we already observed from the particle dispersion results in figure 5.2 and Poincaré sections in figure 5.3. Compared to the other cases, H_n curves for case B at $St = 1 / 2\pi$, shown in figure 5.5 (e), display only the peaks populated by the chaotic regions. This indicates that case B at $St = 1 / 2\pi$ is free of regular zones.

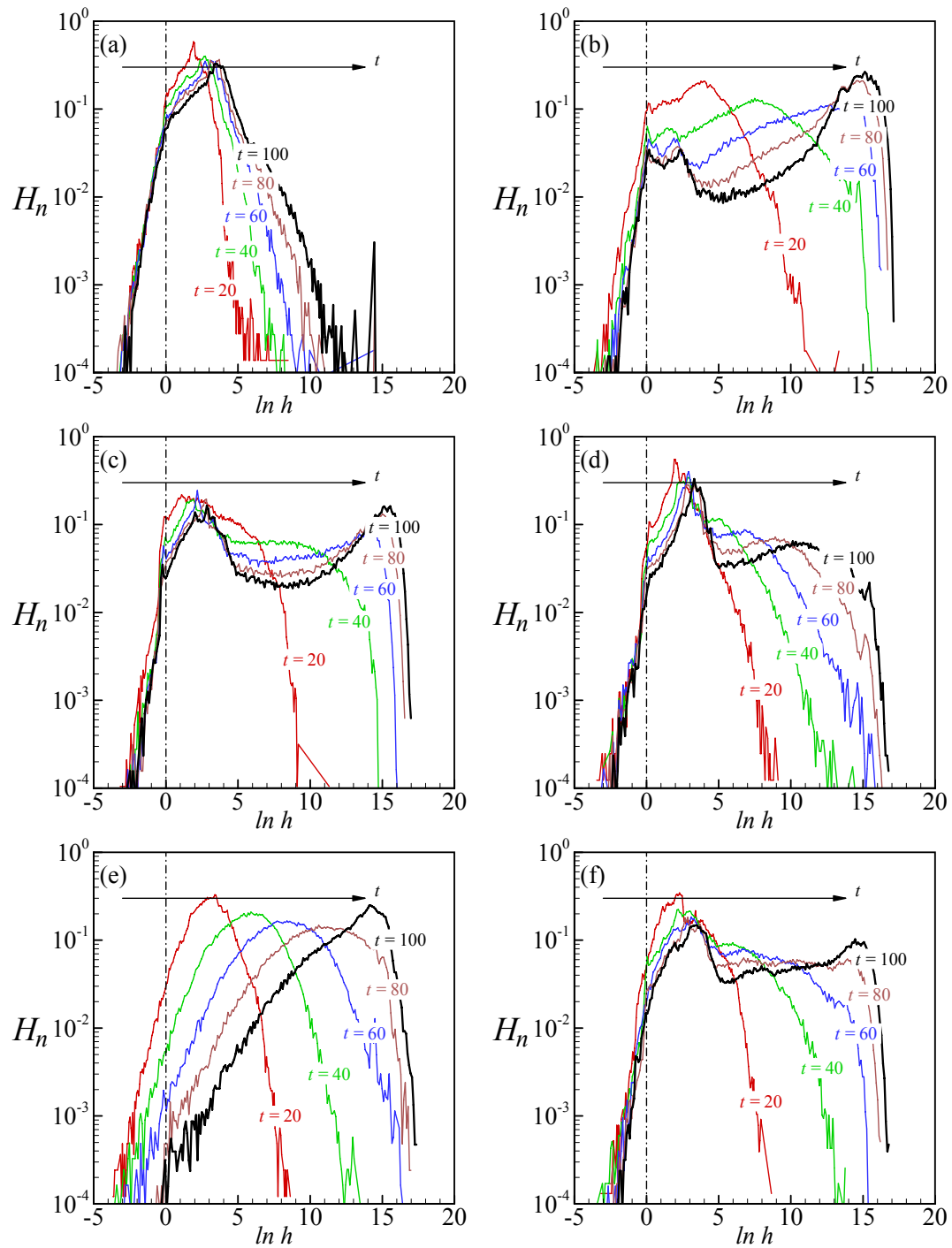


Figure 5.6. Probability density functions (PDF) of stretching values, h of case A at $St = 1 / 2\pi$ (a), $1 / \pi$ (b), $3 / 2\pi$ (c) and case B at $St = 1 / 4\pi$ (d), $1 / 2\pi$ (e), $3 / 2\pi$ (f).

5.6. Numerical simulation of scalar transport

In the previous sections, we have shown the kinematic dependence of stirring and stretching effects using Lagrangian passive particle tracking results. In this section, we present the species mixing results as a function of channel length and Pe . Numerical simulation of micro-scale mixing requires solution of the flow field from the Navier-Stokes equations (2.1.a), and the species transport equation (2.1.c). Details of our numerical formulation and code verification can be found in [9, 11, 21].

In figure 5.6, we show a series of numerical simulation results of mixing of a scalar marker at $Pe = 1,000$ in an 8-block mixer. At the entry of the mixer (left) the marker has concentration values of $\theta = 1$ (red) and $\theta = 0$ (blue) in the upper and lower halves of the domain. Therefore, a perfect mix would reach $\theta_\infty = 0.5$ (green). It is observed that case A at $St = 1 / \pi$ and case B at $St = 1 / 2\pi$ achieve fast homogenization of concentration field, while the others show poor mixing. The difference of mixing efficiencies can be explained by the exponential stretching of fluid filaments under *high chaotic strength*. Exponentially stretched fluid filaments enhance mixing by increasing the area available for diffusion, and by increasing the concentration gradients normal to striations.

Thus, changing of striation thickness can control the local diffusion time scale. Similarities between the contour plots and the particle tracing results in figure 5.2 are noteworthy. In general, it is crucial to use a metric to describe the mixing efficiency, directly based on the concentration values. In order to estimate the mixing efficiency, we used the mixing index (M), which is based on homogenized distribution of concentration values in the domain (i.e. concentration variance). The mixing index (M) [11, 37, 58, 97] is defined in equation (4.16) and the $\langle \dots \rangle$ symbol denotes averaging over the *volume of a single mixing block* in this equation. Based on the initial distribution of the species, a perfect mix would reach $\theta_\infty = 0.5$. According to the definition in equation (4.16), a perfect mix results in $M = 0$. Hence, smaller value of M shows better mixing. For the continuous mixer considered here, the mixing index varies as a function of the channel length, and it can be used as a metric to assess the mixing efficiency. Better comparisons between the various cases are possible using the *mixing index inverse* (M^{-1}). Since, $M^{-1} \rightarrow \infty$, while $M \rightarrow 0$. One can associate the M^{-1} values with the concentration range ($\theta_\infty \pm \sigma$) using equation (4.16). For example, $M^{-1} = 20$ corresponds to $\sigma = 0.025$, which gives 95% mixing efficiency, defined as: $(1 - \sigma / \theta_\infty) \times 100\%$. Similarly, $M^{-1} = 10$ corresponds to 90% mixing.

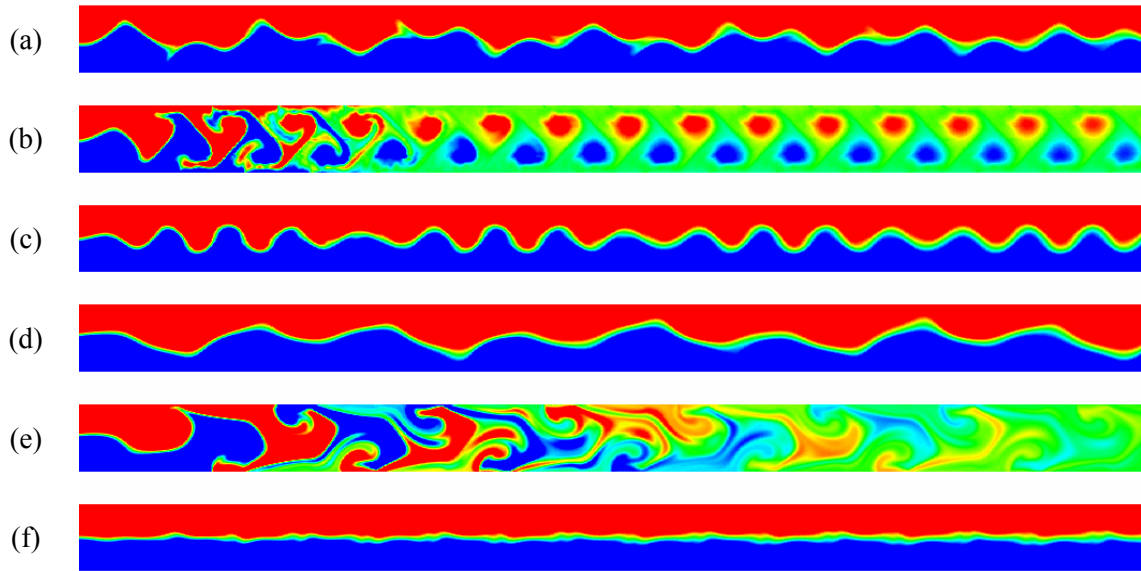


Figure 5.7. Species concentration contours at $Re = 0.01$ and $Pe = 1000$ conditions for case A at $St = 1/2\pi$ (a), $1/\pi$ (b), $3/2\pi$ (c) and case B at $St = 1/4\pi$ (d), $1/2\pi$ (e), $3/2\pi$ (f). Mixing domain is within a range of $0 \leq x \leq 24$ (6 blocks), $-1 \leq y \leq 1$ and above snapshots are obtained at $t = 20\pi$.

In figure 5.7, we present variation of M^1 as a function of the number of mixing blocks for case A at $St = 1 / \pi$ and case B at $St = 1 / 2\pi$ in a logarithmic-linear graph. Within the first 5 mixing blocks ($n \leq 5$), M^1 grows faster for case A at $St = 1 / \pi$ than case B at $St = 1 / 2\pi$. However, this growth slows down after the 5th mixing block, and case B results in better mixing efficiency for $n > 5$. Slow down of mixing for case A at $St = 1 / \pi$ is due to the regular flow regions observed in figures 5.2 (b), 5.4 (b), and 5.6 (b). Adverse effects of these regular flow zones on mixing will become more visible for higher Pe cases, where the species trapped within these zones will mix by diffusion. However, the fully chaotic case B at $St = 1 / 2\pi$ will continue homogenizing the mix exponentially even for high Pe flows. The rate of homogenization of the concentration field for high Pe values can be predicted from the statistics of stretching of multiple fluid filaments [56]. Several theoretical approaches were proposed to explain the exponential decay of passive scalar concentration in chaotic advection and in Batchelor turbulence regime [56, 57, 97]. Quantitative match between the theoretical expectation and experimental/numerically obtained value is nontrivial, and beyond the scope of this paper. In figure 5.8 (a), we plot the concentration contours obtained at four different instances within a period of excitation. In figure 5.8 (b), we show temporal evolution of M^1 for case B at $St = 1 / 2\pi$ in the 8th mixing block. M^1 varies in time due to time-periodic flow, and its fluctuations are limited within an acceptable range to guarantee a stable mixing quality at all times. The RMS value of M^1 is consistently above the requirement for 90% mixing (i.e., $M^1 = 10$). All M^1 values in figure 5.7 has achieved their corresponding statistically steady values for $Pe = 1,000$ flow. For case B at $St = 1 / 2\pi$, we observe *exponential growth* of M^1 in the stream-wise direction. A good mixer should be able to sustain this behavior with increased Pe , where the increase in Pe should be achieved by increasing Sc while keeping the flow kinematics (i.e., Re) unaltered. We performed mixing simulations within the range of $500 \leq Pe \leq 2,000$, and obtained M^1 variation

as a function of the mixing block. In figure 5.9, we present the number of mixing blocks required to achieve 90% mixing as a function of the Peclet number for case B at $St = 1 / 2\pi$. The results show $l_{m, 90} \propto \ln(Pe)$ behavior. This logarithmic dependence is expected for the *fully chaotic* state. Implications of this for mixing different Sc fluids are substantial. Based on the trends in figure 5.9, our mixer design can yield 90% mixing at $l_{m, 90} = 58H$ (i.e., within 15 mixing blocks) and $l_{m, 90} = 83H$ (i.e., within 21 mixing blocks) for $Pe = 10,000$ and $Pe = 20,000$, respectively.

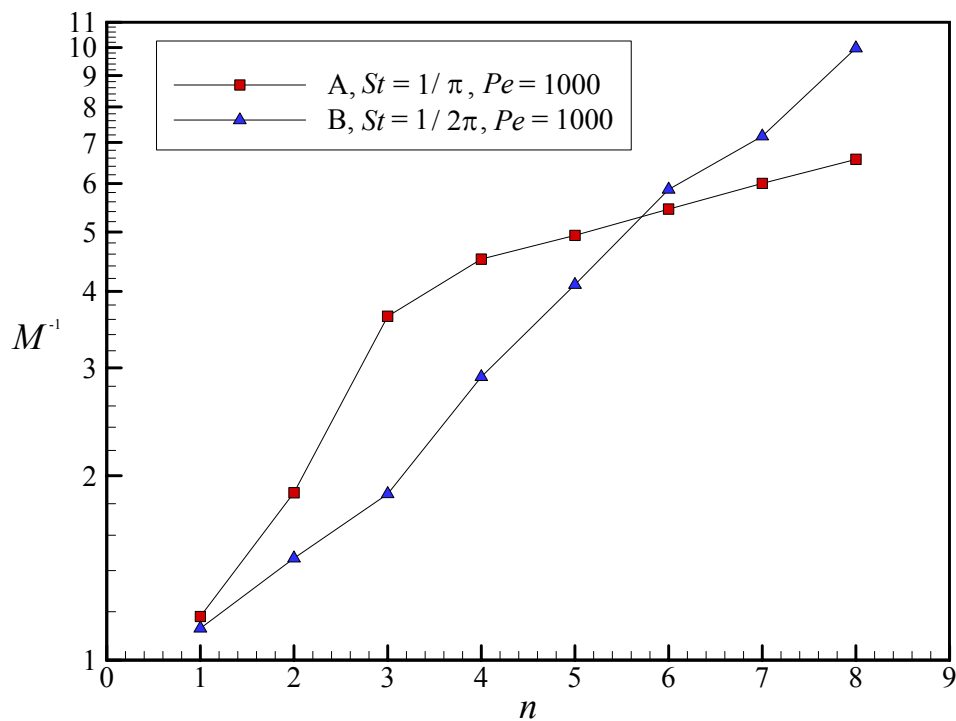


Figure 5.8. M^{-1} variation of case A at $St = 1 / \pi$ and case B at $St = 1 / 2\pi$ as a function of number of mixing blocks at $Pe = 1000$. Re is constantly set as 0.01 to keep the constant kinematic condition.

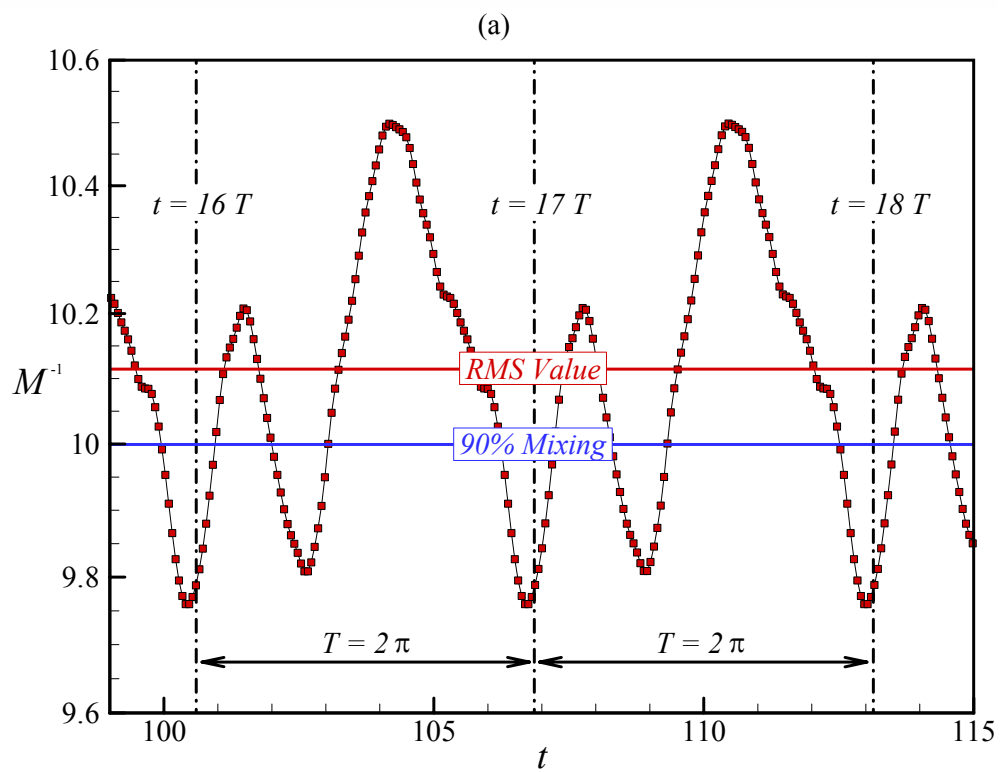
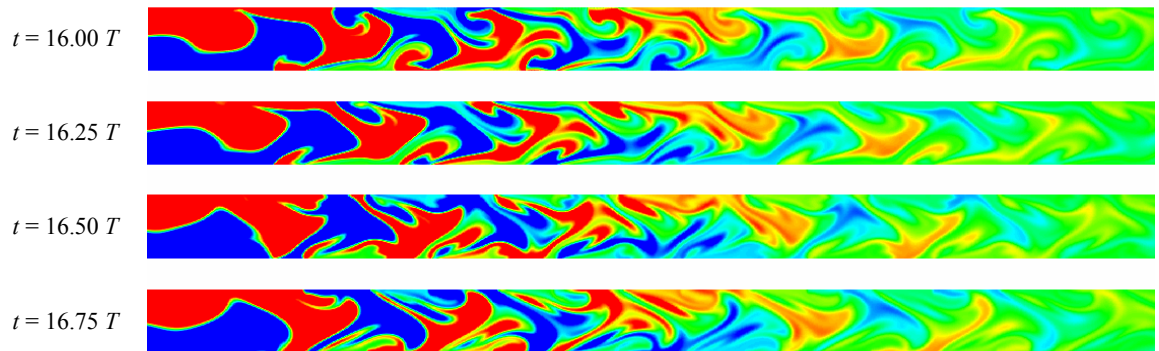


Figure 5.9. Temporal evolutions of M^{-1} of case B at $St = 1 / 2\pi$ with 8 mixing blocks. (a) a series of snapshots obtained during 1 period ($16T \leq t < 17T$) in the time interval of $0.25T$ (b) M^{-1} history exhibits that its fluctuation is limited within acceptable range. Above plots show that current mixer concept provides a stable mixing quality in high level (90% mixing).

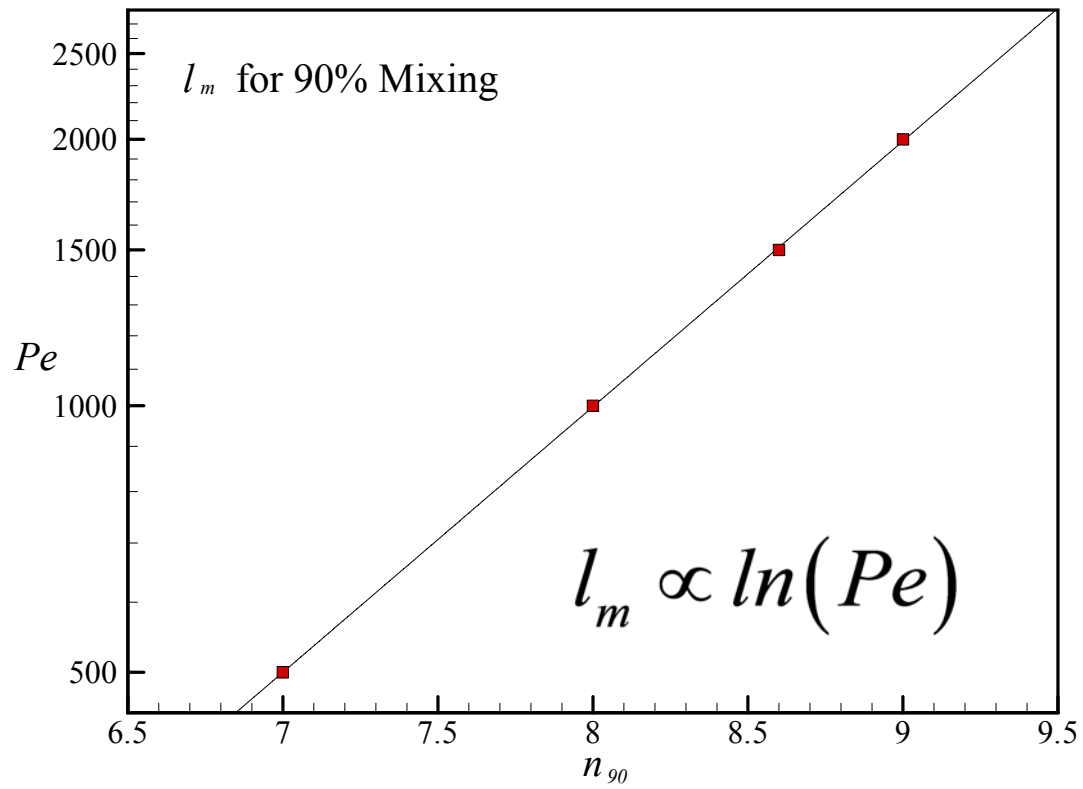


Figure 5.10. Required number of mixing blocks of case B at $St = 1 / 2\pi$ for 90% mixing with $Pe = 500, 1000, 1500$ and 2000 . Re is fixed as 0.01 .

CHAPTER VI

NUMERICAL SIMULATIONS OF CHAOTIC STIRRERS

In this chapter we present analysis of chaotic mixing in two- and three- dimensional cavity flows at $Re = 10$ and 0 (Stokes flow), respectively. In both flows closed form of analytical solutions are not available, thus numerical investigations are performed with high-order spatial discretizations by utilizing computational methods discussed in Chapter II.

6.1. Chaotic stirring in a three dimensional cavity

First, we consider particle dispersion in three-dimensional Stokes flow in a cavity. In the Stokes flow regime the flow can be assumed quasi-static, the mixing fluids considered are highly viscous and, consequently, inertia forces are negligible. Due to the absence of inertial effects, development of a strategy for efficient mixing is desired. Numerous experimental and computational studies have demonstrated that mixing in Stokes cavity flows can be enhanced by time-periodic motion of the bottom and top walls [6-8, 29]. However, most of these studies were limited to two-dimensional analysis. In addition, the authors had to utilize motions of both top and bottom walls in order to generate chaotic trajectories. In this study, by use of z -directional spatial effect, we show that efficient stirring can be achieved even when only the top wall perturbs the flow and induces mixing.

6.1.1. Computational issues

The domain of interest is $\Omega = [0, 2] \times [0, 1] \times [0, 1]$, as shown in figure 6.1 (a). In this study, the mixing is promoted by z -directional periodic oscillations of top wall, as shown in figure 6.1. The boundary conditions used here are as follows:

$$\begin{array}{l} \text{Bottom and lateral} \\ \text{walls} \end{array} \quad : \quad u_x = u_y = u_z = 0, \quad (6.1.a)$$

$$\text{Top wall} \quad : \quad u_x = 1, \quad u_y = 0, \quad u_z = f(t), \quad (6.1.b)$$

where

$$f(t) = \begin{cases} 1 & kT < t < kT + \frac{T}{2} \\ -1 & kT + \frac{T}{2} < t < (k+1) \cdot T \end{cases}. \quad (6.2)$$

where $k = 0, 1, 2, \dots$ is an integer, resulting time periodic flow fields with periodicity T . As given in the problem configurations, dropping u_z , with $L \rightarrow \infty$, flow results in a two-dimensional steady Stokes flow in a cavity, which induces poor mixing.

The time-periodic wall motions are discontinuous. Since highly viscous fluids are assumed, the Reynolds number is small, and Stokes flow equations are used, as described in Chapter II, IV, and V. Since for $d = 3$ no analytical solutions are available for the velocity field in a cavity, numerical techniques need to be applied. The Stokes equations were discretized in space and time using the algebraic factorization scheme as described in Chapter II. The initial velocity and pressure in the cavity were set to zero and the solution of the stationary Stokes equations was computed as an asymptotic case of the unsteady equations. We utilized a sixth-order nodal expansion with 16 hexahedral spectral elements. The total number of elements was fixed during the simulations.

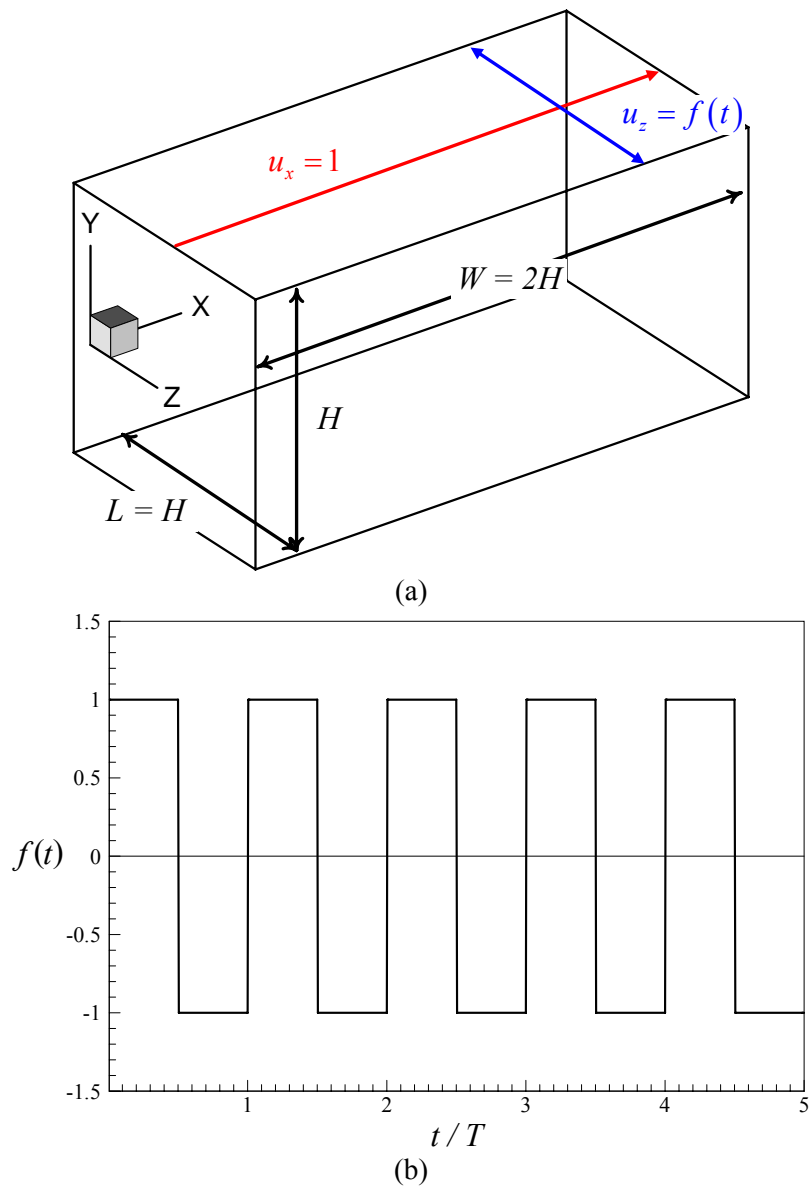


Figure 6.1. Problem configuration for the 3D cavity stirrer: (a) Boundary conditions, and (b) Time history of u_z velocities of top oscillatory lids.

6.1.2. Particle dispersion

We simulated passive tracer particles' motion to examine their behaviors as a function of T . The particles were initially placed in the form of spherical clusters (see figure 6.2 (a), 6.3 (a), and 6.4 (a)), and their Cartesian coordinates are described as below:

$$x = r \cos \frac{\theta}{n_\theta} \sin \frac{\phi}{n_\phi}, \quad y = r \sin \frac{\theta}{n_\theta} \sin \frac{\phi}{n_\phi}, \quad z = r \cos \frac{\phi}{n_\phi}, \quad (6.3)$$

where we define r to be distance (radius) from a point to the origin of the spherical cluster, θ is the azimuthal angle in the x - y plane from the x -axis with $[0, 2\pi)$, ϕ is the polar angle from the z -axis with $[0, \pi]$, and n_θ and n_ϕ are the numbers of particles along θ and ϕ , respectively. We set r to 5 % of cavity width, and $n_\theta = 150$, and $n_\phi = 300$. In numerical collocation schemes the velocity is only known at a limited number of grid points. Tracking passive tracer particles in a flow requires knowledge of the velocity of the fluid at any arbitrary point in the flow domain. Therefore interpolation of the velocity field to a set of arbitrary point is necessary, thus we employed numerical particle tracking technique introduced in Chapter IV, utilizing 4th order Runge-Kutta scheme for high-order temporal integration.

In figure 6.2, 6.3, and 6.4, we present dispersion of 90,000 particles ($45,000 \times 2$) at various times, by successively increasing T , from $T = 4$ to $T = 20$. These fluid particles follow the flow perfectly without slip (passive tracer). The color labeling (red and green) of the particles are decided according to their species. In case at $T = 4$, all particles are concentrated near the center of the stirring zone, 'void' areas (i.e. 'unmixed' zones) are observed even after a long time ($t \geq 50$). And clusters of red and green particles form twisted shapes by time periodic stirring, but cannot be shuffled at all. If passive tracer particles were initially confined in a small zone are dispersing uniformly to the whole mixing domain, and simultaneously the two different colored particles are evenly shuffled, then it can be considered as a chaotic state, which satisfies the desired condition for an efficient mixing. In case of $T = 20$, situation becomes better: particles are shuffled and the volume of dispersion occupies larger fraction than case at $T = 4$. However, case at $T = 20$ in the upper half of the square cavity the mixing is chaotic, while the quality of mixing remains poor near the bottom and side walls of the cavity. Because the stationary walls cause stagnation regions in the lateral and bottom surfaces of the cavity, additional treatments are required to allow the fluid to reach the globally chaotic state, as reported in Anderson *et al.* [30].

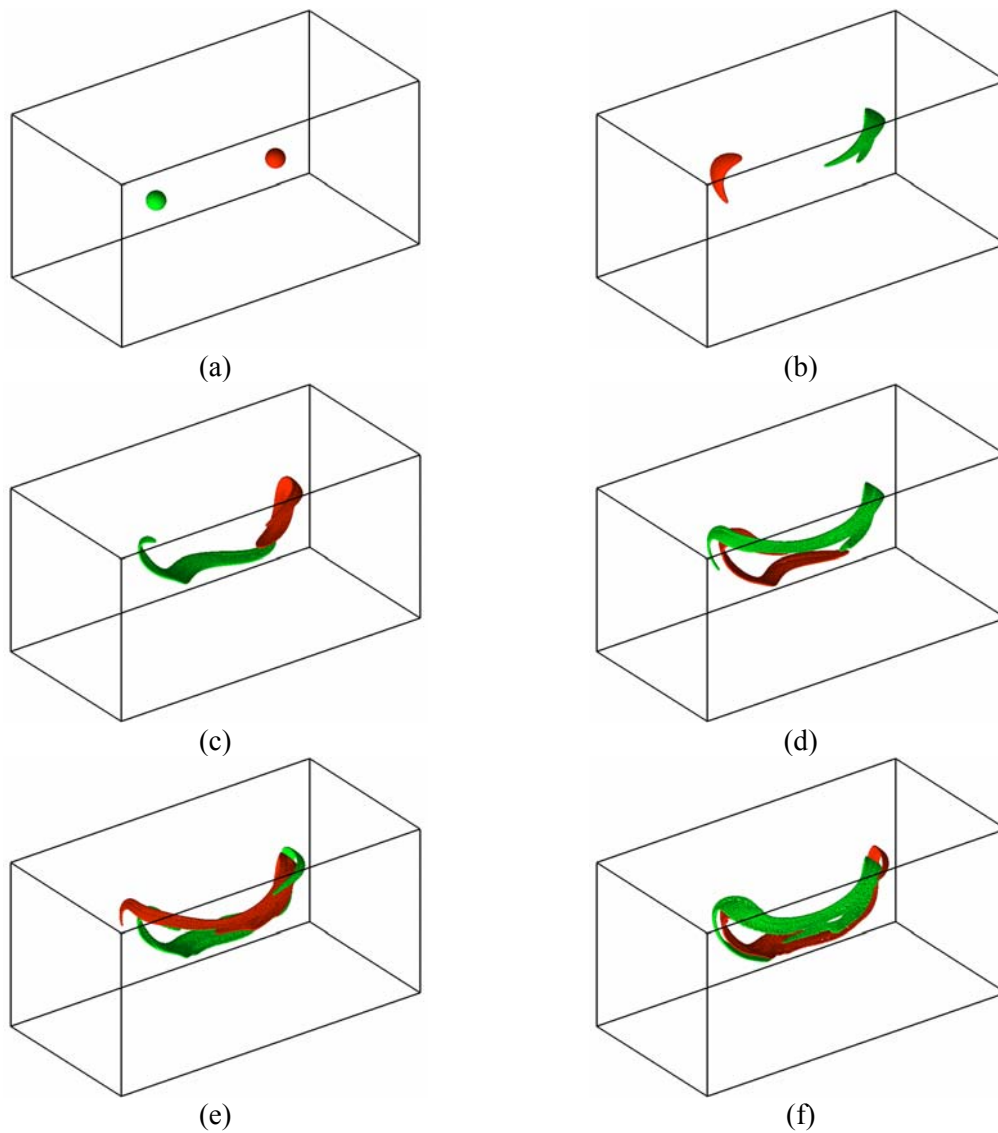


Figure 6.2. Numerical results for the three dimensional cavity stirrer: snapshots of spread of passive tracer particles for case at $T = 4$. A total of 90,000 passive particles are tracked in time. Snapshots show the dispersion state at respective times of (a) 0, (b) 10, (c) 20, (d) 30, (e) 40, and (f) 50.

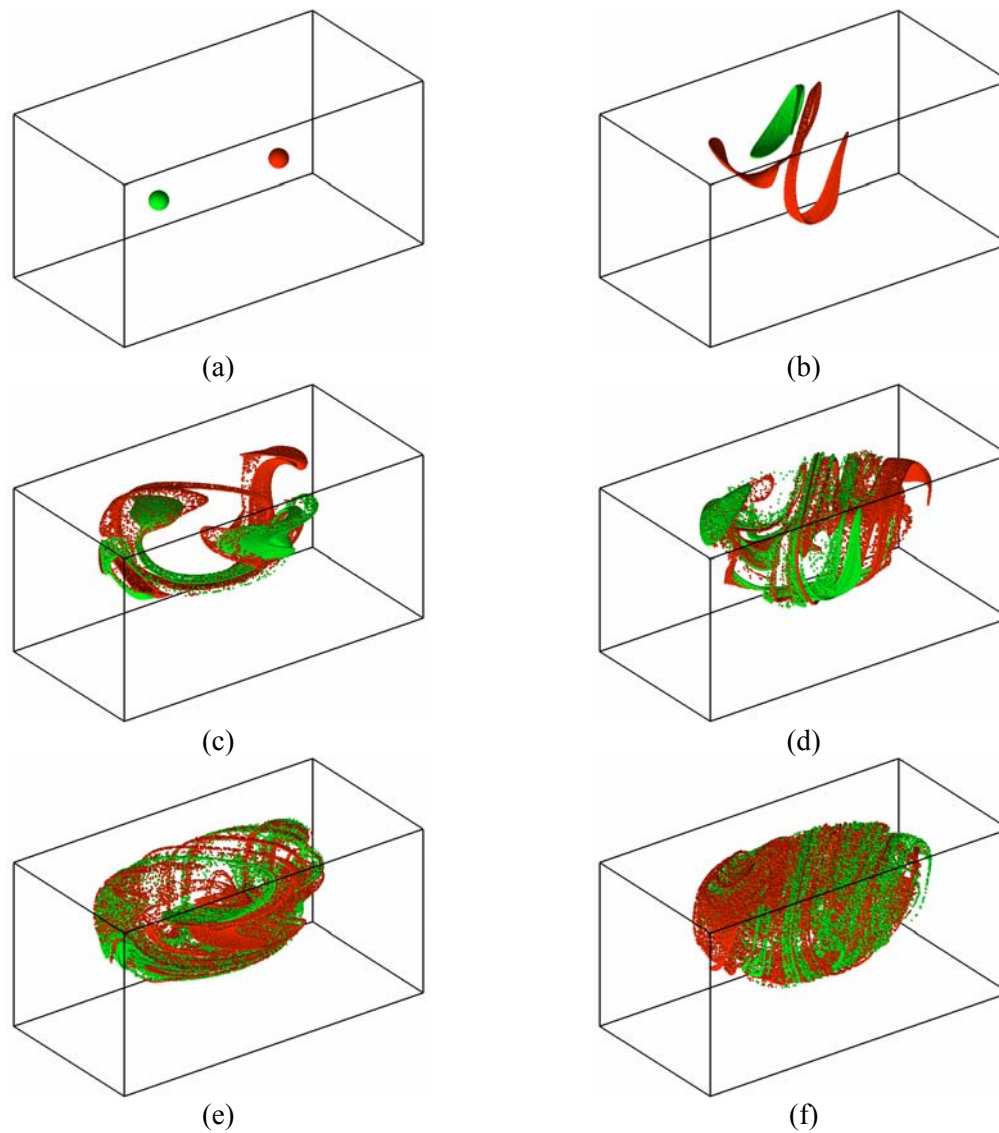


Figure 6.3. Numerical results for the three dimensional cavity stirrer: snapshots of spread of passive tracer particles for case at $T = 8$. A total of 90,000 passive particles are tracked in time. Snapshots show the dispersion state at respective times of (a) 0, (b) 10, (c) 20, (d) 30, (e) 40, and (f) 50.

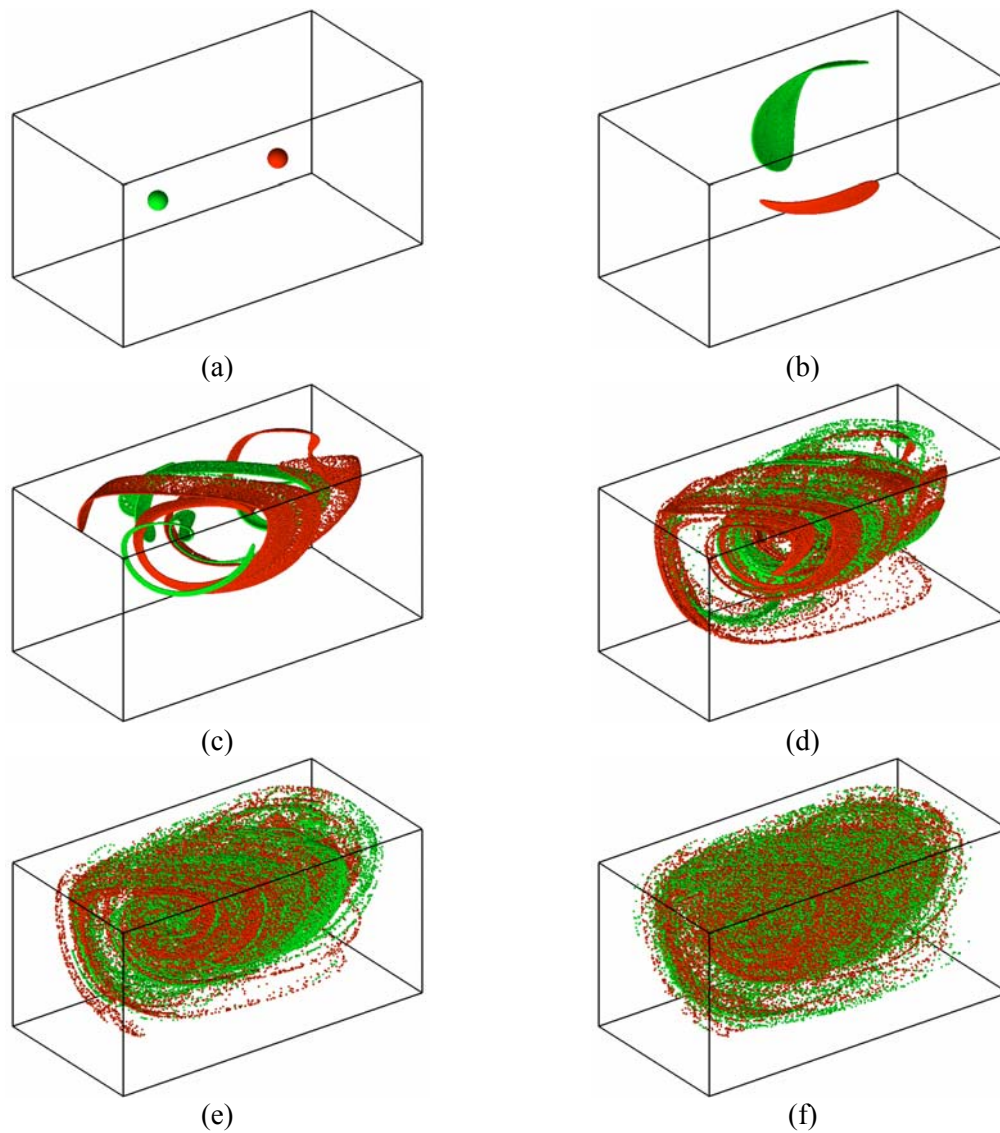


Figure 6.4. Numerical results for the three dimensional cavity stirrer: snapshots of spread of passive tracer particles for case at $T = 20$. A total of 90,000 passive particles are tracked in time. Snapshots show the dispersion state at respective times of (a) 0, (b) 10, (c) 20, (d) 30, (e) 40, and (f) 50.

6.2. Chaotic mixing of cavity flows at finite Reynolds numbers

Next we numerically examine chaotic fluid mixing in a square cavity with time-periodic excitation by moving lids. Taylor-Galerkin spectral element computations were performed for various flow parameters. Global fluid mixing is greatly promoted when an unsteady component of the velocity is superimposed on the steady flow. By utilization of high order interpolation scheme, we tracked several thousands of passive tracer particles, and found that the mixing efficiency is a function of the oscillation frequency. Extensive numerical efforts have been performed to understand the dynamics of mixing by examining the roles of periodic points [30, 108]. The hyperbolic periodic points in the flow and their associated invariant manifolds dominate the dynamics of mixing and transport. However, at the finite Reynolds number regimes, flows are not symmetric, thus the detection of periodic points can be *a big hurdle* in dynamic analyses of mixing flows.

6.2.1. Problem description

The computational domain is $\Omega = [0, 1] \times [0, 1]$, and its corresponding spectral element discretization is shown in figure 6.5 (a) and (b), respectively. We utilized an eighth-order nodal expansion with 10×10 quadrilateral spectral elements. The total number of elements was fixed during the simulation. The elemental discretization is shown by black lines, and quadrature points are shown by pink lines. In this study, we investigate mixing promoted by periodic oscillations of both top and bottom walls in a square cavity, as shown in figure 6.5 (c). The boundary conditions for $\mathbf{u} = (u_x, u_y)^T$ are given as follows:

$$\text{top wall} \quad : \quad u_x = U_{\text{top}}(t) = U \cdot (1 + P \cdot \sin(2\pi \cdot St \cdot t)), \quad u_y = 0, \quad (6.4.a)$$

$$\text{bottom wall} \quad : \quad u_x = U_{\text{bot}}(t) = U \cdot (-1 + P \cdot \sin(2\pi \cdot St \cdot t)), \quad u_y = 0, \quad (6.4.b)$$

$$\text{lateral walls} \quad : \quad u_x = 0, \quad u_y = 0, \quad (6.4.c)$$

where t is the time, U the steady component of the velocity, P amplitude of the oscillating wall velocity, and St the Strouhal number or dimensionless frequency. For scalar mixing, zero Neumann boundary conditions are used on the all walls.

The flow is described by characteristic velocity U , height of cavity H , width of cavity L , excitation frequency ω , and kinematic viscosity ν . Using dimensional analysis, we identify the following dimensionless parameters:

$$Re = \frac{UH}{\nu}, \quad St = \frac{\omega H}{U}, \quad \frac{L}{H} = 1, \quad (6.5)$$

where Re and St are the Reynolds and Strouhal numbers, and the mixer geometry is fixed as $L/H = 1$. The preliminary study considered the effects of St only. Reynolds number is restricted to $Re = 10$ and amplitude P and characteristic velocity U are set as 1. Since for $Re > 0$ no analytical solutions are available for the velocity field in a cavity with oscillatory lid velocity, numerical techniques need to be applied. By adopting Crank-Nicolson representation for the diffusion terms, and applying 2nd order Runge-Kutta for explicit evaluation of the convection terms, the Navier-Stokes equations were discretized in time using the inexact factorization scheme described in Chapter II. The initial velocity and pressure in the cavity were set to zero, and for the range of parameters investigated time-periodicity with period T is induced after a number of periodic motions, escaping from the influence of the initial conditions on velocity and pressure. Tracking passive tracer particles in a flow requires knowledge of the velocity of the fluid at any arbitrary point in the flow domain. Therefore interpolation of the velocity field to a set of arbitrary point is necessary, thus we employed numerical particle tracking technique introduced in Chapter II, utilizing 4th order Runge-Kutta scheme for high-order temporal integration.

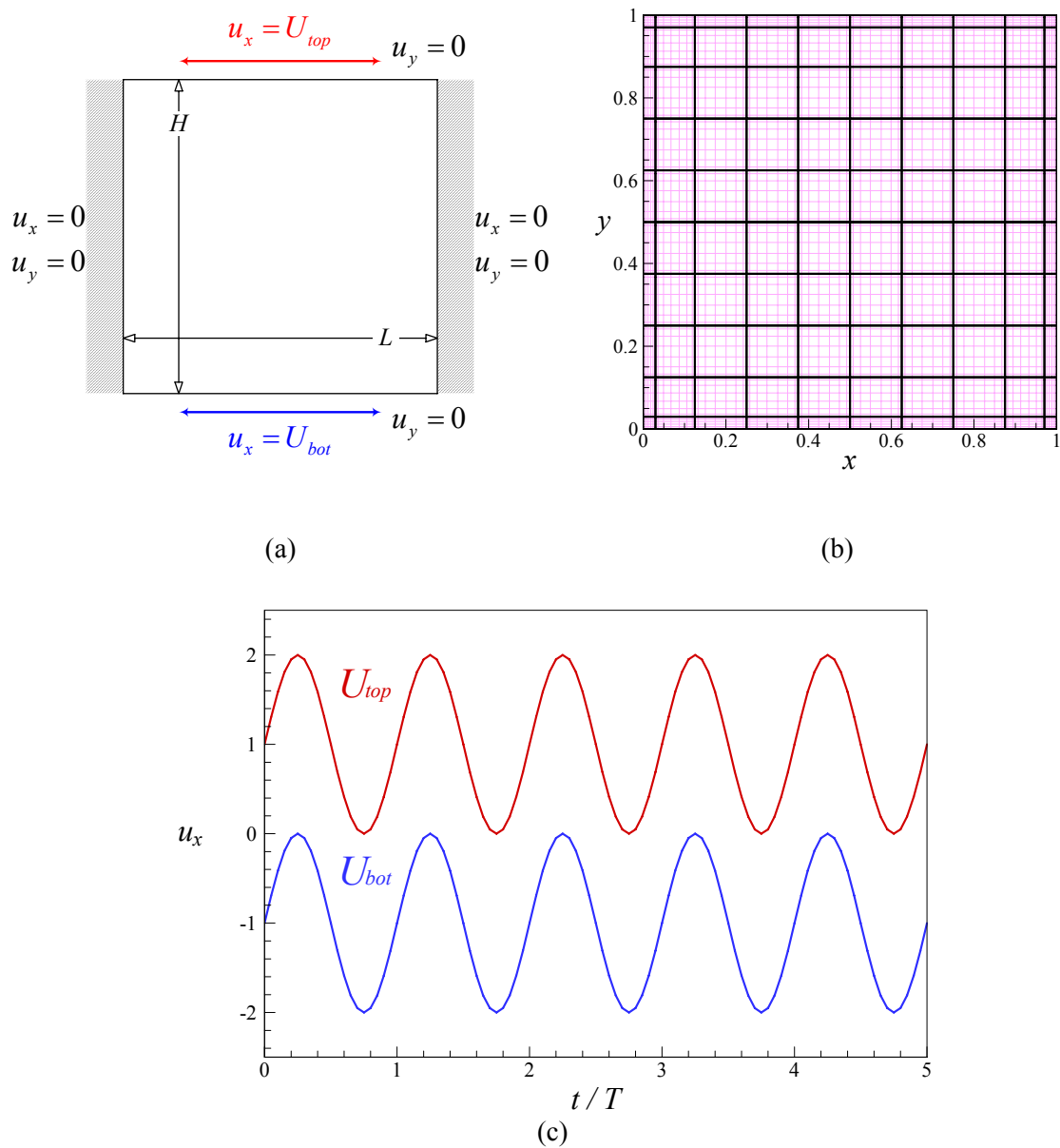


Figure 6.5. Problem configuration: (a) Boundary conditions and geometry of the cavity with time-periodic oscillatory lid velocity ($L = H$), (b) The spectral element mesh consists of 10×10 spectral elements each of 8th order yielding totally 6,561 non-uniformly distributed nodal points, (c) Time variation of the top and bottom lid velocity.

6.2.2. Optimum kinematic conditions

Uniform dispersion of particles that were initially confined in a small zone to the entire mixing domain can be considered as a well-stirred state. Simultaneously, such observations need to be quantified to obtain reasonable measures of the stirring efficiency. In order to find an optimum actuation frequency, we utilized the *box counting method* to quantify the rate at which particles are dispersed by the flow into small uniform boxes [11, 29], and calculate the *stirring index* ε , by use of rule 1 introduced in Chapter IV and [11], by sequentially increasing St .

In figure 6.6, we present the temporal evolution of the *stirring index* ε for various cases, $0.1 \leq St \leq 10$. In these cases, $N = 160,000$ particles are tracked for $t \leq 100$ in $K = 40,000$ boxes. In the figure we observe that the *stirring index* ε for case at $St = 1 / 2\pi$ reaches its asymptotic limit of unity faster than any other cases. Since all results are given as a function of time t , direct comparison between the various cases or time-period of excitation can be done, provided that the stirrer dimensions (H) and the excitation velocity (U) are fixed. Based on these results we can conclude that case excited at $St = 1 / 2\pi$ gives the best stirring state among all the selected cases. As we observe in figure 6.7 (a), particles initially located at the center has spread to cover the entire mixing domain for case at $St = 1 / 2\pi$. Such behavior is desired in an efficient stirrer [5, 11, 29, 30].

Based on above observations, scalar transport simulations are performed for mixing of a scalar marker that has concentration of $\theta = 1$ and $\theta = 0$ in the right and left halves of the domain, respectively. Therefore, the initial interface between the $\theta = 1$ and $\theta = 0$ conditions were at $x = 0.5$ along the vertical centerline, and a perfect mix would reach $\theta = 0.5$ everywhere in the domain. In this study, we fixed both the Reynolds number and varied the Peclet number. In simulations, the velocity field developed from quiescent initial conditions. Two simulation

results at $St = 1 / 2\pi$ and $2 / \pi$ are shown in figure 6.8 and 6.9, respectively. Although the velocity and pressure fields are time periodic, species transport is transient. A comparison of two cases indicates much better mixing quality for the case at $St = 1 / 2\pi$, in which the portion of well mixed regions ($\theta \approx 0.5$, violet contours) are propagated to the whole mixing domain for $t > 15$, although the Peclet number is set to a high value of $Pe = 6,000$. In order to perform quantitative estimation of mixing quality, we calculated mixing index inverse, M^{-1} , using equation (4.16), and its temporal variations for case excited at $St = 1 / 2\pi$ are plotted in figure 6.10 (a), with gradually varying the Peclet number.

In chaotic mixing, the logarithmic relation between mixing time and Pe is often investigated [11, 28, 36, 37, 61, 62]. At a fixed Re (i.e. fixed kinematic motion), Pe dependence of mixing time, t_m for fully chaotic flows is given by [10]

$$t_m \propto \ln(Pe). \quad (6.6)$$

In figure 6.10 (b), we plot the convection time of 90% mixing for case at $St = 1 / 2\pi$ by sequentially changing Pe : $3000 \leq Pe \leq 6000$. In this log-lin graph, logarithmic value of Pe is linearly scaled with convection time for the desired mixing quality, showing $\ln(Pe)$ relation. In fully chaotic state, any regular or periodic zones cannot survive. This means that the fluid filaments are stretched exponentially in any place of fluid domain, then mixing becomes insensitive to Pe . Thus, $\ln(Pe)$ behavior can be observed only in fully chaotic state due to global irregularity of chaotic trajectories [11].

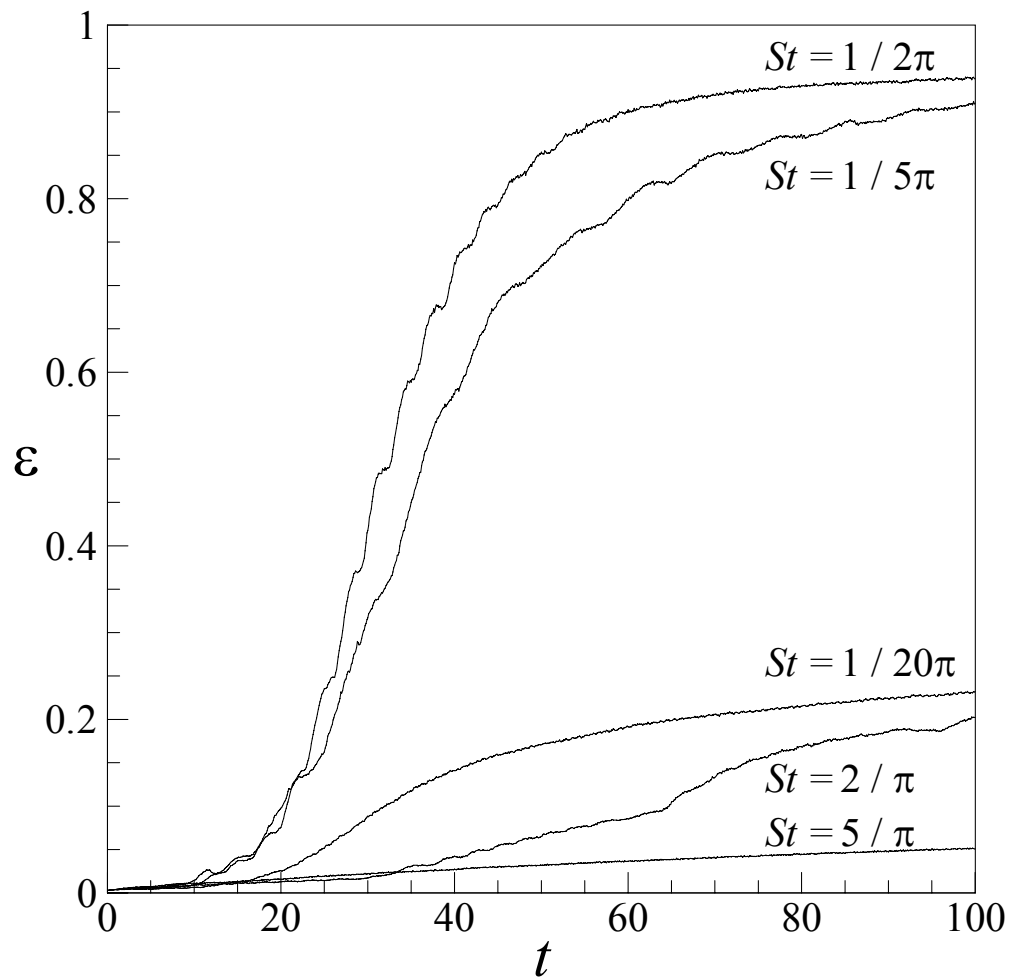


Figure 6.6. Time variation of the stirring index, ε , for cases at $1/2\pi \leq St \leq 5/\pi$ obtained by Rule #1 [11]. Only ε for case at $St = 1/2\pi$ reaches the asymptotic limit of unity.

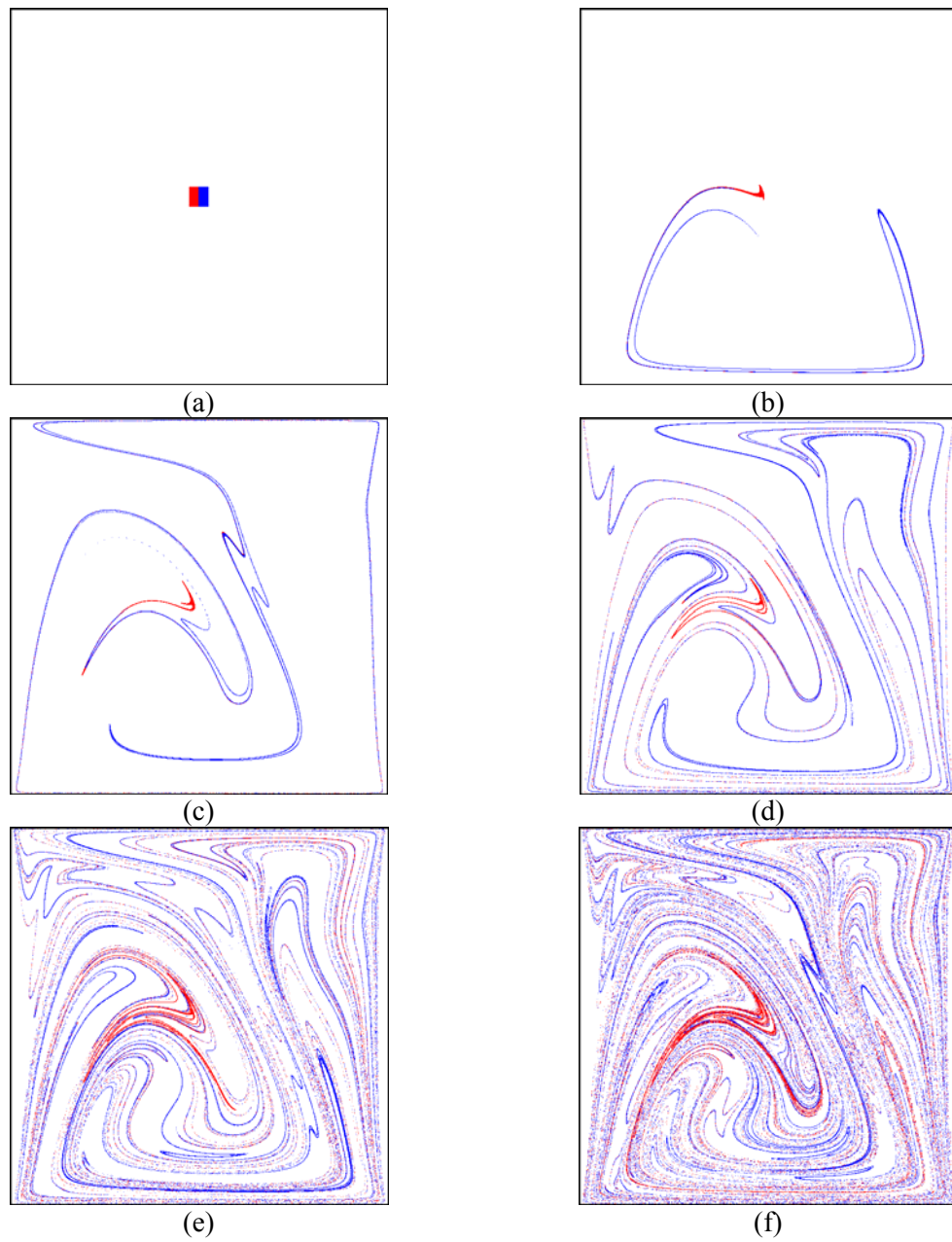


Figure 6.7. Snapshots of dispersion of passive tracer particles for case at $St = 1 / 2\pi$ obtained at (a) initial state, (b) 2 periods, (c) 3 periods, (d) 4 periods, (e) 5 periods, and (f) 6 periods.

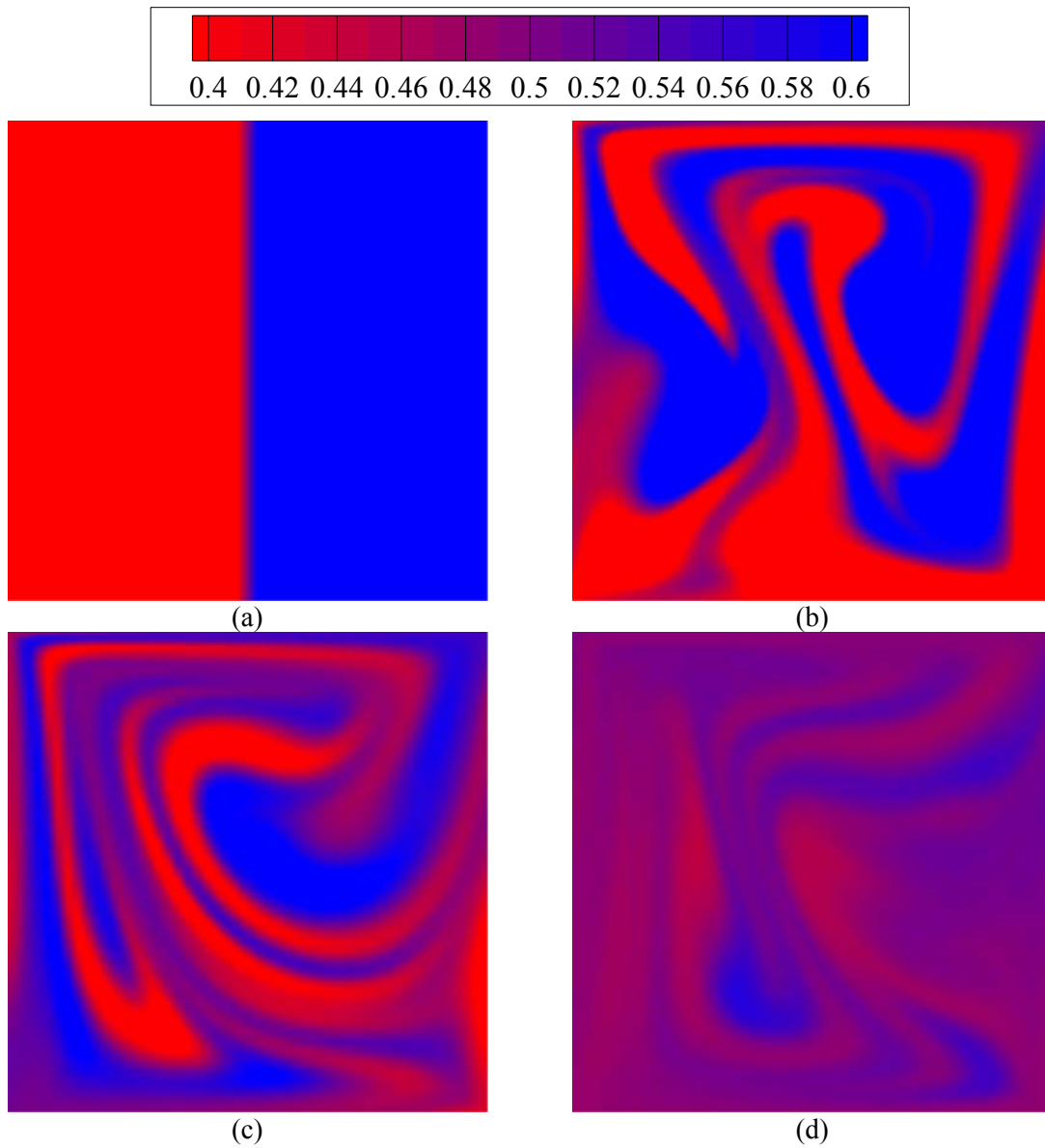


Figure 6.8. Numerical results for the oscillatory driven cavity flow: species concentration contours at $Re = 10$, $Pe = 6000$, and $St = 1 / 2\pi$. Species concentration contours at $t = 0$ (a), 10 (b), 15(c), and 20(d).

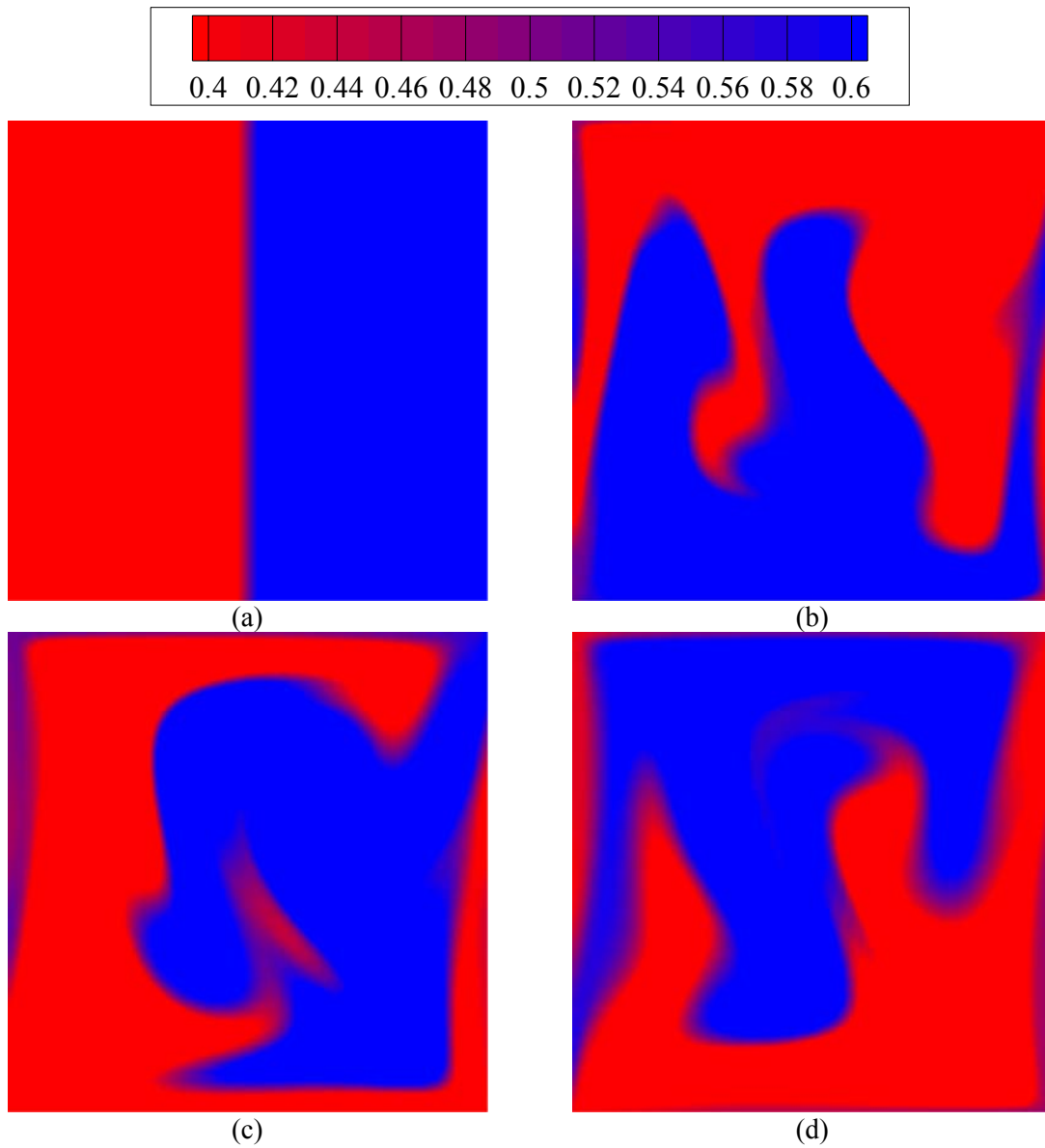
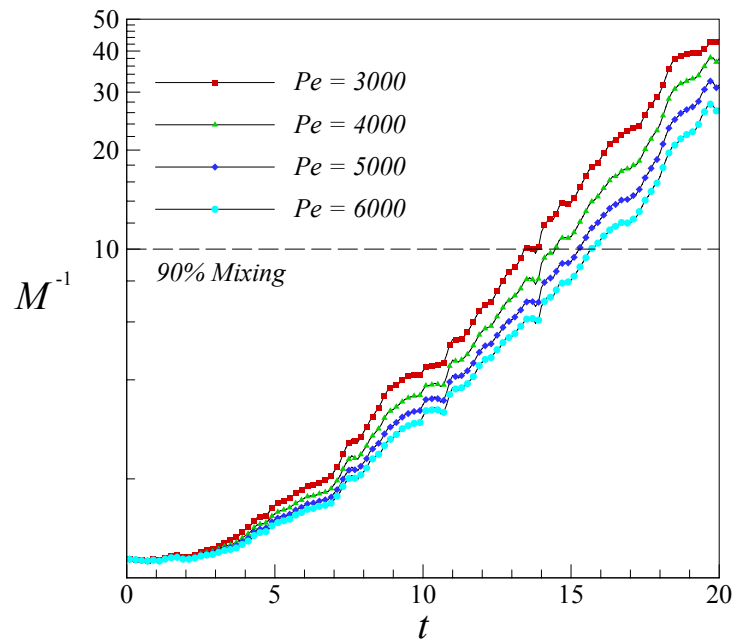
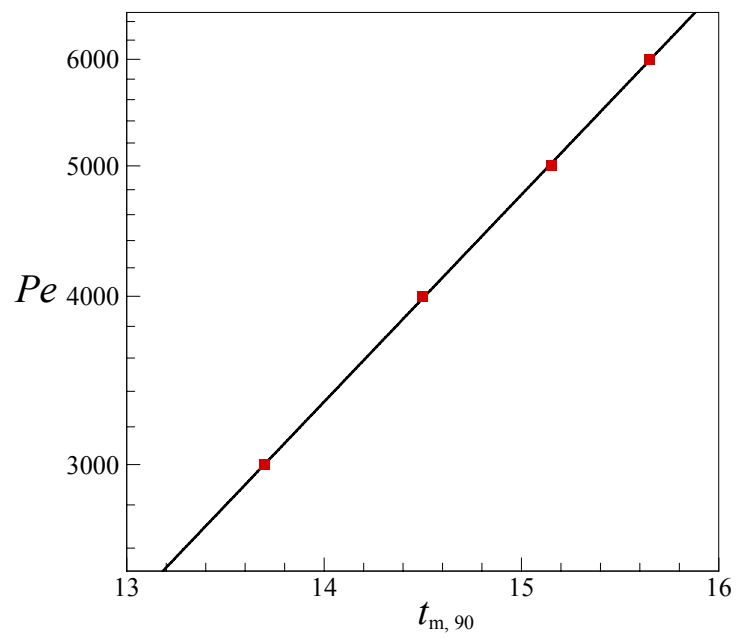


Figure 6.9. Numerical results for the oscillatory driven cavity flow: species concentration contours at $Re = 10$, $Pe = 6000$, and $St = 2 / \pi$. Species concentration contours at $t = 0$ (a), 10 (b), 15(c), and 20(d).



(a)



(b)

Figure 6.10. (a) Variation of M^{-1} as a function of time for case at $St = 1 / 2\pi$, (b) Required time t_m to achieve 90% mixing using cases at $St = 1 / 2\pi$ for various Pe values.

6.2.3. Detection of periodic points

Particle dispersion provides insight into the rate of mixing. By calculating the *stirring index* ε , and performing scalar transport simulations in a wide range of the Strouhal number, best stirring frequency was obtained. However, it is still required to perform the detailed study of dynamic skeleton to understand the relative relation between *mixing* and *advection* in chaotically stirred flows. The main characteristic of chaotic mixing can be determined by the location and nature of the periodic points [74, 109]. The hyperbolic periodic points in the flow and their associated invariant manifolds dominate the dynamics of mixing and transport. By definition, periodic points are points which return to their original points after one or more periods of *periodic* oscillation. A periodic point \mathbf{X}_p of order n is defined as:

$$\Phi_{nT}(\mathbf{X}_p) = \mathbf{X}_p, \quad (6.7.a)$$

$$\Phi_{mT}(\mathbf{X}_p) \neq \mathbf{X}_p, \text{ for } m < n, \quad (6.7.b)$$

$$\Phi_T(\mathbf{X}) = \int_{n-T}^{(n+1)T} \mathbf{u}(t, \mathbf{X}) dt + \mathbf{X}_0, \quad (6.7.c)$$

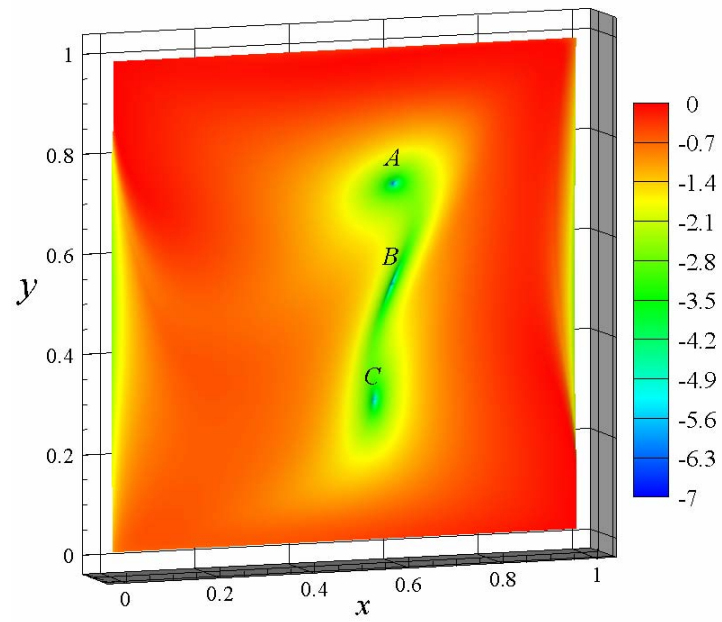
where Poincaré mapping Φ is defined in equation (4.8), T is the duration of one period of motion. At the finite Reynolds number regimes, flows are not symmetric, thus detection of periodic points can be challenging in dynamic analyses of mixing. In determination of the positions of periodic points, the technique developed by Anderson *et al.* was employed [30, 108]. Their method is based on an analysis of displacement and stretching over one period. The displacement function is defined as

$$d(\mathbf{X}) = \|\mathbf{X} - \Phi_T(\mathbf{X})\|_2, \quad (6.8.a)$$

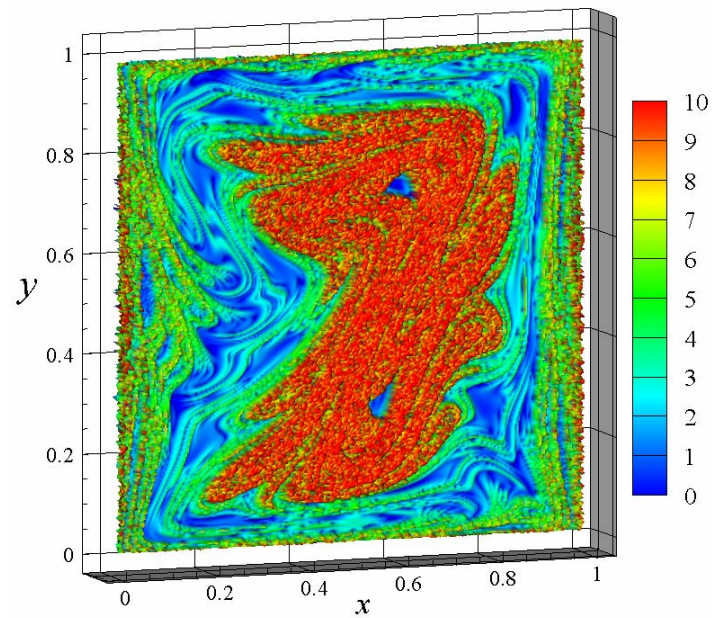
$$d(\mathbf{X}_p) = \|\mathbf{X}_p - \Phi_T(\mathbf{X}_p)\|_2 = 0, \quad (6.8.b)$$

where $\|\cdot\|_2$ is the Euclidean norm, \mathbf{X} denotes any arbitrary point, and \mathbf{X}_p refers to a periodic point. The method used to locate periodic points is essentially based on finding the roots of $d(\mathbf{X}) = 0$ in equation (6.8.b), where $\mathbf{X} = \mathbf{X}_p$. Analysis of marker displacement on a coarse grid over one period should be performed to find an initial guess for the local minima of displacement. Following Anderson *et al.* [30, 108], by utilizing a sequence of finer grids around the local minima, accurate positions of the periodic points were obtained. In figure 6.11 (a), logarithmic values of $d(\mathbf{X})$ of case at $St = 0.5$ are plotted on the initial grid of \mathbf{X} . A grid of 90,000 (300×300) initial points was uniformly placed in the cavity, not touching the solid boundaries. After tracking of one period, three periodic points (A, B, and C) are found with $d(\mathbf{X}) < 10^{-7}$ in the vicinity of the vertical centerline of cavity.

On the same grid of initial positions, the net stretching h defined in equation (4.14) was computed by numerical integration of equation (4.13), as discussed in Chapter IV. In figure 6.11 (b), we present the stretching contours for case at $St = 0.5$ with h values obtained at time $t = 100$. In the figure, x and y are the horizontal and vertical coordinates of the *initial positions* of fluid filaments, while depth indicates h . Periodic points are classified according to the nature of the deformation in their neighborhood. Elliptic (stable) periodic points are at the center of non-mixing rotating regions, called islands, while hyperbolic (unstable) periodic points are centers of stretching in the flow. Since there is only low stretching around the periodic points A and C, it is concluded that the nature of these points is elliptic, while hyperbolic periodic point B, located in the high stretching region, is a hyperbolic periodic point.



(a)



(b)

Figure 6.11. (a) Contour plot of logarithmic values of $d(\mathbf{X})$ of $St = 0.5$ case, (b) Contour plot of $\ln(h)$ for $St = 0.5$ case; Periodic point B is located inside the high stretching zone, while periodic points A and C are located inside the low stretching zones.

6.2.4. Invariant manifold and fast mixing

Periodic points and their associated invariant manifolds are the fundamental components of chaotic mixing patterns [74]. As demonstrated above, elliptic points at the center of non-mixing regions are called regular islands, while the hyperbolic points are centers of stretching and folding. In this section we show that the manifold structures of hyperbolic periodic points are responsible for the advection pattern of material elements, which is central to the understanding of the dynamics of fast mixing, as reported in Jana *et al.* [110]. The invariant manifolds can be categorized into stable and unstable sets by their real parts of eigenvalues of deformation matrix. In order to define invariant manifolds invariant sets E^s and E^u first need to be defined as below [109]:

$$E^s = \left\{ \begin{array}{l} \text{space spanned by eigenvectors corresponding to} \\ \text{eigenvalues whose real part} < 0 \end{array} \right\}, \quad (6.9.a)$$

$$E^u = \left\{ \begin{array}{l} \text{space spanned by eigenvectors corresponding to} \\ \text{eigenvalues whose real part} > 0 \end{array} \right\}, \quad (6.9.b)$$

and their subsets are [109]:

$$W^s(\mathbf{X}_p) = \left\{ \text{all } \mathbf{X} \in \mathfrak{R}^d \text{ such that } \Phi_t(\mathbf{X}) \rightarrow \mathbf{X}_p \text{ as } t \rightarrow \infty \right\}, \quad (6.10.a)$$

$$W^u(\mathbf{X}_p) = \left\{ \text{all } \mathbf{X} \in \mathfrak{R}^d \text{ such that } \Phi_t(\mathbf{X}) \rightarrow \mathbf{X}_p \text{ as } t \rightarrow -\infty \right\}, \quad (6.10.b)$$

where W^s denotes the stable manifold and W^u refers to the unstable manifold, whose physical meaning is described in figure 6.12 (a). A necessary condition for chaos is the crossing of the streamline patterns at two successive times to produce either homoclinic tangles from the intersections of the stable and unstable manifolds of the same hyperbolic point, as depicted in figure 6.12 (b), or heteroclinic tangles from the intersections of the unstable manifold of one hyperbolic point with the stable manifold of another. These tangles induce extreme sensitivity to

the initial conditions, and a consequent inability to predict the outcome of evolution in a chaotic system [10, 102].

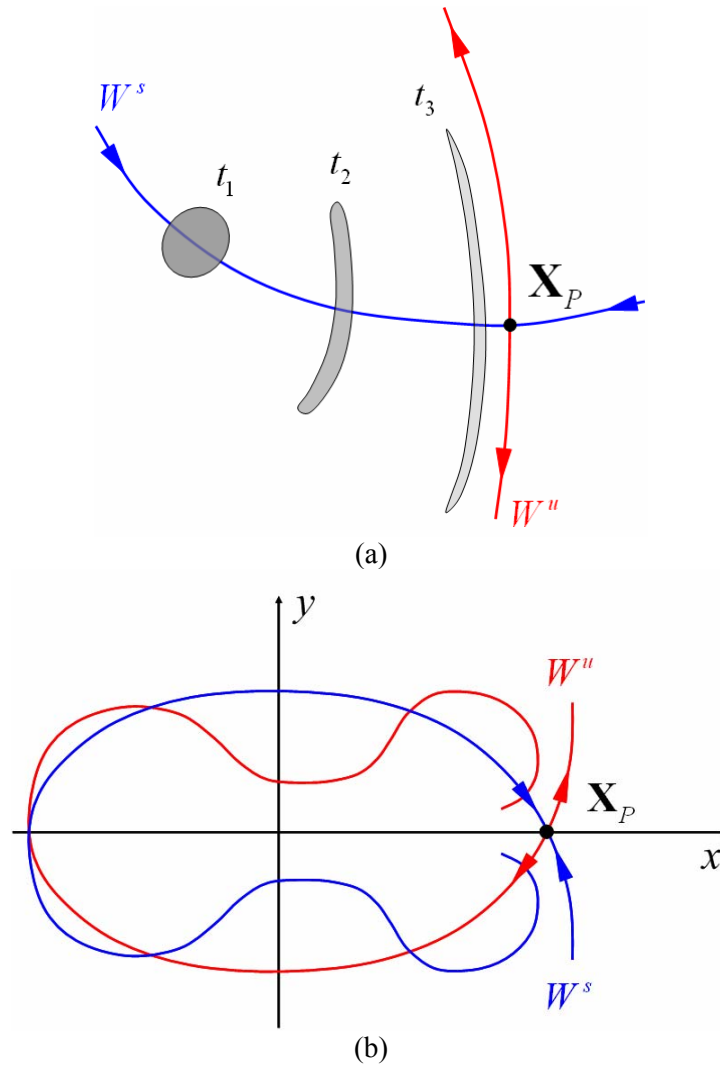


Figure 6.12. (a) Schematics of a droplet converging to an unstable manifold at times t_1 , t_2 , and t_3 , (b) Homoclinic tangle between the stable and unstable manifolds.

In almost all cases, only a few or one of the lower-order hyperbolic periodic points contribute to creation of the mixing template, while the other hyperbolic points add to the fine structure [110, 111]. Therefore, the extent of the main unstable manifold determines if the flow globally mixes. Because of the *highly ramified nature* of the tangled manifold [109], the total length of invariant manifold is infinite, but this infinite length is packed into a subdomain of the mixer [110], and consequently, globally chaotic flow makes the fractal dimension of invariant manifold closer to the spatial dimensions of mixer. Good mixing flows have their mixing template extended throughout the flow domain. It is commonly known that the manifold of period-1 hyperbolic point is the most important to the mixing character of the flow. Thus we extract unstable manifold using periodic point information of case at $St = 0.5$, and examine the role of unstable manifold in highly mixed regions. In this study, we consider only case at $St = 0.5$, because, as discussed above, this case is at a partially chaotic state such that it is possible to observe mixing characteristics in regular regions and chaotic regimes, simultaneously.

It is reported that the manifolds of the periodic points can be used in determination of the shape of the dye striation in the chaotic region [111]. In order to extract the manifold structure of unstable resonant orbit of a particular hyperbolic periodic point, particles surrounding the hyperbolic periodic point are tracked during several periods, as shown in figure 6.13 (a). Originally circular cluster of particles will be *exponentially* stretched along the unstable manifold, and at the same time, squeezed along the stable manifold, but will always surround *segments* of both the stable and unstable manifolds. After a certain number of periods (depending on the initial radius of the circle surrounding the periodic point) the circle will appear as a single curve surrounding part of the unstable manifold. Note that manifolds are infinitely long [109] and this method will only show a segment of the unstable manifold. As described above, the initial circle must be represented as a collection of discrete points. Thus, we tracked a large

amount of passive tracer particles ($N = 10^6$) in order to properly represent the evolving shape of the initially circular region under exponential stretching near the unstable manifold. Such a computational load inherently comes from the method of computation because we are interested in stretching of the circle to several orders of magnitudes larger than its initial radius.

As shown in figure 6.13, after just a few flow periods, a complex structure emerges, closely resembling the unstable manifold of the hyperbolic periodic point B in figure 6.11 (a). The structure continues evolving as the number of periods increases, while the lamellae become increasingly thinner as the result of a complex iterative process. Figure 6.13 depicts that the evolution of the structure is governed by *intrinsic self similarity*, except that a larger number of thinner striations is found each region. Self-similar structure evolved along the unstable manifold enforces time periodicity of mixing. Mixing occurs as a combination of stirring, stretching, and folding, which generates intricate lamellar structures with wide distribution of length scales that span many orders of magnitude [112]. Controlling the concentration gradients normal to striations, the length scales of stretched fluid filaments characterize the rates of diffusional homogenization at small scales of the flow. Unstable manifold passes through the regions populated by particles experiencing the high stretching values correspond to the regions of fast diffusional homogenization in the case of the species transport simulations. Therefore, the unstable manifolds of hyperbolic invariant sets of flow field form the spatial template which organizes the transport and mixing processes. In figure 6.14, in order to clearly observe the difference of stirring state between the fast mixing zones and non-mixed zones, we initially filled

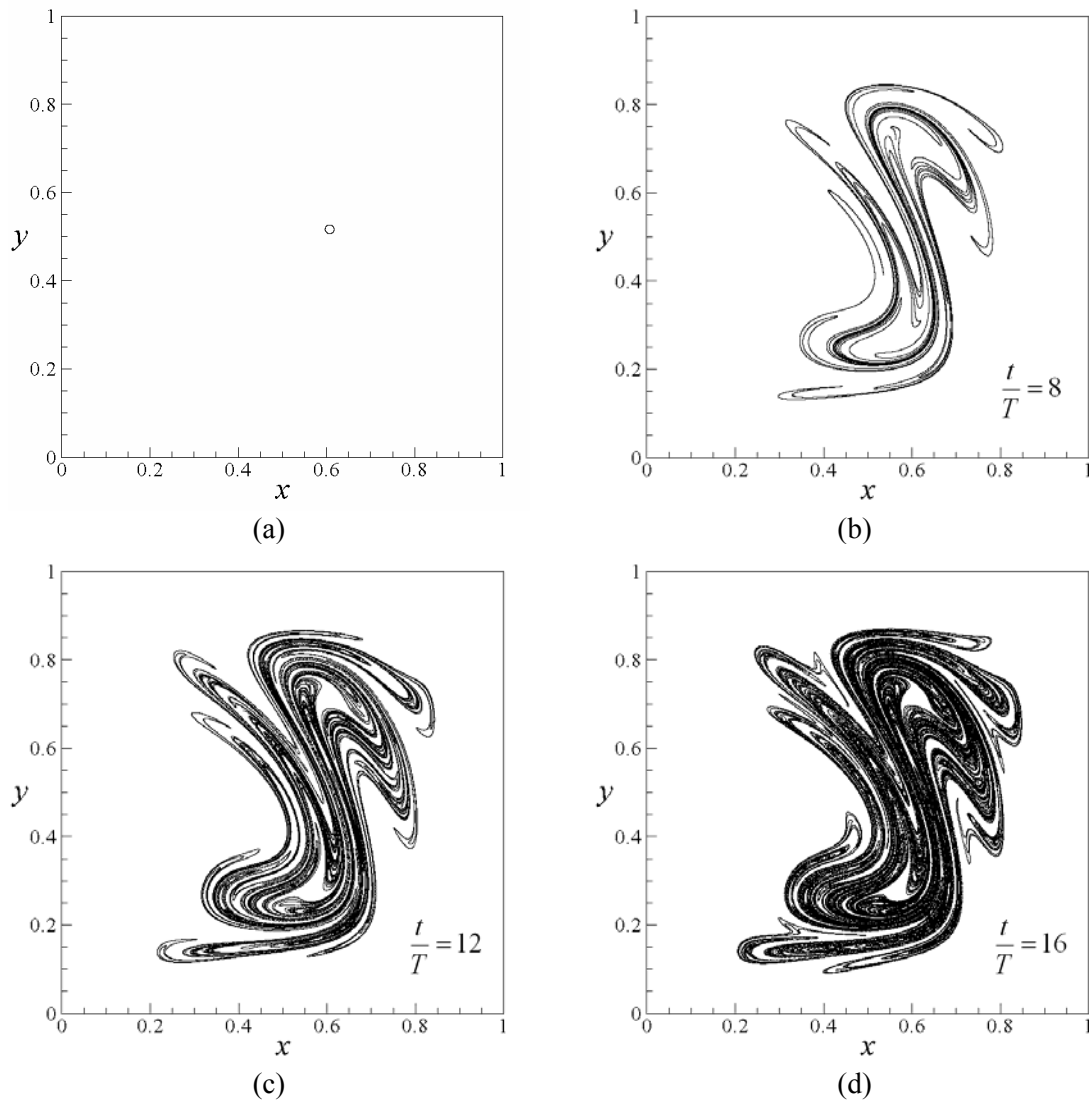


Figure 6.13. (a) Initial circle of points to be tracked for the calculation of unstable manifold: The circle surrounds the hyperbolic periodic point B . Segments of unstable manifold of $St = 0.5$ case is numerically computed at (b) $t/T = 8$, (c) $t/T = 12$, and (d) $t/T = 16$. As time increases, the chaotic flow produces a dynamic template, which is essentially identical to the structure recorded a period earlier, except that a larger number of thinner striations is found in each region.

the cavity with 160,000 particles, which depending on their species, are labeled with a specific color. And the color is inherent to a particle. As shown in figure 6.14, when dispersion of particle is recorded at periodic intervals, well mixed zones between two colored particles sustain temporal periodicity, being controlled by the dynamic template or partially mixed structure [113]. A comparison between figures 6.13 (d) and 6.14 (d) demonstrates very good agreement between the shape of manifold and the distribution of the mixing zones.

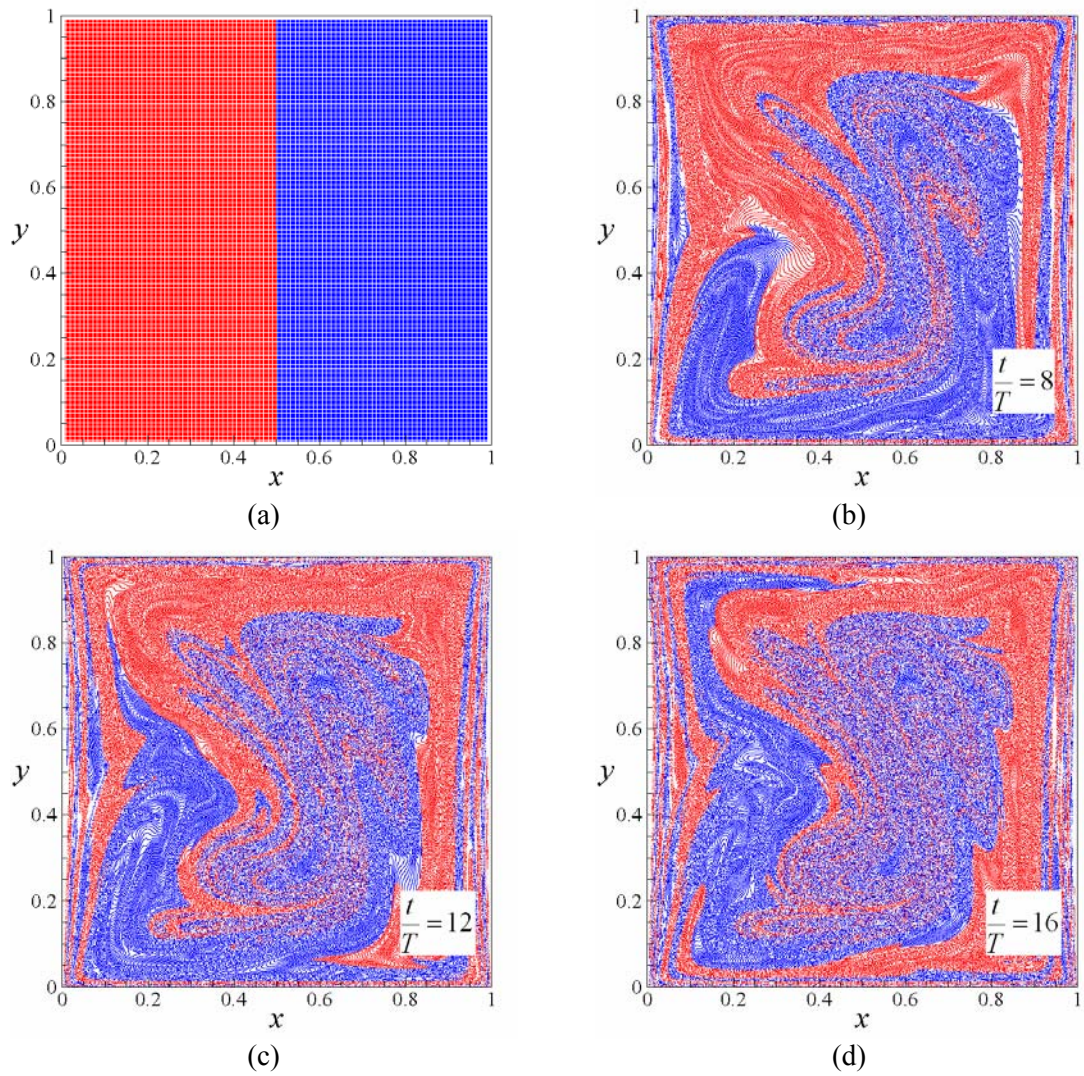


Figure 6.14. (a) Initial positions of colored particles at $t/T = 0$. Tracking results of $St = 0.5$ case are obtained at (b) $t/T = 8$, (c) $t/T = 12$, and (d) $t/T = 16$.

CHAPTER VII

SUMMARY AND DISCUSSION

In this dissertation we presented theoretical and numerical studies of chaotic mixing. In order to achieve both numerical accuracy and efficiency, a spectral element code is developed in Chapter II. In Chapter III, we solved the incompressible flow problems on the structured and unstructured spectral element grids. Several code verification examples are demonstrated, including the singular lid driven cavity flow at $Re = 1000$, flow over a backward facing step at various Re , Karman vortex shedding problems, and flows induced by natural convection in a square enclosure. In addition, the nonconforming technique which we have introduced in this dissertation has been developed to improve the efficiency of classical spectral element methods. The procedure is straightforward and simple, yet strong and efficient. In Chapter IV, using the newly developed numerical techniques discussed in Chapter II, we performed comparative studies of five different diagnosis techniques based on the chaos theory, in order to demonstrate the competitive advantages and shortcomings of each method. In Chapter V, we proposed the newly designed chaotically stirred continuous mixer employed in the micro scale straight channel. Finally, in Chapter VI, it is numerically examined how invariant manifold is associated with chaotic mixing in oscillatory flows in a square cavity at the finite Reynolds number regime.

7.1. Quantification of chaotic strength and mixing in a microfluidic system

In Chapter IV, laminar fluid mixing and scalar transport in micro channels are examined using five different methods for qualitative and quantitative estimations of chaotic stirring and its effects on mixing. The computational cost increases sequentially from the box counting method to Poincaré section, finite time Lyapunov exponent, *PDF* of the stretching field and mixing index methods, respectively. All methods require enhanced numerical accuracy, since spatial and temporal discretization errors may accumulate and lead to smearing of subtle features, such as the KAM boundaries.

The box-counting method, utilizing dispersion of passive tracer particles, enables quantification of the mixing efficiency at various flow conditions. However, the method cannot determine presence of chaos or the chaotic strength. Despite this deficiency, it can be utilized in experimental studies, provided that the particle size, inertia and particle-fluid, particle-particle and particle-solid interactions are characterized. In addition, this method can only be used for mixing quantification in closed domains.

The Poincaré sections allow detection of bad mixing zones, such as islands. Regular islands retard the exponential stretching, and the positions of islands are revealed as *non-dispersing* or *periodic* zones in the Poincaré section. Regular periodic zones are isolated from irregular chaotic zones and make recognizable geometrical shapes. Therefore, bad mixing zones can be determined through a quantitative estimation. However, Poincaré sections can not differentiate the stirring performance for featureless states as shown in figure 4.4. Despite these caveats, it is possible to seed the flow with particles and create Poincaré sections using stroboscopic images of the particles at various time periods. However, the method is inappropriate for unsteady or aperiodic flows, and further challenges exist in compensation of

three dimensionality effects and for continuous flow mixers, where the particles are not confined to a closed domain.

The finite time Lyapunov exponent, $FTLE$, overcomes the shortcomings of Poincaré sections. Positive $FTLE$ values indicate existence of chaos, and determine the chaotic strength. The $FTLE$ value depends on the initial position of passive tracer particles. Therefore $FTLE$ contours can be drawn using a series of particles, and the results identify the regular and chaotic flow zones. The computational cost for calculation of $FTLE$ is approximately double the cost for the Poincaré sections, since the method requires utilization of two initially close particles for each calculation event. Despite its great theoretical value, the $FTLE$ cannot be measured directly in experiments, since it is impossible to control the motion of particles dispersed in the mixing domain. Although, the $FTLE$ values can be calculated after the velocity field is measured using a micro-PIV or an equivalent technique, accuracy of the velocity measurements may affect the result significantly; especially for time-dependent flows, such as the case presented in this dissertation [114, 115].

As an alternative to measuring the $FTLE$, PDF of the stretching field provides physical interpretations in mixing studies. In the globally chaotic state, H_n has only one peak in the high stretching region, forming a Gaussian distribution. However, in non-globally chaotic cases, due to the existence of KAM boundaries, H_n can have sub-peaks in the low stretching region. This method provides overall insights of chaotic advection, but it is computational more expensive than the $FTLE$. In addition, it is difficult to calculate stretching in the mixing domain with complex geometry, since it is difficult to divide the entire domain into small “*equiprobabilistic bins*”. The PDF of stretching can be calculated after experimental measurement of the velocity field. However, accuracy of velocity field measurements can be of concern, since these directly affect the H_n values.

Mixing index inverse (M^{-1}) based on the numerical solution of the species transport equations has utmost relevance to the experimental measurements. Numerical calculation of M^{-1} requires species concentration value at every grid point, while the fluorescence intensity values of molecular dyes obtained via a CCD camera are often utilized for experiments. The M^{-1} value indicates standard deviation of the species distribution in the mixer, which increases exponentially in time even for *regular* cases. However the time rate of change of the M^{-1} increases with enhanced mixing efficiency, and it is maximized for chaotically stirred cases. The mixing time (t_m) required to achieve a desired M^{-1} value exhibits $t_m \propto \ln(Pe)$ for fully chaotic, $t_m \propto Pe^\alpha$ with $\alpha < 0.5$ for partially-chaotic and $\alpha = 0.5$ for regular cases. It is interesting to notice that if regularity is preserved even in small parts of the mixing domain, the mixing time does not scale as $\ln(Pe)$, but exhibit Pe^α behavior. These trends are verified using the *FTLE* values, Poincaré sections and the stretching field analysis. Determination of the Pe dependence of mixing time requires a series of simulations (or experiments) where Pe is increased systematically without altering the flow kinematics (i.e., fixed Re). Simulation of large Pe cases become computationally expensive, and may become prohibitive for $Pe > 10^4$.

Finally, our studies enabled identification of the locally optimized operation conditions for the electrokinetic stirrer of Qian and Bau [2], which exhibits globally chaotic stirring using pattern B&C with time period of $T = 6$, and results in the $t_m \propto \ln(Pe)$ behavior. The stirrer design is unique from the perspective of being able to obtain globally chaotic motion in a microfluidic channel. Spatially periodic side surfaces and zeta potential patterned top and bottom surfaces do not allow any dead flow zones, even near the corners (See figure 4.1). Although this feature may be jeopardized for an actual three-dimensional geometry, most designs with stagnant flow zones would exhibit $t_m \propto Pe^\alpha$ scaling, even if there is chaotic stirring for most parts of the mixer. This subtle point needs to be considered in the design of micro-mixers.

7.2. An electroosmotically stirred continuous flow micro-mixer

In Chapter V, we present detailed analysis of a chaotically stirred continuous micro mixer, conceptually designed and optimized using the diagnosis tools based on the chaos theory. The mixer utilizes zeta potential patterned surfaces and an axially applied AC electric field, which creates time-dependent electroosmotic flow. This is superposed with a steady pressure driven flow that maintains the desired flow rate. In the current study, we kept the kinematic condition a constant at $Re = 0.01$, and characterized the mixing length as a function of the Peclet number by varying the Sc . Varying the Reynolds number would have altered the flow kinematics, and unfavorably affect the mixing characteristics can be observed properly.

Three different diagnostic tools based on the Lagrangian particle tracking of passive tracers are utilized to observe and quantify stirring induced by the design. In particle dispersion simulations, we tracked hundreds of thousands of particles in the channel. Along the channel length, case A at $St = 1 / \pi$ and case B at $St = 1 / 2\pi$ exhibit chaotic motions, forming lobe-like structure patterns. Their dramatic morphological changes of material lines represent the evolution of an interfacial layer in mixing. However, case A at $St = 1 / \pi$ fails to achieve global dispersion, remaining hollow zones, while in case B at $St = 1 / 2\pi$, mixing blocks in down stream are fully filled with passive tracers. Poincaré section analysis is performed to identify regular and chaotic regions for different AC frequencies. Chaotic regions appear as a random array of dots while regular regions are indicated by the presence of well-defined invariant curves - KAM boundaries in the flow. Poincaré section for case A at $St = 1 / \pi$ provides consistency with the dispersion results, qualitatively proving the existence of KAM boundaries. A similar consistency is obtained in case B at $St = 1 / 2\pi$. However, in case B at $St = 1 / 2\pi$, whole domain of Poincaré section is filled with scattered dots and consequently, it is concluded that this case is dominated

under the globally chaotic state. Although Poincaré section enables to provide an intuitive qualitative result, it is often desired to perform extremely long time integration of passive tracer's motion in order to make regular and chaotic territories visible on the Poincaré section. Consequently, integration time usually exceeds physical diffusion time scale and final position of passive tracer can overshoot general channel length. In addition, it is impossible to distinguish higher chaotic strength once Poincaré section becomes featureless. To avoid these drawbacks, we investigate distribution of stretching values. Distribution of stretching values provides physical interpretations in mixing studies. Due to the existence of KAM boundaries, H_n for case A at $St = 1 / \pi$ has sub-peaks in the low stretching region. H_n for case B at $St = 1 / 2\pi$ has only one peak in the high stretching region, forming a Gaussian distribution.

Through the Lagrangian studies we identified a locally optimized operation condition for the continuous electroosmotic mixer, at which globally chaotic stirring is observed. For globally chaotic state mixing length l_m scales as $\ln(Pe)$, which minimizes the mixing length for mixing species with various Schmidt numbers. At non-optimum conditions, which results in regular flow zones, $l_m \propto Pe^\alpha$ scaling is observed. Therefore, presence of non-chaotic zones can significantly reduce the mixing performance. This is a subtle point that needs to be considered in the design of micro-mixers.

7.3. Numerical analysis of the relation between invariant manifold and chaotic mixing in oscillatory driven cavity flow

In Chapter VI, we numerically simulated oscillatory driven cavity flows at $Re = 10$ at various excitation frequencies. In order to understand the reason of fast mixing, an extensive numerical effort was made to extract the dynamic skeleton (invariant manifold), because the invariant manifolds of hyperbolic invariant sets of flow field form the spatial template which organizes the transport and mixing processes. The manifolds of the periodic points can be of great use in determining the geometry of dispersion of the passive tracer particles in mixing flows. For the purpose of detection of the unstable manifold, it is numerically possible to conduct simply surrounding the pre-determined point (hyperbolic periodic point) with passive tracer particles in the formation of circle and then tracking this ‘cluster of particles’. During the simulation, the circular cluster deformed but will always surround a finite segment of the stable and unstable manifolds. As the number of periods increased the length of unstable manifold enclosed by the cluster of particles increased whereas the length of the stable manifold decreased. After a certain number of periods the circle appeared as a single curve surrounding part of the unstable manifold. Given the fact that local formation of fast homogenized region is determined by the unstable manifolds, one can infer the clue to how to answer the question about topological similarity between well-mixed zone of scalar mixing and shuffled region of colored particle tracking results.

REFERENCES

1. Hardt S, Drese K S, Hessel V and Schönfeld F 2005 Passive micromixers for applications in the microreactor and μ TAS fields *Microfluid Nanofluid* **1** 108-18
2. Qian S and Bau H H 2002 A chaotic electroosmotic stirrer *Anal. Chem.* **74** 3616-25
3. Aref H 1984 Stirring by chaotic advection *J. Fluid Mech.* **143** 1-21
4. Strook A D, Dertinger S K W, Ajdari A, Mezic I, Stone H A and Whitesides G M 2002 Chaotic mixer for microchannels *Science* **295** 647-51
5. Jones S W 1991 The enhancement of mixing by chaotic advection *Phys. Fluids A* **3** 1081-6
6. Muzzio F J, Swanson P D and Ottino J M 1991 The statistics of stretching and stirring in chaotic flows *Phys. Fluids A* **3** 822-34
7. Ottino J M, Leong C W, Rising H and Swanson P D 1988 Morphological structures produced by mixing in chaotic flows *Nature* **333** 419-25
8. Liu M, Peskin R L, Muzzio F J and Leong C W 1994 Structure of the stretching field in chaotic cavity flows *AIChE J.* **40** 1273-86
9. Beskok A and Warburton T C 2001 An unstructured hp finite-element scheme for fluid flow and heat transfer in moving domains *J. Comp. Phys.* **174** 492-509
10. Ottino J M 1989 *The Kinematics of Mixing: Stretching, Chaos, and Transport* (Cambridge, UK: Cambridge University Press)
11. Kim H J and Beskok A 2007 Quantification of chaotic strength and mixing in a micro fluidic system *Journal of Micromechanics and Microengineering* **17** 2197-210 (Accessed at www.iop.org/journals/jphysd)
12. Karniadakis G E and Sherwin S J 2005 *Spectral/hp Element Methods for Computational Fluid Dynamics* (Oxford, UK: Oxford University Press)
13. Canuto C, Hussaini M Y, Quarteroni A and Zang T A 1988 *Spectral Methods in Fluid Dynamics* (New York: Springer-Verlag)
14. Couzy W 1995 *Spectral Element Discretization of the Unsteady Navier-Stokes equations and its Iterative Solution on Parallel Computers* (Zurich: Swiss Federal Institute of Technology)
15. Gottlieb D, Hesthaven J S and Gottlieb S 2001/2002 *Spectral Methods for Time-Dependent Problems* (Cambridge, UK: Cambridge University Press)

16. Henderson R D 1994 *Unstructured Spectral Element Methods : Parallel Algorithms and Simulations* (Princeton, NJ: Princeton University Press)
17. Kruse G W 1997 *Parallel Nonconforming Spectral Element Solution of the Incompressible Navier-Stokes Equations in Three Dimensions* (Providence, RI: Brown University Press)
18. Sert C 2003 *Nonconforming Spectral Element Formulations* (College Station, TX: Texas A&M University Press)
19. Timmermans L J P, Mineev P D and Van de Vosse F N 1996 An approximation projection scheme for incompressible flow using spectral elements *Int. J. Numerical Methods in Fluids* **22** 673-88
20. Anagnostou G, Maday Y, Patera A T, Fischer P F and Rønquist E M 1991 Numerical simulation of incompressible fluid flows *Concurrency: Practice and Experience* **3** 667-85
21. Sert C and Beskok A 2006 Spectral element formulations on nonconforming grids: a comparative study of pointwise matching and integral projection methods *J. Comp. Phys.* **211** 300-25
22. Ronquist E M 1996 Convection treatment using spectral elements of different order *Int. J. Numerical Methods in Fluids* **22** 241-64
23. Evans J, Liepmann D and Pisano A P 1997 Planar laminar mixer *Proc. MEMS' 97, 10th IEEE Int. Workshop Micro Electromechanical System Nagoya Japan*
24. Niu X and Lee Y 2003 Efficient spatial-temporal chaotic mixing in microchannels *J. Micromech. Microeng.* **13** 454-62
25. Liu R H, Stremmer M A, Sharp K V, Olsen M G, Santiago J G, Adrian R J, Aref H and Beebe D J 2000 Passive mixing in a three-dimensional serpentine microchannel *J. MEMS* **9** 190-7
26. Rodrigo A J S, Mota J P B, Lefevre A, Leprevost J C and Saadatian E 2003 Chaotic advection in a three dimensional Stokes flow *AIChE J.* **49** 2749-58
27. Jiang F, Drese K S, Hardt S, Kupper M and Schönfeld F 2004 Helical flows and chaotic mixing in curved micro channels *AIChE J.* **50** 2297-305
28. Simonnet C and Groisman A 2005 Chaotic mixing in a steady flow in a microchannel *Phys. Rev. Lett.* **94** 134501
29. Liu M, Muzzio F J and Peskin R L 1994 Quantification of mixing in a aperiodic chaotic flows *Chaos, Solitons & Fractals* **4** 869-93
30. Anderson P D, Galaktionov O S, Peters G W M, Van de Vosse F N and Meijer H E H

- 2000 Chaotic fluid mixing in non-quasi-static time-periodic cavity flows *Int. J. Heat and Fluid Flow* **21** 176-85
31. Lee T H and Kwon T H 1999 A new representative measure of chaotic mixing in a chaos single-screw extruder *Advances in Polymer Technology* **18** 53-68
 32. Hwu T, Young D L and Chen Y Y 1997 Chaotic advections for Stokes flows in circular cavity *J. Engineer Mech* **123** 774-82
 33. Niu X, Liu L, Wen W and Sheng P 2006 Hybrid approach to high-frequency microfluidic mixing *Phys. Rev. Lett.* **97** 044501
 34. Tucker III C L and Peters G W M 2003 Global measures of distributive mixing and their behavior in chaotic flows *Korea-Australia Rheology J.* **15** 197-208
 35. Giona M, Cerbelli S and Vitacolonna V 2004 Universality and imaginary potentials in advection-diffusion equations in closed flows *J. Fluid Mech.* **513** 213-27
 36. Giona M, Cerbelli S and Vitacolonna V 2004 Spectral properties and transport mechanisms of partially chaotic bounded flows in the presence of diffusion *Phys. Rev. Lett.* **92** 114101
 37. Gleeson J P 2005 Transient micromixing: Examples of laminar and chaotic stirring *Phys. Fluids* **17** 100614
 38. Sudarsan A P and Ugaz V M 2006 Fluid mixing in planar spiral microchannels *Lab Chip* **6** 74-82
 39. Xia H M, Shu C, Wan S Y M and Chew Y T 2006 Influence of the Reynolds number on chaotic mixing in a spatially periodic micromixer and its characterization using dynamical system techniques *J. Micromech. Microeng.* **16** 53-61
 40. Hessel V, Löwe H and Schönfeld, F. 2005 Micromixers - a review on passive and active mixing principles *Chem. Engineer. Science* **60** 2479-501
 41. Chang C C and Yang R J 2007 Electrokinetic mixing in microfluidic systems *Microfluid Nanofluid* **3** 501-25
 42. Kang T G and Kwon T H 2004 Colored particle tracking method for mixing analysis of chaotic micromixers *J. Micromech. Microeng.* **14** 891-9
 43. Camesasca M, Manas-Zloczower I and Kaufman M 2005 Entropic characterization of mixing in microchannels *J. Micromech. Microeng.* **15** 2038-44
 44. Kim D S, Lee I H, Kwon T H and Cho D W 2004 A barrier embedded Kenics micromixer *J. Micromech. Microeng.* **14** 1294-301

45. Jeon M K, Kim J H, Noh J, Kim S H, Park H G and Woo S I 2005 Design and characterization of a passive recycle micromixer *J. Micromech. Microeng.* **15** 346-50
46. Lee S W, Kim D S, Lee S S and Kwon T H 2006 A split and recombination micromixer fabricated in a PDMS three-dimensional structure *J. Micromech. Microeng.* **16** 1067-72
47. Cha J H, Kim J S, Ryu S K, Park J Y, Jeong Y W, Park S W, Park S H, Kim H C and Chun K J 2006 A highly efficient 3D micromixer using soft PDMS bonding *J. Micromech. Microeng.* **16** 1778-82
48. Glasgow I, Batton J and Aubry N 2004 Electroosmotic mixing in microchannels *Lab Chip* **4** 558-62
49. Lee C Y, Lee G B, Fu L M, Lee K H, and Yang R J, 2004 Electrokinetically driven active micro-mixers utilizing zeta potential variation induced by field effect *J. Micromech. Microeng.* **14** 1390-8
50. Goulet A, Glasgow I and Aubry N 2006 Effects of microchannel geometry on pulsed flow mixing *Mech. Res. Com.* **33** 739-46
51. Coleman J T, McKechnie J and Sinton D 2006 High-efficiency electrokinetic micromixing through symmetric sequential injection and expansion *Lab Chip* **6** 1033-9
52. Biddiss E, Erickson D and Li D 2004 Heterogeneous surface charge enhanced micromixing for electrokinetic flows *Anal. Chem.* **76** 3208-13
53. Sundaram N and Tafti D K 2004 Evaluation of microchamber geometries and surface conditions for electrokinetic driven mixing *Anal. Chem.* **76** 3785-93
54. Chang C C and Yang R J 2004 Computational analysis of electrokinetically driven flow mixing in microchannels with patterned blocks *J. Micromech. Microeng.* **14** 550-8
55. Holden M A, Kumar S, Castellana E T, Beskok A and Cremer P S 2003 Generating fixed concentration arrays in a microfluidic device *Sens. Actuators B* **92** 199-207
56. Fereday D R, Haynes P H and Wonhas A 2002 Scalar variance decay in chaotic advection and Batchelor-regime turbulence *Phys. Rev. E.* **65** 035301
57. Balkovsky E and Fouxon A 1999 Universal long-time properties of Lagrangian statistics in the Batchelor regime and their application to the passive scalar problem *Phys. Rev. E.* **65** 4164-74
58. Kumar S, Kim H J and Beskok A 2007 Numerical simulations of peristaltic mixing *J. Fluids Eng.* **129** 1361-71
59. Karniadakis G, Beskok A and Aluru N 2005 *Microflows and Nanoflows: Fundamentals and Simulation* (New York: Springer)

60. Sasaki N, Kitamori T and Kim H B 2004 AC electroosmotic micromixer for chemical processing in a microchannel *Lab Chip* **6** 550-4
61. Kim H J and Beskok A 2005 Characterization of mixing in an electroosmotically stirred continuous micro mixer *58th Annual Meeting of the Division of Fluid Dynamics American Physical Society Chicago IL*
62. Kim H J 2004 *Quantification of chaotic mixing in microfluidic system Master's Thesis* Department of Mechanical Engineering, Texas A&M University
63. Biringen S and Danabasoglu G 1989 Oscillatory flow with heat transfer in a square cavity *Phys. Fluids A* **11** 1796-812
64. Nishimura T and Kunitsugu K 1997 Fluid mixing and mass transfer in two-dimensional cavities with time-periodic lid velocity *Int. J. Heat and Fluid Flow* 497-506
65. Panton R L 2005 *Incompressible flow* (Hoboken, NJ: Wiley)
66. Maday Y and Patera A T 1989 Spectral element methods for the Navier-Stokes equations *State of the Art Surveys in Computational Mechanics* (ASME: New York)
67. Bernardi C and Maday Y 1988 A collocation method over staggered grids for the Stokes Problem *Int. J. Numer. Meth. Fluids* **8** 537-57
68. Guermond J L, Mineev P and Shen J 2006 An overview of projection methods for incompressible flows *Comput. Methods Appl. Mech. Engrg.* **195** 6011-45
69. van Kan J. 1986 A second order accurate pressure correction scheme for viscous incompressible flow *SIAM J. Sci. Stat. Comput.* **7** 870-91
70. Fisher P F 1997 An overlapping Schwarz method for spectral element solution of the incompressible Navier-Stokes equations *J. Comp. Phys.* **133** 84-101
71. Donea J, Giuliani S, Laval H and Quartapelle L 1984 Time-accurate solution of advection-diffusion problems by finite elements *Comput. Methods Appl. Mech. Engrg.* **45** 123-45
72. Datta B N 1995 *Numerical Linear Algebra and Applications* (New York: Brooks/Cole Publishing Company)
73. Löhner R, Yang C, Cebal J, Camelli F, Soto O and Waltz J 2006 Improving the speed and accuracy of projection-type incompressible flow solvers *Comput. Methods Appl. Mech. Engrg.* **195** 3087-109
74. Wiggins S 1988 Stirred but not mixed *Nature* **333** 395-6
75. Coppola G, Sherwin S J and Peiro J 2001 Nonlinear particle tracking for high-order

- elements. *J. Comp. Phys.* **172** 356-86
76. Giona M and Cerbelli S 2002 C^∞ -interpolation of discrete fields on regular and irregular grids *J. Comp. Phys.* **176** 145-69
 77. Byrde O, Couzy W, Deville M O and Sawley M L 1999 High-performance parallel computing for incompressible flow simulations *Comput. Mech.* **23** 98-107
 78. Intel Corporation 2008 *Intel Math Kernel Library Reference Manual* (Intel)
 79. Kovasznay L I G 1948 Laminar flow behind a two-dimensional grid *Proc. of the Cambridge Philos. Soc.* **44** 58-62
 80. Botella O and Peyret R 1998 Benchmark spectral results on the lid-driven cavity flow *Comput Fluids* **27** 421-33
 81. Zhang K K Q 2005 A discrete splitting finite element method for numerical simulations of incompressible Navier-Stokes flows *Int. J. Numer. Meth. Engng* **64** 285–303
 82. Keskar J and Lyn D 1999 A Computations of a laminar backward-facing step flow at $Re = 800$ with a spectral domain decomposition method. *Int. J. Numer. Meth. Fluids* **29** 411-27
 83. Underwood R L 1969 Calculation of incompressible flow past a circular cylinder at moderate Reynolds numbers. *J. Fluid Mech.* **37** 95-114
 84. Celik B, Akdag U, Gunes S and Beskok A 2008 Flow past an oscillating circular cylinder in a channel *In Preparation*
 85. Behr M A, Hastreiter D, Mittal S and Tezduyar T E 1995 Incompressible flow past a circular cylinder: dependence of the computed flow field on the location of the lateral boundaries *Comput. Methods Appl. Mech. Engrg.* **123** 309-16
 86. Minev P D, Van de Vosse F N, Timmermans L J P and Van Steenhoven A A 1995 A second order splitting algorithm for thermally-driven flow problems *Int. J. Num. Meth. Heat Fluid Flow* **6** 51-60
 87. Prabhakar V and Reddy J N 2006 Spectral/hp penalty least-squares finite element formulation for the steady incompressible Navier–Stokes equations *J. Comp. Phys.* **215** 274-97
 88. Reddy J N and Gartling D K 2000 *The Finite Element Method in Heat Transfer and Fluid Dynamics* (Boca Raton, FL: CRC Press)
 89. Schasfoort R B M, Schlautmann S, Hendrikse J and Van den Berg A 1999 Field-effect flow control for microfabricated fluidic networks *Science* **286** 942-5

90. Jones S W 1994 Interaction of chaotic advection and diffusion *Chaos, Solitons & Fractals* **4** 929-40
91. Souvaliotis A, Jana S C and Ottino J M 1995 Potentialities and limitations of mixing simulations *AIChE J.* **41** 1605-21
92. Hilborn R C 1994 *Chaos and Nonlinear Dynamics* (Oxford, UK: Oxford University Press)
93. Sprott J C 2003 *Chaos and Time-Series Analysis* (Oxford, UK: Oxford University Press)
94. Suzuki H, Ho C and Kasagi N 2004 A chaotic mixer for magnetic bead-based micro cell sorter *J. MEMS* **13** 779-90
95. Voth G A, Haller G and Gollub J P 2002 Experimental measurements of stretching fields in fluid mixing *Phys. Rev. Lett.* **88** 254501
96. Ottino J M 1991 Unity and diversity in mixing: stretching, diffusion, breakup, and aggregation in chaotic flows *Phys. Fluids A* **3** 1417-30
97. Antonsen T M, Fan Z, Ott E and Garcia-Lopez E 1996 The role of chaotic orbits in the determination of power spectra of passive scalars *Phys. Fluids* **8** 3094-104
98. Horita T, Hata H and Mori H 1990 Long-time correlations and expansion-rate spectra of chaos in Hamiltonian systems *Prog. Theor. Phys.* **83** 1065-70
99. Voth G A, Saint T C, Dobler G and Gollub J P 2003 Mixing rates and symmetry breaking in two-dimensional chaotic flow *Phys. Fluids.* **15** 2560-6
100. Bringer M R, Gerdtts C J, Song H, Tice J D and Ismagilov R F 2004 Microfluidic systems for chemical kinetics that rely on chaotic mixing in droplets *Phil. Trans. R. Soc. Lond. A* **362** 1087-104
101. Ottino J M, Wiggins S 2004 Introduction: mixing in microfluidics *Phil. Trans. R. Soc. Lond. A* **362** 923-35
102. Ott E 1993 *Chaos in dynamical systems* (Cambridge, UK: Cambridge University Press)
103. Soper S A, Henry A C, Vaidya B, Galloway M, Wabuyele M and McCarley R L 2002 Surface modification of polymer-based microfluidic devices *Anal. Chim. Acta* **470** 87-99
104. Lopez-navarrete E and Ocana M 2001 Fine spherical particles of narrow size distribution in the Cr₂O₃-Al₂O₃ system *J. Materials Sci.* **36** 2383-9
105. Kallay N, Torbit Z, Golie M and Matijevit E 1991 Determination of the Isoelectric Points of Several Metals by an Adhesion Method *J. Phys. Chem.* **95** 7028-32

106. Dutta P and Beskok A 2001 Analytical solution of combined electroosmotic/pressure driven flows in two-dimensional straight channels: finite Debye layer effects *Anal. Chem.* **73** 1979-86
107. Dutta P and Beskok A 2001 Analytical solution of time periodic electroosmotic flows: analogies to Stokes' second problem *Anal. Chem.* **73** 5097-102
108. Anderson P D, Galaktionov O S, Peters G W M, Van de Vosse F N and Meijer H E H 1999 Analysis of mixing in three-dimensional time-periodic cavity flows *J. Fluid Mech.* **386** 149-66
109. Wiggins S 1994 *Normally Hyperbolic Invariant Manifolds in Dynamical Systems* (New York: Springer-Verlag)
110. Jana S C, Metcalfe G and Ottino J M 1994 Experimental and computational studies of mixing in complex Stokes flows: the vortex mixing flow and multicellular cavity flows *J. Fluid Mech.* **269** 199-246
111. Swanson P D and Ottino J M 1990 A comparative computational and experimental study of chaotic mixing of viscous fluids *J. Fluid Mech.* **213** 227-49
112. Alvarez M M, Muzzio F J, Cerbelli S, Adrover A and Giona M 1998 Self-similar spatiotemporal structure of intermaterial boundaries in chaotic flows *Phys. Rev. Lett.* **81** 3395-8
113. Muzzio F J, Alvarez M M, Cerbelli S, Giona M and Adrover A 2000 The intermaterial area density generated by time- and spatially periodic 2D chaotic flows *Chem. Engineer. Science* **55** 1497-508
114. Meinhart C D, Wereley S T and Santiago J G 1999 PIV measurements of a microchannel flow *Exp. Fluids* **27** 414-9
115. Santiago J G, Wereley S T, Meinhart C D, Beebe D J and Adrian R J 1998 A particle image velocimetry system for microfluidics *Exp. Fluids* **25** 316-9

VITA

Ho Jun Kim was born in Seoul, South Korea in 1980. He graduated with a B.S. degree from Mechanical Engineering department of the Hanyang University, Seoul, Korea in 2002. In May 2003, he joined the bio-microfluidics group, advised by Dr. Ali Beskok. In August 2004, he got M.S. degree from Mechanical Engineering department of the Texas A&M University. His technical interests are in microfluidic mixing, nonlinear dynamical systems, chaotic advection, topological mixing, scalar transport in creeping flows, spectral element method, finite element method, and particle tracking algorithms. Ho Jun Kim can be reached at tiger.anima@gmail.com. His permanent address is: Jookong Apt.138-201, Joongang-dong, Gwacheon-si, Gyeonggi-do, South Korea, 427-010.